Mechano-biology of heterogeneous tissues using upscaling methods : application to osteoarcoma

Adel Moreno

To cite this version:

Adel Moreno. Mechano-biology of heterogeneous tissues using upscaling methods : application to osteoarcoma. Fluid Dynamics [physics.flu-dyn]. Institut National Polytechnique de Toulouse - INPT, 2022. English. NNT : 2022INPT0015 . tel-04191571

HAL Id: tel-04191571
https://theses.hal.science/tel-04191571

Submitted on 30 Aug 2023

THÈSE

En vue de l'obtention du

DOCTORAT DE L'UNIVERSITÉ DE TOULOUSE

Délivré par :

Institut National Polytechnique de Toulouse (Toulouse INP)

Discipline ou spécialité :

Dynamique des fluides

Présentée et soutenue par :

M. ADEL MORENO

le mardi 1 mars 2022

Titre :

Mécano-biologie des tissus hétérogènes par changement d'échelles : application à l'ostéosarcome

---

Ecole doctorale :

Mécanique, Energétique, Génie civil, Procédés (MEGeP)

Unité de recherche :

Institut de Mécanique des Fluides de Toulouse (IMFT)

Directeurs de Thèse :

M. PASCAL SWIDER
MME PAULINE ASSEMAT

Rapporteurs :

M. BENOIT NOETINGER, IFPEN
MME PASCALE ROYER, Laboratoire de Mécanique et Génie Civil

Membres du jury :

MME ANNE GOMEZ-BROUCHET, CHU TOULOUSE, Présidente
MME AURÉLIE DUTOUR, CENTRE LEON BERARD LYON, Membre
MME NATACHA ENTZ-WERLE, UNIVERSITE STRASBOURG, Membre
MME PAULINE ASSEMAT, TOULOUSE INP, Membre
M. MICHEL QUINTARD, TOULOUSE INP, Membre
M. PASCAL SWIDER, TOULOUSE INP, Membre

Abstract

Osteosarcoma is a primary bone tumour that occurs mainly in adolescents and young adults. The survival rate at 5 years is 70% and drops to 25% for patients with metastases or poor responders to treatment. New developments are needed to improve the specific management of patients. These tumours show strong spatial heterogeneities in bone micro-architecture, in cell populations distribution but also in the response to treatment. At the tissue scale and from a biophysical point of view, osteosarcoma can be classified as a strongly heterogeneous porous medium with mechanical stimuli potentially playing a significant role in its formation and evolution.

We propose a consistent upscaling method to characterize the mechanical properties of such a highly heterogenous porous media. It is based upon a sequential grid-block approach combined to an extend-local method. The methodology is adapted to large size binarized images and especially histological slices obtained in clinical routines. Flow and diffusive models are explored as well as elastic and poroelastic behaviors. Piece-wise constant equivalent parameters such as tissular permeabilities and stiffness coefficients are determined with reliability. Several methodological results are emphasized in this thesis such as the identification of robust equivalent parameters inequalities depending on the grid-block elements boundary conditions or the evaluation of extend-local methods use in stiffness parameters calculations.

In a preliminary clinical study, relationships between tissular mechanical properties and cellular populations are emerging. On the cohort of patients investigated, it is shown that the response to treatment can be correlated to micro-environment architecture and equivalent tissue properties. These results support the search for mechanobiological markers of chemotherapy response for osteosarcoma patients.

Résumé

L'ostéosarcome est une tumeur osseuse primitive qui survient principalement chez les adolescents et les jeunes adultes. Le taux de survie à 5 ans est de 70% et chute à 25% pour les patients présentant des métastases ou ne répondant pas aux traitements. De nouveaux développements sont nécessaires pour améliorer la prise en charge spécifique des patients. Ce type de tumeurs présente de fortes hétérogénéités spatiales dans la micro-architecture osseuse, dans la distribution des populations cellulaires mais aussi dans la réponse au traitement. A l'échelle tissulaire et du point de vue de la biophysique, l'ostéosarcome peut être considéré comme un milieu poreux fortement hétérogène et nous supposons que l'ostéosarcome est sensible aux effets mécaniques lors de sa formation et de son évolution.

Nous proposons une méthode de changement d'échelles pour caractériser les propriétés mécaniques de tels milieux poreux. La méthode s'appuie sur une approche séquentielle "grid-block" combinée à une méthode "extend-local". La méthodologie est adaptée à des images de grandes tailles et notamment aux images binaires de coupes histologiques d'ostéosarcomes obtenues en routine clinique. Des modèles d'écoulement, de diffusion, d'élasticité et de poroélasticité sont étudiés. Les paramètres équivalents, constants par morceaux, de type perméabilités tissulaires et coefficients de raideurs tissulaires sont déterminés avec fiabilité. Plusieurs résultats méthodologiques ont été obtenus tels que les inégalités portant sur les paramètres équivalents en fonction des conditions aux limites imposées sur les éléments du "grid-block" ou la caractérisation du rôle des méthodes "extend-local" dans le calcul des paramètres de raideur.

Dans une étude clinique préliminaire, des relations entre les propriétés mécaniques tissulaires et les paramètres cellulaires sont données. Une cohorte réduite de patients montre que la réponse au traitement peut être corrélée à l'architecture du micro-environnement et à ses propriétés mécaniques. Ceci pourrait soutenir la recherche de marqueurs mécanobiologiques pour le suivi de la réponse au traitement chez les patients atteints d'ostéosarcome.

Framework and collaborations

This thesis work is at the interface with fundamental and life sciences, from mathematics to public health through biology. The ambition of the innovative project in which this work falls is to integrate fundamental and applied science such as mathematics, physics or numerical modeling to known technical and clinical approaches. As the subject is highly multidisciplinary, the relevance of the work lies in strong collaborations between specialists in the various disciplines addressed. They will allow to bring adapted and relevant answers to the various problems raised in this thesis.

This work was conducted within the group ”Milieux Poreux et Biologiques” (MPB) of the Institute of Fluid Mechanics of Toulouse (IMFT), an institute specialized in research on physical and chemical phenomena present in fluid flows. The expertise of the group members, theoretical, numerical or experimental, is mainly based on multi-physics couplings in heterogeneous media.

The thesis is supervised by P. Assémat (CR CNRS, IMFT & MPB) in the framework of her CNRS research project about mechanobiology of osteosarcoma and P. Swider (PU, IMFT & MPB), a specialist in mechanics with a particular interface with living systems, in particular in bone tissue. M. Quintard (DR CNRS, IMFT & MPB), a specialist in porous media and upscaling methods, is a co-supervisor. From a clinical point of view, we worked in collaboration with A. Gomez-Brouchet (CHU Toulouse), anatomo-pathologist of osteosarcoma. This collaboration brings in particular an expertise of clinician in the highly complex framework of the biology and mechanics of osteosarcoma. Finally, the contribution of A. Mancini (IMFT & MPB) has allowed to take into account the clinical biological material by Image-Processing methods (machine learning algorithm).

Remerciements

Voilà venu le temps des remerciements qui viennent conclure tout travail de thèse. Un court texte qui a la lourde tâche de traduire ce voyage initiatique entrepris un mois d'octobre 2018.

Je tiens tout d'abord à remercier Pauline Assémat, qui, par son soutient de tous les jours a su me guider professionnellement, mais aussi humainement durant ces trois années (et demie). Je ne te remercierai jamais assez d'avoir su prendre le risque de me prendre comme élève pour ce travail pluridisciplinaire alors même que ma formation initiale en mathématique pure ne le permettait sans doute pas. Merci aussi pour les petites astuces du quotidien facilitant le travail de chercheur (une esperluette toujours à la fin d'une commande linux !). Enfin, merci pour ta gentillesse qui m'a permis entre autre de vivre plus sereinement cette pandémie. Merci pour tout Pauline !
Je remercie Pascal Swider qui a guidé mes premiers pas dans la recherche. Je ne saurais vous remercier assez de la bienveillance et la constance dont vous avez fait preuve dans votre encadrement et ce même lorsque vous traversiez des moments difficiles. La thèse ne se réduisant pas seulement à la recherche, je voulais aussi vous remercier pour votre aide dans la préparation de mes cours. Votre expérience de la pédagogie m'a fortement aidé dans l'accomplissement de cette tâche où tout était un peu nouveau pour moi et donc difficile à appréhender. Merci pour tout Pascal !
J'aimerais remercier Michel Quintard, un mentor, qui a su me guider dans l'exploration des méthodes de changement d'échelles. Votre collaboration sur ce projet s'est transformée dès les premiers jours en un véritable co-encadrement. Je me souviendrai toujours de nos discussions scientifiques mais aussi de nos discussions des choses de la vie (et notamment celle sur les langues régionales françaises). Chacune de mes questions, qu'elles soient maladroites, naïves ou même les deux, ne sont jamais restées bien longtemps sans une réponse pertinente de votre part. Merci pour tout Michel !

Je remercie les membres du jury d'avoir accepté l'évaluation de mes travaux de thèse et particulièrement les rapporteurs pour leurs corrections qui ont servi à l'amélioration de ce manuscrit. Je voulais remercier tous les membres du groupe Milieu poreux biologique qui ont rendu la vie de bureau à l'IMFT très agréable. Cette thèse aurait sans doute été très différente sans l'aide et l'amitié d'Anthony : merci et accroche-toi ! En arrivant à l'IMFT, j'ai pu compter dès le premier jour sur le trio de choc composé de Baptiste, d'Adlan et de Maxime : merci à vous trois pour votre aide et pour toutes nos belles discussions de l'après-midi ! Pour ces mêmes raisons, je remercie Alexandre qui s'est retrouvé bien malgré lui (au début) embarqué dans ces très longues conversations. Merci à mes collègues et amis thésards Marion, Chris, David and last but not least Omar. Je leur souhaite bonne chance pour leur fin de thèse. Enfin, merci à Sylvie et Yohan pour leurs participations à la construction de ce travail de thèse. J'en profite aussi pour remercier Romain pour sa grande contribution au projet qui va permettre de faire vivre mes codes après mon départ.

À mes frères et sœurs sans qui la vie n'aurait sans doute pas beaucoup de sens. À ma jumelle Myriam alias *Abu sans couteau*, "mode c2i on" : je te remercie pour tes graphs apparaissant dans ce manuscrit. À Malik et à tous ses "jeux" allant du tonneau au premier battle royal Colin-Maillard (version Bizeul) en passant par le serpent la face par terre. À Brahim, alias *Fievel*, pour la tradition bi-décennale du chapitre du mercredi soir et dont les charades n'ont que très peu de sens.

Merci aux petits nouveaux du gang, Alice, Aurore et Damian qui embellissent un peu plus nos vies à tous.
À mes grands-parents, Isidore Moreno, Marie-Thérèse Moreno, Ben Brahim Benyahia et Zohra Aoufi qui ont fait le choix d'offrir un avenir meilleur à leurs descendants.

Je dédie cette thèse à mes parents qui ont réussi l'exploit, malgré les moments très difficiles, d'amener leurs 4 enfants là où ils en sont aujourd'hui. Ils ont toujours su me rendre un peu plus "normal" sans pour autant me changer. Merci infiniment d'avoir tenu bon et de nous avoir offert les plus belles années de nos vies. À ma mère, pour toutes ces balades et la logistique du très difficile pot de thèse : "n'est pas Mam qui veut". À mon père, pour son délicieux ebly à la tomate, sa nouvelle spéciale et autre pétrole dans les pizzas.

Après le CP, j'arrête !

A. Moreno, 2000/2001

Contents

Nomenclature

Acronyms

ECM, OECM, FECM	Extra-Cellular Matrix, Osseous Extra-Cellular Matrix, Fibrous Extra-Cellular Matrix
LCS	Lacunar-Canalicular System
MRI	Magnetic Resonance Imaging
PDE	Partial Differential Equations
FEM	Finite Element Method
FVM	Finite Volume Method
DNS	Direct Numerical Simulation
REV	Representative Elementary Volume
AE	Asymptotic Expansion method
VA	Volume Averaging method
BCs	Boundary Conditions
W	Wall boundary condition
S	Symmetric boundary condition
PL	Open boundary condition
P	Periodic boundary condition
KUBC	Kinematic Uniform Boundary Condition
SUBC	Stress Uniform Boundary Condition
2D, 3D	2 and 3-Dimensional space

List of Symbols

$l,\ L$	Characteristic lengths
$\Phi,\ \varphi$	Porosity
η	Scale separation parameter
ρ	Volumetric mass density
μ	Dynamic viscosity
g	Gravity constant vector
$E,\ E_{OECM},\ E_{FECM}$	Young's modulus, Young's modulus in osseous ECM, Young's modulus in fibrous ECM
$\nu,\ \nu_{OECM},\ \nu_{FECM}$	Poisson's ratio,Poisson's ratio in osseous ECM, Poisson's ratio in fibrous ECM
α	Biot's coefficient
n	Unitary normal vector
$\mathbf{K}$	Permeability tensor
$\mathbf{D}$	Diffusion tensor
$\mathbf{C}$	Stiffness tensor
$\mathbf{S}$	Compliance tensor
$\mathbf{DC}$	Poroelastic stiffness tensor
δ	Buffer region size
$r_p,\ r_s$	Pearson and Spearman's correlation coefficients
$\mathbf{u}$	Velocity
$\mathbf{U}, \mathbf{q}$	Darcy velocity
p	Pressure
$\mathbf{J}$	Diffusive flux
c	Concentration
$\tilde{\mathbf{u}}$	Displacement
σ	Stress tensor
σ_{tot}	Poroelastic stress tensor
ϵ	Strain tensor
∇, ∇_{sym}	Gradient operator, Symmetric gradient operator
$\nabla.$	Divergence operator
Δ	Laplacian operator
$\langle \bullet \rangle_{\Omega}$	Average operator on a domain Ω
$\mathbb{R}$	Real numbers
$(e_i)_{1 \leq i \leq 2}$	Canonical basis of $\mathbb{R}^2$

Chapter 1

Introduction

Contents

This thesis propose a mechanobiological approach to explore new quantitative metrics obtained from clinical histological images in the context of bone cancer study. Various questions raised by biologists and clinician are explored. This introduction chapter presents an non exhaustive literature of the current understanding of osteosarcoma from a clinical, biological and mechanical point of view. Problematics and objectives of the doctoral project are detailed in the last section.

1.1 Osteosarcoma

1.1.1 Osteosarcoma: clinical aspects

Primary bone tumors include osteosarcomas, chondrosarcomas, Ewing sarcomas and other types of rare tumors amongst which osteosarcomas are the most frequent [1]. The World Health Organization defines osteosarcoma as a primary osseous malignant neoplasm composed of mesenchymal cells producing bone tissue, even in small amount. This bone tissue can be mineralised (mineralised extra-cellular matrix ECM) along with immature bone tissue or non-mineralized ECM (osteoid).
In the general population, the pathology occurrence of is 2-3/million/year. Its frequency varies according to age and follows a bi-modal distribution [2] with two peaks found respectively in adolescence and young adults (15-19 years) and in the elderly ($>$ 60 years). Men are affected 1.4 times more than women [3].

The tumors occur most frequently in the metaphyses of long bones, such as the femur, tibia or humerus but can also appear in other types of bones, such as the skull, jaw, ribs and pelvis. Although the etiology of the disease is still poorly understood, some risk factors have been identified such as patient-specific factors (age, genetic diseases, pre-existing bone abnormalities) or environmental factors such as exposure to ionizing radiation and alkaline agents [4].

Typical symptoms of osteosarcoma are local persistent bone pain at rest (especially at night) followed by swelling and limitation of joint movement.
The initial assessment of a suspected tumor comprises a full history, physical examination, and radiographs. Radiography allow a description of osseous changes but cannot always decide on the malignancy of the tumor. In that case, a magnetic resonance imaging (MRI) of the whole bone and its neighboring joints, to not miss skip lesions, has to be conducted. Finally, a biopsy

and its histology examination are needed for diagnosis confirmation. Beside their use for diagnostic, biopsies are used for research purpose [5] and could be a possible tool for personalised patient management, provided relevant markers can be extracted.

The generic term ”osteosarcoma” includes subcategories of the pathology such as high-grade forms including the conventional form which accounts for 90% of osteosarcomas, well differentiated low-grade intramedullary, small cell and telangiectatic [6]. Within the conventional form, about fifteen different forms are characterized according to the nature of the predominant matrix created by the tumor cells (fig. 1.1). The main ones, representing 75% of the cases, are osteoblastic type osteosarcomas (fig. 1.1a) with an essentially mineralized matrix consisting of bone or osteoid. When the matrix is cartilaginous, it is called chondroblastic osteosarcoma (fig. 1.1c). Finally, conventional osteosarcoma is characterized as fibroblastic when fibroblastic cell proliferation is observed or simply when the tumor could not be effectively classified in the two previous categories (fig. 1.1b).

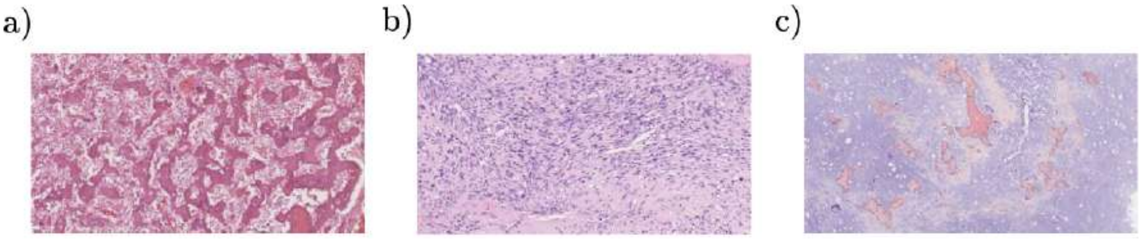

Figure 1.1: H&E stained histological section of the three conventional osteosarcoma categories a) osteoblastic b) fibroblastic c) chondroblastic [6].

While neoadjuvant chemotherapy was a innovative and efficient treatment strategy in the 70-80s, no new therapy since then has been demonstrated to be effective and no robust prognostic stratification exists. To date, the treatment still consists in a neoadjuvant chemotherapy followed by tumor surgical removal through a partial or total resection of the affected bone and a post-operation adjuvant chemotherapy. The MAP (doxorubicin/cisplatin/HD-MTX) regimen is most frequently used as the basis of treatment in children and young adult patients. Osteosarcoma is considered as a radioresistant tumor but recent studies suggest that a radiotherapy may be useful in some cases where there was a no complete resection of the tumor [3].
Patients are categorized according to their response to treatment and more precisely to neoadjuvant chemotherapy according to the classification of Huvos and Rosen, in ”good responder” or ”poor responder” as described in Table 1.1). The treatment response is assessed on histological slide (fig. 1.2). Grades are given according to the percentage of necrotic tumor cells evaluated on the territories of the tumor. Grade I corresponds to less than 10%, Grade II to a percentage between 10 and 90%, Grade III higher than 90%. Patients classified as Grade IV correspond to good responders to chemotherapy with a percentage higher than 99%.

	Grade Huvos et Rosen	Chemotherapy	Necrotic cells %
Bad response	Grade I	No effect	<10%
	Grade II	Low efficiency	10-90%
Good response	Grade III	Moderate efficace	91-99%
	Grade IV	Highly efficient	>99%

Table 1.1: Grading of response to treatment (neoadjuvant chemotherapy) in patients with osteosarcoma according to Huvos and Rosen grades.

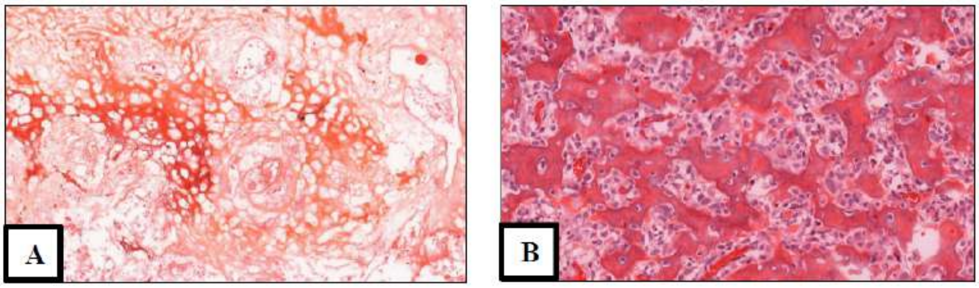

Figure 1.2: "Evaluation of response to chemotherapy according to the Huvos and Rosen classification. (A) Good response: no residual viable tumor cells grade IV. (B) Poor response: persistence of viable tumor cells" grade I [7].

Patients with localized disease have an overall survival rate of 70 to 75% at 5 years and only 25% for patients with metastatic disease, chemo-resistance or relapsed disease [8]. This variability in response to treatment, which can be related to patients [9] and to intratumoral heterogeneity [10], requires new diagnostic and treatment strategies.

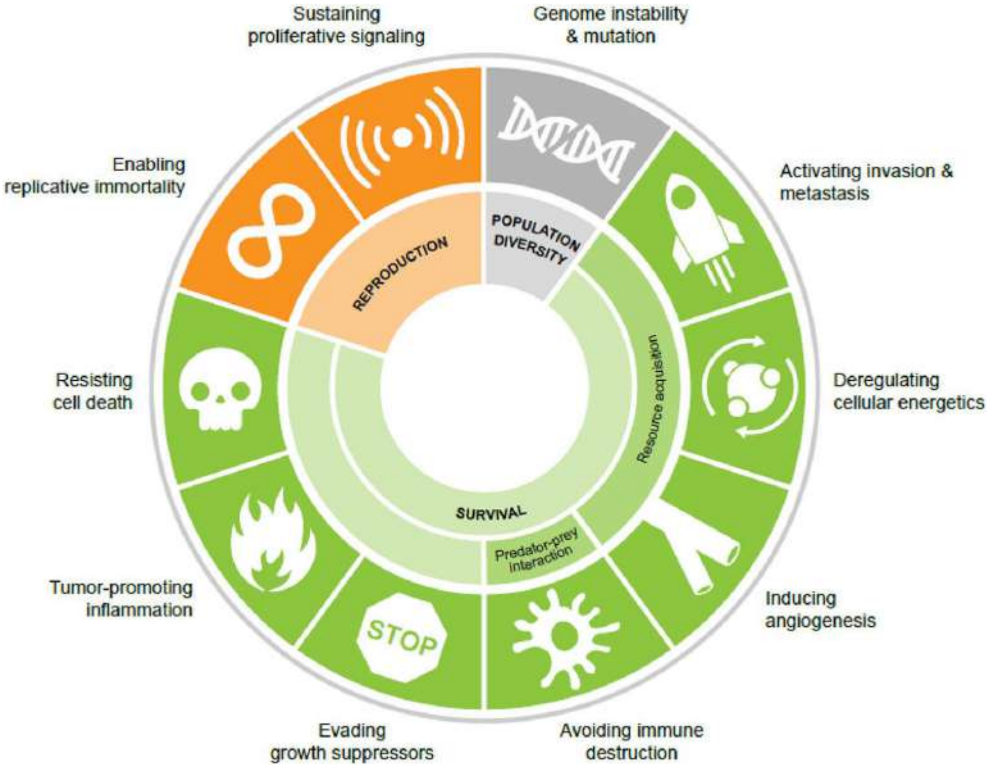

Figure 1.3: Diagram of the generic biological cancer hallmarks. Illustration from [11].

Cancers, including osteosarcoma, follow an evolution on spatial scales at different times of their development with generic biological hallmarks [12] as shown in figure 1.3. Cancers modify their environment in order to maintain a favorable terrain for the tumor to grow and spread. These phenomena induce changes on the architecture and mechanics of the tumor. For example, tumoral angiogenesis plays a crucial role in tumor pressure distribution and consequently in tumoral interstitial flows which in return plays a role on metastasis dissemination [13]. Recently, the inflammatory character (local or chronic) of the tumor has been highlighted and can lead to (1) angiogenesis and (2) increasing the risk of metastasis by a mechanical degradation of the extra-cellular matrix (ECM) [14]. Conversely, mechanical effects are shown to be related to each of these biological effects in the literature. For example, the authors of [15] highlight links between different biomechanical effects on the tumor microenvironment and cancer progression. Indeed, increased stress within the tumor due to cell proliferation disrupts the epithelium and leads to a biological chain reaction (fig. 1.4).

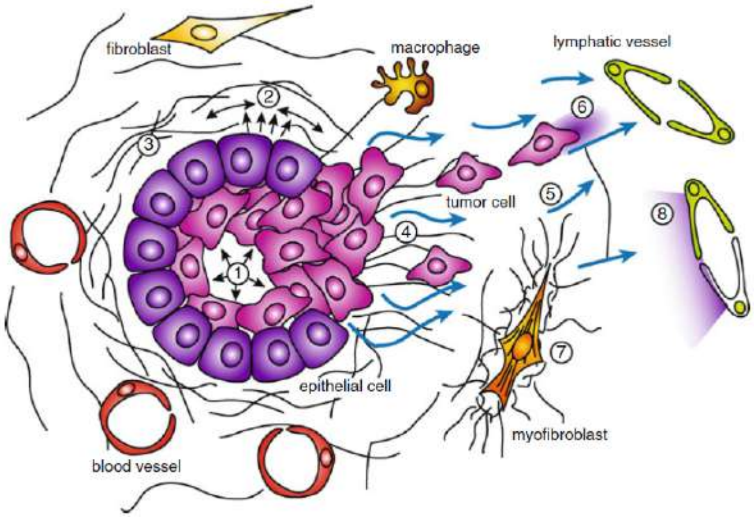

Figure 1.4: "Schematic of the biomechanical forces in the tumor microenvironment. As tumor cells proliferate and disrupt the epithelium, they generate stresses as a result of tumor growth (1). These stresses are transmitted to the surrounding extracellular matrix, generating radial compressive forces and circumferential tensile forces (2). The matrix is also becoming stiffer and more dense (3), and, at the invasive front, the matrix becomes reorganized, favoring tumor cell invasion (4). As the fluid pressure in the tumor increases due to the increase in tumor-associated angiogenesis, interstitial flow and lymphatic drainage increase (5). Tumor cells can use this flow to generate autologous gradients (6). At the same time, interstitial flow induces myofibroblast differentiation (7) and lymphatic chemokine secretion (8)" [15].

To account for the complexity of tumoral evolution, it seems crucial to point out that each of these phenomena are interconnected and act on each other in an nested way at each scale, mixing the purely biological and mechanical stages. Indeed, it is shown that the purely mechanical effects can act in a direct way on the cells of the tumor in controlled in vitro experiments [16] (fig. 1.5). Here, it is shown for instance that phenotype, secretome and cell differentiation can be altered by mechanical effects. Those effects include shear stress flow, compression, stretching and different types of interactions such as Cell-Cell and Cell-ECM interactions.

In the following section, these phenomena are described in more detail, focusing first on the biology of osteosarcoma and then on the mechanics.

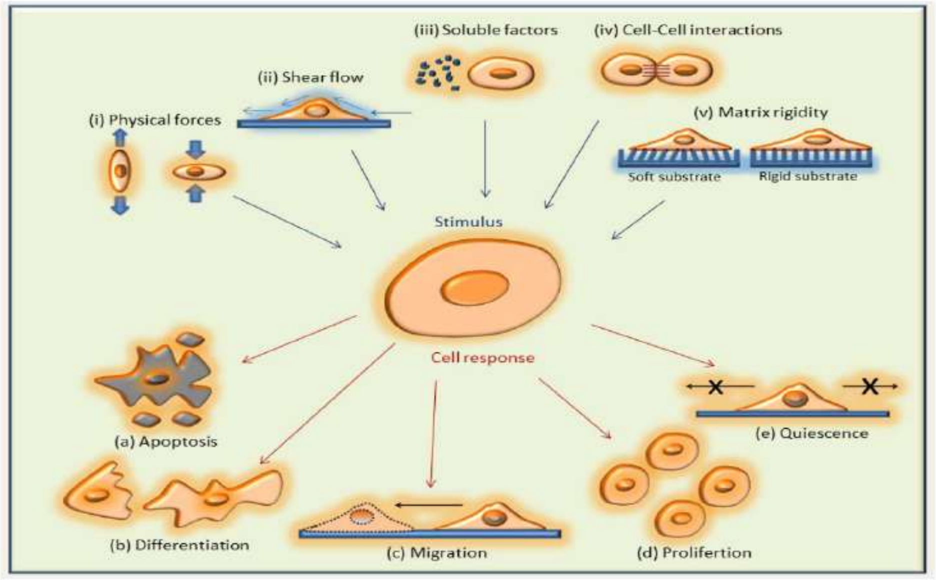

Figure 1.5: ”Cells respond to different microenvironmental stimulus in vivo. A schematic showing the different factors, (i) physical forces, (ii) shear flow, (iii) soluble factors, (iv) cell-cell interactions and (v) matrix rigity that trigger the cells to undergo changes in their behaviors and functions such as (a) apoptosis, (b) differentiation, (c) migration, (d) proliferation and (e) quiescence” [17].

1.1.2 Osteosarcoma: biological aspects

The biological study of osteosarcoma is an extremely complex problem due to the multiscale character of such tumors from a spatial and temporal point of view (fig. 1.6). Indeed, like in any biological system, studies can be performed at different spatial scales. To cite few, pathologies can be studied at the genomic scale, the proteins scale, the tissue scale or the organ scale. Each of these scales is usually studied, in a more or less thorough way, independently and without any quantitative coupling with the others. We have only recently observed the emergence of a multi-modal multi-scale approaches but their application in clinical routine is still to be done. It appears that, like the other main types of primary bone tumors, osteosarcoma constitute a very heterogeneous group of tumors at each of above mentioned scales.

Only recent researches consider the question of heterogeneity at the genome scale (literature review of [7]). Indeed, the inter- and intratumoral heterogeneity has been found to be due to a large chromosomal instability [18] and an identification of many affected genes has been made. Some mutations, more or less recurrent, such as on TP53, RB1, MDM2, ATRX and NF2, may play a role in the initial development of osteosarcoma [19], resulting in copy defects. There are also genetic deletions and genomic alterations characterized by sudden and severe fragmentation of some or all chromosomes, followed by aberrant reassembly. In essence, the problem at this scale seems to be too complicated to appreciate as a whole and remains an open problem to date. New technologies, quite difficult to implement, will probably allow in the future to explore this problem in an efficient way.

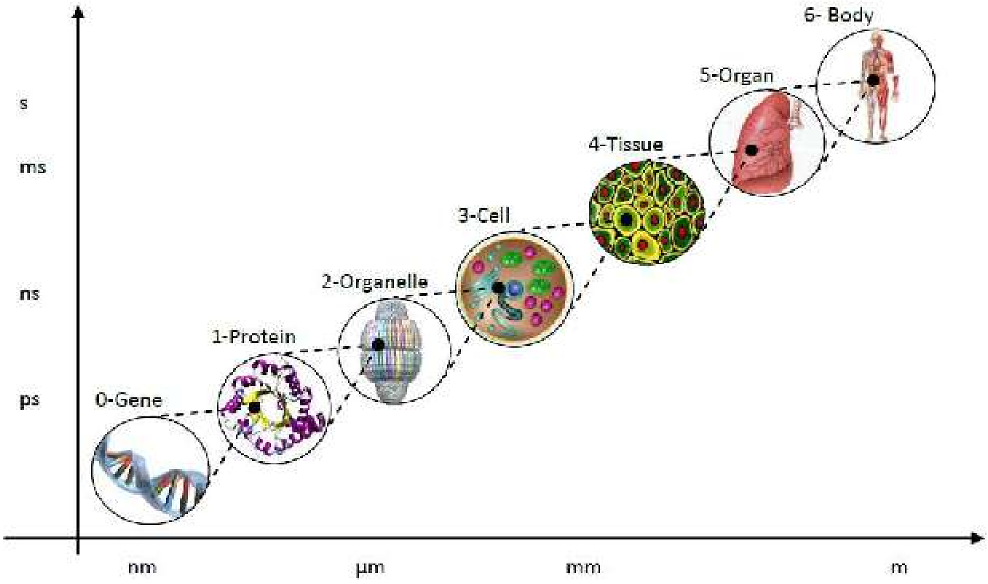

Figure 1.6: Illustration of hierarchical biological system [20].

At the protein scale, it is determined that a deregulation of bone remodeling and resorption takes place in osteosarcoma. These phenomena originate at the protein level, through a disturbance of the RANKL/OPG balance (activating osteoclasts and promoting bone formation respectively). Subsequently, growth factors, such as transforming growth factor-β (TGF-β), are released. They have the direct effect of stimulating tumor growth and metastatic progression [21].

At the macroscopic level, various imaging techniques help to characterize the heterogeneity of osteosarcomas and their tissues. For example, a classification of osteosarcoma can be made through their radiological representation according to the degree of mineralization (via osteocondensation). An MRI can be used to assess the amount of necrosis and peritumoral enhancement which are independent predictors of tumor grade, and were associated with high grade tumors [7]. Diffusion-weighted imaging (DWI-MRI) provides information on the vascular properties of the tissue. DWI-MRI allows characterization of the microscopic structure of the tissue and can differentiate benign and malignant lesions [22].

The microenvironment is the scale of interest in this thesis. Indeed, this scale is the diagnostic one by the anatomo-pathologist and can account for both short-range interactions such as cell/ECM, cell/cell interactions and long-range interactions via soluble species transport from the mechanical point of view. The microenvironment is found in the literature to play a major role in cancers and in osteosarcoma, progression, invasion, metastasis and resistance to treatment of tumor cells [7]. At this scale, the complexity emanates directly from the geometry and the different phases composing the biological object as well as the diversity of cell populations. The biology of the mineralized, non-mineralized and fibrous extracellular matrix, the vessels, the cells population (tumoral, immune and other) and the soluble species, i.e. protein, growth factors and oxygen) intermingle and become even more complex with their respective couplings as shown in figure 1.7a and b.

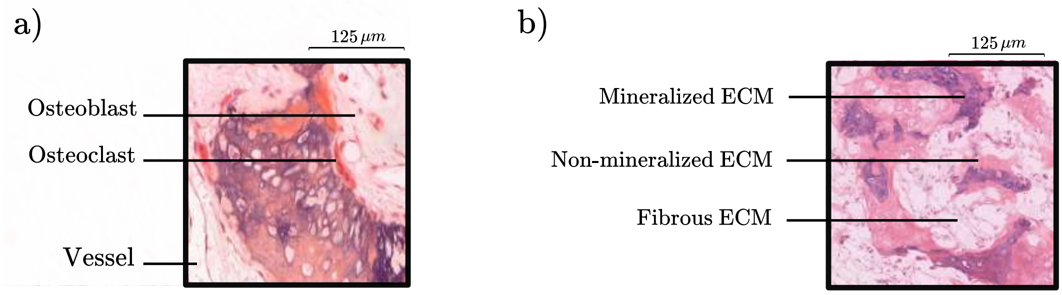

Figure 1.7: Illustration of the principal phases find on osteosarcoma histological slide.

Each element of the microenvironment has been studied quite separately. In the following, we focus on the macroscopic components of the microenvironment, namely the ECM, the vascular network and the cell populations.

The osseous ECM composed of the mineralised and non mineralised neoformed bone phases (fig. 1.7b) is of major interest in the study of osteosarcoma. Indeed, ECM is of interest in the study of cancers in general [23]. Indeed, it plays a significant part in the in tumor microenvironment spatio-temporal evolution as it can modulate cancer hallmarks [24] and can be a barrier to treatments [25, 26]. Also, by influencing the cell populations via their communication or adhesion, it contributes to the metastatic dissemination of osteosarcomatous cells [27].

Concerning the vascular network, angiogenesis is a major contributor to tumor growth and metastatic dissemination through nutrient and oxygen delivery but also intra-/extravasation of cancer cells [28]. Some works focus for instance on the effect of a reduced oxygen supply and explore potential use of therapies targeting hypoxia pathways [29] or on metabolic pathways in osteosarcoma development [30].

Regarding the cellular phase of the microenvironement, different cell populations are studied. This is the case for example of the mesenchymal stem cells. They represent a key element in the oncogenesis process of osteosarcoma since they are able to differentiate into osteoblasts or chondroblasts. Because of their ambivalent role, they are at the origin of controversies, still unresolved to this date, on the nature of the cell responsible for osteosarcoma. These cells have different properties including the ability to indirectly influence the composition of the microenvironment and the ECM.

The immune microenvironment is also very heterogeneous since involving tumor-associated macrophages, dendritic cells, myeloid cells, osteoclast and lymphocytes [31]. The roles of the immune cells are directly modulated by the tumor cells (recruitment, proliferation, differentiation) in order to set up a favorable environment for tumor growth via a breakdown of the immune balance and a local immunosuppression [32]. Some cells such as CD8 seem to be suppressed on bad prognostic and do not seem to have much effect on the response to treatment while CD163 is synonymous with good prognostic and seems to help chemotherapy [33].
Among these immune cells, the osteoclast are very specific immunitary cells (fig. 1.8). Indeed, these are cells of the immune system but they also have an important role in bone remodeling and are therefore, in a way, at the center of the problem. In its immunitary role, the osteoclast population appears to be an indicator of poor prognosis and poor response to treatment. Yet, a clinical trial trying to eradicate the osteoclast population was unsuccessful [10, 34]. The resulting hypothesis is the potential role of bipotent cells, stained both with CD163 (marker of macrophages) and CD68 (marker of osteoclasts) in the response to treatment [10].

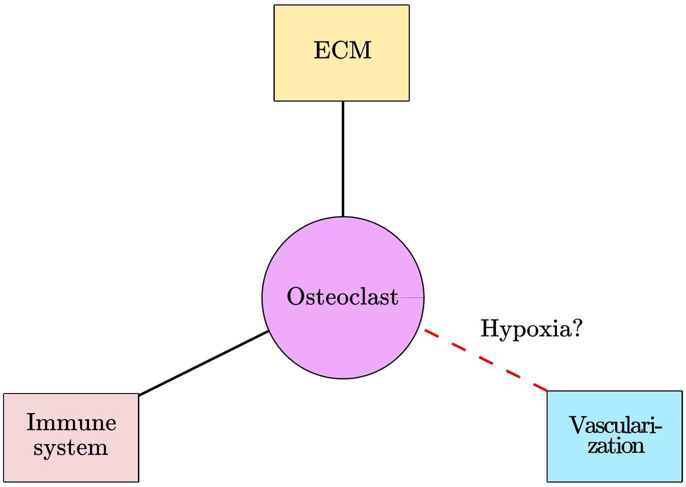

Figure 1.8: Osteoclast central role in the microenvironment of osteosarcome.

A deregulation of bone remodeling and resorption, expressed by osteoclast, is observed. The cancer cells hack [7] the tumor microenvironment for increased bone resorption mediated by osteoclasts, allowing a favorable environment for their development via osteoblast activation and release of growth factors trapped in the bone matrix. As a consequence, a vicious circle appears between bone resorption and tumor cell proliferation, inducing a more rapid development of the tumor (see fig. 1.9).

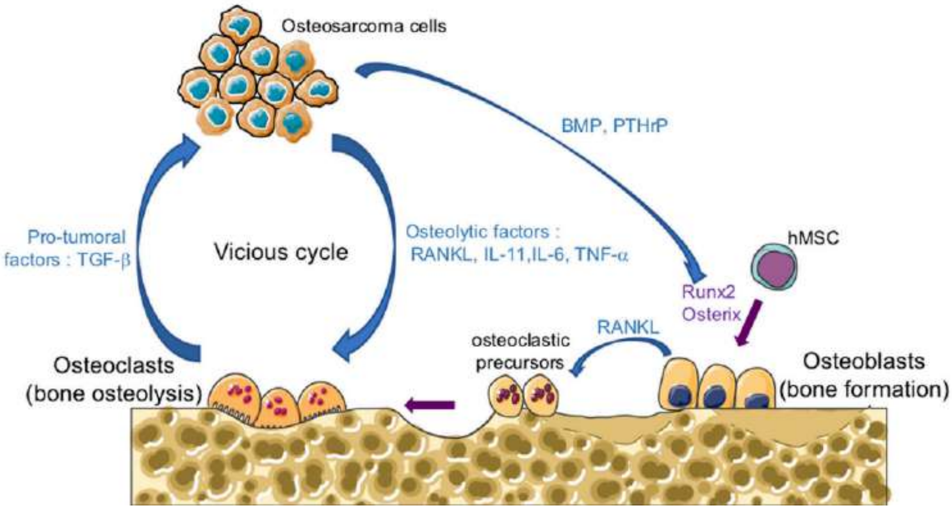

Figure 1.9: Osteosarcoma vicious circle between bone remodeling cells and tumor cells [21].

From the patient management perspective, many therapeutic trials are underway aiming at targeting the above sub-problems but none of them are getting convincing results for now and new metabolic pathways are under study [35]. Some therapeutic approach using anti-angiogenic agents [28] have shown an increase in survival for relapsed patients. Other therapeutic avenues have been explored through the role of osteoclasts in the development of osteosarcoma without much success to date. Finally, the ECM is recently seen as a new therapeutic target, not yet explored [36].

Thus, intra- and inter-tumor heterogeneity is still poorly understood by physicians and biologists, although some hypotheses have been raised. None of them is really agreed upon and does not stand out in a flagrant way. This may be related to the fact that this research is done on a targeted character of osteosarcoma microenvironment. An attempt was made in [7] to characterize the relationship between the microenvironment characteristics (histology and immunohistology study) and tumor scales characteristics (MRI, scanner) but unfortunately it was still difficult to identify obvious correlations between these two scales; most probably due to the bias of biopsy performed in osteolytic regions of the tumor. Therefore, a complex multi-scale (spatial and temporal) model of the multi-phase problem could bring new insight in the study of osteosarcoma.

1.1.3 Osteosarcoma: mechanical aspects

The study of the osteosarcoma mechanics may represent a viable complement to the existing studies as it can be seen as a macroscopic trace of the complexity of biological events at cellular and lower scales, such as metabolic or genetic changes.

The bone is a mechano-sensible organ [37] and its cycle is strongly influenced by mechanical effects. Numerous studies have demonstrated an important role of biomechanical effects in remodeling. Bones are constantly adapting to maintain their strength [38, 39], to grow [40] and to heal [41]. The mechano transduction has been highlighted [42] as a direct link between cellular behavior and mechanics in bone [43, 44]. The interstitial fluid seems to play a significant role, along with other biophysical stimuli such as strain [45] and osmotic pressure shear [46], in osteocyte mechano-sensitivity. More precisely, an interaction between osteoblasts and osteoclasts, responsible for bone formation and resorption, is stimulated under mechanical effects. The piezo-electric effect of collagen has been recently studied and could limit the interstitial flow and thus increase the mass transport and stiffness in the bone [47].

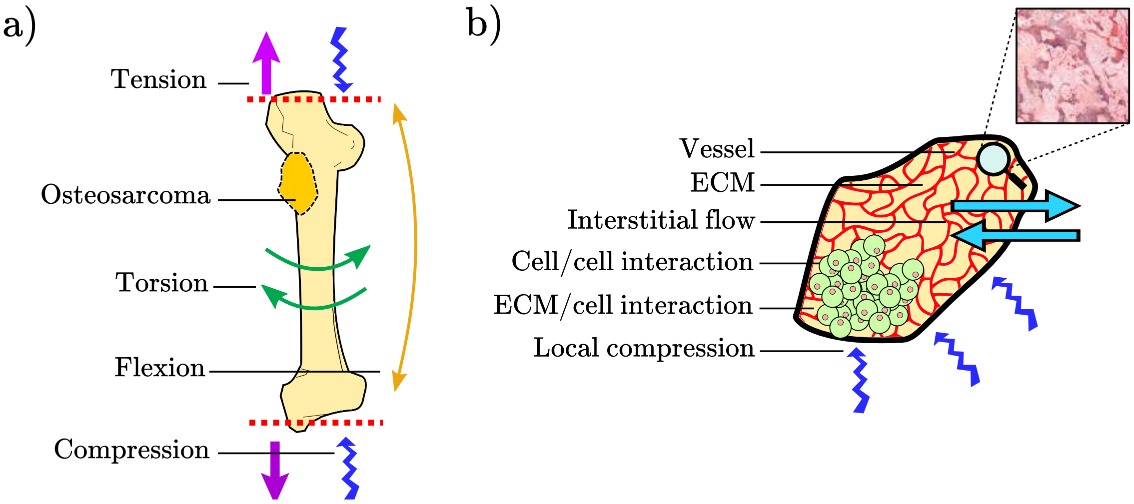

Figure 1.10: Illustration of a) external and b) internal stimuli on osteosarcoma.

Mechanical effects occur at large spatial scales such as stimulation caused by patient physical activity (fig. 1.10a) and local scale within the tumor (fig. 1.10b). At the local scale, identified mechanical effects include, for instance, compressive stresses in response to cells proliferation or fluid transport changes related to tumor angiogenesis [48].

When a primary bone tumor is growing, it deregulates the homeostasis of the bone, inducing a “vicious cycle” in the micro-environment [33] between osteoclasts, stromal cells, osteoblasts , immunological cell populations and cancer cells. This balance disruption at the cell population spatial scale is thus exhibited at the tissue scale by the emergence of osteocondensation or osteolytic lesions in the affected area [10].

Primary bone tumors such as osteosarcoma, by the nature of the affected cells populations, shows a high sensitivity to local and global mechanical effects [15], [49]). In addition treatment efficiency in solid tumor depends on stresses and microarchitecture of the media[50].

Thus, a mechanical approach can represent a first step in the construction of an overall view of the problem. Indeed, by this approach, it becomes possible to explore couplings between complex multiphysics and biological process. To start, the ECM/cell interaction is of interest since it has never been really studied in osteosarcoma or in any type of tumor from real data at this scale. This biological-mechanical approach and the similtaneous study of two scales is highly motivated by results from past clinical trial mentioned, such as [33], as a link between the two scales can be felt.

1.2 Thesis problematics and objectives

The study of osteosarcoma remains to this day a multi-scale problem of great complexity. From its phenotype to the microarchitecture of its microenvironment, heterogeneities within the pathology itself are observed, making the development of a generic follow-up protocol very challenging. Heterogeneity in response to treatment is an open question, both from a biological and clinical point of view.

As in all types of solid tumors, the coupling between mechanics and biology plays an important role in the evolution of osteosarcoma. While numerous clinical questions on osteosarcoma remain opened and could be explored by a mechanobiological approach, two problematics are highlighted in this thesis: 1) Can interstitial flows due to high pressure at the osteosarcoma core [51, 52] and osseous ECM spatial distribution be related to chemotherapy response heterogeneity ? In other words, can the neoformed bone tissue become a barrier to treatments which are transported by interstitial flows? 2) Can elastic response of osteosarcoma to structural stimuli play a role in chemotherapy response heterogeneity ? This question is raised due to the role of mechanical loading on bone ECM structure and in particular through the osteoblast/osteoclast balance which itself seems correlated with immune response [10].

To explore those questions, we hypothesize the existence of a link between the spatio-temporal evolution of osteosarcoma and the mechanics of the tumor microenvironment. Osseous ECM mechanical investigation can be seen as a first step in the global appreciation of the osteosarcoma multi-scale understanding. In particular, the examination of correlations between cell population spatial distribution and ECM physical properties could bring new insight in the understanding of the pathology, of the response to treatment heterogeneity and eventually in the search of immuno-therapy targets.

In order to evaluate quantitatively those correlations, a biomechanical approach is adopted using histological data. We target the emergence of new mechano-biomarkers by this strategy. To achieve this objective, a coherent mechanical modelling of the microenvironment at the tissue scale is needed. Because osteosarcoma at this scale is a porous media, mechanical modeling is challenging. To our knowledge, there is no generic method available in the literature to investigate osteosarcoma (or other biological tissues) mechanical properties using non-idealised data (images from patient follow-up).

The methodological aim of this thesis is to develop such mathematical and mechanistic consistent tool. Because it is unknown which mechanism drives the evolution of osteosarcoma or patient response to therapy, the strategy, initiated by clinical problematics, must relied on a perpetual exchange between models and clinical context.

In the following chapter 2, mechanical models of osteosarcoma of increasing complexity are presented, some definitions and the state of art of the modelling methodology in complex porous media are reported. The chosen workflow is also detailed in this chapter. In chapter 3, the mathematical and numerical study of the transport phenomena in osteosarcoma, such as interstitial flow or diffusion, at the tissue scale are discussed. A validation of the numerical methods is detailled. The chapter 4 will be dedicated to the study of the structural mechanics and poromechanics of osteosarcoma. In the last part (chapter 5), a coherent mechanical/biological approach is presented. Results exploring correlations between patients response to treatments and osteosarcoma mechanical properties are given for a small cohort. Finally, a general conclusion is proposed followed by research perspectives.

Chapter 2

Model and methodology

Contents

In this chapter, the mathematical model of osteosarcoma complex mechanics is described. The model is built on the appropriate literature relative to porous media. A dedicated methodology is developed to evaluate mechanical properties using histological exams from clinical routine. This chapter also describes the overall study workflow from biological, mathematical or numerical perspectives.

2.1 Osteosarcoma: a porous media point of view

In this section, osteosarcoma is described at the tissue level, i.e. from histological sections, and we detail mechanical and biological assumptions made to solve the problem in the framework of porous media. Then, generic methods to study some aspects of porous media mechanics are presented. Finally, an upscaling method designed for osteosarcoma modelling is proposed.

2.1.1 Models of osteosarcoma at the tissue scale

To achieve a consistent mechanical characterization of the osteosarcoma, several assumptions must be made about the physical and geometrical character of the problem as shown in figure 2.1. Indeed, it is challenging to model complex biology of tissues, so biological and physical conjectures are necessary in order to target relevant parameters of the problem. Thus, choosing a modeling approach comes down to making the relevant choices that approximate the original problem while keeping the complexity adequate to answer the clinical or biological questions.

In a first step, we consider stationary mathematical problems. This restriction is trivially motivated by the biological material available. Indeed, histological slides represent a 2D snapshot of the tumor at a given time.

The tumor shows apparent structure changes according to the observation scale featuring strong spatial heterogeneities. As a consequence, a multiscale approach is required.

We will consider the tumor as a strongly heterogeneous porous medium exhibiting three phases that are the fluid phase formed by blood, plasma and marrow, the solid phase formed by the fibrous and osseous ECM which main components are non-mineralized and mineralized tissues, and the cell population mainly constituted by osteoblasts, osteoclasts, and macrophages. The present work focuses on the microenvironment study as detailed in chapter 1.

When observing histological slides, one can see profound changes in its microarchitecture such as calcified and osteolytic regions and in the cell populations compared to healthy tissues. Therefore, abnormal structural mechanics and flows in the tumor and its microenvironment are expected. These variations will induce imbalances in the healthy tissues leading to tumor progression [15]. Thus, different physics and their coupling must be highlighted to obtain a coherent characterization of the osteosarcoma.

To achieve this objective, a consistent and adaptive methodology is necessary to handle the multiscale tissue microarchitecture and its physical behavior in order to propose a relevant mechano-biological exploration of osteosarcoma.

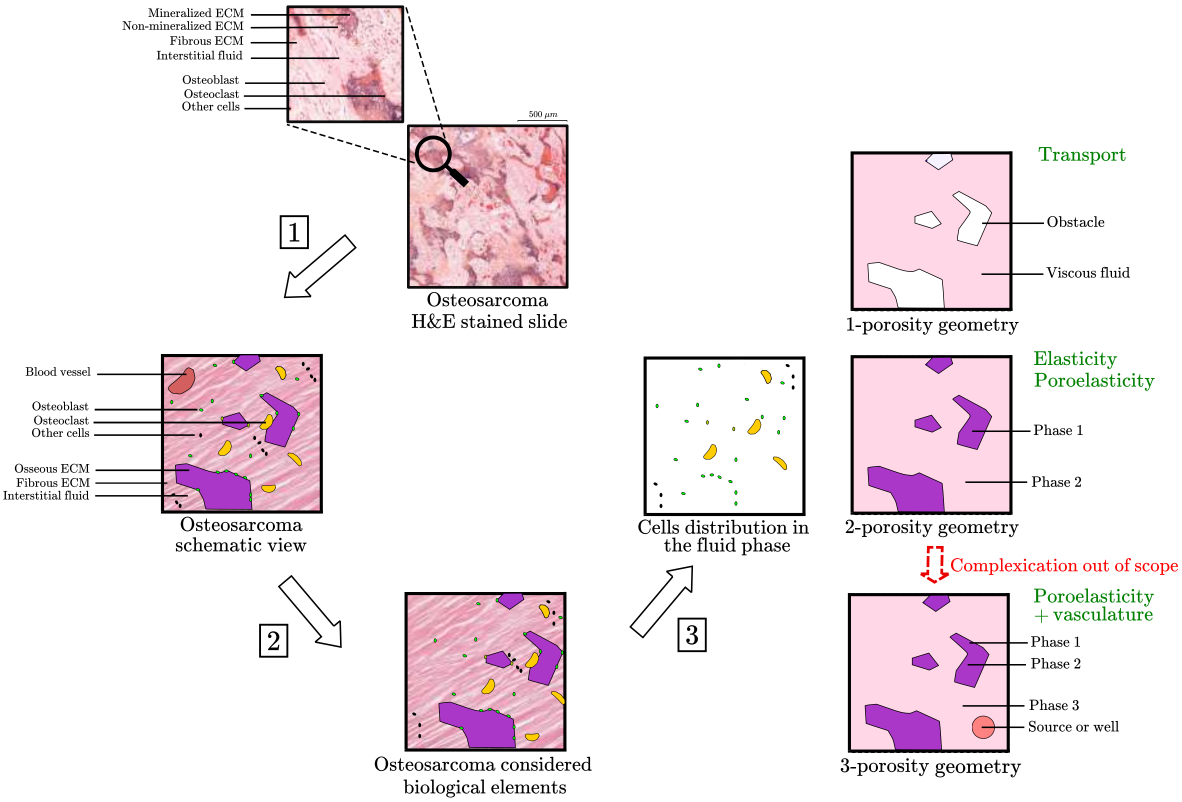

Figure 2.1: Schematic of the mechanical and biological study of osteosarcoma (dual approach) at the tissue scale through biological/mechanical assumptions and approximations in the application to the study of flow ① Histological sections, stained with H&E, of vascularized osteosarcoma. This tumor can be seen as a highly heterogeneous porous medium with multiple porosity ② Vasculature removal hypothesis ③ Dual approach: cell population and ECM distribution are splitted. Geometrical paradigm used for the study of different physics: transport, elasticity and poroelasticity.

Through this process, we consider, in the following, mechanical problems in porous media of increasing complexity, all associated with clinical and biological problematics. As illustrated in figure 2.1, the study of transport phenomena, i.e. interstitial fluid flow and species diffusion in tissues, explores the coupled role of surpressure within the tumor and osseous ECM structure on the response to chemotherapy. In this study, the pink region in figure 2.1 is considered as a fluid phase whereas the white region corresponds to fixed rigid obstacles. The fluid phase description is a strong assumption as in reality, this phase is a fibrous ECM porous medium saturated by a fluid.

Because of the dependence of bone remodelling to mechanical effects, elasticity study investigates the role of osseous ECM deformation on chemotherapy response. In this study both pink and purple region are considered to be structures with different elastic properties. Furthermore, poromechanics can bring answers to transport and elasticity problematics simultaneously. In this exploration, both purple and pink regions become porous materials with various elastic and permeability properties. In this model the nanoscopic lacunar-canalicular network in the purple phase is considered while fibous ECM is also taken into consideration.

Transport in vasculature and surrounding tissue is of interest to study the role of angiogenesis on tumor development and chemotherapy response however it corresponds to the highly complex question of transport in a network (vasculature) combined to the transport in a surrounding heterogeneous porous media (fibrous and bone phase). This question is out of the scope of this thesis.

2.1.2 Definitions and modeling of porous media

In this section, the fundamental notions and formalism of porous media, useful for the good understanding of this work, are introduced. The concept of porous medium allows the study of a significant number of applications from energy and geosciences to climate issues. However, the literature on porous media mechanical models in biological and clinical applications is scarce to non-existent when dealing with non-idealised media.

A porous medium is a geometrical object consisting of a solid matrix or porous skeleton and its complementary called pores. Constitutive materials of the porous skeleton can be continuous and consolidated such as crystals or rocks or discrete and granular such as sand. Pores, interconnected or not, are subcategorized according to their discrete or continuous nature as described in figure 2.2. The distinction between the continuous and discrete terminologies is made according to the pore codimension (0 or 1) and dedicated methods are usually used to solve mechanical problems in each case. Osteosarcoma, as described in fig. 2.1, correspond to a porous medium with continuous pore (codimension 0).

The medium porosity, describing the ratio between the pore void volume and the total volume of the object, ranges from 0 to 1. Furthermore, the porosity nature often drive model classification such as one-porosity or double-porosity models and some are more complex are multi-porosity models (fig. 2.2). The connectivity and the tortuosity, which describe the sinuosity of the microarchitecture, can be associated with the geometrical description of the porous media but may also play a role in the physical behavior [53].

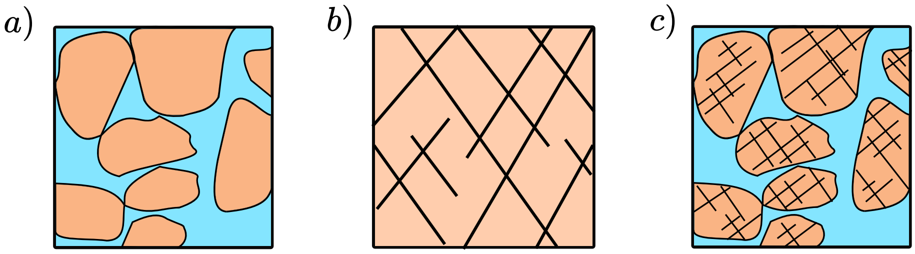

Figure 2.2: Schematic views of different possible porosity levels in porous media. a) A 1-porosity model with interconnected continuous pores of codimension 0. b) Fractured porous media model with discrete pores of codimension 1. c) 2-porosity model comprising the two previous types of porosity.

The solid matrix is generally completed by a fluid material, fully or partially saturating the porous medium. To distinguish between constitutive materials, the keyword *phase*, i.e solid or fluid, is generally proposed. From then on, different physics can be explored such as transport, transfers or poromechanics.

A porous medium phase is spatially homogeneous, at a given scale, if it is similar in each point of space. As a consequence, phase heterogeneity can be taken as the antinomic situation where significant variations into the solid and fluid phases can be observed. Note that in the porous media framework, homogeneity and heterogeneity will be given a slightly different definition (see below section 2.2.1).
The isotropic behavior reflects the invariance of physical responses according to the orientation of architecture and physical boundary conditions. On the contrary, the anisotropy accounts for the dependence on the system orientation.
Finally, a physical system is defined as a system comprising the geometry, i.e the porous medium, and physics under study.

Another important point in the modelling of porous media, is the attention paid to the different scales of observation [54]. To remind the problematic of the osteosarcoma, figure 2.3 illustrates the different scales which are considered by clinicians. The first one is the macroscopic X-ray imaging used for clinical diagnosis, then the tissue scale observed on histological slices used to confirm diagnosis, to guide surgery and to establish chemotherapy response. The cell scale, which is not yet available in clinical routine, is currently explored in research for targeted therapy. The thesis is built around two main scales from the pore scale (close to the cell scale) to the tissue scales (see fig. 2.5).

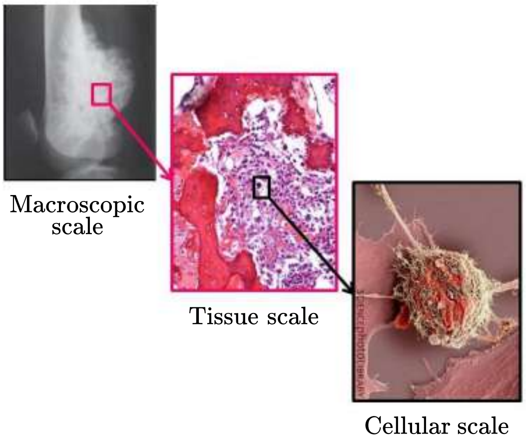

Figure 2.3: Three different possible scales of observation for osteosarcoma. The first one corresponds to an X-ray of the bone affected by the pathology, the second one represents the tissue scale (showing different phases) and finally the last one shows the cellular scale.

A significant number of theoretical and numerical methods are available to describe the physical response of porous media. Some focus on an exact description of the physical phenomena while others are targeting approximations. Finally, there is not an unified approach but rather methods adapted to the scientific objectives.

First, problems can be modeled at the pore scale. This approach allows to describe the behavioral equations in time and space without any simplifying hypothesis provided the porous medium architecture is well known. Numerically, they are solved by Direct Numerical Simulation (DNS), i.e methods for which the whole range of spatial scales is resolved. Their resolution induces limited errors inherent to the numerical algorithm. Pore-scale physical information are accessible with a significant computational cost which is prohibitive in case of complex geometries and/or large domains (illustration 2.4 top images).

Multiscale methods are based on the study of physics at different scales of observation. The first step is to determine the characteristic scales of each physical phenomenon by ascendant and descendant approaches. Once the relevant physical systems have been identified, the couplings and relationships related to the different scales are modeled. Then, the global simulation such as DNS is replaced by a series simulations associated each with different scales. Thus, this method shows a reduction of numerical cost compared with DNS, but it induces a loss of information and accuracy in return.

Pore Network models may be used when complex physics occurs at the pore scale such as phase exchange, non-Newtonian displacement, non-Darcy flow, reactive transport ... (illustration 2.4 bottom images). This approach links single pore processes and permits understanding and the prediction of porous media mechanical behaviors at a larger scale, usually however on volumes smaller than sample size [55]. In this methods porous media geometry is simplified but solid and fluid phases are still considered and the balance equations are also approximated (e.g. Navier-Stokes to a pressure drop relationship for instance).

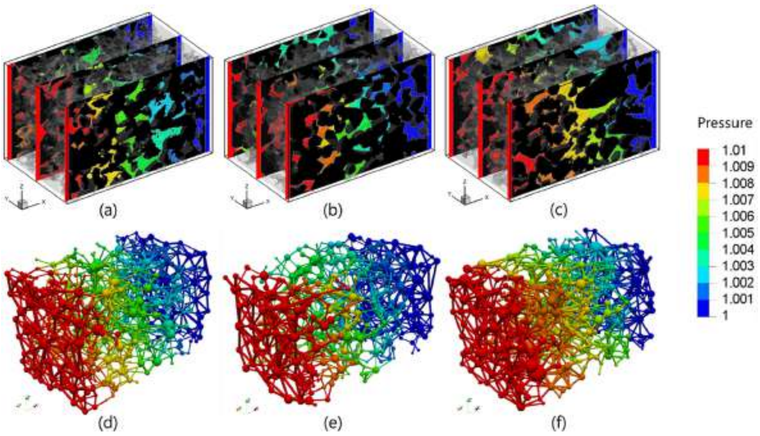

Figure 2.4: Pressure distributions obtained by DNS (on top) and pore network methods (bottom) for a flow going from left to right [56].

The last method presented in this paragraph is upscaling method. The most general objective of upscaling methods is to replace a physical system, including a spatially heterogeneous porous medium and a physics with fast spatial variations, by a new physical system constituted by a smoother domain and a physics with slower variations (fig. 2.5). The physical coefficients at the macroscopic scale scale are calculated from the pore scale and are called the effective or equivalent properties of the system. Thus, through the pore scale behavior of the system, it is possible to obtain a model of behavior at a higher scale. This approach implies the use of averaging of the pore-scale equations and leads to a loss of some details. It must be emphasized that the goal to replace lower-scale models by upper-scale smoothed model cannot be always achieved and that hybrid model coupling transport equations at different scales may be needed. This important issue will not be considered in this work.

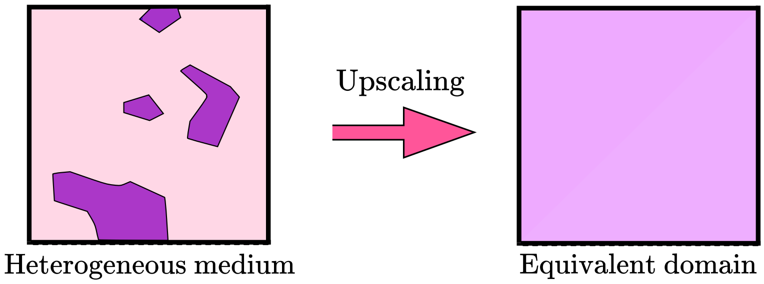

Figure 2.5: An upscaling method allows to substitute to a complex physical system a new physical system much simpler to study.

Mechanical effects acting on the tumor are internal as well as external in nature as illustrated in figure 1.10. Therefore, the link between pore and macroscopic scales has to be elucidated. In this thesis, the DNS approach had to be discarded (except for methodology validation purposes) because of its computational cost due to the complexity and heterogeneity of the osseous ECM structure and the large dimension of histological slices where cell scale information (smaller than pore scale) are clinically relevant. Pore network model would be difficult to implement in osteosarcoma because of the complexity of the micro-architecture and the limited ability to generate the network itself.

However, an upscaling method is well-adapted to study mechanical effects at the tumor scale or at least at the scale of a whole histological section and their influence on cellular responses.

2.2 State of the art on upscaling methods

This section provides a description of the main concepts associated with uspcaling methods. The main methods of deterministic homogenization are then given. These theoretical methods are essential since they provide a rigorous framework for the determination of physical systems at the higher scale and their associated parameters. The homogenization methods are classified according to the spectrum of the physical system they deal with and the restrictive assumptions they consider.

2.2.1 Upscaling methods: concept and definitions

The upscaling process gives a representation of a physical system by describing the average behavior and accounts for global effects by removing the fluctuating effects at the pore scale (fig. 2.6a). These methods permits the modelling of complex systems including several physics and couplings while involving various spatial scales with partial differential equations (PDEs) simplification.

The first models were obtained empirically and experimentally such as the Darcy's law (1856), the Brinkman's equations (1949), the dispersion equation (1979). These empirical transport models often used some empirical correlations for their effective properties, such as the Kozeny-Carman law (1927, 1937 and 1956). The analytical results of the latter can only be applied to limited geometries such as packed bed of solid with a limited choice of physics such as flow and diffusion.

To implement the upscaling of generic physical systems, some methods rely on rigorous mathematical and physical tools to derive macroscopic physical systems from the pore scale modelling. This is the case of homogenization methods. They were originally developed for elliptic equations in periodic media such as asymptotic expansion [57] or in the formal derivation of laws that were empirical such as the Darcy's law in volume averaging [58]. They have since been extended to other steady or unsteady physics such as convection, flow and elasticity.

These methods rely on two fundamental elements which are the "representativity" of the physical system and an averaging operator. These two points allow a macroscopic modelling to be proposed using the average of pore scale physical quantities [54].

Characterizing the physical system representativity is an essential step. The aim is to search for a sub-volume of the entire domain to account for its macroscopic properties. Such a sub-volume is called a representative elementary volume (REV) of the physical system. The REV is dependent upon the intrinsic characteristics of the porous medium, i.e. porosity, but also upon the physics involved.

A region of interest for which a macroscopic property is constant (resp. variable) through the process of upscaling and also independent from boundary conditions is considered as homogeneous (resp. heterogeneous), as illustrated in figure 2.6b. Therefore, the REV induces macroscopic properties independent from the domain size as well as boundary conditions. Properties are then defined as effective properties.

Some REV representation are intended to be deterministic, others statistical depending on the choice of homogenization method. According to De Marsily [59], "the size of the REV is defined as a volume (1) sufficiently large to contain a great number of pores so as to allow us to define a mean global property, while ensuring that the effects of the fluctuations from one pore to another are negligible (2) sufficiently small so that the parameter variations from one domain to the next may be approximated by continuous functions, in order that we may use infinitesimal calculus". Bear [60] defines a REV as a volume capable of capturing a quantity representative of its heterogeneity. Drugan and Willis [61] define it as "the smallest material volume element of the composite for which the usual spatially constant (overall modulus) macroscopic constitutive representation is a sufficiently accurate model to represent mean constitutive response". Hill [62] describes it as a heterogeneous region that :"is entirely typical of the whole mixture on average”and ”contains a sufficient number of inclusions for the apparent properties to be independent of the surface values of traction and displacement, so long as these values are macroscopically uniform.” When using stochastic volume elements, the REV accounts the variability in the microstructure over different statistical realisations [63].

The scale separation is then defined. As shown in figure 2.6a, mechanical phenomena are analysed according to their oscillation frequency and the mathematical methodology is based upon the uncoupling between pore scale and macroscopic fields. The REV concerns intrinsic material properties such as porosity whereas the scale separation concerns fields of mechanical responses such as fluid velocity and pressure, displacements, etc. From a purely physical point of view, scale separation describes, in any continuous approach, the difference in spatial oscillations of pore-scale properties with respect to the spatial variable of the macroscopic domain. It is this consideration that is exploited in the upscaling methods. Indeed, this characteristic of continuous systems can be analytically described and allows the physical and mathematical simplification of the equations for a description of the physics through a macroscopic point of view.

Thus, the presence of REV always underlies the existence of scale separation in the upscaling sense. Generally, the ratio of the characteristic length at the pore scale and the characteristic length at the macro scale is much lower than unity.

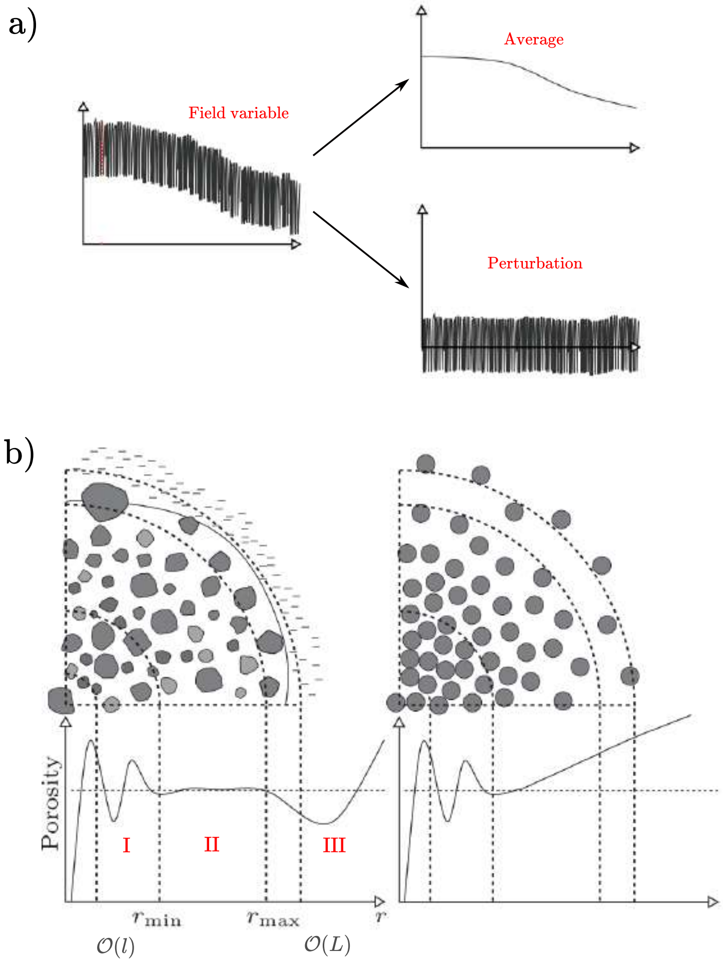

Figure 2.6: a) Scale separation decoupling the spatial oscillations of the field variables into a mean part (slow variations) and a disturbance (rapid oscillations). b) Determination of an REV in respect to the porosity parameter (left). The region **I** corresponds to the micro-heterogeneity effect at the characteristic l-scale, the region **II** where an REV defined as the property is seen as homogeneous (quasi-constant) and the region **III** where the medium can be heterogeneous again at the characteristic L-scale. In the porosity gradient case (right), a REV cannot be defined as the porosity evolves continuously in respect to the scale. Illustration from [64].

In the context of this thesis, statistical methodology could have been envisaged. However, stochastic models face difficulties to determine an homogeneous medium corresponding to the stochastic microstructure. As a consequence it is often prohibitive in term of computational costs [65, 66]. Moreover, it is often challenging to provide the elucidation of mechanisms involved. In our work the aim is to explore the mechano-biological events involved into the pediatric tumor, thus we consider deterministic methods in our strategy.

2.2.2 Deterministic homogenization methods

In this paragraph, a review of the main deterministic homogenization methods is proposed. Methods based upon restrictive assumptions are described. Then, methods bypassing some of these limitations are detailed.

The two main methods of deterministic homogenization build the bridge from the pore scale, characterized by the length l, to the macroscopic scale, characterized by the length L. They are described as the asymptotic expansion (AE) [57] and the volume averaging (VA) [58]. A comparative study showing their similarity is proposed in [67]. A review of the main results of the asymptotic expansion is proposed in [68, 69]. As an illustration, we consider, at the pore scale, their respective historical physical system.

In the AE case, we consider the elliptic equation (2.1) on a periodic domain Ω (of boundary $\partial\Omega$), where a periodic tensor A exhibit strong spatial oscillation. This can describe a diffusion problem.

$$\begin{cases} -\nabla \cdot (A \cdot \nabla c) = f & \text{in } \Omega \\ c = 0 & \text{on } \partial\Omega \end{cases} \tag{2.1}$$

Here c represents a concentration field and f is a source term.

The AE method put the original pore scale problem (2.1) into a sequence of similar problems (2.2) indexed by a parameter η. This η describes the spatial periodicity of each periodic cell of the domain and the non-dimensional number characterizing the scale separation with x and $y = \frac{x}{\eta}$ being the macroscopic scale and the pore scale respectively. Thus, the real physical problem is matched to a single parameter η.

$$\begin{cases} -\nabla \cdot (A(\frac{x}{\eta}) \cdot \nabla c_\eta) = f & \text{in } \Omega \\ c_\eta = 0 & \text{on } \partial\Omega \end{cases} \tag{2.2}$$

Here c_η correspond to solution of the problem associated with the η parameter.

The limit solution of the asymptotic problem is searched in the form of an integer series (2.3), periodical in y, on a unit cell of the domain.

$$c_\eta(x) = \sum_{i=0}^{\infty} \eta^i c_i(x, \frac{x}{\eta}) \tag{2.3}$$

The effective or homogenized limit problem (2.4) is obtained when η tends formally to 0 and gives the macroscopic behavior. The asymptotic solution is given by the first term of (2.3). The effective property $A^\star$, which is constant, is obtained from solving the so-called cell problems (encapsulating information from the pore scale).

$$\begin{cases} -\nabla_x.(A^\star \cdot \nabla_x c) = f & \text{in } \Omega \\ c = 0 & \text{on } \partial\Omega \end{cases} \tag{2.4}$$

For a true physical problem corresponding to a finite parameter η, the solution found is an asymptotic approximation. A noticeable advantage is that the approximate effective property can be complemented by the error calculation.

An illustrative example is proposed in figure 2.7. An elliptical equation 2.1 is solved on a unitary geometry composed of a packed bed formed by square obstacles. Boundary conditions are a given by a non-homogeneous Dirichlet condition at the external border ($c = 1$) and an homogeneous Neumann condition at the fluid-solid interface ($\partial_n c = 0$). Finally, a unity source term is imposed in the domain ($f = 1$).

Effective behavior through AE is calculated by using the same outer boundary condition and source term. Comparison of the AE model with the DNS, used as control, is proposed (fig. 2.7a and b). The concentration profile along a horizontal path is given in figure 2.7c and results are in very good agreement.

To correct the behavior of the homogenized model (fig. 2.7c), one can consider the theory of effective boundary conditions [70] which will not be discussed in this work.

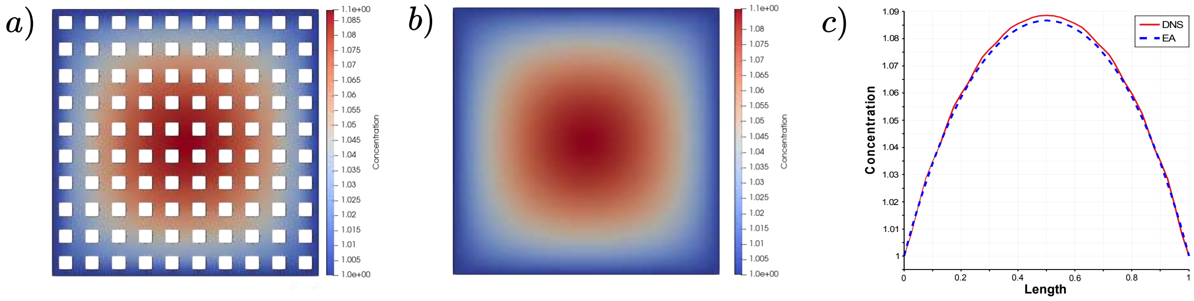

Figure 2.7: Deterministic periodic homogenisation by asymptotic expansion of an elliptic equation $\nabla \cdot (\nabla c) = 1$ with a uniform Dirichlet boundary condition (equal to 1) on a unitary packed bed formed by square obstacles. a) DNS concentration field amplitude (FEniCS®). b) Homogenized concentration field amplitude (FEniCS®). c) Plot line comparison of the two fields for $x = 0.5$.

The VA method is based upon the direct spatial averaging of the pore scale physics. Here, it will be illustrated on the derivation of the incompressible Darcy equation from a incompressible Stokes equation which model the fluid flow in a porous skeleton.

Key points are the choice of the integration domain of governing equations and the averaging operator [71]. The averaging process is achieved by using convolution according to the REV. The separation of scales is associated with the hierarchy of physical problems and it is expressed by equation (2.5) where the velocity field u can be decomposed in a sum of $\langle u \rangle$, the average, and $\tilde{u}$ the perturbation, respectively, as previously illustrated in figure 2.6a.

$$u = \langle u \rangle + \tilde{u} \tag{2.5}$$

This decomposition is inserted in the Stokes pore scale equation (fig. 2.8 left model). By doing so, the average system equation is not closed. To solve this, approximation of the perturbation is obtained on a unit cell of the REV, it is the closure problem (fig. 2.8 middle model). This unit cell is a representative domain of the REV where the invariance of the solution of the pore scale physical problem is verified with periodicity on cell frontiers[1]. Finally, governing equations at the macroscopic scale (the Darcy equation fig. 2.8 right model) are found and completed by determining the effective properties from the closure problem on the unit cell.

---

[1] A unit cell also corresponds to a space convolution of REV.

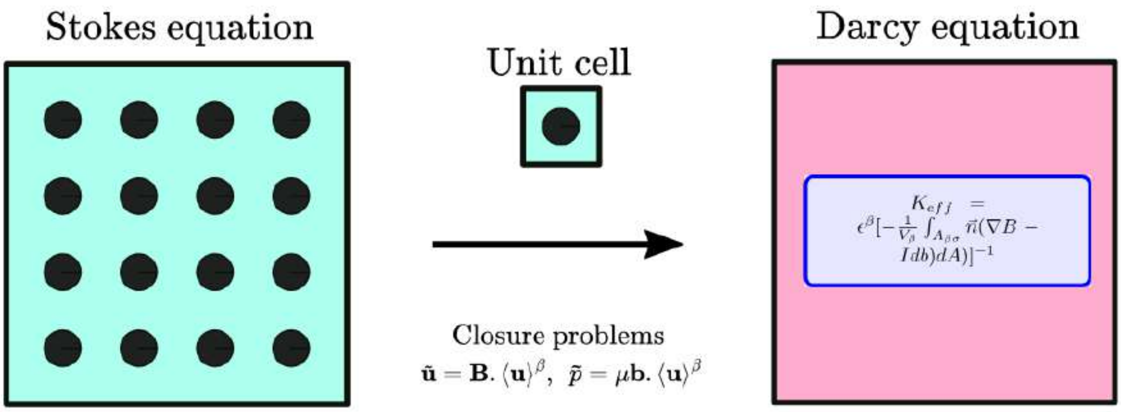

$$\begin{cases} \mu\nabla^2\mathbf{u} - \nabla p = -\rho\mathbf{g}, \\ \nabla.\,\mathbf{u} = 0, \\ \text{BCs} \end{cases}$$

$$\begin{cases} \nabla^2\mathbf{B} - \nabla.\,\mathbf{b} = \frac{1}{V_\beta}\int_{A_{\beta\sigma}} \mathbf{n}_{\beta\sigma}.\,(-\mathbf{I}\mathbf{b} + \nabla\mathbf{B})\,dA \\ \nabla.\mathbf{B} = 0 \\ \langle\mathbf{b}\rangle^{\beta} = 0 \\ \mathbf{B} = -\mathbf{I},\ \text{on } A_{\beta\sigma} \\ \text{Periodicity of } \mathbf{B},\mathbf{b} \end{cases}$$

$$\begin{cases} \langle\mathbf{u}\rangle = -\frac{\mathbf{K}_{eff}}{\mu}.\,(\nabla\langle p\rangle^{\beta} - \rho\mathbf{g}), \\ \nabla.\,\langle\mathbf{u}\rangle = 0, \\ \text{BCs} \end{cases}$$

Figure 2.8: Historical determination of the incompressible Darcy flow equation from the incompressible Stokes flow at the pore scale by the Volume Averaging method. In those equations u is the velocity and p the pressure while κ_{eff} is the effective permeability. Other notations are explicited in [72].

The AE and VA methods are two methodologies designed to predict macroscopic fields and physical properties. AE is based upon more initial mathematical aspects such as the scaling equations while VA is built upon initial physical considerations. Indeed, the VA method does not require a priori periodicity assumption since it is only used when solving the closure problem at the unit cell by the BCs choice. On the contrary, the AE method needs this initial assumption. Also, the scale separation with VA, i.e $\eta = \frac{l}{L}$ is constant and strictly positive, in opposition from the one arising in AE.

The VA method seems to be more flexible to deal with real porous media in the sense that it admits a priori a larger spectrum of admissible geometry than the AE; where the scaling of the pore scale problem into a succession of periodic unitary problems can be limiting. This last argument is subject to debate in the scientific community and some authors supporting the AE [73] indicate, that under certain assumptions, a random structure leads to the same macroscopic description as a periodic structure. The necessary and sufficient hypotheses for the good conduct of the classical AE method are in fact the spatial local stationarity (i.e. no porosity gradient) and the scale separation.

Other homogenization methods have been proposed in the literature such as the mixture theory [74], the effective medium theory [75] or the two-scale convergence method [76]. The Mixture theory [74] or hybrid mixture theory [77] are phenomenological methods based upon restricted forms of macroscopic governing equations. They are dedicated to multiphasic fluid flows. In the effective medium theory [75], the unit cell is immersed into a medium corresponding to the effective behavior. The solution is multiple since associated with a significant number of available approximations such as the Green's function or the Maxwell-Garnett, Clausius-Mossotti and Bruggeman formulas. The two-scale convergence method is based upon robust mathematical developments [76]. It is similar to the AE method while explicitly stating the topologies (limit meaning) and the functional distributional spaces. Those methods have been discarded in this work as they are not well adapted to the problem of interest.

Some extensions have been proposed to overcome the restrictive assumption of strict periodicity by introducing a gradient of porosity.

Developments in [78] and [79] are associated to AE. An example on the processing of porosity gradients by AE is given in figure 2.9 where a DNS and the AE model simulation are compared.

Here, the effective property $A^\star(x)$ is not constant but depends on the diameter of the obstacle considered. Indeed, multiple unit cell problem need to be solved as the diameter of the obstacle is not constant; a constant effective property is associated with each unit cell.
For the VA method, the concept of evolving heterogeneities is proposed [80].
These extended methodologies (coming from AE or VA) give similar effective properties. Indeed, when calculating the effective coefficients $A^\star$ on each cell as a function of scaled obstacle diameters, similar results are obtained with non-local stationary heterogeneity, as shown in figure 2.10.

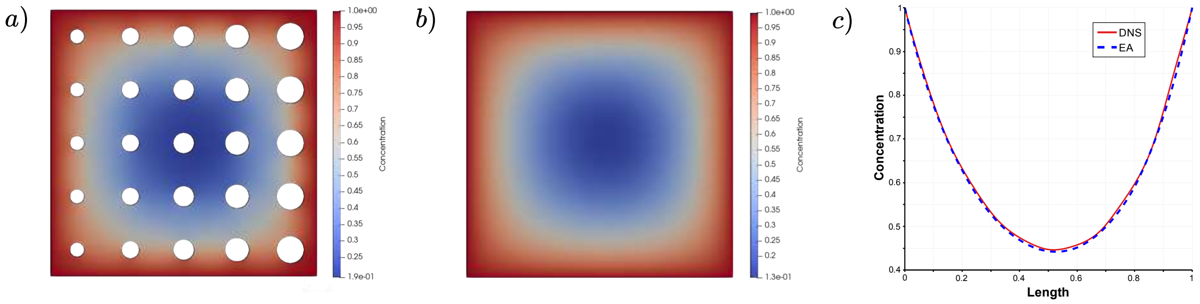

Figure 2.9: An extension AE to unitary porosity gradient geometry on a arrangement of discs following [78]. An elliptic equation with coefficient equal to 1 and negative unitary source term is considered, i.e $\nabla.(\nabla c) = -1$. Boundary condition are given by $c = 1$ on external boundary, $\partial_n c = 0$ on internal boundary. a) DNS concentration field amplitude (FEniCS). b) Homogenized concentration field amplitude (FEniCS). c) Plot line comparison of the two fields for $x = 0.2$.

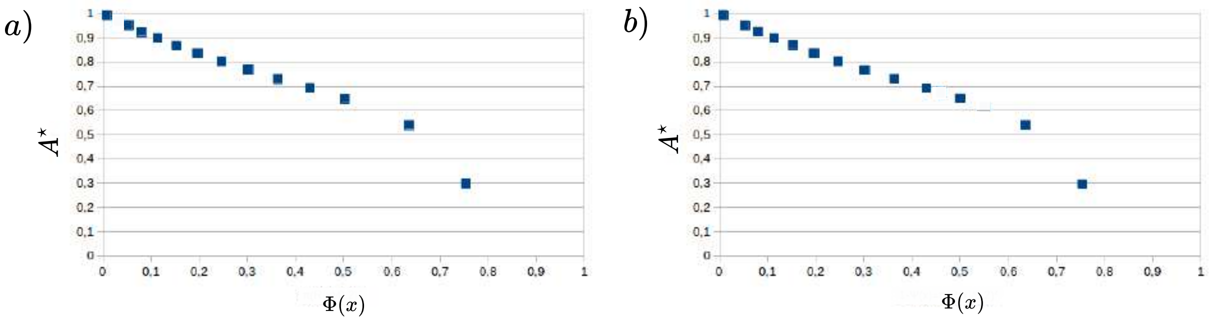

Figure 2.10: Comparison of the AE and VA extension to porosity gradient paradigm on a arrangement of discs for an elliptical equation. a) Effective coefficient A^* evolution as a function of the diameter $\Phi(x)$ of the scaled obstacles for the EA extension (FEniCS). b) Effective coefficient A^* evolution as a function of the diameter $\Phi(x)$ of the scaled obstacles for the VA extension (FEniCS).

Other approaches could avoid constraints of periodicity and REV such as the Σ-convergence [81]. They are generally based on two-scale convergence but, unfortunately, are still distant from potential physical applications because of their fundamental concept such as the so-called homogenization algebras.

2.3 Upscaling and biological tissues

When biological tissues are considered, most of studies concern bone mechanics and are solved using deterministic homogenization. Considered physics are elasticity, poroelasticity coupled with diffusion [82], piezoelectricity [83]. Some studies account for specific geometry such as double porosity [84] or porosity gradient [85]. Additional applications concern vascularized tumors [86, 87, 88]. All methodologies consider cases of idealized microstructures.

Unfortunately, when REV is missing, the scale separation is not verified and above methodologies cannot be applied. This is precisely the case of osteosarcoma which is a strongly heterogeneous medium at the tissue scale. Approaches previously described find redhibitory limitations and dedicated strategies have to be implemented.

Indeed, in osteosarcoma, the presence of a REV is not verified. The heterogeneity of the phase distributions (with respect to the osseous ECM) varies continuously by increasing window method (fig. 2.6b). By plotting the evolution of the porosity for these increasing windows, we find only very locally and for very specific areas of the osteosarcoma REV sizes of 800 px × 800 px (neo-formed bone). It is important to note that the determination of a local REV, which is very rare and exceptional, does not allow for a systematic study of the osteosarcoma by homogenization approach, since strong geometrical variations are observed on all the histological sections. As a consequence, a single effective value cannot correctly reflect this heterogeneity.

2.4 Upscaling methods adapted to osteosarcoma study

This section describes the main methods of upscaling that are compatible with the processing of clinical material, i.e. histology sections.
Upscaling methods applied to complex porous media have to deal with two main difficulties: the heterogeneity of the physical responses as well as the anisotropic characteristics of variables and parameters. Here, we discuss upscaling methods applicable to heterogeneous porous media. They are based on periodic homogenization of the physical models of interest. Macroscopic properties are obtained by using the direct averaging of physical quantities such as fluid velocity, pressure etc.
Some analytical methods are available such as bounds-based approaches [89], power-averaging [90] and renormalization [91]. Unfortunately, those techniques are less generic compared to homogenization. For example, in the power-averaging case, only the diagonal equivalent property can be predicted and anisotropy is lost. Nevertheless, an extension of the renormalization to non-diagonal equivalent properties is proposed in [92] but this method is discarded in this thesis since we are looking for a generic method allowing the treatment of multiple physics.

2.4.1 Grid-block methods

One of the most flexible and accurate upscaling methods, saving most of pore-scale information, considers the numerical pore scale solutions over the whole domain of interest according to different directions of space, which has the advantage of accounting for the complete anisotropy. The upper scale model is then obtained by direct spatial averaging of pore scale physical quantities, thus the macroscopic property is constant over the domain (left image on figure 2.11). This technique allows to replace the heterogeneous behavior of domain by a so-called equivalent behavior without any restrictive assumption about geometry and microarchitecture. In the following, we consider the terminology equivalent properties, mostly used in fluid mechanics when macroscopic properties are obtained without REV. Apparent properties terminology is also found in the literature but is more dedicated to structural mechanics. The equivalent properties are not intrinsic or effective and they may vary according to boundary conditions and size of the calculation domain. Convergence is eventually achieved by increasing the domain size and effective properties are found if a REV size is reached.

This approach has a high numerical cost and may induce a significant loss of microscopic information if the domain size is large. Grid-Block upscaling methods [89] implement this process in a sub-division of the macroscopic domain as described in figure 2.11 (right image). The methodology consists of direct averaging of the pore scale physics over each sub-domain of the grid. This technique of low numerical cost, gives piecewise constant equivalent macroscopic properties at the scale of the whole domain of interest, thus saving heterogeneous and anisotropic properties of the porous medium. The grid-block method is a kind of approximate numerical upscaling method in the sense that without REV, it is necessary and essential to obtain a macroscopic description representative of the heterogeneity of the phase distribution at the pore scale.

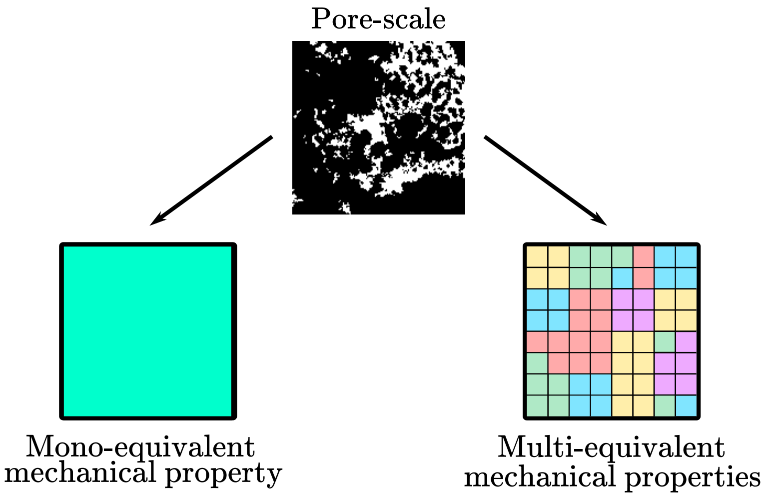

Figure 2.11: Grid-block upscaling process from pore-scale giving either global (whole geometry) or block precision equivalent properties.

Piece-wise equivalent properties on the grid are dependent upon boundary conditions on sub-blocks of the subdivision of the original domain. Boundary conditions are specified according to the pore scale physical model to determine the equivalent property on each sub-block.

Sub-methods of averaging are developed according to the management of boundary conditions. We can find the local method, the extend-local method and the quasi-global also called local-global method.
The local method is a standard grid-block process. Each sub-domain of the grid is independent from its neighbors and boundary conditions on sub-blocks are dictated by the explored physics and they are fixed arbitrarily since they are inaccessible in natural conditions.
The influence of boundary conditions on the output measures, i.e equivalent properties and averaged fields, can be attenuated using the extend-local procedure [93] as described in figure 2.12. Each local sub-domain is immersed into a close neighborhood of characteristic size δ, then computation of pore scale physics is achieved in a region larger than the original sub-block (blue region fig. 2.12a). The upscaling is then performed on the target local sub-block[2] (yellow region fig. 2.12b).

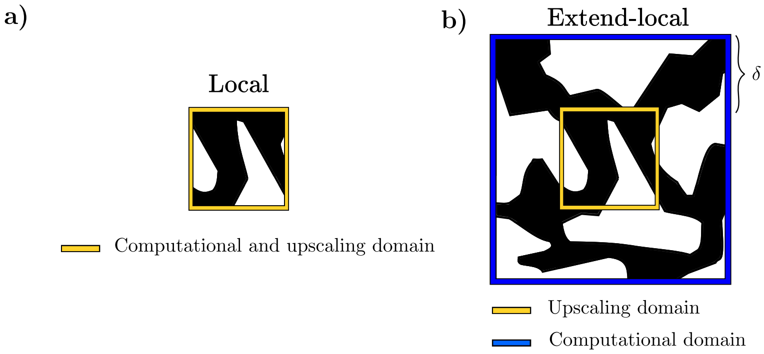

Figure 2.12: Comparison of purely local vs extend-local upscaling on a sub-block. a) In the local averaging approach, the computational and upscaling domains merge. b) In the extend-local averaging approach, the upscaling domain is a strict subset of the computational domain where an extend neighboring of size δ is considered.

---

[2] In case of the biological complexity of the osteoasarcoma, the local sub-block is immersed in its surrounding biological environment which allows tissue equivalent properties to be obtained with reliability.

In the local-global method [94], an initial computation at the macroscopic scale can guide the choice of sub-domain boundary conditions; only if the pore scale physics is not too complex. The coarse simulation built on a coarse mesh, gives a first estimation of boundary conditions to be applied in an iteration of the local or extend-local grid-block methods on each sub-block.
In the fluid flow case, an harmonic interpolation can be used. Then, the equivalent response of a sub-block only depends on the interpolated boundary conditions. An iterative process can be implemented to improve accuracy.

In the context of osteosarcoma, the local and extend-local methods seem well adapted because of the complexity of the problem and the size of clinical data, i.e. digitalized histological slices. Indeed, a local-global scheme requires an iteration of the grid-block process as well as global simulations with a significant computational cost.

2.4.2 Sequential upscaling process

A porous medium generally shows a continuum of observation scales. However, in classical upscaling methods only two scales are considered but subsidiaries scales may give relevant information. Indeed, these subsidiaries scales allow a better prediction of the physical properties as described schematically on figure 2.13.

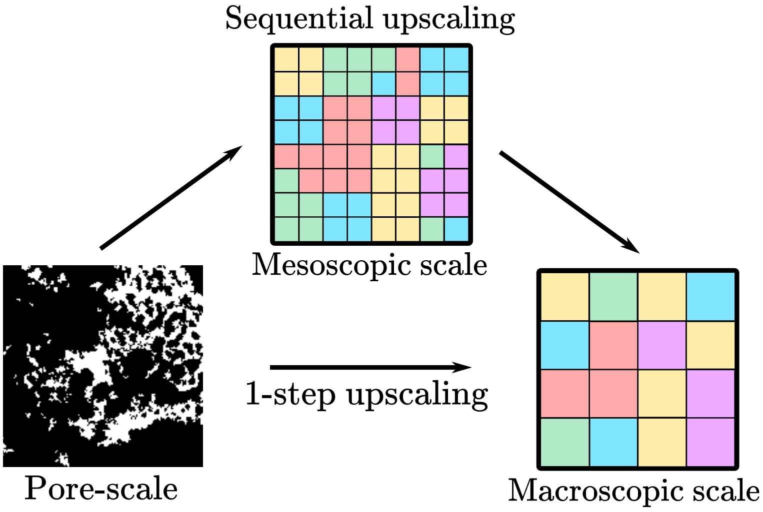

Figure 2.13: Comparison of direct (1-step) and sequential (2-step) upscaling processes. A subsidiary scale is considered in the sequential framework accounting for the mesoscopic effects.

Therefore, it is possible to go from the pore scale to the macroscopic scale by considering a cascade of upscaling through a succession of intermediary scales. Some works study this sequential process from classical method of homogenization like volume averaging [95, 96], as illustrated in figure 2.14, or by asymptotic expansion [97].
This method allows a better understanding and analysis of the object of study by providing geometric or physical characteristics at different scales of observations, which is not the case with a classical upscaling method.
Compared to a one-step grid-block upscaling scheme, the sequential grid-block method allows to process numerically large geometries, as it limits drastically the required computer memory by splitting finite element matrices [98], while providing fast prediction of equivalent properties. Note that changes in the nature of the PDEs at each scale can occur and may also allow a reduction in numerical costs.

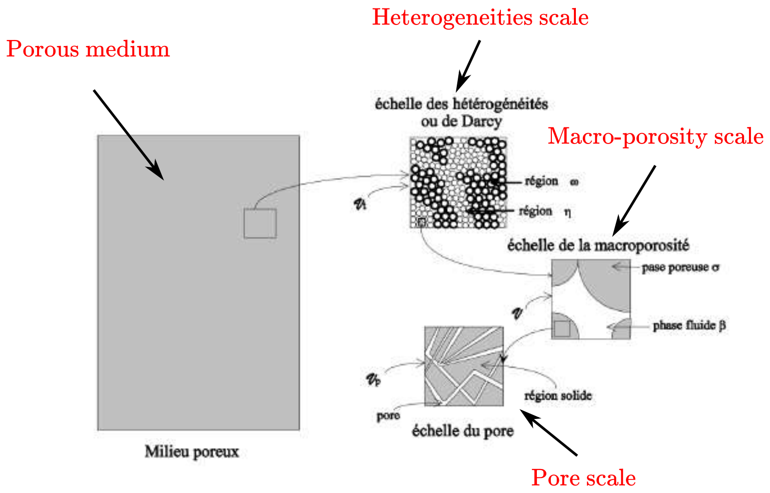

Figure 2.14: A sequential upscaling approach, for an arbitrary porous medium, using volume averaging and two intermediary scale [96].

In the following, we consider a two-steps sequential method, as illustrated in figure 2.15, with the addition of a single scale subsidiary compared to the classical grid-block. Thus, the characterization of the object will be done at three scales: at the pore scale (which we will call L_1) and through mechanical descriptions equivalent to the L_2 and L_3 scales.

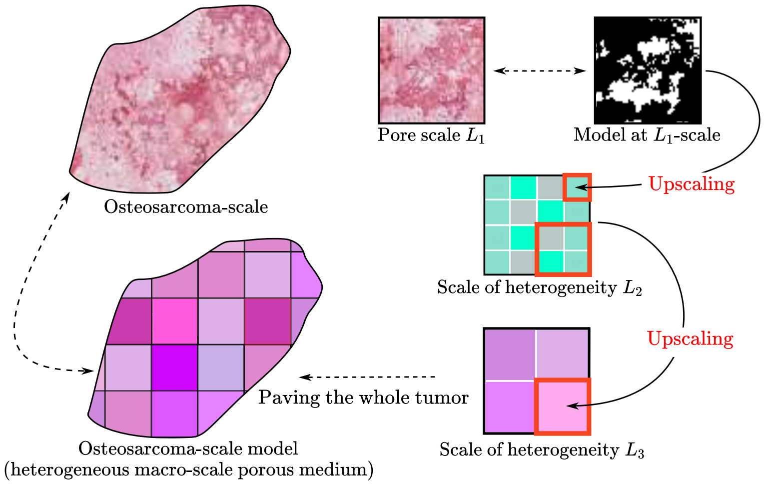

Figure 2.15: A 2-steps sequential upscaling approach by grid block, applied to osteosarcoma.

2.5 Workflow developed in the thesis

In this section, we develop the overall work flow of the thesis. First, we describe how the clinical material was obtained. Then, the numerical methods are explained; from the image processing of histological slides to the actual calculation of the equivalent properties. Finally, a summary of the global workflow is proposed.

2.5.1 Clinical data post-processing

Histological slides were obtained at the IUCT by the team of Pr A. Gomez-Brouchet. They correspond to a group of patients with high-grade conventional osteosarcoma and are obtained on surgically removed tumors after a neoadjuvant chemotherapy. After a 4mm thickness cutting of the tumor, it is decalcifed, fixed and placed into parrafin. Using a microtome (Thermo scientific; HM 340 E), the paraffin blocks were cut with a thickness of $4\mu m$. Sections are placed on white slides (Thermo scientific; SuperFrost Plus) and stored at 4°C.
A H&E staining is performed corresponding to a successive application of hematin (basic nuclear

stain) and eosin (acid cytoplasmic stain). Then, the cells are marked according to their nuclei (purple/black) and their cytoplasm (pink). The osseous ECM shows a gradient of color from orange-pink to dark purple depending on the degree of calcification of the tissue. Slices are scanned using a digital slide scanner (NanoZoomer-XR Hamamatsu).

Image Segmentation (fig. 2.16a) was performed, according to the work of Anthony Mancini (PhD student at IMFT), using Matlab© with a machine learning k-nearest neighbors algorithm (KNN) to label different elements of the slice such as the bone phase, the cells and the interstitial phase [99]. The KNN method is a supervised pattern recognition algorithm. A new observation is classified according to the k nearest neighbors and its given label will be the majority label of these k neighbors. This method is applied to label different elements from color distributions. Two labels are of particular interest: the bone and the cell phase. From the bone label (mineralized and non-mineralized ECM), a binary image is extracted (fig. 2.16b).
A post-processing is performed in which we remove all connected parts that have less than 10 pixels (corresponding to noise) followed by a smoothing of segmented bone borders.
The cell phase is also binarized. Because of the size of the histological sections, segmentation is performed on a mosaic of images. The number of cells on a sub-image corresponds to the number of connected parts of pixels classified as ”cell”. If a cell is between two or more sub-images, it will not be counted more than once since the cell will be associated with the block in which its barycenter is located. Note that red blood cells are not counted as cells, but have their own label. The cell density is obtained by dividing this number by the number of pixels that are not labeled as ”bone”. As a result, the cell density is obtained only in the pores (unit given by number of cells per ”fluid“ mm^2), avoiding biased correlations. Thus, a sub-image with a large bone phase does not necessarily correspond to a region with low cell density.

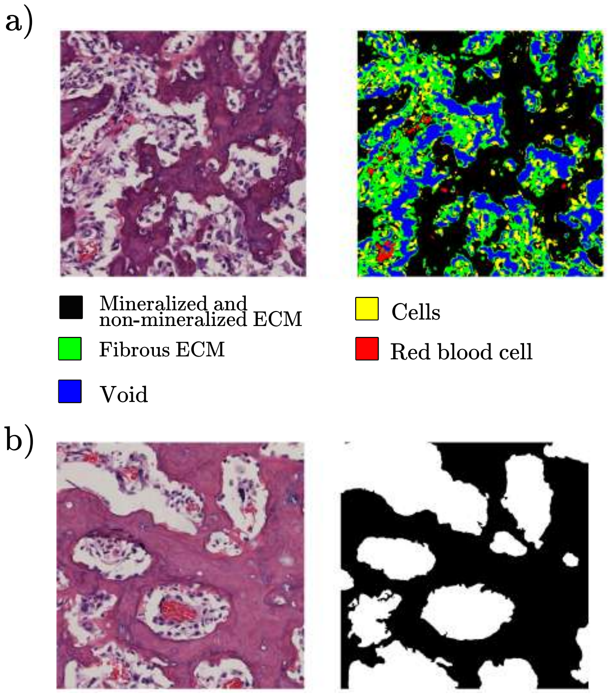

Figure 2.16: Segmentation of H&E histological slide. a) A KNN algorithm to label the phases that compose the osteosarcoma tissue. b) Binarization according to the labels given by the KNN process and deletion of small connected parts (Anthony Mancini thesis).

2.5.2 Numerical workflow

To represent the physical models numerically, different discretization methods are possible and they can be separated into two main families according to their integrals or differentials nature. When dealing with integral scheme, i.e. finite element (FEM) and finite volume (FVM) methods, complex geometries can be considered using irregular meshes and explicit error approximations. For differential method, i.e. finite difference method, the error can also be minimized by considering regular grids.

In this work, we decided to use integral scheme and the finite element method since it permits to handle multi-physical analysis with mixed formulation and explore complex geometrical architecture. The FEM provides an effective numerical resolution of PDEs. The discrete form of the weak solutions, i.e. resulting from the distribution representation of the governing equations, is expected to give an approximation of the strong solution of the problem. The solution is found in specific integration points of the mesh and then interpolated. The process conducts to the resolution of a linear system in the form $AU = B$. Drawback can be find in the FEM compared to the FVM such as the non-control of local fluxes but adaptation can be available.

Many FEM software are available, either free (FEniCS, FreeFem++) or commercial packages (ANSYS, NASTRAN, COMSOL, Abaqus). In the following, FEniCS [100] is chosen for its adaptive and intuitive design. This tool is requiring an understanding of the mathematics underlying FEM, but it permits to solve a large spectrum of PDEs and their couplings through an intuitive writing of weak formulations. Components of FEniCS are also designed for parallel processing.

To generate complex meshes and manage results post-processing, GMSH [101], an open-source 3D mesh generator software, is used [3]. Scripting language (C++, C, Pyhton etc) are available.

Matlab is used to pre-condition binarized osteosarcoma histological slides [4]. The overall numerical workflow is shown in figure 2.17.

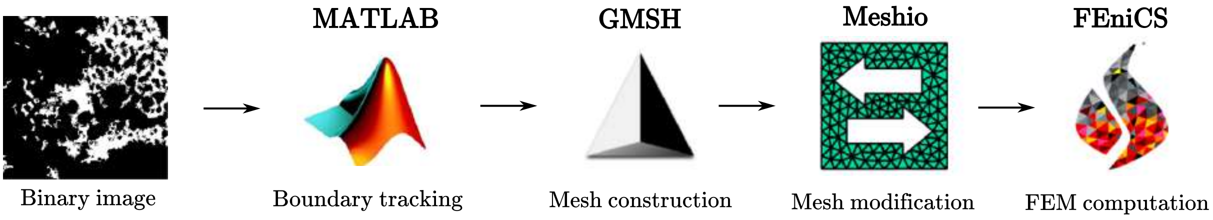

Figure 2.17: Overall numerical worflow: from a binarized osteosarcoma image to an effective physic computation on FEniCS.

2.5.3 Summary of the workflow

In case of heterogeneous porous media, the classical homogenization methods are not directly applicable because the upper scale physics depends strongly on the microstructure of the object. To overcome this limitation, the grid-block computational homogenization method is used to determine the upper scale properties.

With the improvement of image processing techniques, it is possible to work at scales with increasingly fine and complex microstructures. Obviously, such precision has a drawback: simulations on very large volumes involve a significant computation cost, sometimes inaccessible. To solve this problem, we decide to add a two-step sequential functionality to the grid-block method. It is characterized by a process iteration at a subsidiary scale. The sequential approach reduces the cost in memory and computation time while providing an accurate prediction of physical equivalent properties at different scales while preserving anisotropy, a point that will validated in the following chapters of the thesis.

---

[3] Note that Meshio is necessary for a translation of the mesh files produced by GMSH in understandable files for FEniCS (a pruning is necessary for 2D mesh).

[4] for the tracking of internal boundaries

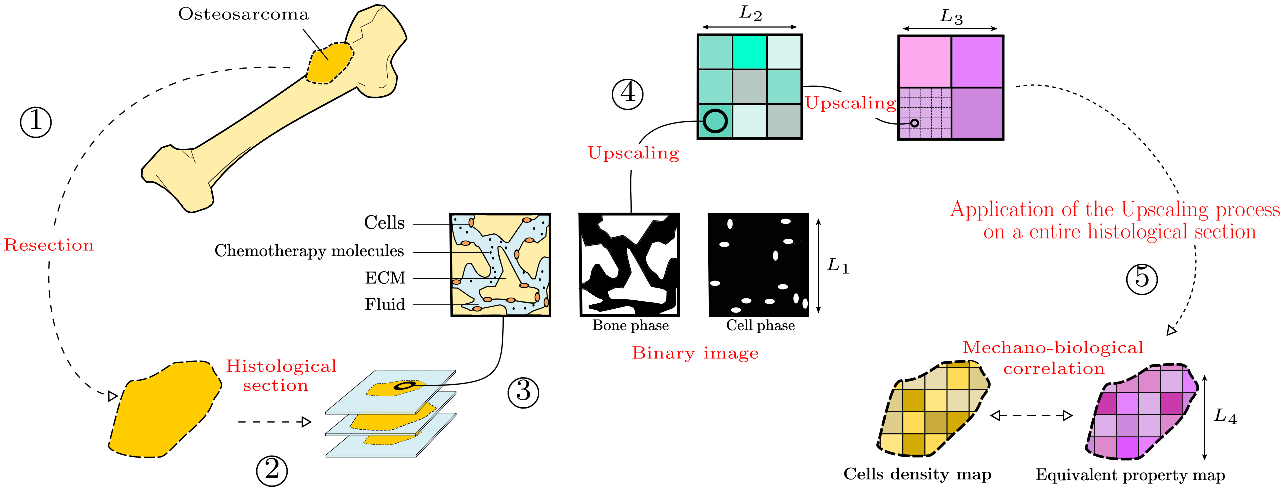

Figure 2.18: A general mechanical study of osteosarcoma. (1) Osteosarcoma is removed surgically from patient. (2) A microscopic study of the tumor is carried out by the pathologist using osteosarcoma histological sections from the Biology Resources Center-*CHU Toulouse* and digitalized. (3) Image processing of the histological sections is done to obtain binary images of the bone and cell phases. (4) A sequential Grid-Block upscaling process is applied on bone phase image which decreases the cost of computations regarding CPU time: here with two iterations admitting three lengths L_1, L_2 and L_3. (5) Search of correlation between cell density and equivalent mechanical properties at the L_4 tumor scale. Potential identification of mechano-biomarkers.

In conclusion, our aim is to provide a consistent computational homogenization method to estimate, from a deterministic point of view, the 2D equivalent physical properties of osteosarcoma considered as a biological porous media strongly heterogeneous.
The grid-block method is implemented and an extend-local method is used to limit biases of boundary conditions. A sequential approach is used to limit computational cost. Mechanical equivalent parameters correlated to cellular densities obtained from the segmentation will allow the response to chemotherapy to be explored by implementing a mechanobiology approach. The overall methodology is described in figure 2.18.
Although some methodological bricks of this workflow are available in the literature their association, adaptation and further development is innovative. It is also for the first time applied on biological tissue and patient follow-up images. This thesis work describes and validates, for the first time to our knowledge, this workflow in a complete way.

The following chapter will focus on the development and validation of this workflow in the case of transport phenomena.

Chapter 3

Transport in osteosarcoma

Contents

The aim of this chapter is to describe flow and diffusive transport into the tumoral tissue through a consistent mechanistic approach by upscaling. The extend-local and the 2-steps grid-block methods are explored for flow and diffusive transport. An important part of the study is the determination of the mathematical models at higher scales which can be different, according to the deterministic homogenization theory, from those to be considered at the pore scale models.

The first step concern the study of interstitial flow in osteosarcoma where we consider a Stokes equation at the pore scale. This choice not only allows us to propose an original use of the extend-local method but also to better take into account small scale phenomena at the large scale. In a second part, an application of the same methodology to mass transport is considered. In both cases the resolution of continuous equations by the finite element method is described.

3.1 Context and model

The grid-block method has been frequently used to study flow and diffusive transports [102, 103] (see section 2.4.1). Initially, the extend-local methodology was implemented to solve elliptic equations, such as diffusive transport or to some extend incompressible Darcy flow [104]. Concerning the sequential method (section 2.4.2), very few works have been done on it. Most of the studies of the literature assume scale separation of the treated problem and the resulting upscaled properties are effective [95, 97].

To our knowledge, the coupling between the extend-local method and the sequential method to describe flow and mass transport in strongly heterogeneous media has never been studied. This is the challenge dealt with in this chapter.

As described in chapter 2, several assumptions must be made about the geometric character of the physical system to achieve a consistent mechanical characterization of flow and mass transport in osteosarcoma. The chosen model, at the pore scale, is illustrated on figure 3.1.

Here, the tumor is assumed to be avascular in order to focus on the interstitial flow. This assumption is legitimized from a biological point of view by the high pressure in the core of the tumor due to 1) cell proliferation in a confined environment and 2) vessel leakage.
The tumor tissue is considered as a 2D biphasic structure, i.e. a fluid phase and a solid phase with interconnected pores. The solid phase is representing the osseous ECM. The fluid phase, saturating the porous matrix, includes the fibrous ECM and the interstitial fluid [1]. Essentially, a 1-porosity model is chosen, i.e. there is no sub-porosity at a lower scale, and the geometries is like a two-dimensional perforated media.
The presence of cell populations is not considered in this mechanistic approach and cell distribution will be identified separately (see chapter 5).

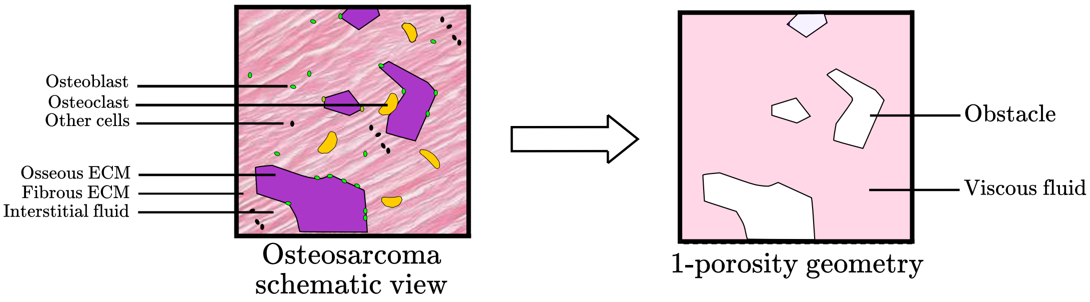

Figure 3.1: Biological and mechanical approximation of osteosarcoma in the transport study.

3.2 Interstitial flow

In this section, we thoroughly present the mathematics of the chosen upscaling method through its application to interstitial fluid flow in osteosarcoma. The concept of the upscaling process outlined in this section will be used in the rest of the thesis. In a second section, we look at the numerical parameters of the developed methodology and their effect on the upscaling scheme. Finally, a comprehensive study of the upscaling method will be conducted according to its various intrinsic parameters (grid-block dimensions and boundary condition choices for example). The resulting equivalent permeability tensors behavior will be studied through their: diagonal terms expressing the flow dependence to pressure gradient, extra-diagonal terms expressing the flow dependence on a orthogonal direction to the pressure gradient (also representative of anisotropy), spectral radius or main permeability (highest eigenvalue) associated with the strength of the main flow and eigenvectors representing intrinsic principal directions of permeabilities and flow, not oriented by the pressure difference.

3.2.1 Development of the grid-block method

At the pore scale, the model considered is a 1-porosity model, described in figure 3.1. In the following, Ω and $\partial\Omega$ are representing domains and boundaries, respectively, such as (1) $\Omega = \Omega_f \cup \Omega_s$ where Ω_f and Ω_s correspond respectively to the fluid and solid parts of the domain (2) $\partial\Omega = \partial_{int}\Omega \cup \partial_{ext}\Omega$, where $\partial_{int}\Omega$ and $\partial_{ext}\Omega$ are the internal, which correspond to fluid/solid boundaries and external boundaries, ie boundaries on the L_1 grid and external boundaries of the studied domain.

A sequential grid-block method (section 2.4) in two steps, as described in figure 2.13, is developed to predict the interstitial flow in 2D histological sections of osteosarcoma. In this case, the overall 2-steps workflow is described in figure 3.2. Three scales L_1, L_2 and L_3 are used, ordered such as $L_1 < L_2 < L_3$. Since no assumptions are made about scale separation or REV, lengths are not characteristic and they can be chosen arbitrarily. Two successive upscalings are performed, from the L_1-scale to the L_2-scale then from the L_2-scale to the L_3-scale.

---

[1] A simplifying biological assumption is made as no explicit distinction will be made between the fibrous ECM and the interstitial fluid: instead we consider a viscous fluid representative of a mixture between these two phases.

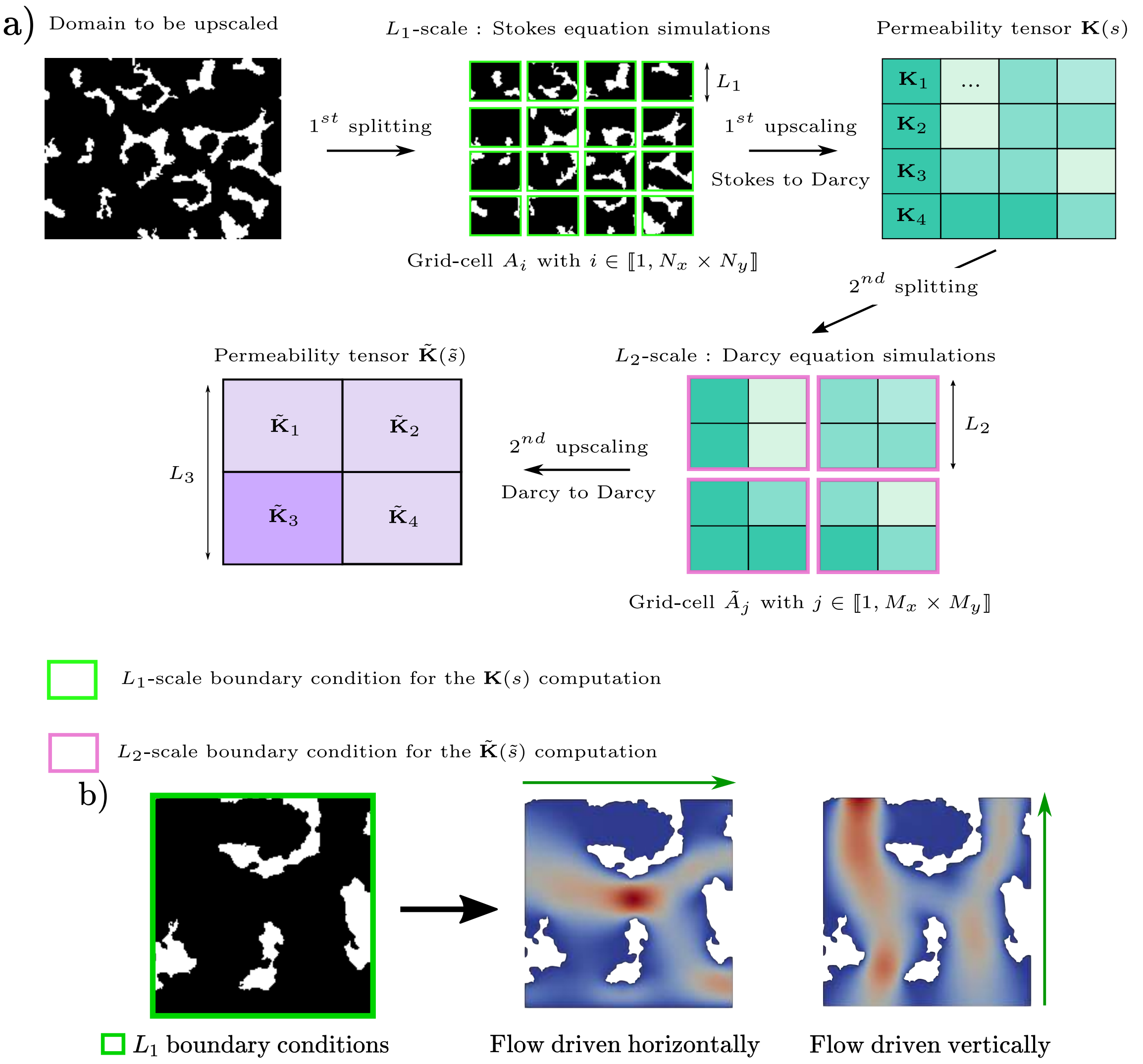

Figure 3.2: a) Sequential Grid-block upscaling scheme applied to the momentum transport where the L_1-scale behavior is described by Stokes equation. A 2-steps grid-block upscaling method is considered resulting in a Darcy regime both at the L_2 and L_3 scales. b) Velocity magnitude of two representative Stokes flow calculations, obtained by imposing a horizontal and vertical pressure gradient, as performed to calculate L_2-scale permeability.

At the pore scale L_1, where the micro-architecture is strongly heterogeneous, the fluid flow is characterized by predominant viscous effects corresponding to flow with a low Reynolds number. It is assumed to be Newtonian and incompressible. Therefore, the flow driven by a pressure gradient ∇p_{L_1} is modeled by the governing equations in Ω which correspond to the following Stokes problem [2]:

$$\begin{cases} \mu \nabla^2 \mathbf{u}_{L_1} - \nabla p_{L_1} = -\rho \mathbf{g}, \quad \text{on } \Omega_f \ (L_1\text{-scale}) \\ \nabla . \mathbf{u}_{L_1} = 0, \quad \text{on } \Omega_f \\ \mathbf{u}_{L_1} = 0, \quad \text{on } \partial_{int}\Omega \\ \text{Boundary conditions (BCs) on } \partial_{ext}\Omega \end{cases} \tag{3.1}$$

where μ and ρ are fluid viscosity and density, respectively, and $\mathbf{u}_{L_1}$and $\mathbf{g}$ are fluid velocity and gravity, respectively. In the following, the gravity term is not considered because of its supposed negligible role on interstitial flow in osteosarcoma.

Thus, for a given model at the pore scale, the developed 2-steps grid block method differs by the boundary conditions (BCs) applied on the edges of the domains, at L_1-scale but also, as we will see later, at L_2-scale. A comparison of the results obtained by the totality of the boundary

---

[2] The choice of the pore scale physics (3.1) allows from a numerical point of view an original study of the chosen upscaling scheme.

conditions discussed below is conducted in section 3.2.4.2.

The first uspcaling, from the L_1-scale to the L_2-scale, is based upon the splitting of the initial domain into $N_x \times N_y$ sub-domains, named A_i with $i \in [[1, N_x \times N_y]]$, having the same size $D_x \times D_y = L_1^2$. L_2-scale equivalent permeability tensors $\mathbf{K}_i$ are computed on each subdomain A_i. In order to construct a complete tensor, i.e. relating the complete anisotropy of a subdomain, it is necessary to consider two Stokes flows driven by the pressure gradient δP (pressure difference between the inlet and outlet boundaries), one in each direction of space. Moreover, to determine explicitly the extra-diagonal coefficients of the equivalent tensor, it is not possible to simply consider an integration on the boundaries, i.e to consider total flow rates. Indeed, for a wall condition, the extra-diagonal terms could not be deduced from this method. Instead, we rather consider the averaged velocities (3.2), provided here on a sub-block named A for convenience.

$$\langle \mathbf{u}_{L_1} \rangle_A = \frac{1}{|A|} \int_{A_f} \mathbf{u}_{L_1} \mathrm{d}S \tag{3.2}$$

where $|A|$ corresponds to the total surface area, also taking into account the obstacles areas A_s. At this scale, A_f represents in fact only the pore space where fluid flow is considered.

Then, the equivalent permeability tensor at the L_2-scale, for a given subblock A is given under the matrix equation (3.3) following [102].

$$(\mathbf{K})_{lk} = \Big(-\mu \langle \mathbf{u}_{L_1,k} \rangle_A^l \frac{L_1}{(\delta P)^l} \Big)_{1 \leq l,k \leq 2} \tag{3.3}$$

where superscripts l correspond to the flow test direction namely 1 for horizontal direction and 2 for vertical direction as illustrated on figure 3.2b, and subscripts k correspond to space variable components.

From now, the flow is described at the intermediate scale L_2, on a piecewise smoothed geometry $\tilde{\Omega}$, by the incompressible Darcy equation (3.4). The permeability tensor $\mathbf{K}(s)$ is piecewise constant (s is the L_2-space variable) and takes its values on the splitting among the $\mathbf{K}_i$. Velocity $\mathbf{U}_{L_2}$ is the Darcy velocity or filtration rate [3] and p_{L_2} is the pressure gradient at the L_2-scale.

$$\begin{cases} \mathbf{U}_{L_2} = -\dfrac{\mathbf{K}(s)}{\mu} . \nabla p_{L_2}, \quad \text{on } \tilde{\Omega} \ (L_2\text{-scale}) \\ \nabla . \mathbf{U}_{L_2} = 0, \quad \text{on } \tilde{\Omega} \\ \text{BCs on } \partial\tilde{\Omega} \end{cases} \tag{3.4}$$

This result is motivated by the classical homogenization results [68] on a periodic geometry with a single porosity and a consolidated solid matrix.

For the second upscaling, the smaller scale physical system is now made up of the $\tilde{\Omega}$ geometry and the flow is described by equations (3.4). Because of the elliptic nature of the problem to be solved, it is acceptable to consider a splitting of $\tilde{\Omega}$ coarser than the one operated on Ω previously. It is made of $M_x \times M_y$ subdomains $\tilde{A}_j$ overlapping the previous one with $N_x \geq M_x$ and $N_y \geq M_y$. Then, a new set of permeability tensors $\tilde{\mathbf{K}}_i$, constant on $\tilde{A}_i$, is obtained after the upscaling of equation (3.4) and using a specific post-processing.

The post-processing to consider L_3-scale full equivalent permeability tensor can only relies on calculation of the averaged velocities and pressure gradients over the whole domain [105]. Indeed, some approach consider only integration over boundary but this does not permit the calculation of anisotropic terms for all boundary conditions, especially the impervious one. In the same way as in the first upscaling, at least two flow tests solving (3.4) are needed in the two space directions to account for the complete anisotropy of the domain. For each test $i \in [[1, 2]]$,

---

[3] The Darcy velocity is a volume flow per unit area and it is different from the effective velocity of fluid particles. Discrepancies can be exacerbated with low porosity media and/or heterogeneous architectures.

where 1 corresponds to the horizontal direction and 2 to the vertical direction, we consider for a given piecewise smooth sub-block named $\tilde{A}$, the following averaging

$$\langle \mathbf{U}_{L_2} \rangle_{\tilde{A}} = \frac{1}{|\tilde{A}|} \int_{\tilde{A}} \mathbf{U}_{L_2} \; dS \tag{3.5}$$

$$\langle \nabla p_{L_2} \rangle_{\tilde{A}} = \frac{1}{|\tilde{A}|} \int_{\tilde{A}} \nabla p_{L_2} \; dS \tag{3.6}$$

Note that using the interstitial velocity may induce continuity problems at interfaces. By using specific hypothesis in homogenization theories (such as VA) some terms depending upon pressure gradients are of higher order and can be neglected. Then, the average flux vector can be used.

As we solve two Darcy flow tests, we obtain a total of four equations with

$$\mu \langle \mathbf{U}_{L_2,s_1} \rangle^j_{\tilde{\Omega}} = -(\tilde{K}_{11} \langle \partial_{s_1} p_{L_2} \rangle^j_{\tilde{\Omega}} + \tilde{K}_{12} \langle \partial_{s_2} p_{L_2} \rangle^j_{\tilde{\Omega}}) \tag{3.7}$$

$$\mu \langle \mathbf{U}_{L_2,s_2} \rangle^j_{\tilde{\Omega}} = -(\tilde{K}_{21} \langle \partial_{s_1} p_{L_2} \rangle^j_{\tilde{\Omega}} + \tilde{K}_{22} \langle \partial_{s_2} p_{L_2} \rangle^j_{\tilde{\Omega}}) \tag{3.8}$$

where the superscript j correspond to a given test flow, the L_2-space variable is noted $s = (s_1, s_2)$ and $\tilde{\mathbf{K}}$ is the equivalent tensor at the L_3-scale for the sub-block $\tilde{A}$.
Finally, the above equations can be synthesized in matrix form, expressed by (3.9).

$$\begin{pmatrix} \langle \partial_{s_1} p_{L_2} \rangle^1_{\tilde{A}} & \langle \partial_{s_2} p_{L_2} \rangle^1_{\tilde{A}} & 0 & 0 \\ 0 & 0 & \langle \partial_{s_1} p_{L_2} \rangle^1_{\tilde{A}} & \langle \partial_{s_2} p_{L_2} \rangle^1_{\tilde{A}} \\ \langle \partial_{s_1} p_{L_2} \rangle^2_{\tilde{A}} & \langle \partial_{s_2} p_{L_2} \rangle^2_{\tilde{A}} & 0 & 0 \\ 0 & 0 & \langle \partial_{s_1} p_{L_2} \rangle^2_{\tilde{A}} & \langle \partial_{s_2} p_{L_2} \rangle^2_{\tilde{A}} \end{pmatrix} \begin{pmatrix} \tilde{K}_{11} \\ \tilde{K}_{12} \\ \tilde{K}_{21} \\ \tilde{K}_{22} \end{pmatrix} = -\mu \begin{pmatrix} \langle \mathbf{U}_{L_2,s_1} \rangle^1_{\tilde{A}} \\ \langle \mathbf{U}_{L_2,s_2} \rangle^1_{\tilde{A}} \\ \langle \mathbf{U}_{L_2,s_1} \rangle^2_{\tilde{A}} \\ \langle \mathbf{U}_{L_2,s_2} \rangle^2_{\tilde{A}} \end{pmatrix} \tag{3.9}$$

A new Darcy equation (3.10), on a new domain $\tilde{\tilde{\Omega}}$, is obtained with a piecewise constant permeability tensor $\tilde{\mathbf{K}}(\tilde{s})$, where $\tilde{s}$ is the L_3-space variable, $\mathbf{U}_{L_3}$ and ∇p_{L_3} are the Darcy velocity and pressure gradient at L_3-scale, respectively. Here, the 2-step process is stopped for illustration purposes, while the sequential approach could involved further steps [4].

$$\begin{cases} \mathbf{U}_{L_3} = -\dfrac{\tilde{\mathbf{K}}(\tilde{s})}{\mu} . \nabla p_{L_3}, \quad \text{on } \tilde{\tilde{\Omega}} \ (L_3\text{-scale}) \\ \nabla . \mathbf{U}_{L_3} = 0, \quad \text{on } \tilde{\tilde{\Omega}} \\ \text{BCs on } \partial \tilde{\tilde{\Omega}} \end{cases} \tag{3.10}$$

In appearance, the nature of the physical system (3.10) is similar to (3.4). On the other hand, this new system, encapsulating information from lower scales, smooths the spatial oscillations of the field variables through a smoother domain and thus allows an important numerical simplification.

The transition from equation (3.4) to equation (3.10) is not trivial in the sense that the nature of the mathematical models are not necessarily identical, even in the case of elliptic equations. We give here some elements allowing to justify the nature of the model chosen at the L_3-scale and more precisely of equation (3.10) in the osteosarcoma case. We distinguish two main possible extensions of the traditional Darcy flow which are the Darcy-Brinkman and Darcy-Forcheimer equations.
The Darcy-Forcheimer model [106] expresses the non-linear effects of the flow. Through the addition of a correction term directly depending on the Reynolds number, the inertial effects of the flow are taken into account. In osteosarcoma and more precisely in the fibrous ECM, this Reynolds number is sufficiently low as mentioned above to not consider this correction.
The Darcy-Brikman equation, on the other hand, describes a flow in a medium with high porosity (> 95%, [107]) and allows to consider interface phenomena between the fluid and pores

---

[4] Boundary condition are considered at the L_3-scale but, we emphasize, are not considered as effective but of the form of that described below.

boundary (inducing a shear stress). This equation represents the transient regime between the Darcy equations and a free viscous flow. In the case of osteosarcoma, the overall porosity is way lower (important production of bone) and the geometry $\tilde{\tilde{\Omega}}$ considered at L_3-scale is piece-wise smooth making the Darcy-Brikman model irrelevant.

As expressed previously, boundary conditions are required to solve the sets of equations (3.1) and (3.4). They are imposed at L_1-scale and L_2-scale, respectively as shown in figure 3.2 for the Stokes equation. We recall that the permeability tensors resulting from the grid-block process are dependent on the boundary conditions without REV assumptions.

At the L_1-scale, a no-slip condition of fluid is imposed on the internal boundaries $\partial_{int}\Omega$. Three type of possible boundary conditions on the external border $\partial_{ext}\Omega$ are then described by equations (3.11), (3.12) and (3.13), associated with wall, symmetry and open boundary conditions, respectively.

- **Wall condition (W)**
  This first condition is the most intuitive since it represents numerically the experimental permeameter measurements [108]. We impose a pressure difference in the domain (inlet and outlet). On the other edges, those parallel to the direction of the flow, a no-slip condition is imposed, leading to an interdiction of transverse flow, as illustrated in figure 3.3a.

$$\begin{cases} p_{L_1} = 1 \text{ and } \partial_n \mathbf{u}_{L_1} = 0, \text{ at the inlet} \\ p_{L_1} = 0 \text{ and } \partial_n \mathbf{u}_{L_1} = 0, \text{ at the outlet} \\ \mathbf{u}_{L_1} = 0, \\ \text{ on external edges parallel to the pressure difference direction} \end{cases} \tag{3.11}$$

- **Symmetry condition (S)**
  This second condition is the symmetric condition and corresponds in some way to a relaxation of the wall condition [102]. Here, we still impose a pressure difference in the domain to drive the flow but the no-slip condition of (3.11) is replaced by a condition of nullity of the normal components, as illustrated in figure 3.3b. This weakening of the wall condition still leads to a prohibition of transverse flow but allows some sliding in the direction of the flow (tangent velocity may be non zero).

$$\begin{cases} p_{L_1} = 1 \text{ and } \partial_n \mathbf{u}_{L_1} = 0, \text{ at the inlet} \\ p_{L_1} = 0 \text{ and } \partial_n \mathbf{u}_{L_1} = 0, \text{ at the outlet} \\ \mathbf{u}_{L_1} \cdot \mathbf{n} = 0 \text{ and } [-p_{L_1} Id + \mu \nabla \mathbf{u}_{L_1}] \cdot \mathbf{n} = 0, \\ \text{ on external edges parallel to the pressure difference direction} \end{cases} \tag{3.12}$$

- **Open boundary condition (PL)**
  This third condition allows the consideration of transverse flow and is a direct adaptation to the Stokes regime of a boundary condition coming in fact from a Darcy model. It was proposed by Bamberger [109, 102]. A pressure difference is still imposed in the inlet and outlet but the other boundaries are no longer closed, as illustrated in figure 3.3c.

$$\begin{cases} p_{L_1} = 1 \text{ and } \partial_n \mathbf{u}_{L_1} = 0, \text{ at the inlet} \\ p_{L_1} = 0 \text{ and } \partial_n \mathbf{u}_{L_1} = 0, \text{ at the outlet} \\ [-p_{L_1} Id + \mu \nabla \mathbf{u}_{L_1}] \cdot \mathbf{n} = -(1 - \dfrac{x_{L_1}}{L_1}) \cdot \mathbf{n}, \\ \text{ on external edges parallel to the pressure difference direction} \end{cases} \tag{3.13}$$

  where x_{L_1} can be the vertical or horizontal spatial variable depending on the direction of the pressure difference and L_1 the sub-cell length, $\mathbf{n}$ the normal and Id the identity matrix.

Note that boundary conditions at flow inlet and outlet consider velocity and pressure. Imposing a pressure and a normal velocity favors flow preferential paths (experimentally verified phenomenon). In opposition, imposing only a constant velocity would generates artificial pressure gradients and can induce a high velocity in places with low permeability.

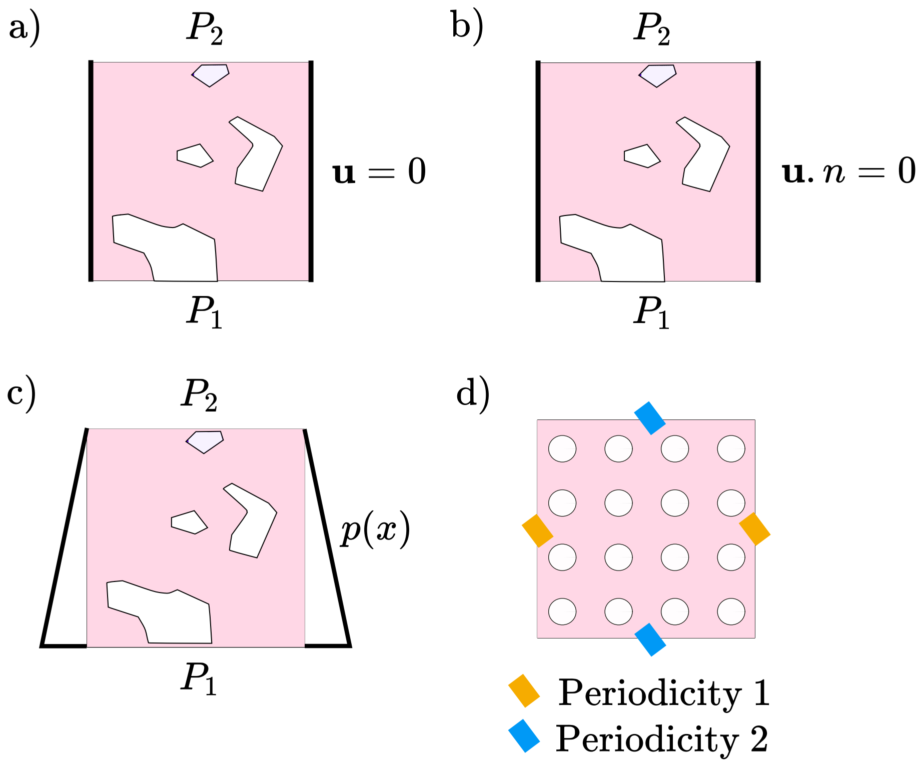

Figure 3.3: Illustration of considered boundary conditions at the L_1-scale. a) The wall condition. b) The symmetry condition. c) The open boundary condition. d) The periodic condition.

At the L_2-scale, an impervious condition expressed by equation (3.14) on equation (3.4) is matched to the wall and symmetry conditions at the L_1-scale as a homogeneous Neumann condition on the flux $\mathbf{U_{L_2}}$ describes an impermeable wall in the Darcy framework. By extension of the first BCs, we still refer to the L_3-scale tensor calculated partially by the L_1-scale wall and symmetric conditions by the name wall and symmetric (even if the L_2 scale condition is associated with the impervious condition). The open boundary conditions also needs a new consistent description at this scale and is expressed by equation (3.15).

- **Impervious**
  This first condition of the Darcy model corresponds in fact to permeameters. We impose a pressure difference in the inlet and outlet domain with both edges remaining impermeable. This method kills transverse flows and was initially used to determine diagonal tensors reflecting a limitation of the method to isotopic geometry. Since then, this method has been adapted for the construction of total equivalent tensors, i.e. also considering extra-diagonal terms which include the anisotropy [95, 110].

$$\begin{cases} p_{L_2} = 1, \text{ at the inlet} \\ p_{L_2} = 0, \text{ at the outlet} \\ \mathbf{U}_{L_2} \cdot \mathbf{n} = 0, \\ \text{ on edges parallel to the pressure difference direction} \end{cases} \tag{3.14}$$

- **Open boundary**
  The second boundary condition to be imposed on the Darcy model is the open boundary condition. This is exactly the Bamberger configuration. Again, pressure difference is imposed in inlet and outlet and a linear pressure gradient is imposed on the other boundaries,

following a decrease along the pressure difference. Authors of [111] called this boundary condition the "Immersion" boundary conditions as the "*sample appears to be "immersed" in an infinite domain with a "far field" hydraulic gradient imposed everywhere outside*" the sub-block. This is illustrated in figure 3.4b.

$$\begin{cases} p_{L_2} = 1, \text{ at the inlet} \\ p_{L_2} = 0, \text{ at the outlet} \\ p_{L_2} = 1 - \dfrac{s}{L_2}, \\ \text{ on edges parallel to the pressure difference direction} \end{cases} \tag{3.15}$$

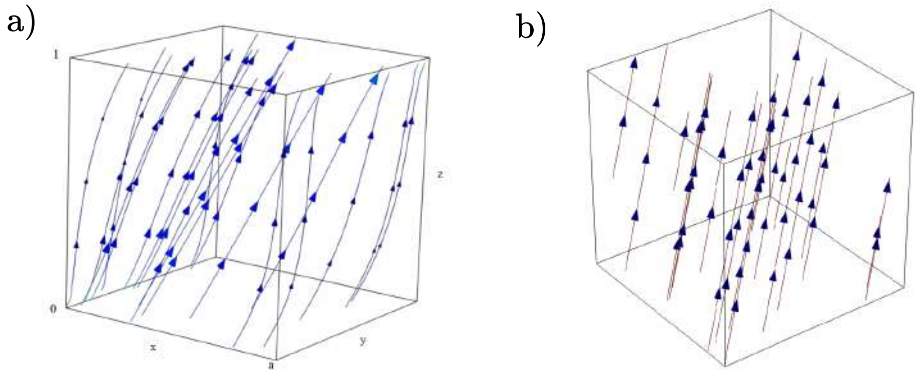

Open boundary condition **Impervious condition**

Figure 3.4: Illustration of streamlines resulting from two boundary conditions with a 3D 1-porosity model and considering an elliptical equation with a macro-scale gradient $-\mathbf{e}_3$. a) When the boundaries are impervious. b) When an open boundary condition is used [112].

In further development and validation of our strategy, periodic geometrical patterns of porous media are used as control to evaluate the accuracy of this sequential grid-block approach. In that case, homogenization theory can be directly applied [113, 114, 115].

A periodic condition (see fig. 3.3d), is considered through the classical AE method by the resolution of Stokes-like cells problem. At the L_1-scale, they take the form on the unit cell named Y:

$$\begin{cases} \nabla p_i - \nabla^2 \mathbf{w}_i = \mathbf{e}_i & \text{in } Y_f \\ \nabla.\mathbf{w}_i = 0 & \text{in } Y_f \\ \mathbf{w}_i = 0 & \text{on } \partial_{int} Y \\ y \to \mathbf{w}_i, p_i & Y\text{-periodic} \end{cases} \tag{3.16}$$

where $(\mathbf{e}_i)_{1 \leq i \leq 2}$ is the canonical basis of $\mathbb{R}^2$ driving the flow, $\mathbf{w}_i$ the local periodic velocity and p_i the local periodic pressure.

At the L_2-scale, one has to resolve Darcy like cell problems on $\tilde{Y}$:

$$\begin{cases} -\nabla \cdot (\mathbf{K}(y) \cdot (\mathbf{e}_i + \nabla p_i)) = 0 & \text{in } \tilde{Y} \\ y \to p_i & \tilde{Y}\text{-periodic} \end{cases} \tag{3.17}$$

where $p_i(y)$ is the local periodic variation solved for an averaged gradient $\mathbf{e}_i$.

The periodic conditions considered here come from the theory of deterministic homogenization. As the osteosarcoma does not present any REV or separation of scales, all the conditions are obviously not met for a strict application of this method. We consider here, after periodization of the object to artificially generate the periodicity, that each sub-block of the splitting is representative of its own REV. These conditions are seen here as a boundary condition allowing to obtain an equivalent (and not effective!) property of each sub-block of the section. For heterogeneous and anisotropic porous media, the use of periodic condition at the pore scale

L_1 would affect the spatial statistical characteristics of the medium [102] since they require a spatial periodization causing percolating and anisotropy problems while requesting a larger computational domain (fig. 3.5). In the following, we use the symmetry periodization method, illustrated in figure 3.5b, as it has the advantage of not causing artificial percolation problems.

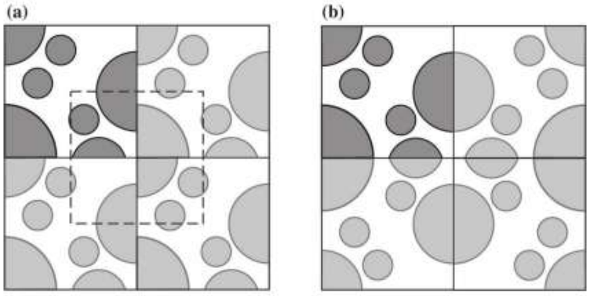

Figure 3.5: Different process of periodization [102] a) by translation b) by symetrization.

Finally, all boundary conditions will be applied consistently across both upscalings in the sense that no crossover between BCs is considered.

To finish, at each step of the sequential method, the tensors must be represented by definite-positive matrices [116] in order to guarantee that the energy is always dissipated by the flow. The symmetry of these matrices is generally required but not necessary and in some cases not desirable [5]. Indeed, symmetry allows to compute real (non complex) principal permeabilities of any configuration through the computation of the eigenvectors. On the other hand, this symmetrization causes the loss of anisotropy information contained in the extra-diagonal terms of the matrix representation [6].

3.2.2 Weak formulation (FEM)

This section describes the methodology of stable discretization of incompressible Stokes equation and Darcy-type equations expressed at L_1-scale and L_2-L_3 scales, respectively.
The finite element method is preferred for its ergonomy facing the complexity of tissue microarchitecture and mechanical responses. Despite this, FEM does not deal straightforwardly with weak solutions in a space of divergence-free functions $(H^1(div))^2$ [117] and methods to enforce incompressibility are needed.

A mixed formulation of the 2D incompressible Stokes equations is used: the velocity and the pressure will be approximated simultaneously. By doing so, we consider the weak formulation (3.18) through mixed element method with
$(H^1(div))^2 = \{\mathbf{u} \in (H^1)^2(\Omega),\ -\int_\Omega \nabla.\mathbf{u}q\ dx = 0 \text{ with } q \in L^2(\Omega)\}$. Here, the pressure is like a Lagrange multiplier to enforce incompressibility [118].

find $(\mathbf{u}, p) \in (H^1)^2 \times L^2(\Omega)$ such that for all $(\mathbf{v}, q) \in (H^1)^2 \times L^2(\Omega)$

$$\begin{cases} \mu \displaystyle\int_\Omega \nabla\mathbf{u} \cdot \nabla\mathbf{v}\ dx - \int_\Omega \nabla \cdot \mathbf{v}p\ dx = \int_\Omega f \cdot \mathbf{v}\ dx + \mu \int_{\partial\Omega} \partial_n \mathbf{u} \cdot \mathbf{v}\ d\sigma - \int_{\partial\Omega} p\mathbf{v} \cdot \mathbf{n}\ d\sigma \\ -\displaystyle\int_\Omega \nabla \cdot \mathbf{u}q\ dx = 0 \end{cases} \tag{3.18}$$

where, for the sake of simplicity, we decide to drop in (3.18) the different indices present in (3.1) and adopt a generic notation. Note that we add a source term f (taken as zero in our

---

[5] In certain cases such as periodical conditions or linear pressure conditions, tensor symmetry can be proved at the upper scale, only if the tensor at the lower scale is also symmetric [116]

[6] The Onsager relations cannot prove the symmetry and do not say anything about the anisotropy of an equivalent property.

applications).
For some physical system, pressure need to be in a subspace of $L^2(\Omega)$, consisting of L^2-functions with zero mean value on Ω (enforced with Lagrange multiplier), for the problem to be well-posed as the pressure is determined up to a constant. This the case for periodic cell problems (3.16) [7]. In opposition, a Neumann condition on velocity over the whole boundary will result in a velocity up to a rigid body velocity and a unique pressure [119].

At the L_1-scale, the so-called discrete inf-sup condition is needed to solve the incompressible Stokes equation. It is shown that the Taylor-Hood elements pair (P_k, P_{k-1}) satisfies this condition with $k \geq 2$ [120]. In the following, we consider the Lagrange pairing (P_2, P_1). Physically, it means that the velocity approximation is quadratic whereas that of pressure is linear.

Through the dual discretization, we obtain a discrete formulation of the problem described by the matrix system (3.19). Variables u, p, are nodal variables, i.e. velocity and pressure, f is a source term. B and B^t are the divergence and gradient matrices, respectively. A is a Laplacian–type matrix. That block matrix is symmetric but indefinite.

$$\begin{bmatrix} A & B \\ B^t & 0 \end{bmatrix} \begin{bmatrix} u \\ p \end{bmatrix} = \begin{bmatrix} f \\ 0 \end{bmatrix} \tag{3.19}$$

A dedicated solver and preconditioner are requiered to resolve the saddle point problem (3.19). Indeed, standard iterative linear solvers fail to converge for symmetric positive indefinite system and the difficulties are increased for large system. To overcome this problem, a minimal residual method (MINRES) [121] and an algebric multigrid preconditioner (AMG) [122] are chosen.

At L_2-scale of the upscaling sequential method, an incompressible Darcy flow has to be solved. As previously, the discretization method based upon mixed finite elements is implemented and the weak problem is expressed by equations (3.20) [8].

find $(\mathbf{U}, P) \in (H^1)^2 \times L^2(\Omega)$ such that for all $(\mathbf{V}, Q) \in (H^1)^2 \times L^2(\Omega)$

$$\begin{cases} \mu \displaystyle\int_\Omega \mathbf{K}^{-1} \cdot \mathbf{U} \cdot \mathbf{V} \; dx - \int_\Omega \nabla \cdot \mathbf{V} P \; dx = - \int_\Omega P \mathbf{V} \cdot \mathbf{n} \; d\sigma \\ \qquad\qquad\qquad\qquad\qquad\qquad - \displaystyle\int_\Omega \nabla \cdot \mathbf{U} Q \; dx = 0 \end{cases} \tag{3.20}$$

To fulfill the discrete inf-sup condition, the Brezzi-Douglas-Marini finite elements (BDM) for the velocity and piecewise constant elements for the pressure are considered [124]. Another function space could also be chosen to approximate the $H^1(div)$ space for the velocities in the lowest-order Raviart-Thomas elements (RT) [125] [9].
Moreover, pressure partial derivatives are required to obtain a non-trivial L_3-scale permeability tensor using equation (3.9). On a discontinuous Lagrange function space, pressure is piecewise constant, i.e. element by element, which implies nil derivatives. The solution is to project the discontinuous pressure on the continuous Lagrange space at higher approximation order, i.e. an order 2 or 3.

3.2.3 Numerical convergence study

In this sub-section, we deal with specific numerical problems of the proposed upscaling approach. After discussing mesh generation at each scale and their impacts on the convergence

---

[7] To constrain the problem one can also impose a pointwise constrain

[8] In the periodic case (3.17), the pressure is unique up to a constant and a solution exist by the Fredholm alternative [123]

[9] The degree of freedom of the RT and BDM spaces can only fix the normal component on the facets of the mesh. Thus a Dirichlet boundary condition is impossible by the very nature of the equation, hence the use of a single boundary condition (3.14) at higher scales.

process of physical outcomes, we examine the effect of the osseous boundaries smoothing. Then, a mesh dedicated to extend-local method at the L_1-scale is proposed and finally, the smoothing procedure of fluid-solid interface in binarized histological images is discussed.

3.2.3.1 Meshes convergence

Gmsh®, an open source finite element mesh generator [10], and Matlab® [11] especially the "bwboundary" function for the numerical tracking of boundary $\partial_{int}\Omega$, are used to generate the meshes at both scales.

At pore scale L_1, the mesh concerns interconnected pores saturated by fluid. The description of interface, i.e. $\partial_{int}\Omega$, between the fluid phase and the solid phase (osseous ECM), requieres a specific procedure. The Delaunay frontal algorithm is used to obtain triangular and unstructured mesh, as shown in figure 3.6a. At L_2 and L_3 scales, the same mesh algorithm is used to generate an unstructured mesh with triangular constant size element. According to splitting of the grid-block procedure, element respect the discontinuities of the piecewise smooth domain $\tilde{\Omega}$, as shown in figure 3.6b, here for a 2×2 L_1-splitting.

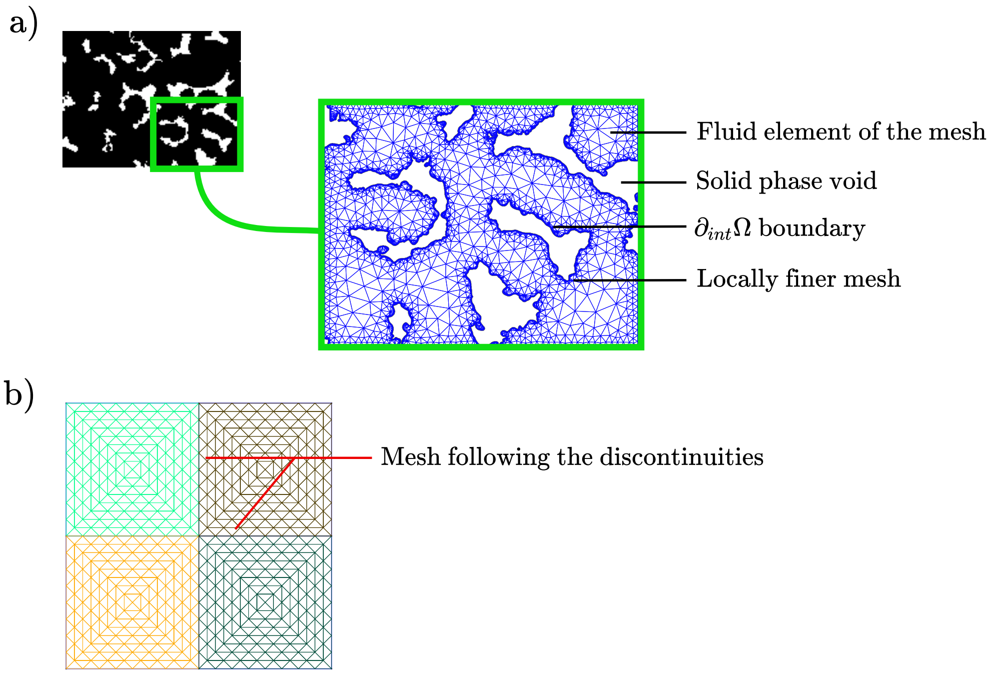

Figure 3.6: Illustration of meshes performed at each scale of the grid-block method for a 1-porosity model a) Perforated, triangular and unstructured mesh at L_1 scale of Ω. b) Triangular and unstructured mesh following the discontinuities of $\tilde{\Omega}$ at L_2 scale.

Remark: From a practical point of view, we were restricted in the optimization of the mesh construction since a software used by GMSH (namely OpenCascade) made impossible the use of B-spline to trace the interfaces between the two phases (especially the one intersecting the external borders). We have therefore trivially connected each point of this boundary by a segment, thus increasing the computation time. Of course, other methods could have been implemented and are currently tested.

A compromise must be found between the accuracy of physical outcomes and computational cost. Usually, mesh convergences in FEM are achieved by using the sensitivity of nodal variables to the mesh size and distance to a reference solution if such a solution is available. With

---

[10] Christophe Geuzaine and Jean-François Remacle. Gmsh: A 3-d finite element mesh generator with built-in pre- and post-processing facilities. International Journal for Numerical Methods in Engineering, 79:1309 – 1331, 09 2009.

[11] MATLAB version 7.10.0. Natick, Massachusetts: The MathWorks Inc., 2010.

upscaling scheme, it is relevant to examine both impacts on local mechanical response at the pore-scale and global response at the macro-scale. First, meshes with constant surface elements are considered. This constant is in correspondence with the mesh density. In GMSH, a characteristic length corresponds roughly to the length of elements edges [12].

The Stokes flow at the local L_1-scale is explored. The convergence process is studied using a 1600 px × 1600 px osteosarcoma binarized image, i.e a 740 μm × 740 μm image as shown in figure 3.7a. The mesh ranges from about 65103 elements with a GMSH size of 30 (Table 3.1) to 210103 elements with a GMSH size of 6 (Table 3.1). Fluid pressures of 0 and 1 are applied on left and right boundaries, respectively and symmetry on the top and bottom boundaries drives an horizontal flow. The denser mesh is used as control since no analytical solution can be used as reference. For local mechanical convergence, the evolution of the horizontal component of fluid velocity along the path located at 800 px vertically is targeted as shown in figure 3.7c. For global property convergence, first component velocity average behavior and its error are plotted in figure 3.7b.

As shown in figure 3.7c, the convergence of local velocity is obtained with a GMSH mesh characteristic length of 16. The convergence of the average velocity is obtained for a GMSH characteristic size of 20, with a relative error of 4%. Finally, good accuracy is obtained considering element size of 16 and under.

GMSH size	Nb of elements
6	213038
8	145070
10	114492
12	97440
14	87350
16	80608
18	75872
20	72480
22	69964
24	68104
26	66644
28	65434
30	64474

Table 3.1: Correspondence between GMSH characteristic mesh size with the number of elements constituting the mesh for the convergence study of the Stokes discretization.

---

[12] not exactly the true upper limit but the optimatized length as edges can be longer or shorter; for example, if the image size is given in pixel, a GMSH characteristic size of 6 will correspond roughly to 6 px.

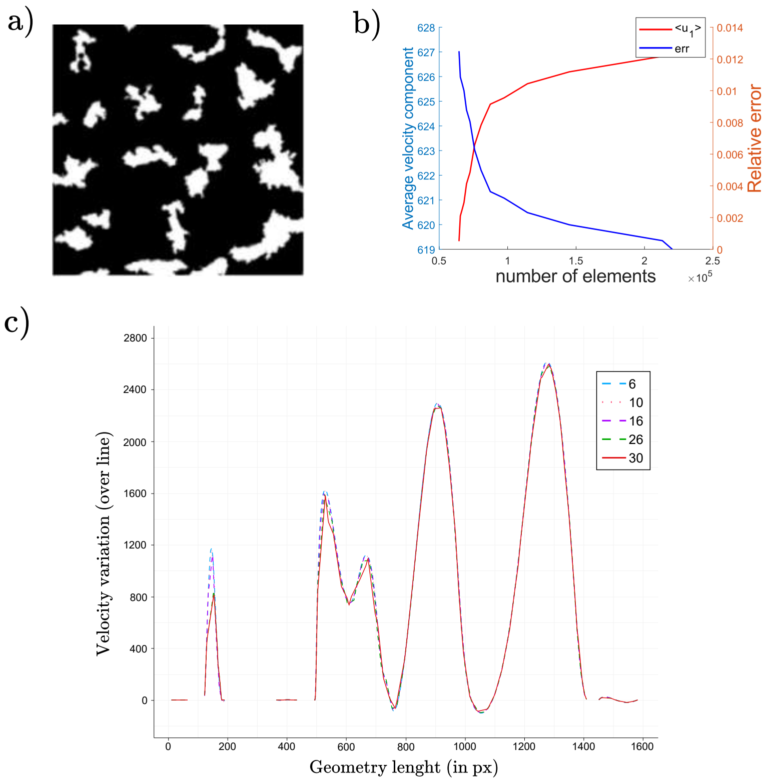

Figure 3.7: Mesh convergence for the incompressible Stokes equations are performed on a 1600 px × 1600 px osteosarcoma image. Flow is imposed from left to right and a symmetry boundary condition is considered on top and bottom of the domain. a) The equivalent behavior is studied through the first velocity component of $\langle \mathbf{u}_{L1} \rangle_\Omega$ in function of the number of elements considered in the mesh densification. b) The pore scale magnitude first velocity component is plotted over the line $y = 800\,\text{px}$ in function of the GMSH mesh characteristic size.

In a similar way, the mesh convergence at L_2 and L_3 scales is studied using a similar method while concerning Darcy flows. Velocity component and its average are studied in case of an horizontal flow driven on a piecewise smooth geometry of size 2000 px × 2000 px with a 5×5 splitting and permeability imposed randomly. The convergence is obtained fora GMSH characteristic size of 20.

3.2.3.2 Boundaries smoothing effect

When a histological section is segmented, the result is always subject to the noise of the method. In our case, the resolution of the images of the original biological material can be altered by the chemical and manual treatment of the samples but also by the image acquisition. As a result, the phases can be difficult to differentiate and a subjective bias is introduced. This has a direct impact on digital methods of acquisition of binarized images. After segmentation (fig. 2.16), there is a portion of the binary image where the nature of the phase is uncertain (where cell, mineralized ECM, non-mineralized ECM and other phases are blended). This bias has been evaluated to be 5% in average (A. Mancini thesis).

In this section, we quantify the nature of the boundaries uncertainties by discussing the smoothing of internal boundaries $\partial_{int}\Omega$, on the equivalent property at the L_2 scale, when a no-slip boundary condition on the Stokes velocity is imposed on the fluid/solid interface. A smoothing technique must be chosen with a capacity to minimise the construction time of the mesh associated with the domain while maintaining the main geometrical features to which the physical systems are sensitive. Thus, the study is based on the comparison of the porosity (geometric character) and the equivalent permeability (mechanical character) responses to the smoothing methods and smoothing parameters.
Two methods have been studied: 1) a dilatation/erosion method with the same disc-shaped

structural element (strel) [13] with an increasing radius 2) an application of an increasing window median filter. The influence of the roughness of $\partial\Omega_{int}$ on L_2-scale equivalent permeability tensor is only performed with symmetric BCs. In the following, the boundary smoothing methods are tested on images of increasing size, ranging from 500 px × 500 px to 2000 px × 2000 px). This method allows in particular to quantify if a smoothing method at fixed parameters plays an increasingly important role as the dimension of the studied domain decreases.

The first smoothing method consists of an application of the Matlab built-in functions "imdilate" and "imerode" with the same disc-like strel (fig. 3.8). A succession of smoothing with increasing radii is considered (between 1px and 8px). This will allow us to see if the same roughness (the smoothed one) plays an increasingly important role as the dimension decreases. For this purpose, we consider a 2000 px × 2000 px image and we truncate it into a succession of sub-images of the desired size [14].

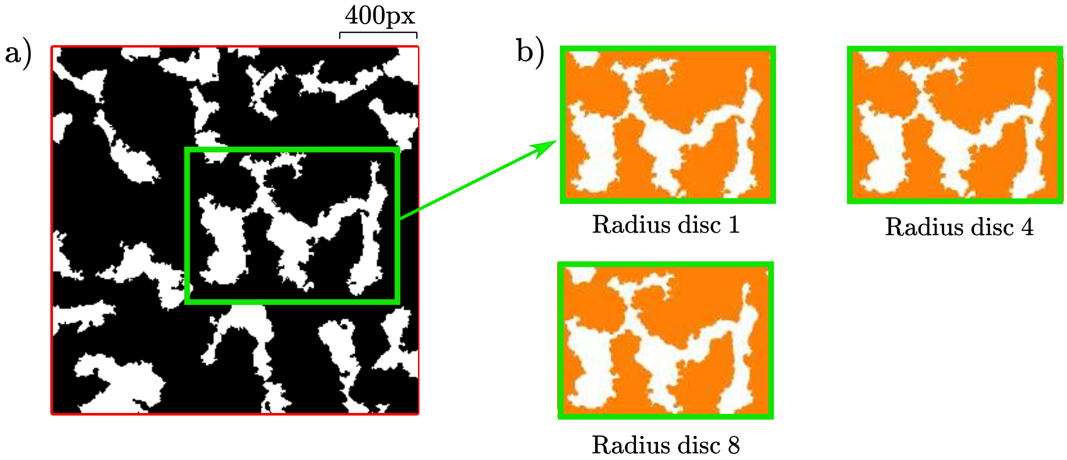

Figure 3.8: Effect of smoothing by dilatation/erosion with different radii on the osseous boundaries for a 2000 px × 2000 px image. The dilatation/erosion process is applied using a 2D morphological structuring element (strel), corresponding to a disc of radius 1px, 4px and 8px, successively.

It can be noticed on figure 3.9c that porosity show very limited variations whatever the image size. The effective permeability was almost insensitive to the process with relative error lower than 1%, as shown in figure 3.9b [15]. The impact upon CPU time user for mesh construction was negligible for the smallest images, i.e. 500 px × 500 px, whereas the benefit can rise up to 70% with the larger image, i.e. 2000 px × 2000 px px, as shown in figure 3.9c.

---

[13] "*a flat morphological structuring element is a binary valued neighborhood, either 2D or multidimensional, in which the true pixels are included in the morphological computation, and the false pixels are not.*" MATLAB

[14] For this purpose, we considered a much larger cohort of images than shown here demonstrating the same phenomenon.

[15] note that, as the strel size increase, permeability decrease for this method.

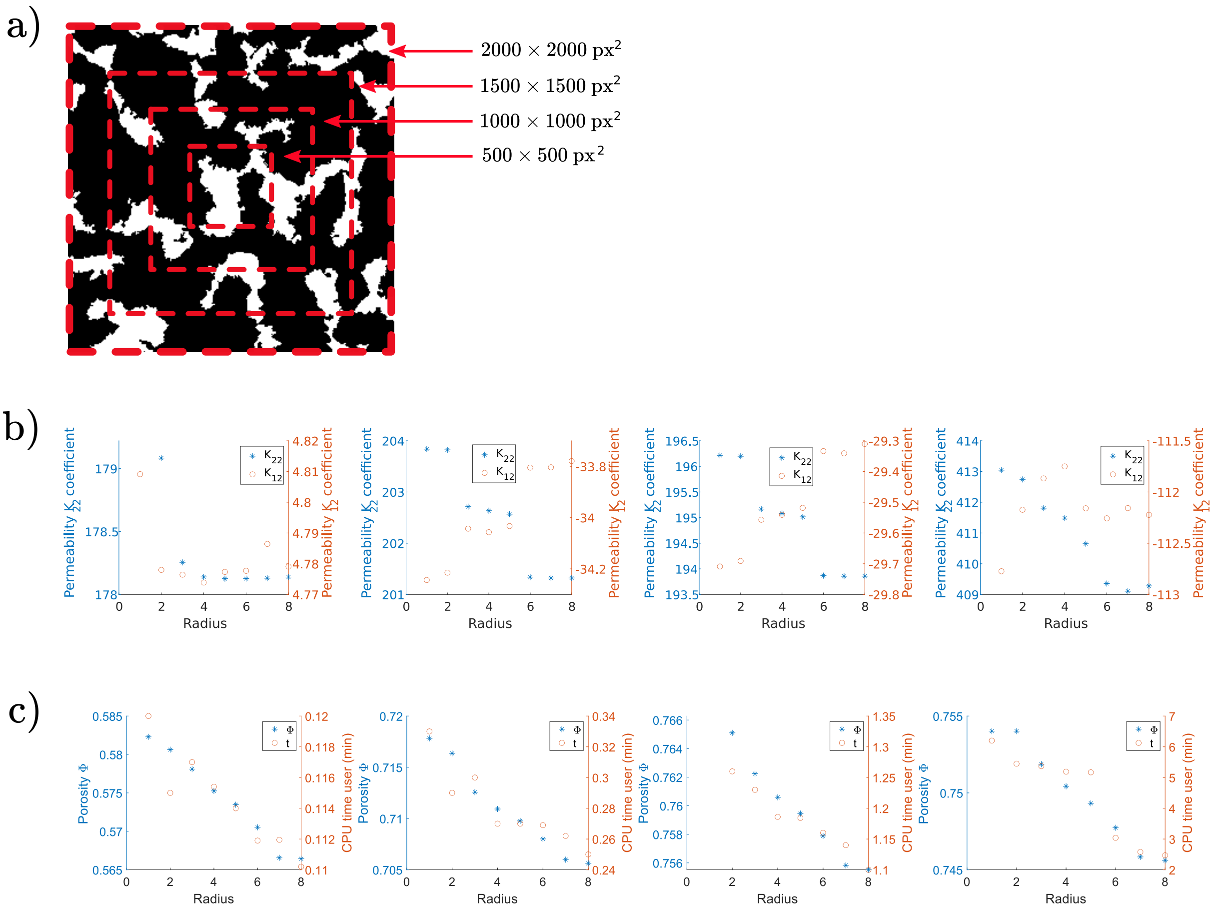

Figure 3.9: Effect of smoothing by dilatation/erosion with different radii by increasing window (dimension ranging from 500 px × 500 px to 2000 px × 2000 px. a)Geometry smoothing effect on diagonal (blue) and extra-diagonal (orange) equivalent permeability tensor components (left to right: 500 px × 500 px, 1000 px × 1000 px, 1500 px × 1500 px, 2000 px × 2000 px). b) Geometry smoothing effect on porosity (blue) and CPU time mesh construction (left to right: 500 px × 500 px, 1000 px × 1000 px, 1500 px × 1500 px, 2000 px × 2000 px). Matlab® built-in function, i.e. ”imdilate” and ”imerode” are used.

Secondly, a median filter smoothing method is applied with a smoothing spectrum similar to the above dilation/erosion method. Results are shown in figure 3.10. Maximal relative error on porosity is lower than 1% and error on effective diagonal permeabilities are lower than 8%. At the same time the gain is about 1 min on CPU time user for mesh construction.

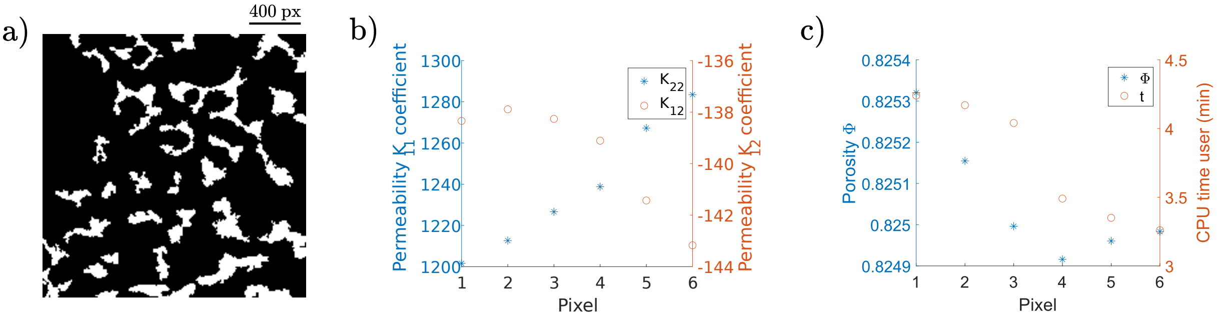

Figure 3.10: Smoothing by median filter with different numbers of pixels on a 2000 px × 2000 px image: mechanical and topological effect. a) Binary image. b) Equivalent permeability coefficients evolution as a function of the median filter radius. b) Porosity and CPU user time evolution in function of the median filter radius. Software ImageJ® is used.

Particular attention must be given to this stage of the study since any uncontrolled smoothing method can quickly lead to aberrant results. For example, with Gauss filter using a standard deviation σ, the topological properties are rapidly degraded, for very low standard deviation, and it may cause a continuous non-monotonous change in the geometric properties leading to an alteration of the mechanical ones (percolation loss).

In conclusion, we find that the two smoothing methods give similar results on porosity and effective permeability variations. First, it shows that the local topology of the pore is not strongly modified and this concerns the porosity determination, but it can also be noticed that the no-slip condition at the internal boundary $\partial_{int}\Omega$, limit the role of interface local roughness. This can explain the limited variation of effective permeabilities. Therefore, the uncertainties related to the exact identification of the fluid/solid interface, from the biological data, have very little effect on the calculation of equivalent properties when a non-slip condition is imposed.
A larger cohort of clinical images allowed these conclusions to be validated. It can be added that only results with symmetric boundary conditions at L_1 scale are presented and we checked that the other BCs previously detailed in section 3.2.1 exhibited same tendencies.

Since no real control over this smoothing is possible, we decide to smooth clinical images by using the dilatation/erosion process with a strel disc of small radius, i.e. 4px, in the following studies. The smoothing effect on the equivalent properties will then be minimal. This smoothing is also essential for the smooth running of the meshing process on GMSH [16].

3.2.3.3 Extend-local meshes specificities

Previously in paragraph 2.4.1, we showed the relevance of the extend-local process in the overall upscaling method, especially for clinical images showing no REV. In paragraph 3.2.3.1, we discussed the mesh construction with an homogeneous mesh characteristic size along each geometrical entity. Here, we are studying the potential benefit of a semi-variable construction (S-V), for the extend-local method, based upon a constant and dense meshing for the local L_1-subcell (targeted for upscaling) while the buffering zone is meshed with a density which depends on the distance to a fluid/solid boundary. The mesh shown in figure 3.11a concerns a sample size of $1600\,\text{px} \times 1600\,\text{px}$ with a local cell size of $600\,\text{px} \times 600\,\text{px}$. Again, the variables of interest for convergence purpose are the porosity and equivalent permeability tensor properties.

To check the dependence of extend-local method to this choice of mesh, in figure 3.11b, we plot the variations of the largest eigenvalue of the equivalent permeability at the L_2-scale (spectral radius) as a function of the size of the neighbouring region δ for the two types of mesh, i.e. constant (blue cross) and semi variable (blue circle). We do the same for the porosity of the complete geometry: the initial domain and with its buffer zone (the orange stars and circles correspond respectively to the constant and semi-variable porosity).
It can be seen that porosity and equivalent permeability are weakly influenced by the type of mesh on which they are calculated (i.e constant or semi-variable) because the resulting entities are perfectly merged. Then, a calculation on a semi-variable mesh can be considered instead of a calculation on a homogeneous mesh, without any bias.

The main benefits of the semi-variable mesh construction are that it leads to faster calculations while accuracy of predicted results is preserved regardless of the δ buffer size. Indeed, by plotting the construction times of two meshes (in red and blue for the constant M-CST and the semi-variable M-SV) and of the FEniCS simulations (in green and purple for the constant S-CST and the semi-variable S-SV) as a function of the size of the neighbouring region (fig. 3.11c), we notice a difference in total computation time coming mainly from the equations solving. As the geometry is rather small, the mesh construction times are similar for both cases. This is not the case for larger images since the semi-variable method is found to reduce the construction time. This is of particular interest to explore complex and very large sized binarized histological images.

---

[16] in relation to the definition of GMSH lineloop which may not be closed for raw images.

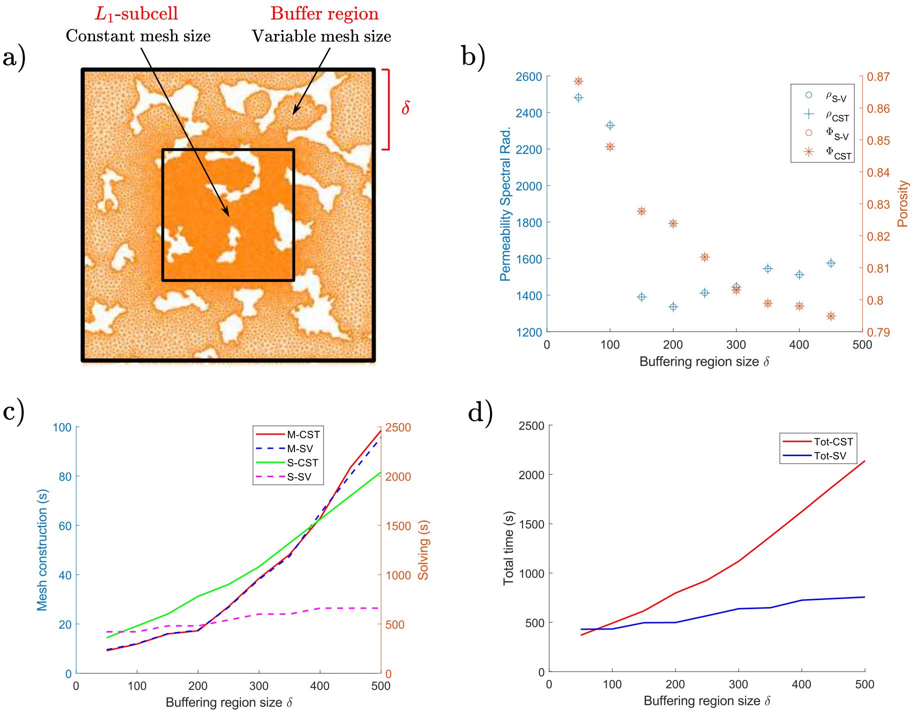

Figure 3.11: Comparison of the two meshing types, constant CST and semi-variable SV, in the application of the extend-local method. a) The geometry is meshed in a semi-variable way as a constant size is imposed on the 600 px × 600 px L_1-cell while the neighboring region mesh size depend on the distance to a boundary. b) Resulting equivalent permeability tensor highest eigenvalue (spectral radius) for the two types of meshes together with the overall porosity behaviour, in function of the buffer region size δ. c) Mesh construction and solving time in function of the buffer region size δ. d) Total time (mesh and solver) for the two type of meshes in function of the buffer region zone δ. Times are given in CPU time for a PC with 3 processors and 30GB of memory.

Note that the constant mesh construction can lead to a change of porosity of the target L_1-cell, i.e where the upscaling is done, between the purely local geometry and the one considering a 20px buffer zone, if the mesh size is not sufficiently dense. Indeed, when considering a constant mesh size and the evolution of the target L_1-cell porosity alone Φ_{loc} (orange dashed line in fig. 3.12), we notice a jump in value between $\delta = 0$px and $\delta = 20$px (i.e. the first step of the extend-local method) and this for two L_1 values (fig. 3.12b and c). This jump is due to the variability of the mesh at the border between integration domain and buffering zone when the last is considered. Traditionally, to solve this problem, much smaller constant mesh sizes would have to be considered on the whole domain (buffer region included), resulting in heavier calculations. In opposition, for the semi-variable construction, only a denser mesh within the L_1-cell and its direct neighboring is sufficient. This smooths the porosity jump (10^{-3} difference order) between the two values of $\delta = 0, 20$px (fig. 3.12d), while keeping a coarser mesh size in the buffer region [17].

This geometrical consideration is absolutely necessary as it can have repercussions on the mechanical equivalent response of the physical system. Indeed, a similar jump is observed on the resulting permeability tensor highest eigenvalues, according to different BCs (solid, dashed or dotted blue lines on fig. 3.12b and c). This raises the question of whether the porosity jump has a direct effect on the equivalent permeability one. Figure 3.12d shows that this is not the case. Indeed, a semi-variable mesh construction together with denser constant mesh within the L_1-cell is built, smoothing the porosity variation. The initial jump of the equivalent spectral radii remains and one only highlights the expression of the intrinsic effects of the BCs choice alone (without artefacts from the geometric discretization).

---

[17] It would also have been possible to consider a constant mesh only on the L_1-cell edges and variable according to the distance to the boundary everywhere else. It's not the method chosen here.

In the incoming work, a semi-variable mesh will be considered at the L_1-scale for the extend-local method.

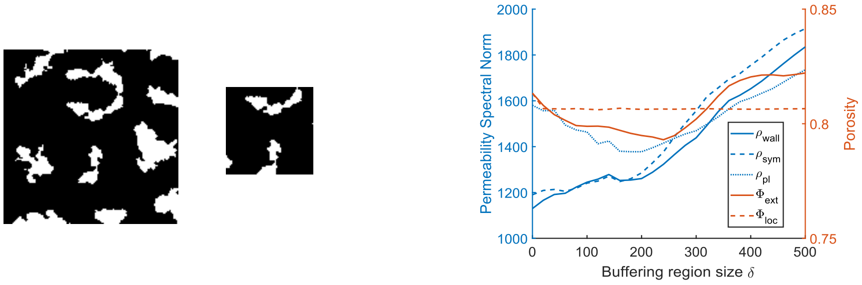

a) Two local L1-cells (1000x1000px and 500x500px^2) b) Extend local study for the 1000x1000px^2 local cell

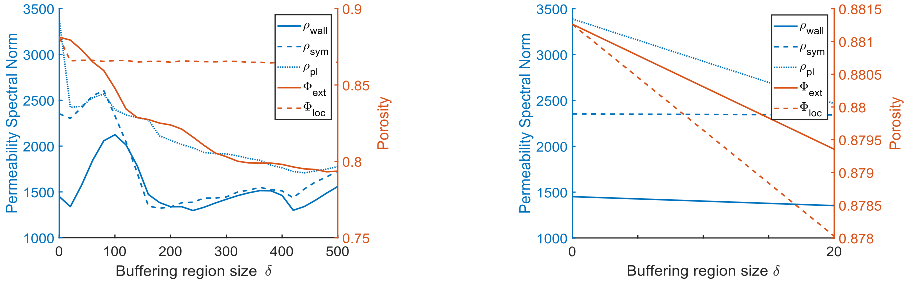

c) Extend local study for the 500x500px^2 local cell d) Mesh refinement effect (500x500px^2 local cell)

Figure 3.12: Application of the extend-local method with δ for two different L_1 lengths. a) Two L_1-cell size are considered with 500 px × 500 px and 1000 px × 1000 px. b) Computations of equivalent mechanical property (highest eigenvalue) and geometrical (porosity) through the extend-local method for a constant meshing of the 1000 px × 1000 px L_1-cell and δ values ranging from 0px to 500px. Φ_{loc} represents the calculation of the porosity on the integration domain when a buffer region is added, Φ_{ext} is the porosity of the integration domain plus the buffer region. The amplitude ρ_{wall}, ρ_{sym} and ρ_{pl} corresponds to the equivalent permeability spectral radii at the L_2 scale. c) Similar computations for the500 px × 500 px L_1-cell. d) Effect of a mesh refinement on the L_1-cell on the same computations for a semi-variable meshing of the two first steps of the extend-local method.

3.2.4 Influence of the sequential and extend-local methods parameters

In this section, we are applying the upscaling methods previously described. We start with the extend-local scheme and its dependence on its intrinsic parameters such as the L_1 length, the size δ of the buffer zone or the choice of the boundary conditions. Then we are investigating the impact of splitting and boundary conditions on the sequential grid-block method. Applications concern periodic model porous media and tumor tissue.

3.2.4.1 Extend-local method study

In the following, the extend-local method will be studied. The incompressible steady Stokes problem is described by equation (3.1) at the L_1-scale. To obtain the permeability tensors of the Darcy equation (3.4) at the L_2-scale, arbitrary boundary conditions are associated to equation (3.1). Four boundary conditions are considered: wall BC expressed by equation (3.11), symmetry BC expressed by equation (3.12), linear pressure BC expressed by equation (3.13) and periodicity (3.16). The aim is to evaluate the impact of these choices upon the computation outcomes, i.e. effective permeability tensors. The roles of parameter δ defining the buffer region size and L_1 corresponding to the local scale, on the equivalent permeability at the L_2-scale, are investigated.

We first consider a 40 px × 40 px periodic porous medium called PM1 as shown in figure 3.13a. It is a periodic array of disks of diameter 10px, and we consider a unique buffer region size, corresponding to a period of the geometry as shown in fig. 3.13a. It exhibits a separation of scales with an overall porosity of 0.803. The characteristic length of 10 px corresponds to the space between each circular obstacle. In this isotropic case, the effective permeability tensor is reduced to a scalar. Four sets of boundary conditions are considered and permeabilities noted $\overline{K}$ at the L_1 scale and $\overline{K}^{\star}$ at the L_2-scale are non-dimensionalized by the periodic characteristic surface [102]. Considering a periodic geometry, the solution involving periodic boundary conditions is the deterministic periodic homogenization solution and gives the exact solution.

Resulting permeabilities $\overline{K}$, at the L_2, are shown in figure 3.13b for the local and extend-local upscaling methods. The local L_1-L_2 upscaling (filled circle curve fig. 3.13b) results in a good approximation of the reference solution **P** by using symmetrical conditions **S** and linear conditions **PL** whereas the wall condition **W** gives an underestimation. These results are in agreement with [102].
The L_1-L_2 extend-local process (empty circles curve fig. 3.13b) homogenizes the permeability for each boundary condition compared to the reference L_1-L_2 periodic solution. Compared to the reference local periodic solution, the extend-local method gives a lower permeability of about 4% [18].
Therefore, for this very special case, an improved accuracy of the extend-local L_1-L_2 upscaling method compared to the local one is confirmed for the three non-periodic boundary conditions.

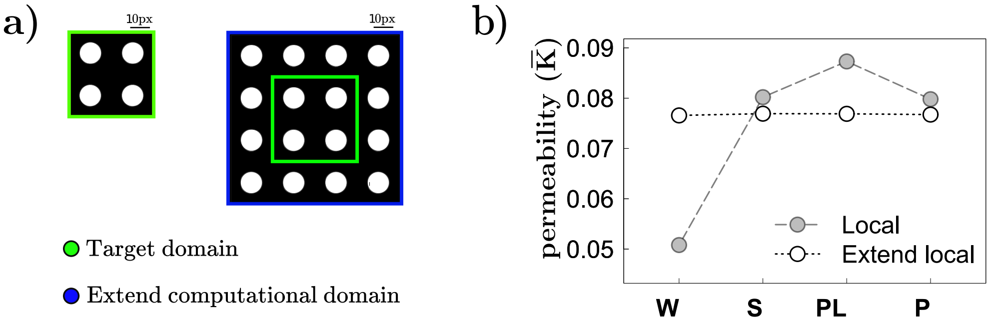

Figure 3.13: a) Extend-local method applied to PM1, a periodic array of discs, with a period size buffer region. b) Resulting scalar equivalent permeabilites comparison, for this geometry, obtained by the local and the extend-local method in function of the four boundary conditions (Wall (W), Symmetry (S), Linear (PL) and Periodic (P)).

The next step concerns the influence of buffering size δ on the accuracy of the extend-local method. As shown in figure 3.14, we consider a periodic geometry called PM2 and a binarized histological section of tumor.

---

[18] We remark that there is a decrease in the extend-local periodic permeability case compared to the local one; this bias can be attenuated if one consider a double periodicity in the mesh, i.e a mesh where periodic elements are imposed not only on the extend computational domain boundaries but also on the target block.

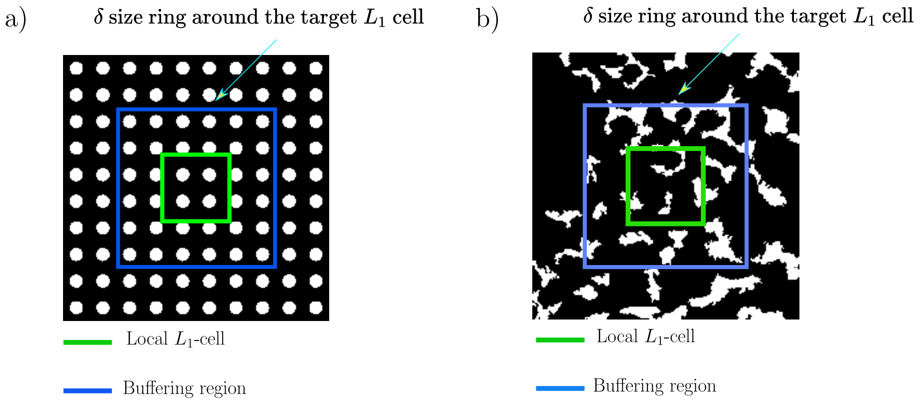

Figure 3.14: Application of the extend-local method on two geometries with different topological characteristics considering a local cell (green) and continuously increasing extend region a) 2000 px × 2000 px periodic geometry. b) 2500 px × 2500 px osteosarcoma binary image.

PM2 is a stack of periodic and isotropic 2D disc of total size 2000 px × 2000 px with discs of 100 px diameter and with a 100 px distance between two obstacles. Calculations are made for a local cell of length $L_1 = 400$px comprising four disc and for buffer zones ranging from 0 to 400 px with a 10 px step. Meshes are taken with constant mesh sizes. Note that a value different from L_1 would result in a long term phase shift of the curves accompanied by significantly different initial values (edge effect). Furthermore, the curves would remain almost identical. Results are shown in figure 3.15b. We plot the resulting scalar non-dimensional permeability in function of the δ-size of the buffering region, for the 4 boundary conditions (**W** is represented by circles, **S** by crosses, **PL** by squares and **P** by asterisk). The overall porosity variation curve is added in orange.

The extend-local at the L_1 scale allows us to homogenize (fig. 3.15b) the values of the permeability value according to the four BCs and this whatever the size of the L_1 local cell (generally when a half-period for the buffer zone is reached). First, note that for $\delta = 0$ px, the values correspond exactly to the above purely local case (fig. 3.13b). It can be noticed that for larger δ, the curves are repeated periodically (according to the period of the geometry) with decreasing amplitudes in the permeability and porosity fluctuations. Considering a sufficiently large buffer zone, a decrease in the amplitude of the permeability indicates a convergence towards the exact solution. Indeed, edge effects, at their strongest when the edges of the geometries intersect the obstacles, decrease for large δ.
Thus, it is shown that the extend-local method allows in the case of the PM2 geometry, even for small δ, to choose indifferently among the four BCs in the calculation of the permeability at the scale L_2 when a REV hypothesis is considered.

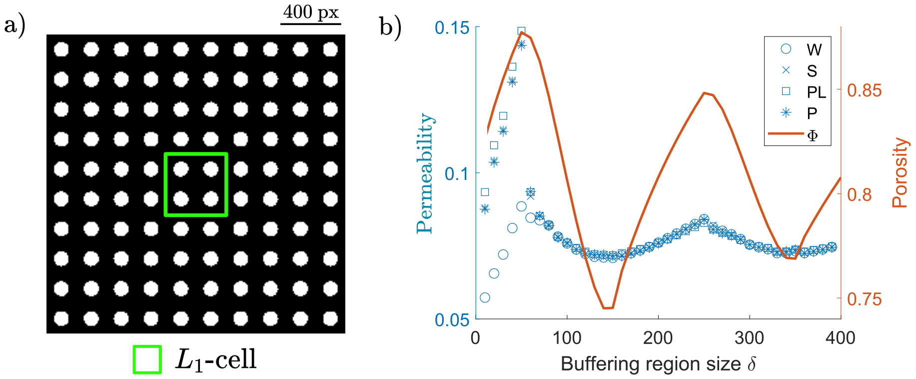

Figure 3.15: Application of the extend-local method to PM2, a periodic array of discs, and to a 400 px × 400 px local cell with the four BCs: wall, symmetry, linear and periodic. a) The periodic geometry. b) Permeability $\overline{K}$ and porosity values as functions of the extend region size δ.

The L_1-L_2 extend-local method is now applied to tumoral tissue (fig. 3.14b). We consider six osteosarcoma sub-samples of size $500 \times 500\,\mathrm{px}^2$, $600 \times 600\,\mathrm{px}^2$, $700 \times 700\,\mathrm{px}^2$, $800 \times 800\,\mathrm{px}^2$, $900 \times 900\,\mathrm{px}^2$ and $1000 \times 1000\,\mathrm{px}^2$. We choose the diagonal coefficient K_{11} and extra-diagonal coefficient K_{21} to analyse the results. We plot for each L_1-cell size, the behavior of the coefficients as a function of the size of the buffering region δ and this for three different BCs: the wall condition (3.11) (**W**) is plot in blue, the symmetric (3.12) (**S**) in red and open boundary condition (3.13) (**PL**) in orange. We plot on the same graph the variations in total porosity of the computational domain (purple dot graph) [19].

Figure 3.16 shows a decrease in the difference of diagonal equivalent permeability tensor for the three boundary conditions when $\delta \geq 100\,\mathrm{px}$. Note that coefficient resulting from **W** and **S** are perfectly merged and this for all considered L_1 lengths.
Thus, the uncertainties of equivalent permeability calculations, inherent to the choice of boundary conditions, at the L_1-scale, can be reduced for the diagonal terms by the extend-local process [89].

We would like to point out that no convergence is achieved in the values as a function of δ. It can be observed that these values remain very sensitive to the computational domain global porosity; the permeability graphs behavior, for each BCs, being sensitive to total porosity fluctuations. However, convergence is not the objective of this approach because the goal of the grid-block method is to take into account the heterogeneities in phase distribution in a reliable way.

Remark: The range of permeability value is consistent with the literature. As they are exposed in this thesis in px^2, a pixel size being $0.466\mu\mathrm{m}$, they effectively lies around $10^{-12}\mathrm{m}^2$.

---

[19] The resulting permeabilities can be non-dimensionalized by the L_1-scale value. In the same way, one can define the dimensionless magnitude of the tensor. This will essentially be used in the chapter 5.

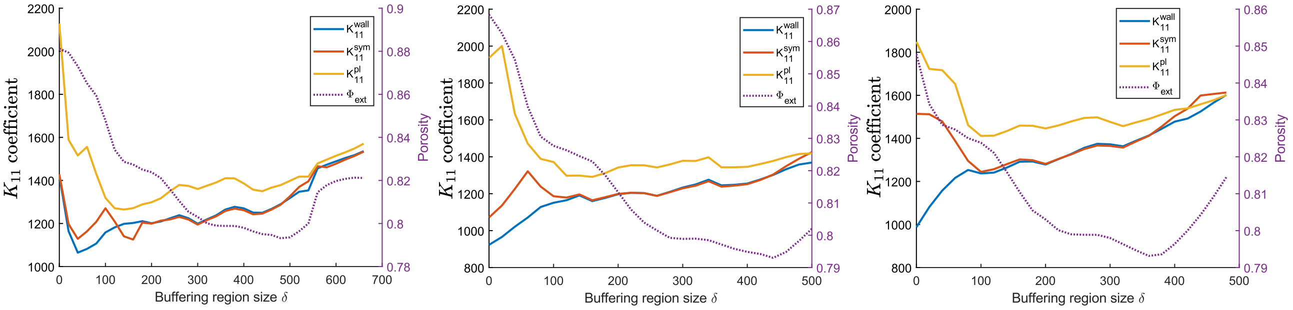

a) local cell L_1 500x500px b) local cell L_1 600x600px c) local cell L_1 700x700px

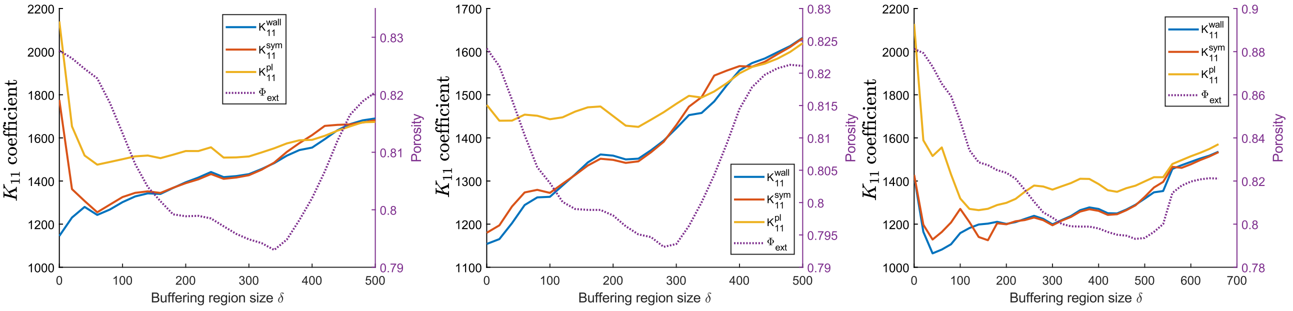

d) local cell L_1 800x800px e) local cell L_1 900x900px f) local cell L_1 1000x1000px

Figure 3.16: Behavior of the equivalent permeability diagonal coefficient K_{11} resulting from the extend-local method in function of δ. The study is conducted on multiple L_1-subcell size: 500 px, 600 px, 700 px, 800 px, 900 px and 1000 px.

When extra-diagonal terms are studied, as shown in figure 3.17, **W** and **S** results are similar, even for small δ, whereas **PL** results seems quite erratic in comparison. This come from the fact that the open boundary condition does allow transverse flow in opposition to the impervious boundary conditions (wall and symmetry). In some extreme cases, the linear boundary conditions can not "see" an obvious non percolation geometry (fig. 3.18), and in opposition to the wall and symmetric conditions, provides a non-zero permeability. This bias must be taken into account if we want to consider a non-percolating geometry as having a zero permeability.

As shown in appendix A, extra-diagonnal permeability coefficients play a significant role in the equivalent spectral radii and deserve a specific attention.

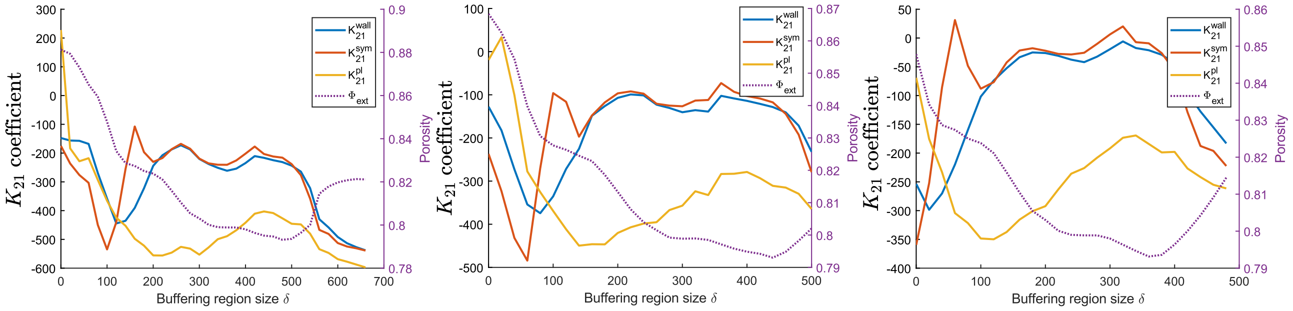

a) local cell L_1 500x500px b) local cell L_1 600x600px c) local cell L_1 700x700px

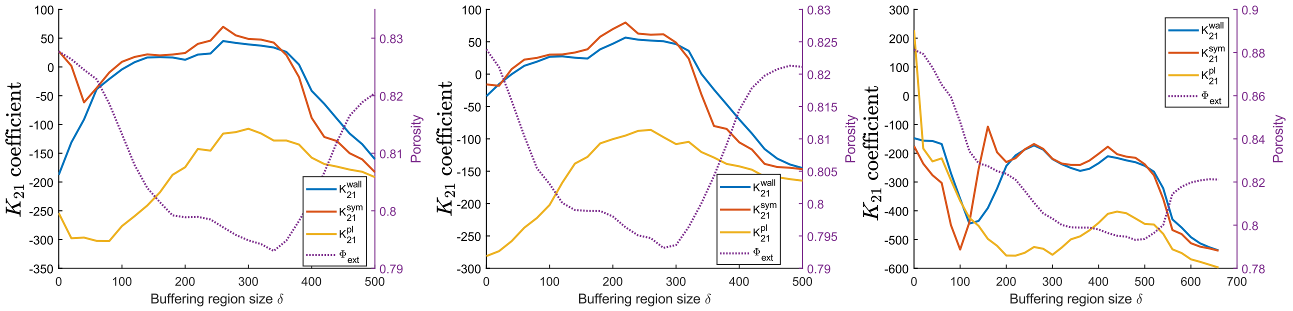

d) local cell L_1 800x800px e) local cell L_1 900x900px f local cell L_1 1000x1000px

Figure 3.17: Behavior of the equivalent permeability extra-diagonal coefficient K_{21} resulting from the extend-local method in function of δ. The study is conducted on multiple L_1-subcell size: 500 px, 600 px, 700 px, 800 px, 900 px and 1000 px.

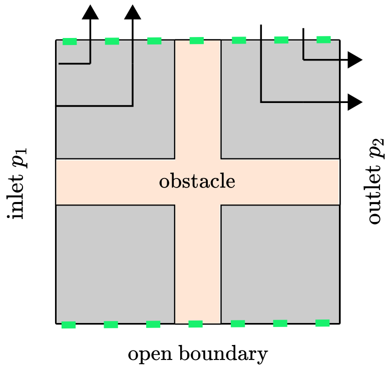

Figure 3.18: Effect of the open boundary condition, on a flow driven from left to right and on a non-percolating geometry, allowing transverse flows.

In conclusion, the extend-local methods allows to predict permeabilities at L_2-scale while limiting the role of BCs, especially for diagonal coefficients. In case of complex biological structure, it can also provide a consistent biological characterization of the permeability tensor at the L_2-scale by immersing local sub-domain into its realistic biological architecture. By doing so, equivalent permeability computation on a block is affected only by natural properties, preferred path and percolation for example, as in illustrated in figure 3.19.

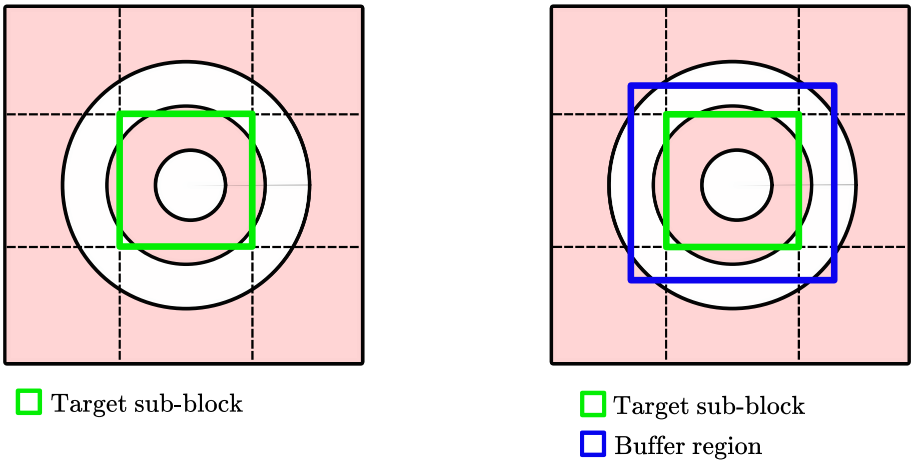

Figure 3.19: Schematic view of the loss of global percolation and preferred path. Using a local grid-block upscaling at the L_1-scale (left), the target sub-block is ”wrongly” given a positive permeability. Using an extend-local method, the target block is given ”rightly so” a null permeability.

3.2.4.2 Sequential upscaling method study

In this section, we discuss the accuracy of the sequential upscaling method applied to interstitial flow in osteosarcoma and isotropic periodic geometries. The incompressible Stokes equation (3.1) is considered at the L_1-scale and Darcy flow is considered on piecewise homogeneous media at L_2-scale and L_3-scale associated to governing equations (3.4) and (3.10), respectively. In the following, the sequential method is studied with a purely local method for the L_1-L_2 upscaling in order to separate induced effects from the extend-local approach.

This method is very useful when the geometry is complex and when the computation time and the memory cost of the one-step upscaling method are expected to be too large (fig. 3.20). We know that according to the BCs considered, the permeability tensors will be quite different either in their diagonal terms or simply in their extra-diagonal terms. But the permeability tensor is also not constant through the sequential process even with the same boundary condition. Indeed, three different tensors are obtained for three different splitting at the L_1-scale, even when considering the same boundary condition (fig. 3.20).

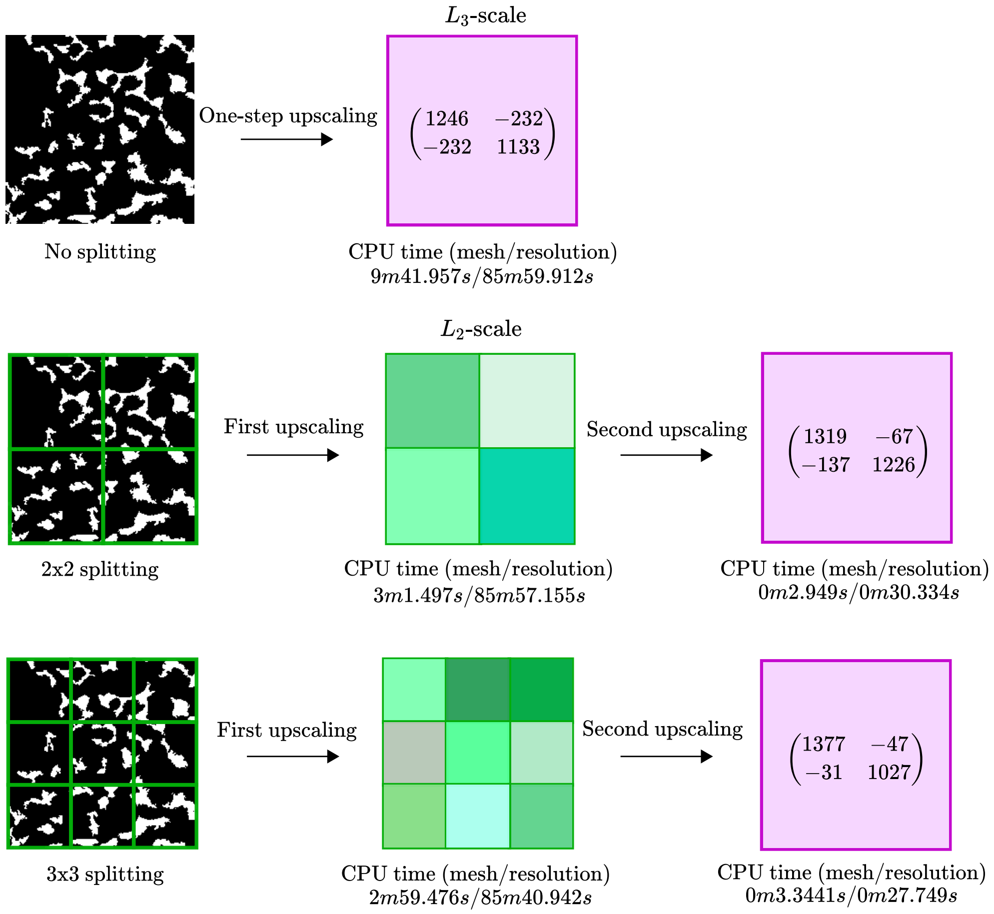

Figure 3.20: Equivalent permeability tensor at the L_3-scale, through the sequential method, where a symmetric and wall BCs are considered at L_1 and L_2 scales, for 3 different splittings (with their corresponding full time resolution).

Without loss of generality, we will consider only one cell on the L_3-paving, as illustrated on figure 3.20. Indeed, a study on a complete L_3-paving, i.e with multiple L_2-subcells, will only result in similar behavior L_2-cell by L_2-cell. The splittings considered at the L_1-scale are ranging from 1×1 to 5×5 [20]. Here, the density of the splitting is constrained by the size of the images but also by the heterogeneous character of the osteosarcoma. Indeed, a too dense L_1-splitting of the small images would lead to an irrelevant substitution of pore scale equations (Stokes type) by subsidiary equations (Darcy type). For instance, a domain fully in the solid phase or in the pore-space would lead to inconsistencies.

We start with a periodic array of disks shown in figure 3.21a similar to the structure PM1 previously used in paragraph 3.2.4.1. The reference solution of this problem is well-controlled and given by the 1-step periodic homogenization. The splitting at the L_1-scale for the first step of the sequential upscaling scheme consists in four identical 4×4 sub-domains and as previously, the porosity is 0.803 (fig. 3.21b). The four possible sets of boundary conditions are considered and the resulting scalar permeabilities at the L_3-scale are noted $\overline{K}^{\star}$. We plot the resulting permeability curves at the L_3-scale for the one-step (black dots) and 2-step (grey dots) methods (fig. 3.21c). It is also interesting to see the permeabilities resulting from a 2-step method considering permeabilities at the L_2-scale computed with extend-local method (empty dots).

Finally, it appears that results at the L_3-scale are similar to those obtained at the L_2-scale in figure 3.13b. Thus, no loss of information is noted in the 2-steps upscaling process regardless of the technique used on the intermediate upcaling, for a periodic and isotropic geometry. In this case, a 2-step method coupled with the extend-local upscaling give better results than with a

---

[20] where 1×1 correspond to the one-step method.

1-step or a local 2-steps scheme as all resulting permeability values, at the L_3-scale, are close to the one obtained by the direct homogenization method.

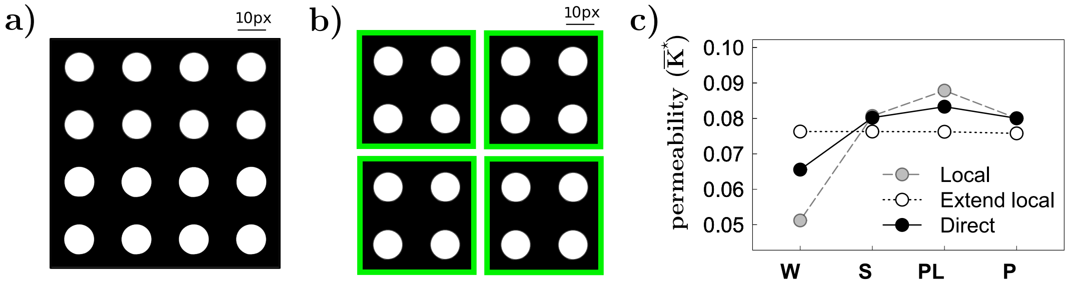

Figure 3.21: Application of the 2-step grid-block method to PM1, a periodic disc array according to the four BCs: wall, symmetry, linear and periodic a) The periodic geometry b) L_1 splitting equal to 2×2. c) Resulting L_3-scale equivalent permeabilities values obtained by the 1-step and the 2-steps methods (through a local or extend-local intermediary L_1-L_2 upscaling) in function of the four same boundary conditions.

The sequential upscaling method applied to the tumoral tissue is now considered. We consider a binarized image of 5000 px × 5000 px as shown in figure 3.22a [21]. No symmetrization of the tensors at the L_2-scale is performed to preserve as much as possible the BCs intrinsic effects. However, a symmetrization of the permeability tensor may be necessary at the L_3-scale for fast post-processing purpose and the calculation of eigenvectors and eigenvalues (real value versus complex results otherwise).

Remark: (Practical consideration) The L_1-L_2 upscaling requires solving a Stokes flow for an increasingly dense splitting. Thus, it is very likely that a permeability calculation for a pure fluid block, i.e. without any solid matrix, must be performed. To constrain the problem, having a unique velocity determination [119], we decide to add a little obstacle (with a $\frac{L_1}{100}$ length) in the upper right corner of the pure fluid geometry in order to fix the velocity value somewhere in the domain (no-slip boundary conditions). This practical consideration smooth out the numerical workflow as this artificial change in porosity has little to no effect on the resulting equivalent tensor [22].

Coefficients of the permeability matrix and spectral radii are plotted in figure 3.22b and figure 3.22c for the four BCs and four L_1-splittings ranging from 2×2 (sublocks being of dimensions 2500 px × 2500 px) to 5×5 (1000 px × 1000 px). The values arising from the **W**, **S**, **PL** and **P** conditions are respectively given in blue, red, yellow and green [23].

While dominant flow is constant for all four BCs, **S** and **P** give almost constant diagonal coefficients regardless of the splitting size. **PL** gives an overestimation of almost a factor 2 and **W** underestimates them. This effect is even stronger with a sequential method since two successive upscalings are performed. As a result, the more the splitting density increases, the more this phenomenon of over- or underestimation is significant. The sequential method orders the diagonal permeabilities according to inequations (3.21) [24]. Note that diagonal values of **P** are closed to **S** and strictly comprises between **W** and **PL**. We insist here on the fact that **P** solutions are altered by the spatial symmetrization of the domain as described in figure 3.5a. Therefore, **P** solutions are not general since another type of symmetrization would probably lead to different

---

[21] Four 5000 px × 5000 px osteosarcoma geometries were used in this section, coming from a segmentation/binarization of an H&E section. The four images have shown similar results through the sequential method, that's why we choose to present a part of the results only on one image.

[22] Another method would be to consider an extend-local method and place the notch in one of the corners of the buffer zone as far away from the upscaling zone as possible.

[23] in this paragraph, we choose to simply refer to the L_3-scale equivalent tensor by the terminlogy K instead of $\tilde{K}$

[24] Note that the relation hold when considering the 1-step method in addition to the different splits. For convenience and consistency, we have considered here only the tensors resulting from the two-step method.

results.

$$K_W^{diag} \leq K_S^{diag}, K_P^{diag} \leq K_{PL}^{diag} \tag{3.21}$$

Inequality (3.21) is all the more pronounced through splitting. A general order relation on equivalent permeability diagonal coefficients, in respect to the splitting, could have been expected but this is not the case here (or else very qualitatively).

From a qualitative point of view, relation (3.21), obtained at the L_3-scale, is consistent with the literature for the first upscaling from Stokes to Darcy [102] and second upscaling [110]. Additionally, it can be mathematically proved for specific boundary conditions similar to equations (3.11) and (3.13) for specific random porous media [126].

Remark: Note that negative diagonal term can be obtained through this method on the second upscaling when considering very particular geometrical paradigms [127] (like checkerboard geometries made of very large and null values). To overcome this problem on osteosarcoma, one can either (1) increase the delta size of the extend-local method, if this method is considered (2) iterate the process on the relevant sub-domain according to different splitting (starting if possible with a one-step method) until a positive sign is obtained.

As in the diagonal terms case, the highest eigenvalue remains quite sensitive to boundary conditions which have the same effect of over- or underestimation (fig. 3.22c).

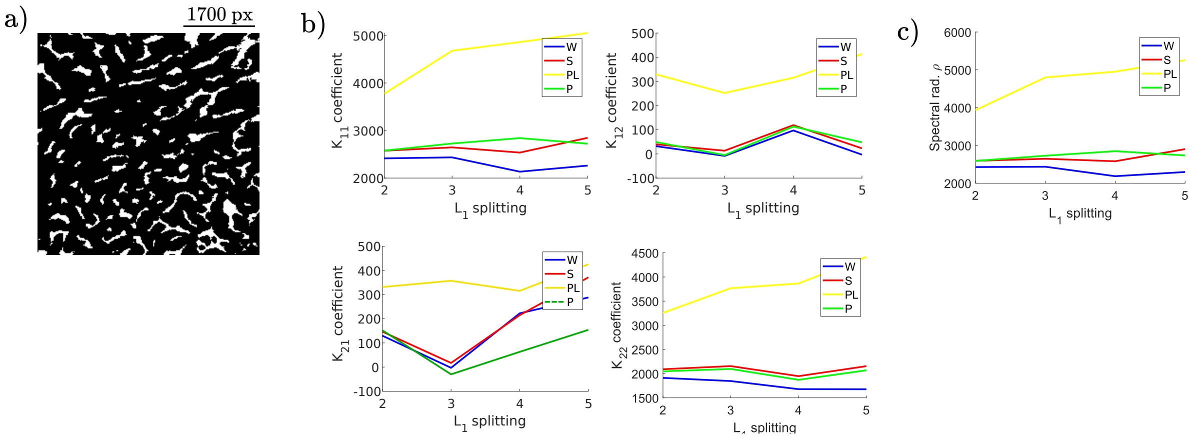

Figure 3.22: The sequential process is applied to the second osteosarcoma image with four different BCs through denser L_1-splitting. a) Binary image of osteosarcoma. b) Equivalent permeability coefficient response, at the L_3-scale, to the sequential process c) Spectral radii (highest eigenvalue) behavior, at the L_3-scale, to the sequential process.

Extra-diagonal permeabilities coefficients evolve with large amplitudes according to splitting size and the BC nature, as shown in figure 3.22b [25]. Impervious boundary solutions, i.e wall and symmetry, are close and strongly varying according to the splitting. In opposition, extra-diagonal terms resulting from the **PL** condition are a little more constant according to the splitting and keep the same sign. Note that the sequential method with the open boundary condition symmetrizes in a remarkable way each of the resulting tensors L_3 (in most cases with $d = \frac{|K_{ij}-Kji|}{|K_{ij}+Kji|} \sim 10^{-3}$).

The principal directions or tensor eigenvectors are plotted in figure 3.23 in respect to boundary conditions and splitting. They represent the non-oriented flow directions. This local information remains important at higher scales when a L_3-paving is considered. Indeed, these entities allow us to keep a local characterization of the domain anistropy after the sequential upscaling process.

---

[25] Assuming subsequent results on the principal flow direction, a perfect constancy through the splitting is difficult to achieve for extra-diagonal terms since the diagonal values increase or decrease according to it but the principal directions must remain as unchanged as possible, which always makes extra-diagonal terms vary.

The principal directions at the exit of the sequential method show an overall similarity BCs by BCs and according to splitting. For the impervious boundary conditions (**W** and **S**), they practically merge. Some differences are observed with the directions resulting from the **PL** conditions especially in the orthogonality of the vectors, as the open boundary condition have orthogonal orientation (thanks to the condition propensity to symmetrize the tensors at the exit of sequential process). The orthogonality, in the impervious boundary condition case, is recovered when considering symmetrization of the tensors. In the case of the periodic boundary condition, the directions keep a very good consistency across the splittings and its discrepancy with the other three BCs most certainly come from the symmetrization of the geometry, which leads to a total loss of the anisotropy of the original domain.
Therefore, the principal directions of permeability are qualitatively well preserved through the different boundary conditions and splitting.

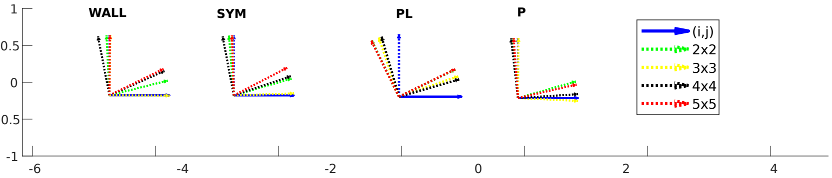

Figure 3.23: Principal direction, accounting for the non orientated flow direction, overall behavior through the sequential process (in respect to boundary condition and L_1-splittings). Orthonormal cartesian frame $(O, \vec{i}, \vec{j})$ is added in blue.

The intrinsic effects of the sequential method have been discussed but it is relevant to study the coupling with the extend-local method at the L_1-scale, on ostesoarcoma, as previously treated for the periodical geometry PM1. Results are given in appendix C. It is found that it drastically reduce the gap between the diagonal coefficient resulting from the open boundary condition and other BCs.

The sequential method is applied to larger osteosarcoma images to evaluate the performances in case of challenging clinical data. The 16 000 px × 16 000 px binarized image is shown in figure 3.24. The fluid flow obtained using the 2-steps method is compared to a pore scale flow (3.1) obtained by Direct Numerical Simulation (DNS). For the DNS, flow is driven from left (inflow) to right (outflow) with symmetric BCs on the top and bottom boundaries together with a no-slip condition on the fluid/solid interface. The 2-steps computation is performed with a 8×8 L_3-paving accounting for the scale couple $(L_1, L_2) = (1000\,\text{px}, 2000\,\text{px})$. Boundary conditions are symmetric (3.12) and impervious (3.14) for the L_1-L_2 and L_2-L_3 successive upscaling.

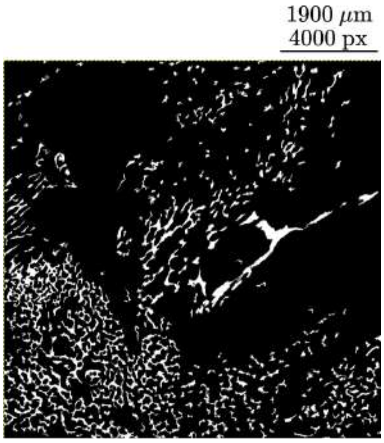

Figure 3.24: Osteosarcoma binary image of size 16 000 px × 16 000 px.

Pressure fields are shown in figure 3.25a for the DNS and on figure 3.25b for the upscaling method. The geometry anisotropy inducing specific features in the DNS pressure field are recovered by the upscaling. A quantitative comparison between the two calculations is done through the horizontal pressure profiles (see fig. 3.25c) in regions of high (top graphs) and low (bottom graphs) porosity. Overall, the direct (DNS) and macroscopic (2-step) pressure calculations are in good agreement, at the first order.

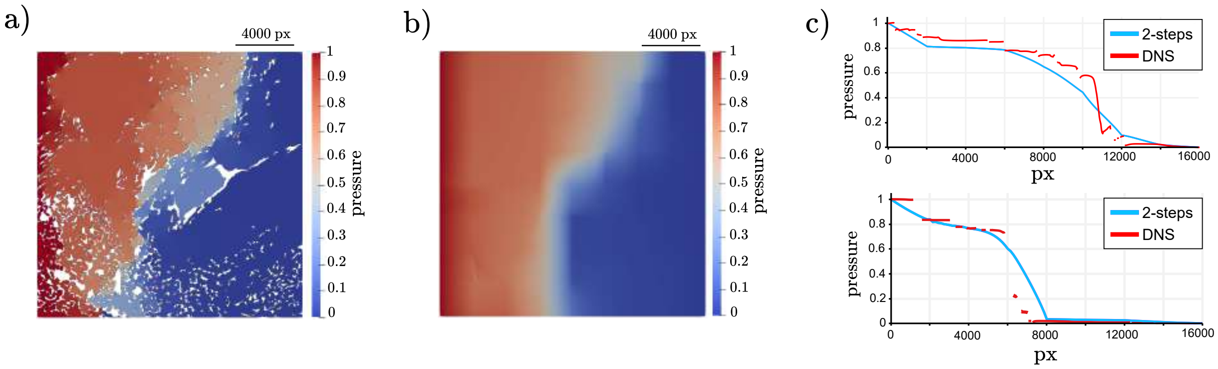

Figure 3.25: Results comparison between a DNS and 2-steps computations on a 16 000 px × 16 000 px geometry. a) Pressure field amplitude of a creeping flow going from left to right. b) Pressure field obtained after solving equation (3.10) obtained by the 2-steps method with $L_1 = 1000\,\mathrm{px}$, $L_2 = 2000\,\mathrm{px}$ and symmetry conditions. c) Pressure profiles comparison over horizontal lines ($y = 11\,000\,\mathrm{px}$ on top and $y = 4000\,\mathrm{px}$ at the bottom).

Finally, we propose to investigate the statistical distribution of equivalent permeabilities at the L_2-scale. If permeability limit distribution could be found, this approach would allow to avoid time consuming computation at local L_1-scale (Stokes equation) while using fast results at L_2-scale (Darcy equation) [128, 95]. Denser L_1-splittings ranging form 4×4 to 16×16 and one cell at the L_3-scale are used. **W**, **S** and **PL** boundary conditions are used and permeability statistic histograms are given in appendix D. As shown in figure 5 and 6 of the appendix, the BCs and successive splitting do not show significative influences on histograms.
Unfortunately, normal distribution are not clearly readable both for diagonal and non-diagonal permeabilities. This confirm the strongly heterogeneous properties of the biological tissue investigated. As it stands, the exploration of a statistical approach to flow in osteosarcoma is not conclusive due to the highly heterogeneous nature of the geometry.

In conclusion, the sequential method applied to the study of the flow perfectly fulfills the essential properties of an upscaling technique already determined for a 1-step method in previous works [129] such as the order relationship on diagonal coefficient $\boldsymbol{W} \leq \boldsymbol{S} \leq \boldsymbol{PL}$. This relation is verified in this new workflow, considering an incompressible Stokes equation at the small scale for the first time, and is all the more pronounced through splitting since a succession of permeability calculations are performed. Finally, the heterogeneity of the osteosarcoma at the L_1-scale is properly taken into account through the equivalent grid-block properties of the L_3-scale.

3.3 Mass transport

Diffusive mass transport in osteosarcoma can play a role in the tumor evolution and in chemotherapy process [130]. Our approach can also complement emerging research and clinical modalities such as FRAP and Diffusion MRI to explore tissue properties [131].
Figure 3.26 is presenting the assumptions of the proposed approach. The convective properties of tissue are not considered and diffusive transports concerns the fluid phase. As previously, the geometrical paradigm is a 1-porosity model. The equivalent diffusion tensor ($\mathrm{m}^2\mathrm{s}^{-1}$), translating the complete anisotropy of the medium, is targeted. The Fick's law in porous media is used while establishing the relationship between the diffusive flux and the chemical species concentration

gradient.

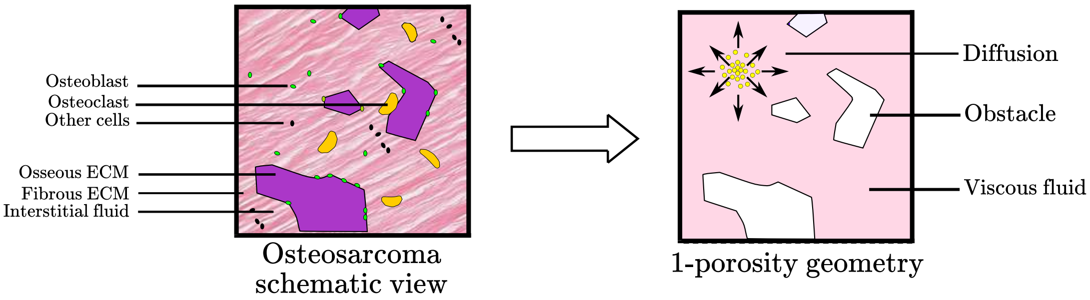

Figure 3.26: Biological and mechanical approximation of osteosarcoma in the diffusive transport case.

The upscaling methods workflow previously presented is applied to purely diffusive mass transport. The sequential method is first presented. Then, mesh convergence and influence of boundary conditions are studied. Finally, we report main results related to the extend-local and sequential methods.
Note that this section is seen as a direct extension of the previous one in the sense that we briefly explore the sequential method for tranport by diffusion.

3.3.1 Development of the grid-block and extend-local methods

A two-step grid-block method is developed to account for the diffusion in heterogeneous media and three ordered scales of observations, i.e. L_1, L_2 and L_3, are considered.

At the pore scale L_1, an elliptic equation is considered representing the diffusion equation of a generic passive tracer. The concentration is assumed to follow a Fick's law and the conservation equations only on Ω_f (where $\Omega = \Omega_f \cup \Omega_s$) and are expressed by equation (3.22) where $\mathbf{J}$ is the diffusive flux, c the specie concentration and $\mathbf{D}$ the diffusion tensor.

At this scale, boundary conditions on $\partial_{ext}\Omega$ can be either impervious or open boundary as expressed by equation (3.23) and(3.24), respectively (they are essentially the same than in the Darcy model). An impervious (wall) boundary condition is considered on $\partial_{int}\Omega$.

$$\begin{cases} \mathbf{J} = -\mathbf{D} \cdot \nabla c, \quad \text{on } \Omega_f \\ \nabla \cdot \mathbf{J} = 0, \quad \text{on } \Omega_f \\ \text{Boundary conditions on } \partial\Omega = \partial_{int}\Omega \cup \partial_{ext}\Omega \end{cases} \tag{3.22}$$

- **Impervious (wall)**

$$\begin{cases} c_{L_1} = 1, \text{ at the inlet} \\ c_{L_1} = 0, \text{ at the outlet} \\ \mathbf{J}_{L_1} \cdot \mathbf{n} = 0, \\ \text{ on edges parallel to the concentration difference direction} \\ \mathbf{J}_{L_1} \cdot \mathbf{n} = 0, \text{on } \partial_{int}\Omega \end{cases} \tag{3.23}$$

- **Open boundary**

$$\begin{cases} c_{L_1} = 1, \text{ at the inlet} \\ c_{L_1} = 0, \text{ at the outlet} \\ c_{L_1} = 1 - \dfrac{X_{L_1}}{L_1}, \\ \text{ on edges parallel to the concentration difference direction} \\ \mathbf{J}_{L_1} \cdot \mathbf{n} = 0, \text{on } \partial_{int}\Omega \end{cases} \tag{3.24}$$

Periodic boundary conditions can also be used through AE homogenization and corresponding to a diffusion like problem on a unit cell Y, as expressed by equation (3.25) where $c_i(y)$ is the local periodic variation obtained for an averaged gradient e_i.

$$\begin{cases} -\nabla.(\mathbf{D}(y)\cdot(\mathbf{e}_i+\nabla c_i))=0 & \text{in } Y \\ y\rightarrow c_i & Y\text{-periodic} \end{cases} \tag{3.25}$$

As we make the assumption of purely diffusive transport through osteosarcoma, at the L_2-scale, a diffusion equation is obtained through the Grid-Block uspcaling, admitting a piecewise constant equivalent diffusion tensor [103], encapsulating the local information, i.e. the underlying porosity. This tensor is full, i.e extra-diagonal terms are also determined as each sub-block computations account for the two space directions.

For the second upscaling, BCs are identical to L_1-scale by removing the wall condition on $\partial_{int}\Omega$ since the geometry is now piecewise smooth with no internal boundaries. An iteration on the upscaling process allows to consider the L_3-scale with another diffusion equation and a new piecewise constant diffusion tensor.

The post-processing to get the equivalent diffusion tensor at L_2 and L_3 scales is similar to those in flow case, i.e equations (3.3) and (3.9). At L_1-scale, it is given according to averaged diffusive fluxes and the macroscopic concentration gradient as expressed by equation (3.26), where $\mathbf{D}$ is the L_2-scale equivalent diffusion tensor for a given A sublock of the L_1-splitting, $\langle\mathbf{J}_k\rangle^l_A$ is the average flux from pore scale and δC is the macroscopic concentration gradient. Equation (3.27) expressed the relationship between flux averages and explicit derivations of concentration at L_2-scale, where $\tilde{\mathbf{D}}$ is an L_3-scale equivalent diffusion tensor of a given sub-block $\tilde{A}$, $\mathbf{J}_{L_2}$ and c_{L_2} the L_2-scale flux and concentration, respectively. Definitions of superscript are detailed in paragraph 3.2.1 and correspond respectively to the flow tests, i.e horizontal and vertical concentration difference.

$$\forall i\in [\![1,N_x\times N_y]\!],\quad (\mathbf{D})_{lk}=\Big(-\langle\mathbf{J}_k\rangle^l_A\frac{L_1}{(\delta C)^l}\Big)_{1\leq l,k\leq 2} \tag{3.26}$$

$$\forall i\in [\![1,M_x\times M_y]\!],\ \begin{pmatrix} \langle\partial_{s_1}c_{L_2}\rangle^1_{\tilde{A}} & \langle\partial_{s_2}c_{L_2}\rangle^1_{\tilde{A}} & 0 & 0 \\ 0 & 0 & \langle\partial_{s_1}c_{L_2}\rangle^1_{\tilde{A}} & \langle\partial_{s_2}c_{L_2}\rangle^1_{\tilde{A}} \\ \langle\partial_{s_1}c_{L_2}\rangle^2_{\tilde{A}} & \langle\partial_{s_2}c_{L_2}\rangle^2_{\tilde{A}} & 0 & 0 \\ 0 & 0 & \langle\partial_{s_1}c_{L_2}\rangle^2_{\tilde{A}} & \langle\partial_{s_2}c_{L_2}\rangle^2_{\tilde{A}} \end{pmatrix}\begin{pmatrix}\tilde{D}_{11}\\ \tilde{D}_{12}\\ \tilde{D}_{21}\\ \tilde{D}_{22}\end{pmatrix}=-\begin{pmatrix}\langle(\mathbf{J}_{L_2,s_1}\rangle^1_{\tilde{A}}\\ \langle(\mathbf{J}_{L_2,s_2}\rangle^1_{\tilde{A}}\\ \langle(\mathbf{J}_{L_2,s_1}\rangle^2_{\tilde{A}}\\ \langle(\mathbf{J}_{L_2,s_2}\rangle^2_{\tilde{A}}\end{pmatrix} \tag{3.27}$$

The mathematical consideration such as the weak formulation form and finite element spaces are those of the prior section, especially corresponding to the L_2 and L_3 scales of the flow study (BDM or RT space). More precisely, to overcome the mass loss problem, a dual mixed formulation of equation (3.22) like problem is implemented at each scale according to equation (3.28).

find $(\mathbf{J},C)\in(H^1)^2\times L^2(\Omega)$ such that for all $(\mathbf{V},Q)\in(H^1)^2\times L^2(\Omega)$

$$\begin{cases} \displaystyle\int_\Omega \mathbf{D}^{-1}\cdot\mathbf{J}\cdot\mathbf{V}\,dx-\int_\Omega\nabla\cdot\mathbf{V}C\,dx=-\int_\Omega C\mathbf{V}\cdot\mathbf{n}\,d\sigma \\ \displaystyle\int_\Omega\nabla\cdot\mathbf{J}Q\,dx=0 \end{cases} \tag{3.28}$$

3.3.2 Numerical convergence study

At the L_1-scale, equivalent and pore scale mesh convergence study, respectively accounting for equivalent properties and field variable responses, are performed on the $\mathbf{J}$ flux. Here, a constant scalar diffusion coefficient is considered at the pore scale. The same geometry than in section 3.2.3.1 is used. The evolution of flux averaging, the relative error in respect to the denser mesh and the overall flux magnitude along a path, are plotted in figures 3.27a and b.

At the macroscopic scale, a plateau is found with the first meshes and for denser meshes for the local field variable.

Finally, in the rest of the section, we choose to consider small GMSH elements size ~ 8 for two practical reasons (1) in order to mesh the osseous ECM border as well as possible for the study of the roughness boundaries role in the diffusion process (2) to allow an unbiased study of the extend-local method with a better smoothing of the porosity of the local cell L_1 through the variation of the δ of the neighboring region.
Note that at the L_2-scale, mesh convergence is already done in section 3.2.3.1.

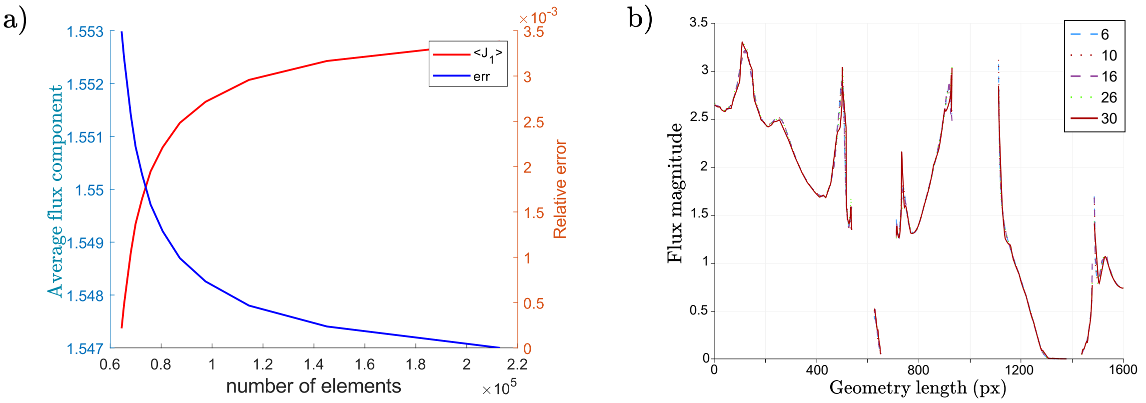

Figure 3.27: Mesh convergence for the diffusion problem on osteosarcoma a) Mesh effect on equivalent properties through the averaging of the diffusive flux first component. b) Mesh effect on pore scale variable through flux magnitude profiles over a line $y = 800\,\text{px}$.

In the next step, the influence of local roughness of solid phase, i.e. osseous ECM boundaries, on the L_2-scale equivalent diffusion tensor is studied. A dilatation-erosion method with a disk-shaped strel which radius varies between 1 px and 8 px is implemented. Results in figure 3.28 show the variation of coefficient D_{11} of the equivalent diffusion tensor for three 1500 px × 1500 px images and wall condition on the outer edges and a constant diffusion coefficient at the L_1-scale. The ECM boundary roughness show no significant influence on diffusion coefficient.

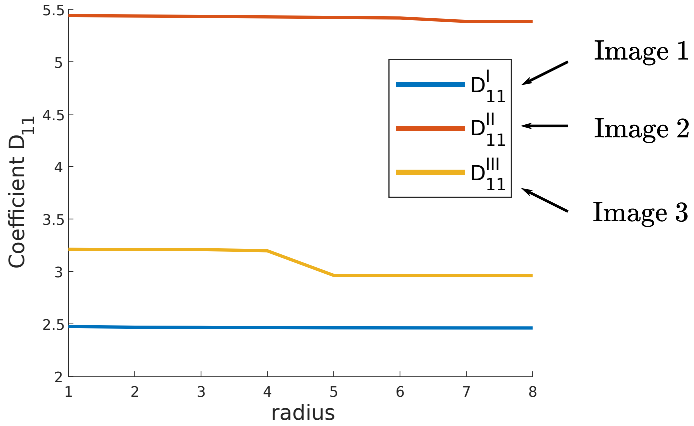

Figure 3.28: Effect of dilation/erosion smoothing on the equivalent tensor diagonal coefficient D_{11} for three 1500 px × 1500 px images.

The last step concerns the extend-local method meshes and the impact of semi-variable meshes. Constant meshes have GMSH element sizes fixed to 8 for each δ and semi-variable meshes have element sizes varying from 8 for the L_1-local sub-cell and to a size adapted to the distance between internal and external boundary outside the sub-cell. Buffering δ size is ranging from 100px to 500px. We plot, on figure 3.29, the evolution of the equivalent coefficient D_{11} resulting from the constant meshes (blue cross) and semi-variable meshes (blue cirle) together

with the porosity (in orange).
Variations of porosity and D_{11} are limited and semi-variable and constant meshes give similar results according to the buffer region size.

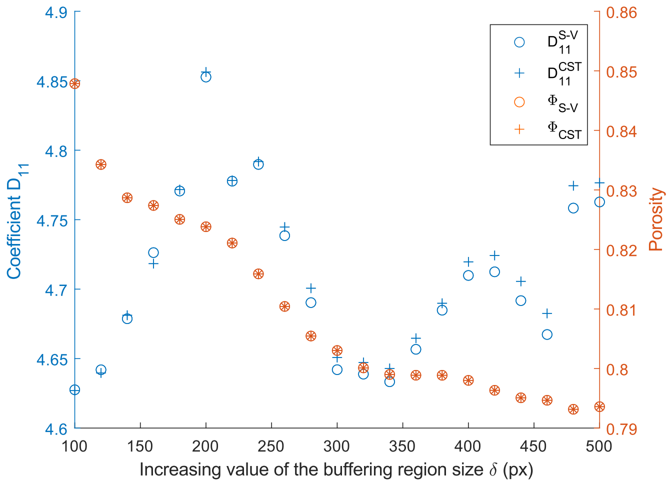

Figure 3.29: Comparison between semi-variable and constant meshes for the extend-local method applied to pure diffusion. Resulting equivalent diffusion tensor coefficients D_{11} are plotted (blue) in function of the buffer region size δ for the two types of meshed. Porosity is illustrated in orange.

In the 1-porosity model and throughout the rest of the section, i.e the study of the extend-local and sequential method in the mass transport case, the diffusion tensor considered in (3.22) at the L_1-scale is reduced to the case of a scalar to describe the diffusion of a tracer in the fluid part Ω_f only [26]. In this section, for purely methodological purposes, we consider an arbitrary diffusion coefficient given by $D = 5$ px^{2}s^{-1}.

3.3.3 Influence of the sequential and extend-local methods parameters

In this section, the extend-local and sequential methods are explored in the context of diffusive mass transport through their dependence on their intrinsic parameters.

3.3.3.1 Extend-local method study

We study the extend-local method at the L_1-scale. First, the robustness of the method is evaluated on a periodical geometry and then it is applied on biological tissue.

The periodic geometry PM2 chosen is the same stack of discs of size 2000 px × 2000 px (fig. 3.30a). We choose a single L_1-subcell of size 400 px × 400 px with δ sizes going from 0 to 400px with a step of 10px. The resulting scalar diffusion are plotted in figure 3.30b. The wall, open boundary and periodic conditions are respectively drawn by crosses, squares and asterisks. The porosity of the total domain (i.e. considering the buffer region) is plotted in orange.

The resulting equivalent diffusion coefficient are very close and merge completely since the beginning and their overall behavior is always dependent on the geometry period and porosity variation, with much lower oscillation magnitudes compared to the Stokes flow case. The fast convergence is explained by geometric properties and slow variation of diffusive properties since the diffusion coefficient was constant at the pore scale [27].
It appears that the benefit of extend-local method is limited for this type of physical system.

---

[26] the porous medium being somehow seen as a perforated porous medium, the diffusion in the solid phase Ω_s at this scale is not considered.

[27] Please note that for some δ values of this periodic geometry, a refinement of the mesh sizes is necessary for a good implementation of the periodicity on GMSH (otherwise leading to a false null value of the permeability)

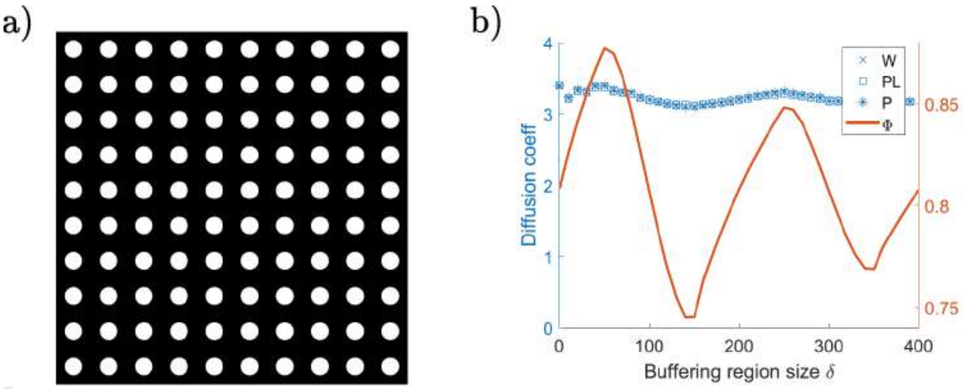

Figure 3.30: Extend-local process applied to periodic geometry with a 400 px × 400 px local L_1-subcell together with buffer region δ ranging from 0 px to 400 px with a 10 px step. a) Periodic geometry. b) Equivalent scalar diffusion coefficient for three boundary conditions (wall, open boundaries and periodic ones) in function of the δ size together with the overall porosity variation).

For the biological tissue, we consider one L_1-subcell size equal to 700 px × 700 px with δ ranging from 0 px to 500 px as shown in figure 3.31. The resulting equivalent diffusive properties coefficient from the wall and open boundary conditions are plotted respectively in red and black while the porosity is in purple (fig. 3.31b and c).

Tendencies previously found in the convective responses are also observed for the diffusive properties excepting the impact of boundary conditions which show lower effects here (in the magnitude difference). A small δ ($\approx$ 100 px) significantly reduce the bias due to BCs for diagonal coefficients, i.e. D_{11} and D_{22} and for spectral radii. The extra-diagonal terms are still sensitive to BCs. Larger δ might have an impact as shown by the D_{22} evolution.
Again, this method always requires a compromise between computation time and the nature of the physical system considered, if one targets L_1-sub-block immersed in its near environment (close to the purely local problem) or in its more global environment (better biological characterization).

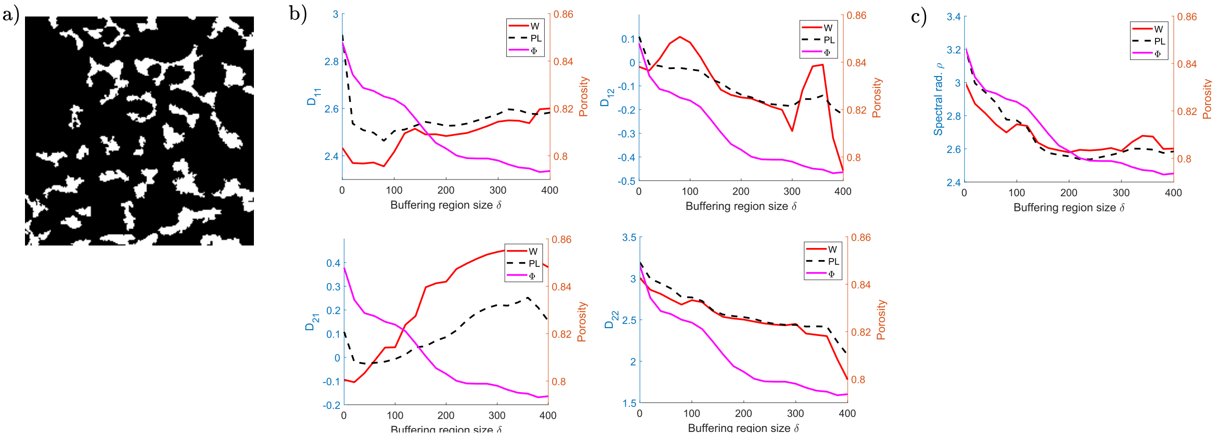

Figure 3.31: The extend-local process is applied to heterogeneous porous media with three different BCs (wall and open boundaries) through increasing buffer region size δ. a) Osteosarcoma binary image. b) Equivalent diffusion coefficient response, at the L_2-scale, to the extend-local process. c) Spectral radii (highest eigenvalue) behavior, at the L_2-scale, to the extend-local process.

3.3.3.2 Sequential method study

The 2-steps grid-block upscaling method is applied on binarized image shown in figure 3.32a. The studied properties of the resulting tensors are made with the different splitting and boundary conditions, i.e. wall (plotted in red), open boundary (plotted in black) and periodic condition (plotted in green). We consider the L_3-scale equivalent tensor coefficients (diagonal and extra-diagonal), the spectral radius and the principal directions.

One can observed an overestimation and underestimation respectively for the open boundaries and wall boundary conditions. Globally, the magnitudes of the differences between BCs according to the splitting are smaller than in the flow case. Note that the periodic BC behaves like the impervious boundary condition for this physical system as the tensor coefficients follow the exact same response according to the splitting. Finally, we have the same tendency for tensor symmetry emanating from the open boundary condition.
Finally, it can be possible to propose and ordering of equivalent diffusion diagonal coefficients as expressed by the inequality (3.29).

$$D_W, D_P \leq D_{PL} \tag{3.29}$$

Concerning the principal directions (fig. 3.33), the eigenvectors are relatively similar according to the splitting and the BCs. As the tensor are not symmetrical, except for the one resulting from the open boundary condition, the found directions are not orthogonal. Note that eigenvectors can be numerically calculated with opposite direction since eigenvectors are invariant by linear transformations.

Consequently, the sequential method applied to diffusive mass transport is very similar to the momentum transport. It is possible to characterize accurately the upscaling in the osteosarcoma case as the essential properties of resulting diffusion tensor are conserved through the method parameters.

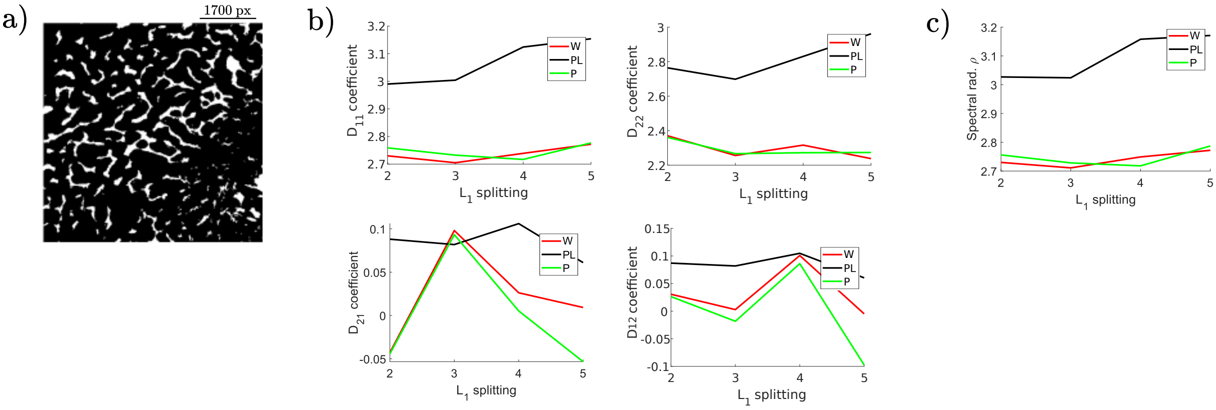

Figure 3.32: The sequential process is applied to 5000 px × 5000 px osteosarcoma image with four different BCs (wall, open boundaries and periodic ones) through different splitting. a) Osteosarcoma binary image. b) Equivalent diffusion coefficient response, at the L_3-scale, to the sequential process for the three BCS and in function of the L_1-splittings. c) Spectral radii behavior, at the L_3-scale, to the sequential process for the three BCS and in function of the L_1-splittings.

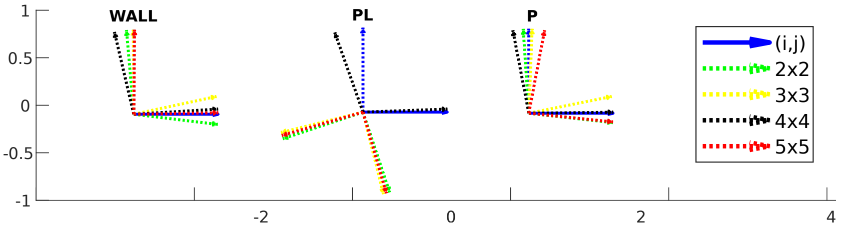

Figure 3.33: Principal directions, accounting for the non orientated flux direction, overall behavior through the sequential process for the 5000 px × 5000 px osteosarcoma image and the three BCs, in function of the L_1-splittings.

3.4 Conclusion and discussion on the transport study

In this chapter, we have developed a mechanically consistent upscaling methods for the description of flow and diffusive transport in osteosarcoma. The found optimised workflow includes grid-block methods with extend-local computations associated with sequential upscaling. Our targeted application is biological tissue from osteosarcoma which is particularly heterogeneous. The extend-local method allows to drastically reduce the bias induced by the choice of boundary conditions on grid block elements border. The accuracy of the proposed method provides is carried from the pore scale to the higher scale.
In a second step, we have shown that the 2-step grid-block upscaling method allows to represent faithfully the mechanical properties of the object as they are preserved for different splitting and boundary conditions. The upscaling method preserves the ordered relations of permeability tensor and diffusive tensor as follows:

$$K_W^{diag} \leq K_S^{diag}, K_P^{diag} \leq K_{PL}^{diag} \tag{3.30}$$

$$D_W^{diag}, D_P^{diag} \leq D_{PL}^{diag} \tag{3.31}$$

The reliability of results will be of interest to explore correlations between tissue mechanical properties and biological responses in osteosarcoma.

In this chapter, we have considered three non-characteristic spatial scales i.e. which could be chosen arbitrarily as long as they are ordered according to $L_1 < L_2 < L_3$. Note that this is allowed here because of the uniform nature of the equations (Stokes, Darcy or elliptic) where the very nature of equivalent parameters does not varies through the geometries regions. We emphasize that this is not always true. For other transport physics such as advection-diffusion(-reaction), which reflect a combination of two different phenomena, the scales must be constrained. Indeed, in order to obtain a relevant upscaling, the equivalent properties must then account for the two processes respective magnitude, i.e. a region may present a purely diffusive or convective character or a mixture of both. Therefore, the nature of the upper scale equation can be very different depending on the region of the geometry considered. Thus, a particular attention must be given, at each step of the method, to the splittings and the scales. To do this, studies of the physical behavior at each scale could be necessary. For example, on the L_1-scale, it seems relevant to separate the geometrical parts with strong convection and purely diffusive features. To automate this procedure, we can think of percolation phenomena for relevant splitting through flow-based procedures [132] or more abstract procedures such as elliptic-base grid generation [133]. The generation of these splittings, non-uniform by nature, will allow us to better capture the dominant phenomena on each part of the geometry for a relevant resolution of the equations. It would also be possible to consider models with N-equations [134].

The methodology developed in this chapter is directly applicable to the 3D case. An application of the upscaling methods to the exploration of osteosarcoma in three dimensions, although difficult in the current state due to the unavailability of biological material, would allow us to extend the validation of the numerical methods since the geometric (and thus physical) properties of the object will be different. We can for example think of the problem of percolation which will be very different from the 2D case and statistical percolation distribution limit may be reached. In the 3D case, the sequential approach is highly relevant since it will drastically reduce the numerical cost of such simulations while faithfully characterizing the transport phenomena.

In the following chapter, we develop and study the same uspcaling methods for linear elasticity and poroelasticity model in the framework of small deformations.

Chapter 4

Structural mechanics in osteosarcoma

Contents

The structural mechanics of bones and tumor has been vastly studied in the literature. For example, in the mathematical and mechanical study of tumors [88], they are generally considered as elastic objects (clusters of cells) in which a fluid flow can be considered, leading to a poroelastic modelling [135] of those objects. This model is based on the high dependence of tumor growth on mechanical stress, typically due to confinement by the surrounding tissues and their interactions with ECM (see chapter 1). In the bone case, this theory contributed to a better understanding of the mechanosensory system [37], as fluid shear stresses due to mechanical loading induce an osteocytes biological response, which drives the bone remodelling.
While the contribution of structural stresses on osteosarcoma development have not yet been explicitly studied in the literature, because those tumors are characterized by an osseous ECM production, it is assumed that those stresses play a significative role in osteosarcoma spatio-temporal dynamics. In addition, because this pathological remodelling may be related to an immune response, potentially through osteoclasts and pathological metabolic pathways associated with these cells, it is interesting to investigate their role in the response to treatments.

In this chapter, the aim is to add a new element in the upscaling approach to study the elasticity and poroelasticity of osteosarcoma. We decided to adopt a new approximation of the osteosarcoma physical system for the study of the elasticity and poroelasticity. In the first part of this chapter, the osseous ECM phase is seen as a homogeneous structure discarding lacuno-canalicular system (LCS). The osteosarcoma will then be considered as a porous medium with two solid phases, osseous and fibrous ECM, respectively phase 1 and 2 on figure 4.1.
In the poroelasticity case, these two structural phases are crossed at each point by a fluid phase (interstitial fluid and LCS flow) modeled by a Darcy flow. The choice (arbitrary) of the permeability, in each of the two phases, can be seen as the choice (still arbitrary) of the viscosity μ in our previous studies (the orders of magnitude of the literature are nevertheless respected).

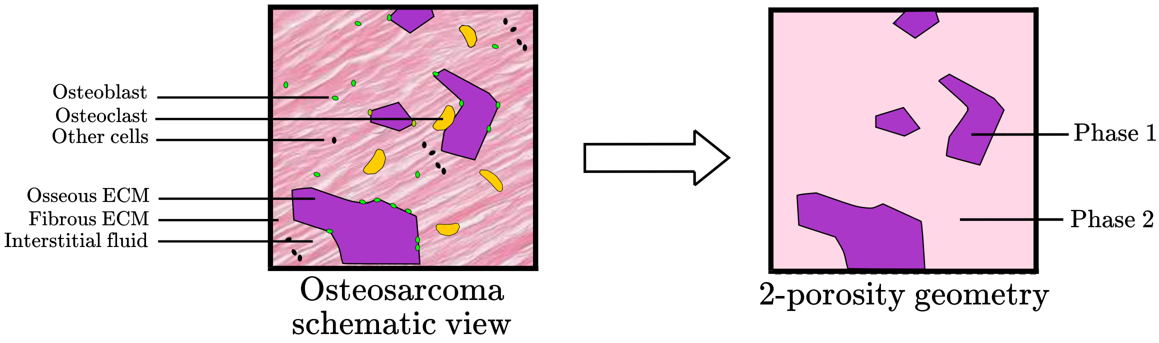

Figure 4.1: Structural mechanics in 2D osteosarcoma requires a change of geometrical paradigm: a 2-porosity model is considered in the rest of the chapter. The fibrous and osseous phases are explicitly taken into consideration. In the poroelasticity study, a Darcy flow will be considered in both phases, hence the terminology of 2-porosity model.

The grid-block method applied to linear elasticity at low deformation is well known for the effective response, i.e. when a REV can be determined, or for the equivalent response [136, 137, 63]. On another hand, the extend-local and sequential methods have, to our knowledge, never been explicitly developed for this physics.

In the poroelasticity framework, the literature is quite scarce since the majority of the work focuses on homogenization, with REV assumptions, of transient problems [138]; in this paper, authors consider an unknown "external" pressure and an undrained test. Therefore, the extend-local method has never been developed to reduce the bias related to the choice of BCs.
The choice of coherent BCs for this physics is a sensitive issue in the context of osteosarcoma. Indeed, the consideration of non-periodic BCs remains very marginal in the literature and only a few studies have been done [139], where the authors are interested in the equivalent character of the poroelastic response. As a result, very few works have focused on grid-block and sequential methods in the poroelastic case.

This chapter is splitted in two parts. In the first section, an application of the upscaling scheme to structural elasticity alone is considered. Then, we propose developments for the poroelasticity case.

4.1 Linear Elasticity

In this section, we study the linear elasticity of a heterogeneous material through the upscaling methods. In a first part we will describe the mathematical model associated with the 2-step grid-block method. The extend-local method at the L_1-scale will be described in a second part. Finally, the apparent elasticity tensor behavior through the sequential upscaling is studied numerically on different osteosarcoma binarizations.

4.1.1 Development of the grid-block method

We describe the biological structure at the tissue level L_1, as a bi-phasic solid porous medium. No fluid phase is considered in first approximation to focus on the elastic response of the ECM only. The two solid phases are identified with osseous ECM and fibrous ECM and are characterised by a difference in their elastic properties at the pore scale. A simplifying assumption is made through the isotropy of each solid component. Therefore, a 2-porosity model is chosen.
We consider a domain Ω, composed of the osseous and fibrous ECM solid phases, and its external boundaries as $\partial\Omega = \partial_{int}\Omega \cup \partial_{ext}\Omega$. A two-steps grid-block method is used to simulate the elastic response of the tissue obtained from 2D histological sections. As previously, three scales are considered (L_1, L_2 and L_3) corresponding to a pore, intermediary and macroscopic scales

and two successive upscaling are performed.

At the pore scale L_1, the linear elastic behavior is modelled considering small strains. The total heterogeneous solid domain Ω is considered in a static equilibrium leading to the the following equilibrium equation (4.1):

$$-\nabla \cdot (\boldsymbol{\sigma}(\tilde{\mathbf{u}}_{L_1})) = 0, \tag{4.1}$$

where the second order tensor $\boldsymbol{\sigma}$ is the stress tensor (Pa) and $\tilde{\mathbf{u}}_{L_1}$ the displacement at the L_1-scale (m). No body force, via a source term, is considered.

When a domain is subject to a loading, change occurs in its shape and its size. The second order symmetrical strain-rate tensor $\boldsymbol{\epsilon}(\tilde{\mathbf{u}}_{L_1}) = \nabla_{sym}\tilde{\mathbf{u}}_{L_1} = \frac{\nabla\tilde{\mathbf{u}}_{L_1}+(\nabla\tilde{\mathbf{u}}_{L_1})^t}{2}$ (dimensionless), describes the deformation of the structural volume element [1].

The two tensors $\boldsymbol{\sigma}$ and $\boldsymbol{\epsilon}$ depend linearly on each other and the elastic behavior can be expressed by Hooke's law, which can be written with a tensor notation as

$$\sigma_{ij}(\tilde{\mathbf{u}}_{L_1}) = C_{ijkl}\epsilon_{kl}(\tilde{\mathbf{u}}_{L_1}) \tag{4.2}$$

where the fourth order tensor $\mathbf{C}$ (Pa), namely the stiffness tensor, is constant in each phases with $\mathbf{C} = \mathbf{C}^{OECM}\chi_{OECM}+\mathbf{C}^{FECM}\chi_{FECM}$, χ_{OECM} and χ_{FECM} being respectively the characteristic function of the osseous and fibrous ECM.
It is assumed that phases, osseous and fibrous ECM, exhibit isotropic behavior [63]. Thus, the tensor $\mathbf{C}$ in (4.2) is known for each phase, and its components are written according to the Young's modulus E and Poisson's ratio ν of the two phases.
Governing equations of tissue at the L_1-scale is given by:

$$\begin{cases} \sigma_{ij}(\tilde{\mathbf{u}}_{L_1}) = C_{ijkl}\epsilon_{kl}(\tilde{\mathbf{u}}_{L_1}), \quad \text{on } \Omega \\ -\nabla \cdot (\boldsymbol{\sigma}(\tilde{\mathbf{u}}_{L_1})) = 0, \quad \text{on } \Omega \\ \text{Displacement continuity at } \partial\Omega_{int} \\ \text{Boundary conditions on } \partial\Omega_{ext} \end{cases} \tag{4.3}$$

The strain and stress tensor symmetry ($\sigma_{ij} = \sigma_{ji}$ and $\epsilon_{kl} = \epsilon_{lk}$), implies that only nine of the 24 coefficients C_{ijkl} are necessary to a complete description of the relation. Another symmetry consideration allows to reduce the number of independent coefficient to six. Finally, using Voigt's convention, one can write the Hooke's law in (4.3) through the matrix equation (4.4).

$$\begin{bmatrix} \sigma_{11}(\tilde{\mathbf{u}}_{L_1}) \\ \sigma_{22}(\tilde{\mathbf{u}}_{L_1}) \\ \sigma_{12}(\tilde{\mathbf{u}}_{L_1}) \end{bmatrix} = \begin{bmatrix} C_{11} & C_{12} & C_{13} \\ & C_{22} & C_{23} \\ symm & & C_{33} \end{bmatrix} \begin{bmatrix} \epsilon_{11}(\tilde{\mathbf{u}}_{L_1}) \\ \epsilon_{22}(\tilde{\mathbf{u}}_{L_1}) \\ 2\epsilon_{12}(\tilde{\mathbf{u}}_{L_1}) \end{bmatrix} \tag{4.4}$$

At the L_1-scale, as the domain Ω is piecewise isotropic according to its two phases, each elastic phase behavior can be represented with the following relation

$$\begin{bmatrix} \sigma_{11}(\tilde{\mathbf{u}}_{L_1}) \\ \sigma_{22}(\tilde{\mathbf{u}}_{L_1}) \\ \sigma_{12}(\tilde{\mathbf{u}}_{L_1}) \end{bmatrix} = \frac{E_i}{(1+\nu_i)(1-\nu_i)} \begin{bmatrix} 1-\nu_i & \nu_i & 0 \\ & 1-\nu_i & 0 \\ symm & & \frac{1-2\nu_i}{2} \end{bmatrix} \begin{bmatrix} \epsilon_{11}(\tilde{\mathbf{u}}_{L_1}) \\ \epsilon_{22}(\tilde{\mathbf{u}}_{L_1}) \\ 2\epsilon_{12}(\tilde{\mathbf{u}}_{L_1}) \end{bmatrix} \tag{4.5}$$

where E_i is the Young's modulus and ν_i the Poisson ratio of a given phase i of the 2-porosity model.

Remark: The relation between the strain and the stress is given by taking the inverse equation (4.2) as follow

$$\epsilon_{ij}(\tilde{\mathbf{u}}_{L_1}) = S_{ijkl}\sigma_{kl}(\tilde{\mathbf{u}}_{L_1}) \tag{4.6}$$

---

[1] The use of the symmetrical strain-rate tensor ϵ, instead of the non-symmetrical one, arise from mathematical property of the inner product of a symmetric tensor and an anti-symmetric one (see following weak formulation).

where **S** is the compliance tensor.
In the following, we consider equation (4.3) as it is possible to retrieve the compliance tensor by a tensor inversion. Note that, under the Voigt's notation matrix representation, this inverse is not trivial and requires an appropriate mapping of the stiffness and compliance matrices.

Three types of boundary conditions on the external boundary will be considered in the determination of the equivalent stiffness tensor at the L_2-scale: the kinematic uniform boundary conditions (KUBC) imposing a uniform displacement, the static uniform boundary conditions (SUBC) imposing a traction force and the periodic condition, all arising from computational homogenization. The computational homogenization periodic condition is considered in this chapter as the literature is very developed in its comparison with the other two BCs. The AE method [140] is not considered here. It requires the periodization of the porous medium.
These BC are the most common ones and others exist in the form of mixed conditions in the literature [141].
The three retained conditions are respectively written as:

- KUBC (prescribing a uniform displacement on the boundaries)

$$\tilde{\mathbf{u}}_{L_1} = \mathbf{A} \cdot \boldsymbol{x} \text{ where } \mathbf{A} \text{ is a constant second order tensor and } \boldsymbol{x} \text{ the space variable} \tag{4.7}$$

- SUBC (prescribing a uniform traction on the boundaries)

$$\boldsymbol{\sigma}(\tilde{\mathbf{u}}_{L_1}) \cdot \mathbf{n} = \boldsymbol{\Sigma} \cdot \mathbf{n} \text{ where } \boldsymbol{\Sigma} \text{ is a constant second order tensor} \tag{4.8}$$

- Periodic [142] (arising from computational homogenization)

$$\begin{cases} \nabla \cdot \boldsymbol{\sigma} = 0 & \text{in } \Omega \\ \boldsymbol{\sigma} = \mathbf{C}(y) : \boldsymbol{\epsilon} & \forall y \in \Omega \\ \boldsymbol{\epsilon} = \mathbf{A} + \nabla_{sym}\mathbf{v} & \text{in } \Omega \\ \mathbf{v} & \Omega\text{-periodic} \\ \boldsymbol{\Sigma} = \boldsymbol{\sigma} \cdot \mathbf{n} & \Omega\text{-antiperiodic} \end{cases} \tag{4.9}$$

  where **A** is a constant second order tensor, **v** the periodic fluctuation and y the local space variable. Here, the formulation consider the periodic fluctuation **v** as the main unknown. One can also resolve for a total periodic displacement $\tilde{\mathbf{u}}_{L_1}$ but this cannot be easily implemented in FEniCS as it require features not available.

The application of the grid-block upscaling method to the theory of linear elasticity is not straightforward in the sense that two formulations are possible to obtain the equivalent properties in computational homogenization framework [143], i.e equilibrium and energy. The reciprocity of these two formulations is demonstrated when we consider boundary conditions respecting the Hill-Mandel property, i.e $\langle \boldsymbol{\sigma}(\tilde{\mathbf{u}}_{L_1}) : \boldsymbol{\epsilon}(\tilde{\mathbf{u}}_{L_1})\rangle_\Omega = \langle \boldsymbol{\sigma}(\tilde{\mathbf{u}}_{L_1})\rangle : \langle \boldsymbol{\epsilon}(\tilde{\mathbf{u}}_{L_1})\rangle_\Omega$, ensuring that the mechanical work density at L_1-scale is conserved when upscaling to the L_2-scale [2]. Note that the energy based formulation allows to demonstrate the symmetry of the equivalent stiffness tensor [145].

For the first uspcaling, the domain Ω is divided into $N_x \times N_y$ sub-domains of dimension L_1^2. By imposing three different elastic tests according to unitary macroscopic tensor $\mathbf{A}_i$ or $\boldsymbol{\Sigma}_i$ with $i \in [[1, 3]]$, one can compute the equivalent stiffness matrix at the L_2-scale, as shown in figure 4.2 for KUBC like tests. The exact procedure is detailed below.
One have, according to the divergence theorem, for a given boundary condition [146]:

$$\text{KUBC} \;\Rightarrow\; \langle \boldsymbol{\epsilon}(\tilde{\mathbf{u}}_{L_1})\rangle_\Omega = \mathbf{A} \tag{4.10}$$

$$\text{SUBC} \;\Rightarrow\; \langle \boldsymbol{\sigma}(\tilde{\mathbf{u}}_{L_1})\rangle_\Omega = \boldsymbol{\Sigma} \tag{4.11}$$

where **A**, $\boldsymbol{\Sigma}$ are second order tensor.

---

[2] The Hill-Mandel condition is equivalent to $\frac{1}{|\Omega|}\int_{\partial\Omega}(P - \langle \boldsymbol{\sigma}\rangle_\Omega.n).(\tilde{\mathbf{u}}_{L_1} - \langle \boldsymbol{\epsilon}\rangle_\Omega.\boldsymbol{x})ds = 0$, where P and $\tilde{\mathbf{u}}_{L_1}$ are the traction vector density on the boundary and the displacement vector, respectively [144].

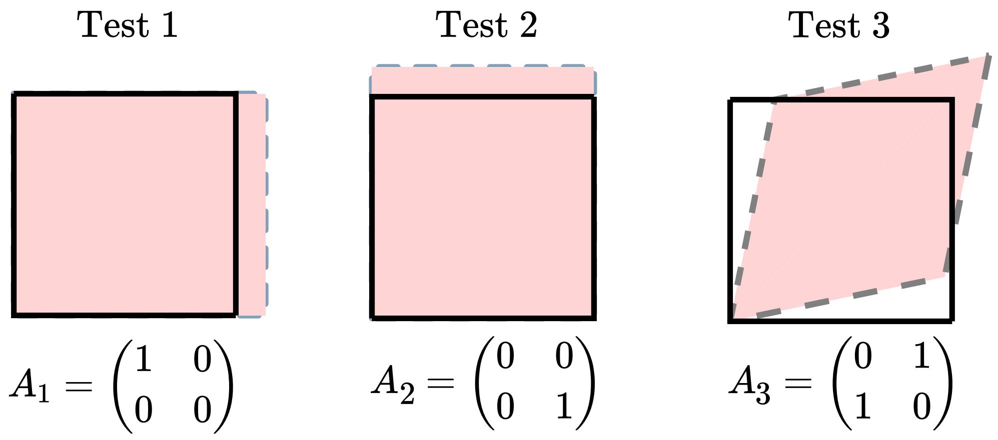

Figure 4.2: Three KUBC elastic tests for the determination of the equivalent elastic tensor.

In the periodic and KUBC case, each component of the stiffness matrix is easily given as trivial linear relations are obtained between the L_2 stress and strain thanks to (4.10). For example, if one take the first elastic test with the tensor A_1 (such as $A_{11} = 1$) then:

$$\begin{bmatrix} \langle \sigma_{11}(\tilde{\mathbf{u}}_{L_1}) \rangle \\ \langle \sigma_{22}(\tilde{\mathbf{u}}_{L_1}) \rangle \\ \langle \sigma_{12}(\tilde{\mathbf{u}}_{L_1}) \rangle \end{bmatrix} = \begin{bmatrix} C_{11}^{L_2} & C_{12}^{L_2} & C_{13}^{L_2} \\ & C_{22}^{L_2} & C_{23}^{L_2} \\ symm & & C_{33}^{L_2} \end{bmatrix} \begin{bmatrix} 1 \\ 0 \\ 0 \end{bmatrix} = \begin{bmatrix} C_{11}^{L_2} \\ C_{12}^{L_2} \\ C_{13}^{L_2} \end{bmatrix} \tag{4.12}$$

In the SUBC case, we obtain rather a system of 9 equations for 6 unknowns, namely $C_{11}^{L_2}$, $C_{12}^{L_2}$, $C_{13}^{L_2}$, $C_{22}^{L_2}$, $C_{23}^{L_2}$. To solve this problem, a least squares method and a minimization of the cost function are performed to define the matrix coefficients [139]. Indeed, as one has consider the stiffness relation (4.3) and not a compliance one, the equivalent stiffness tensor cannot be trivially computed thanks to relation (4.11).

From that point on, this post-processing method will be used for each BCs since it allows to keep the same Hooke type relation without using the compliance for SUBC. Note that it gives the same results in the periodical and KUBC cases.

Therefore, a new description of the physical system at the intermediate scale L_2 is found comprising (1) a piecewise smooth geometry $\tilde{\Omega}$ and its boundary $\partial\tilde{\Omega}$ (2) a novel elasticity equation in which the stiffness tensor $\mathbf{C}^{L_2}(s)$ is piecewise constant:

$$\begin{cases} \sigma_{ij}(\tilde{\mathbf{u}}_{L_2}) = C_{ijkl}^{L_2} \epsilon_{kl}(\tilde{\mathbf{u}}_{L_2}), & \text{on } \tilde{\Omega} \\ \nabla \cdot (\boldsymbol{\sigma}(\tilde{\mathbf{u}}_{L_2})) = 0, & \text{on } \tilde{\Omega} \\ \text{BCs on } \partial\tilde{\Omega} \end{cases} \tag{4.13}$$

For the second upscaling, an iteration of the above procedure is conducted on a coarser grid form and the physical system described by (4.13). A new set of stiffness matrix is obtained at the L_3-scale [147], through the same post-processing method, giving a new linear elastic behavior at the L_3-scale with a piecewise constant stiffness matrix $\mathbf{C}^{L_3}(\tilde{s})$, on a new piecewise smooth domain $\tilde{\tilde{\Omega}}$ as follows:

$$\begin{cases} \sigma_{ij}(\tilde{\mathbf{u}}_{L_3}) = C_{ijkl}^{L_3} \epsilon_{kl}(\tilde{\mathbf{u}}_{L_3}), & \text{on } \tilde{\tilde{\Omega}} \\ \nabla \cdot (\boldsymbol{\sigma}(\tilde{\mathbf{u}}_{L_3})) = 0, & \text{on } \tilde{\tilde{\Omega}} \\ \text{BCs on } \partial\tilde{\tilde{\Omega}} \end{cases} \tag{4.14}$$

The two-steps grid-block method stops here.

4.1.2 Weak formulation (FEM)

The discretization of the elasticity problem relies on an appropriate geometry meshing and a stable Hooke's law discretization.

The mesh is again constructed by the GMSH's Delaunay built-in frontal algorithm. The mesh

covers entirely the domain as the osseous and the fibrous ECM phases are discretized.
The weak formulation associated with (4.3) is expressed by equation (4.15).

find $\tilde{\mathbf{u}} \in (H^1)^2$ such that for all $\mathbf{v} \in (H^1)^2$

$$\int_\Omega \boldsymbol{\sigma}(\tilde{\mathbf{u}}) : \boldsymbol{\epsilon}(\mathbf{v}) \; dx = \int_\Omega (\mathbf{C} : \boldsymbol{\epsilon}(\tilde{\mathbf{u}})) : \boldsymbol{\epsilon}(\mathbf{v}) \; dx = \int_{\partial\Omega} \boldsymbol{\sigma}(\tilde{\mathbf{u}}) \cdot \mathbf{n} \cdot \mathbf{v} \; ds \tag{4.15}$$

where we drop subscript associated with the considered scale for simplicity.
This problem (4.15) is ill-posed for uniform Neumann-like conditions [63] as the solution is determined up to rigid body motion, i.e. translation and rotation. Thus, the use of the SUBC type boundary condition requires nullspace enforcement [3] [148]. In the same way, the solution is given up to a translation in the periodic case. One way to circumvent this issue is to consider Lagrange multiplier.

A two-field mixed finite element approach is possible to models (4.3) taking into account two unknowns in the displacement and the stress through the resolution of a saddle-point problem. A significant advantage of this method is that it allows to better capture the incompressible or nearly incompressible elastic behavior i.e. with a Poisson's ratio close to 0.5. In opposition, the functional linked to the principle of virtual work (4.15) is undetermined as Poisson ratio tends to the limit case and can lead to spurious deformations such as locking effect for piecewise linear and continuous elements [149]. Far from the limit value, the one-field and two-fields formulations are found in good agreement.

For the biological tissue investigated, the hypothesis of incompressibility is not valid [150], and a discretization based on displacement is well-adapted. As no mixed-formulation is used, finite element spaces do not pose any particular problem and Lagrange space can be trivially considered to discretize the displacement field. Moreover, no precondtioner in 2D is necessary as the problem converges quickly. For large images, weak formulations can be solved with the parallel sparse direct solver MUMPS. In this case, we use a biconjugate gradient solver together with an algebric multigrid preconditioner.

4.1.3 Numerical parameters, method parameters

We study the effect of the mesh at the L_1-scale through pore scale field variables and L_2-scale equivalent properties. A mesh conforming to the two phases is built with GMSH by giving a fixed value of the meshes according to the nature of the phase. Thus, a mesh convergence study according to the two phases is necessary. Specifically, we study for two fixed elastic material parameters in the two phases, a SUBC problem with an unitary macroscopic Σ tensor on $1600\,\text{px} \times 1600\,\text{px}$ image. The binarized image is shown in figure 4.3a.
The behaviour of a macroscopic and unidirectional Young's modulus, defined as $E_{11} = \frac{\langle \sigma_{11} \rangle_\Omega}{\langle \epsilon_{11} \rangle_\Omega}$, for various densities of the mesh is shown in figure 4.3b. No difference is noticed as the osseous ECM and fibrous ECM mesh characteristic length increases.
Concerning pore scale variable convergence, the overall displacement is plotted over a line ($y = 800\,\text{px}$) for different mesh characteristic lengths showing convergence as soon as we consider a GMSH size of 16 for the meshes, as shown in figure 4.3c.

---

[3] we are looking for deformation preserving volume i.e the condition $\nabla.(\tilde{\mathbf{u}}) = 0$.

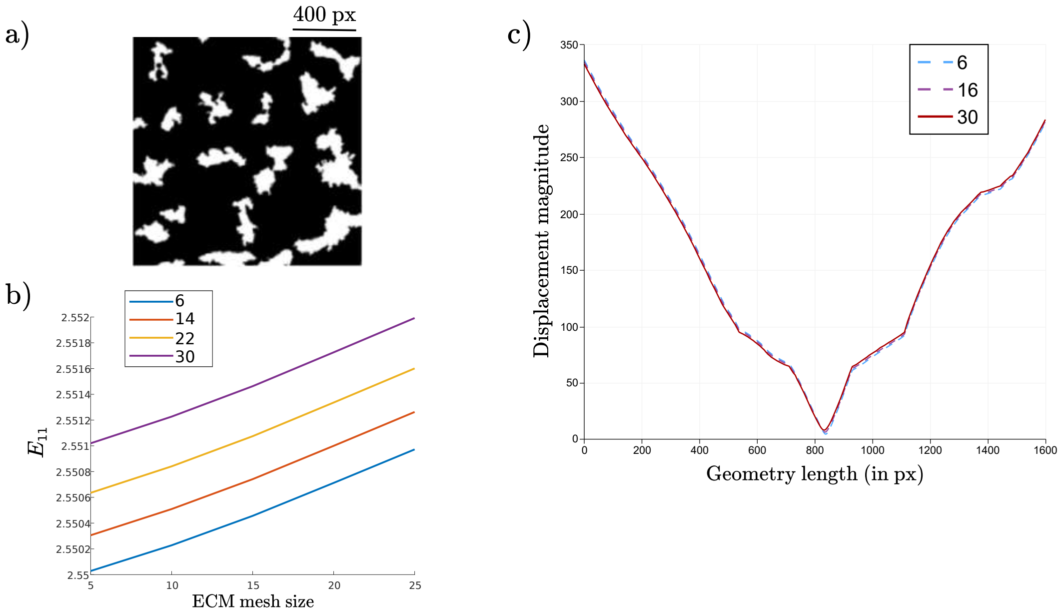

Figure 4.3: Mesh convergence study according to the two phases for the linear elastic equation in respect to the GMSH characteristic element size a) Osteosarcoma binary image b) Equivalent unidirection Young's modulus E_{11} resulting from multiple osseous ECM mesh characteristic size in function of the fibrous ECM GMSH characteristic size, using a SUBC boundary condition. c) Mesh effect on a pore scale field variable on the magnitude of the displacement over a line ($y = 800\,\mathrm{px}$) for multiple GMSH mesh characteristic size of the osseous ECM and a given fibrous ECM GMSH mesh characteristic size.

We have checked that the smoothing method of $\partial_{int}\Omega$ boundary had no effect on the predicted elastic properties but results are not presented here and the protocol detailed in chapter 3 and section 3.2.3.2 was used for further studies.

4.1.4 Influence of the sequential and extend-local methods parameters

4.1.4.1 Extend-local method study

In this section, we study the effects of the extend-local method on the stiffness tensor, at the L_2 scale after resolution of (4.3). We will consider a set of elastic parameters at the pore scale as $(E_{OECM}, E_{FECM}, \nu_{OECM}, \nu_{FECM}) = (500\,\mathrm{MPa}, 50\,\mathrm{MPa}, 0.3, 0.35)$, where the subscripts OECM and FECM correspond respectively to the osseous and fibrous ECM phases. For methodological purposes, we consider a set of arbitrary elastic quantities, with a moderate contrast on Young's modulus and Poisson's ratios not far from those found for a bone [150]. Note that different values will result in the same qualitative response of the extend-local method and the ratio between Young's moduli is examined latter in this manuscript.

To do this, all the three boundary conditions are considered: the SUBC, the KUBC and the periodic boundary conditions.
As for the previous physics (transport mechanisms), it is useful to reduce the bias inherent in the choice of boundary conditions. It is interesting to note that this numerical process is actually used in the experimental field with, for example, the use of standardized tensile specimens: their ends are enlarged, so that boundary conditions influence is limited in the region of interest.
We study the evolution of resulting stiffness matrix coefficient C_{ij} trough increasing δ neighboring size, for a constant local L_1-cell.

In the extend-local case and more particularly for periodical boundary conditions, the macroscopic relations of the type (4.10) and (4.11) do not hold anymore since the averaging is done on a sub-cell of the total computational domain. The least square strategy adopted to determine the equivalent property is then used. In the periodic case for example, we have by periodicity, on the whole domain, $\langle \boldsymbol{\epsilon} \rangle_\Omega = \langle \mathbf{A} \rangle_\Omega + \langle \nabla_{sym} \mathbf{v} \rangle_\Omega = \mathbf{A}$ because $\mathbf{v}$ is a periodic fluctuation. In the extend-local method case, as we proceed the upscaling only on a sub-cell L_1, it leads to $\langle \boldsymbol{\epsilon} \rangle_{L_1\text{-}cell} = \langle \mathbf{A} \rangle_{L_1\text{-}cell} + \langle \nabla_{sym} \mathbf{v} \rangle_{L_1\text{-}cell}$ without further simplifications.

To validate the approach, a periodic geometry is considered and is the same as in the previous section 3.2.4.1 as shown in figure 4.4a. The calculations for a single length of the local cell are presented with $L_1 = 400\,\text{px}$. The δ-size of extend region is ranging from 0 to 400 px by steps of 20 px. We plot the resulting stiffness matrices coefficient in figure 4.4b and 4.4b for the three boundary conditions (KUBC in blue, SUBC in red and the periodic condition in orange).

Coefficients (diagonal and extra-diagonal) end up being perfectly merged according to all the BCs. The C_{11} and C_{22} coefficients follow the same evolution since the geometry is isotropic. Note that values do not stabilize exactly around the local periodic solution (as it corresponds computational BCs and not the exact solution [4]). It do not oscillates with porosity for large δ contrary to transport calculations in chapter 3. The geometry being isotropic, the extra diagonal coefficients C_{13} and C_{23} are close to zero (see equation (4.5)). Small variations are observed for small δ but remain close to the zero. For larger δ, coefficients converge effectively towards 0.

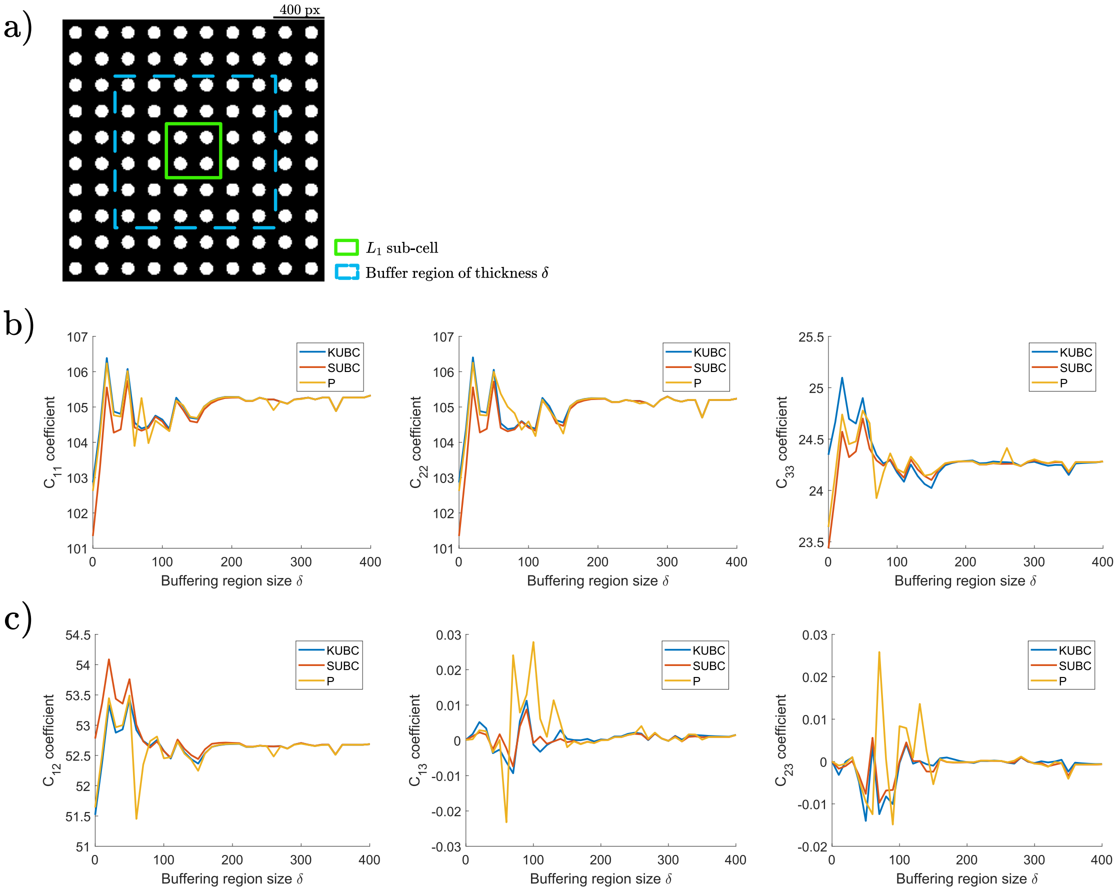

Figure 4.4: The extend-local method is applied in the framework of linear elasticity at small deformation for a periodic geometry a) Periodic geometry. b) Behavior of the stiffness matrix diagonal coefficients (in MPa), at the L_2-scale, according to the buffer size and for the 3 boundary conditions ; KUBC in blue, SUBC in red and the periodic condition in orange. c) Behavior of the stiffness matrix extra-diagonal coefficients (in MPa), at the L_2-scale, according to the buffer size and for the same boundary conditions.

The binarized image of biological tissue is shown in figure 4.5a. Results obtained with a single L_1 length, i.e with $L_1 = 1000\,\text{px}$, are presented. We plot stiffness coefficients as a function of the buffering size δ for the KUBC (in blue) and the SUBC (in red) conditions. For this study, periodic conditions are discarded because of the bias they introduce in the symmetrization of

---

[4] as it does not come from the theoretical homogenization such as AE or VA.

the geometry since the total periodized domain also includes the buffer zone.

As shown in figure 4.5b, we notice a convergence of the diagonal terms toward an asymptotic value according to the two BCs. Extra-diagonal coefficients show decreased discrepancies in convergence, which still depends on the porosity evolution for the first steps of the method, as shown in figure 4.5c.

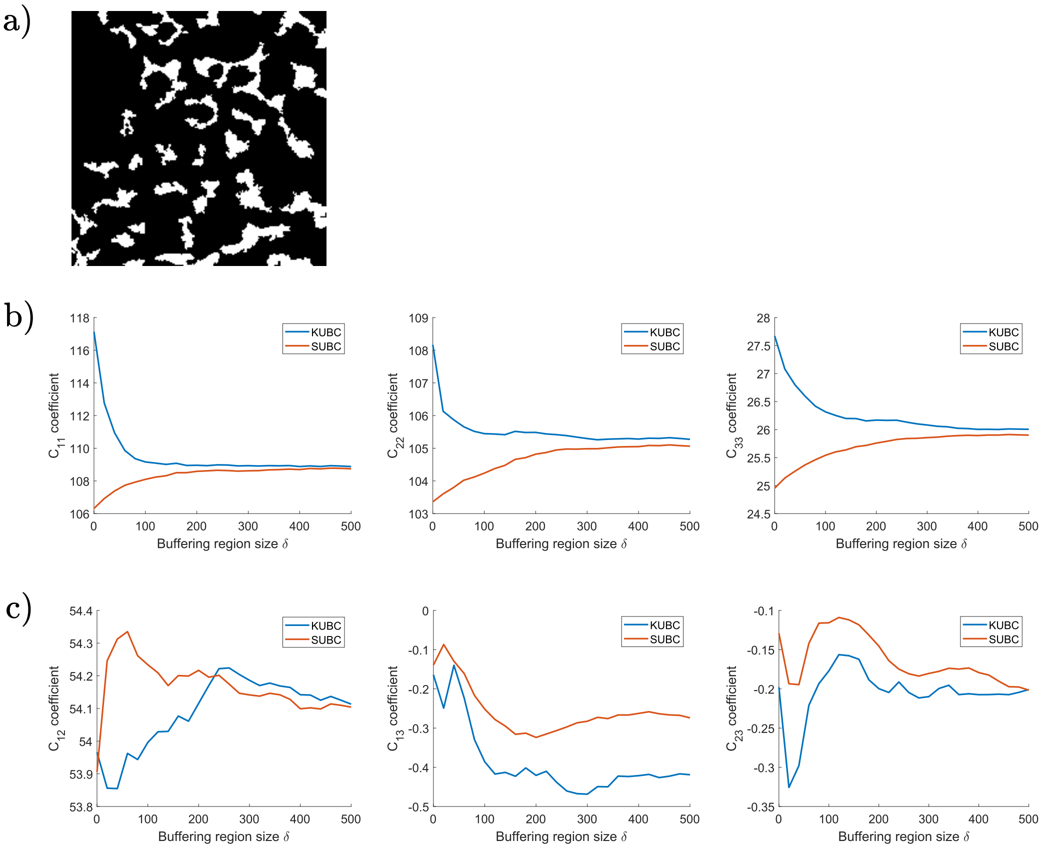

Figure 4.5: The extend-local method is applied on an osteosarcoma geometry a) Osteosarcoma geometry b) Behavior of the stiffness matrix diagonal coefficients (in MPa), at the L_2-scale, according to the buffer size and for two boundary conditions (KUBC, SUBC) c) Behavior of the stiffness matrix extra-diagonal coefficients (in MPa), at the L_2-scale, according to the buffer size and for the two boundary conditions KUBC and SUBC.

In opposition to transport problems, convergence of the extend-local applied to linear elasticity can be achieved for sufficiently large buffer zones; regardless of the chosen geometry, whether it is periodic isotropic or from a real osteosarcoma image. As a result, the bias inherent in the choice of boundary conditions can be completely erased for the calculation of elastic equivalent properties.

The initial difference between the static and kinematic boundary conditions are all the more pronounced if the contrast between the Young's moduli is high [151]. This is due to the fact that KUBC boundary conditions impose a uniform displacement regardless of the phase along the boundary. On the contrary SUBC, which imposes a force on the boundary, induce a resulting contrast in the displacement depending on the phase.
For high contrast elastic phases, the extend-local method smooths this difference for small neighboring region ($\delta \approx 100\,\mathrm{px}$) by underestimating the equivalent property as would the SUBC condition. For example, we consider the evolution of the equivalent coefficient C_{11} at the L_2-scale when considering a constant fibrous ECM Young modulus equal to 5 and for osseous ECM, a Young's moduli ranging from the value given in the set $\{5\,\mathrm{MPa}, 50\,\mathrm{MPa}, 500\,\mathrm{MPa}, 5000\,\mathrm{MPa}, 50\,000\,\mathrm{MPa}, 500\,000\,\mathrm{MPa}\}$. We plot the resulting coefficient for the SUBC and KUBC conditions boundary, respectively in red and blue, given two buffer region sizes $\delta = 0\,\mathrm{px}$ (fig. 4.6a) and 100 px (fig. 4.6b).

Extend-local method effectively reduces the inherent bias of boundary condition but greatly undervalues equivalent coefficient resulting from the KUBC condition around those of the SUBC. To address this problem of strong contrast, some authors recommend considering only the matrix, in a sort of extend-local method, without considering any solid inclusion on the edge [152]. It would also be interesting to consider a kind of effective medium method described in [102]. In chapter 5, where high contrast are considered, we are more interested in the qualitative rather than quantitative aspects of mapping equivalent properties.

In the rest of the chapter, we choose limited contrasts between the elastic parameters of the two phases for the sake of clarity.

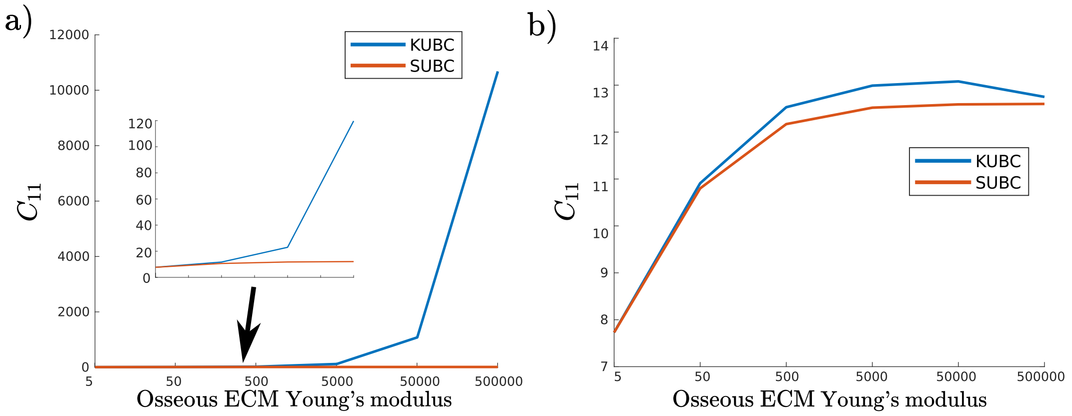

Figure 4.6: Study of the elastic parameters contrast effect on the resulting equivalent properties, represented by the C_{11} coefficient (in MPa), at the L_2-scale according to the KUBC and SUBC boundary condition and in function of different osseous ECM Young's modulii (for a fix fibrous ECM modulus equal to 5). a) The local upscaling method is applied $\delta = 0\,\text{px}$. b) The extend-local method is applied with $\delta = 100\,\text{px}$.

4.1.4.2 Sequential method study

In this section, we will study the sequential method together with a local method at the L_1-scale, in the framework of linear elasticity. Linear elasticity has been extensively studied in the context of grid-block upscaling. Most of the results developed here are known at the L_2-scale and the open question is to verify if they are preserved in the framework of the sequential procedure and at the L_3-scale.

We recall that at the L_1-scale, the stiffness matrix are piecewise constant according to the solid phases of the osteosarcoma. At the L_2-scale, the equivalent stiffness matrix is piecewise constant according to the considered splitting. Three standard boundary conditions are considered, consistently at each scale; the KUBC, SUBC and the periodic boundary conditions. The elastic parameters of the phases are those of the previous section, i.e $(E_{OECM}, E_{FECM}, \nu_{OECM}, \nu_{FECM}) = (500\,\text{MPa}, 50\,\text{MPa}, 0.3, 0.35)$. Again, different Young's modulus will result in different quantitative result but with a similar qualitative response.

The computational homogenization states [153] that on a REV, the effective parameters are equals whatever are the boundary conditions, that is:

$$\mathbf{C}_P = \mathbf{C}_{KUBC} = \mathbf{C}_{SUBC} \tag{4.16}$$

The equivalent properties of the stiffness tensor in heterogeneous porous media is also very well understood [136]. Indeed, we have in the sense of quadratic forms [5], the following inequation:

$$\mathbf{C}_{SUBC} \leq \mathbf{C}_P \leq \mathbf{C}_{KUBC} \tag{4.17}$$

---

[5] i.e in the sense that $\forall x,\ x^t A x \leq x^t B x$

A theoretical result also accounts for the splitting effect by stochastic average of the obtained results at the L_2-scale [137] with:

$$\overline{\mathbf{C}^f_{SUBC}} \leq \overline{\mathbf{C}^c_{SUBC}} \leq \overline{\mathbf{C}^c_{KUBC}} \leq \overline{\mathbf{C}^f_{KUBC}} \tag{4.18}$$

where the superscripts f, c stand for fine and coarse grid respectively, and the "overline" notation represents the stochastic average operator [6].

Remark: Please note that inequality (4.17) is verified in the above extend-local framework.

The resulting stiffness matrices through the two-step sequential process are computed on a binary image, shown in figure 4.7a, and having a dimension of 5000 px × 5000 px. The L_1-splitting ranges from 2×2 to 5×5 [7] and only one L_3-cell is considered in the L_3-paving with merging L_2 and L_3 scales. Results are shown in figure 4.7. KUBC resulting L_3-scale equivalent coefficients are plotted in blue, those from SUBC in red and finally those from the periodic condition in yellow.

In order to check the consistency of the results and the numerical implementation, we will use relation (4.17) at the intermediary scale L_2. This inequality induce an explicit scalar inequality of the same nature on the diagonal coefficients C_{11} and C_{22} [136], such as

$$C_{11}^{SUBC} \leq C_{11}^{P} \leq C_{11}^{KUBC} \tag{4.19}$$

$$C_{22}^{SUBC} \leq C_{22}^{P} \leq C_{22}^{KUBC} \tag{4.20}$$

It is interesting to see how tensors from periodic conditions will behave in the relation (4.17) as we proceed to unconventional geometry symmetrization.

Similar to the transport case, it is also interesting to see how the resulting tensors behave at the L_3-scale as a function of the L_1-splitting size and if it is possible to determine a relation similar to (4.18) in the deterministic framework of the sequential method.

Relation (4.18) and deterministic version of (4.18) are verified for the 2-steps upscaling method as shown by the evolution of C_{11} and C_{22}. Interestingly, the periodic resulting coefficients always lie between the other two boundary conditions even with the geometry symetrization process.

---

[6] One can show the existence of a quadratic inequality for the compliance tensor **S** according to the splitting and the boundary conditions essentially given by the inverse of (4.17) and (4.18). Mixed conditions were also considered in [136].

[7] made to accommodate the consistencies of the graphical representation because periodic BC in the one-step method is not considered here; note that one-step method in the KUBC and SUBC cases give appropriate results.

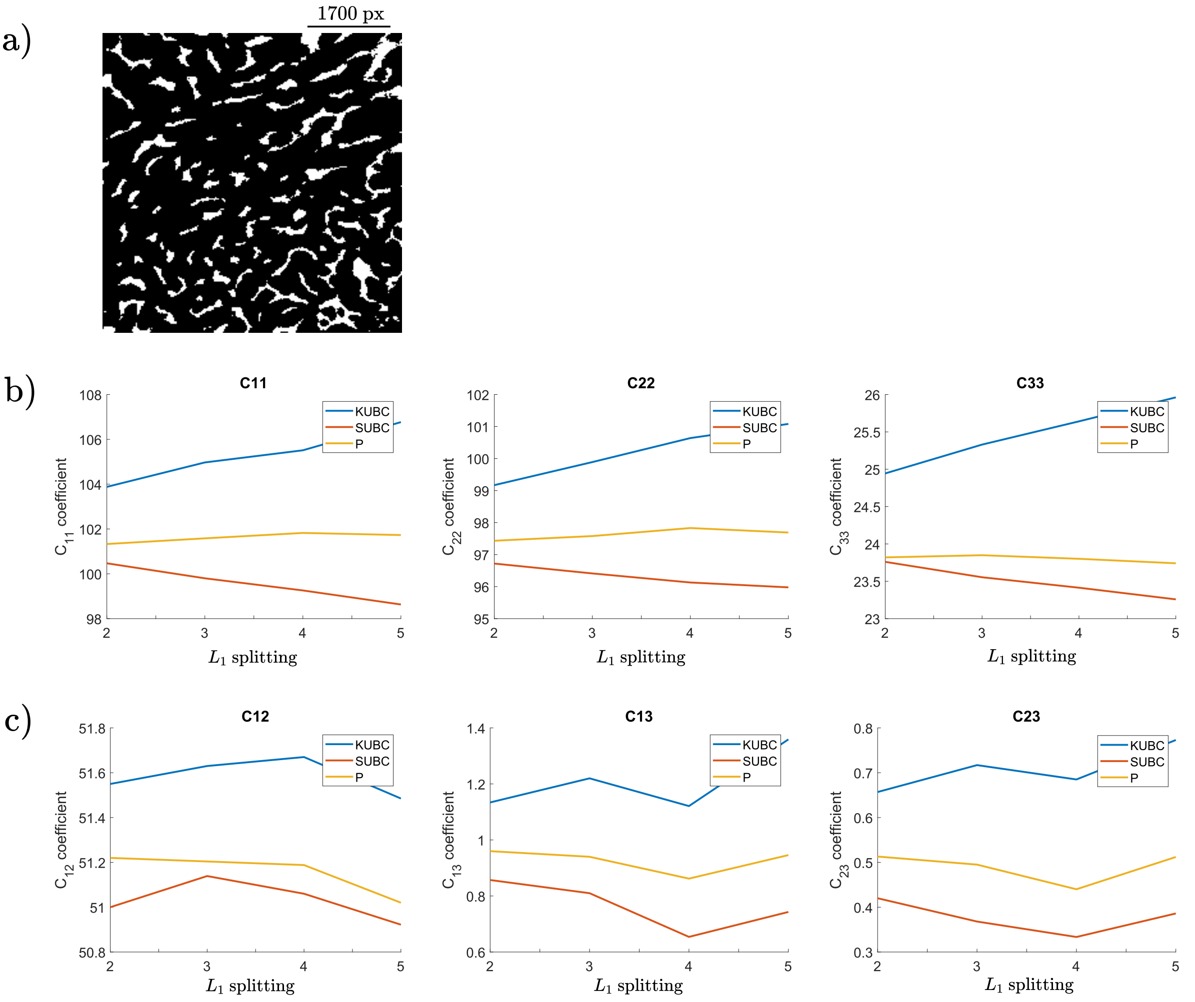

Figure 4.7: The 2-step method is applied on a 5000 px × 5000 px osteosarcoma image for linear elasticity model. a) Osteosarcoma binary image. b) Behavior of the stiffness matrix diagonal coefficients (in MPa), at the L_3-scale, according to the L_1-splitting and for three different boundary conditions (KUBC, SUBC and periodic). c) Behavior of the stiffness matrix extra-diagonal coefficients (in MPa), at the L_3-scale, according to the L_1-splitting and for three different boundary conditions (KUBC, SUBC and periodic).

In the same way as in the previous section 3.2.4.2 in the study of the flow problem, we validate the sequential process on a large image shown in figure 3.24 (16 000 px × 16 000 px). The displacement field resulting from the local 2-steps method is compared to those of a DNS. The boundary condition chosen on the four external boundaries to carry out the calculations is similar for both simulations and is an imposed displacement boundary condition KUBC (4.7) corresponding to a hundredth of the geometry length. The 2-step method is performed with an 8×8 L_3-paving together with a 2×2 L_1-splitting corresponding respectively to $L_1 = 1000\,\text{px}$ and $L_2 = 2000\,\text{px}$ and a consistent KUBC boundary condition across the two scales. Material properties are as follows: $(E_{OECM}, E_{FECM}, \nu_{OECM}, \nu_{FECM}) = (500\,\text{MPa}, 5\,\text{MPa}, 0.3, 0.35)$. The two displacement magnitude fields are shown on figure 4.8a and b. Here, we plot the displacement magnitude over two lines $y = 11\,000\,\text{px}$ and $y = 4000\,\text{px}$, respectively on top and bottom of figure 4.8c; with the DNS results given in red and the 2-steps in blue.

The displacement calculated with DNS or 2-step method are very similar. It is therefore possible to correctly represent the local displacement, even without REV assumption, with the 2-steps process [8].

---

[8] Parallel Programming with MPI does not seem to be trivial in elasticity through FEniCS. Indeed, a peak in RAM usage can make the calculation impossible (the above computations have been performed in serie on a computer with high memory available in the laboratory). An optimization of the use of MPI in our code seems necessary to adequately distribute the available cores.

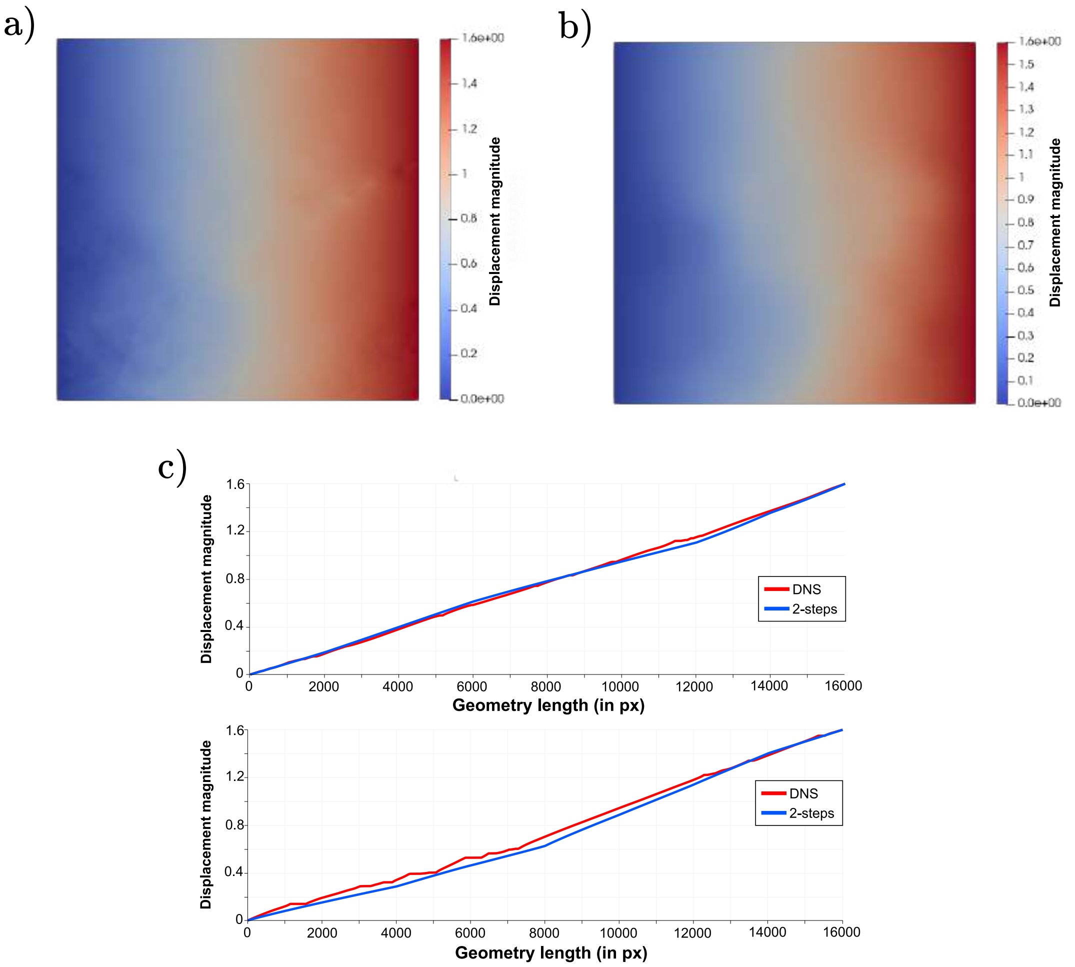

Figure 4.8: Comparison between DNS and 2-step computations on the $16\,000\,\text{px} \times 16\,000\,\text{px}$ geometry (chapter 3 and figure 3.25) for the elastic model validation; with a set of elastic parameters such that $(E_{OECM}, E_{FECM}, \nu_{OECM}, \nu_{FECM}) = (500\,\text{MPa}, 5\,\text{MPa}, 0.3, 0.35)$. a) Illustration of the displacement magnitude field after solving (4.3) with a KUBC boundary condition problem like. b) Illustration of the displacement magnitude obtained after solving equation (4.14) obtained by the 2-step method with $L_1 = 1000\,\text{px}$, $L_2 = 2000\,\text{px}$ and a KUBC conditions. c) Displacement magnitude profiles comparison over horizontal lines ($y = 11\,000\,\text{px}$ on top and $y = 4000\,\text{px}$ at the bottom).

In conclusion, the sequential grid-block method applied to the study of the linear elastic response of biological tissue is perfectly consistent and quantitative inequalities, at the L_3-scale, are found to be in agreement with those find in the literature for the first upscaling. The extend-local method allows a better characterization of the equivalent property at the L_2-scale by an significant reduction of the bias related to the choice of the boundary conditions. The sequential grid-block is shown to be relevant in describing the mechanical properties of large osteosarcoma images.
A consistent study of the osteosarcoma elastic behavior is of great importance since it will be used in the following poroelasticity case.

4.2 Poroelasticity

We increase the complexity by considering that the elastic behavior of osteosarcoma is modified by the presence of the fluid, which transforms the problem into a poroelasticity problem. The couplings of governing laws of two phases, i.e. fluid and solid, require specific developments. The founding works of this physics are those of Biot (1935,1941) and Terzaghi (1923) [135].

The stationary regime of poroelasticity is considered, the fluid fully saturates the porous medium and structural deformations are quasi-static. The coupling between the fluid flow and the elastic response of the solid phases is considered weak in our approach. The fluid pressure field is determined by the imposed flow and permeability tensor. The solid stress field is then influenced by the fluid pressure.

We choose a 2D geometrical paradigm similar to linear elasticity at small strain with a 2-porosity model and underlying porosity is considered for each phase. The model is described in figure 4.9. At the local L_1-scale, ECM is considered as a two-phase solid, i.e. osseous tissue and fibrous tissue, saturated by a fluid following a Darcy flow regime. Each phase is considered isotropic and scalar permeability is associated with each phase, i.e Lacunar-Canalicular System (LCS) is now considered.

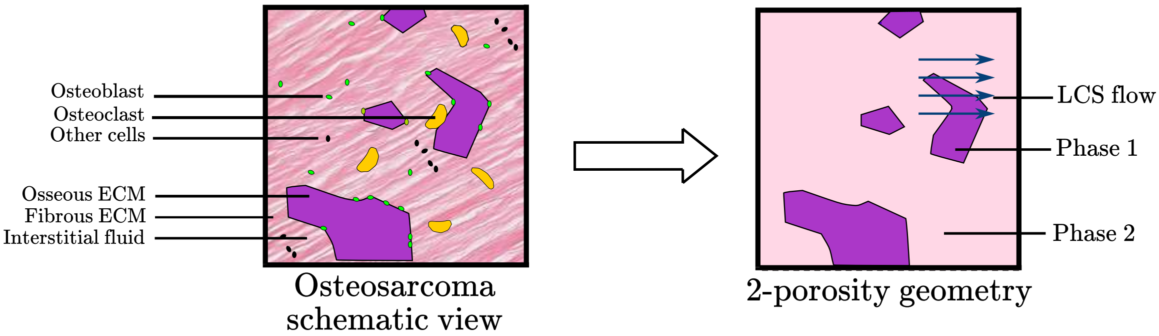

Figure 4.9: 2-porosity poroelasticity model accounting for the flow in the two phases.

The poroelastic response of this heterogeneous material is explored using a methodology similar to that of the elastic response described previously. We first describe the mathematical model associated with the 2-steps grid-block method. In a second and third part, the extend-local method at the L_1-scale and the sequential method are respectively studied.

4.2.1 Mathematical model

We consider the stationary linear poroelasticity with small strain at the L_1-scale. Stress tensor is related to the strain tensor by a modified Hooke's law as follows:

$$\boldsymbol{\sigma_{tot}}(\tilde{\mathbf{u}}_{L_1}) = \mathbf{DC} : \boldsymbol{\epsilon}(\tilde{\mathbf{u}}_{L_1}) - \alpha p_{L_1} Id, \tag{4.21}$$

where α is the Biot coefficient accounting for the compressibility of phases, $\tilde{\mathbf{u}}_{L_1}$ being the displacement field and p_{L_1}, the fluid pressure field.

The Ω body is maintained at equilibrium which is rewritten according to the total stress in equation (4.22).

$$-\nabla \cdot (\boldsymbol{\sigma_{tot}}(\tilde{\mathbf{u}}_{L_1})) = 0, \tag{4.22}$$

where no body force via a source term is considered and a negative sign is taken by convention.

When considering a stationary regime, no reciprocity of the coupling is possible in the governing equation of the flow as the pressure field is not modified by elastic stress and strain changes. Therefore, a Darcy equation describes the fluid flow and local equilibrium assumption [9] is made [96, 154]. The resulting fluid pressure field can be solved separately and put into the modified Hooke's law (4.21) as a simple parametric function.

Remark: In the general poroelastic framework, the continuity equation associated with the flow cannot be solved independently of the stress and strain fields and is written as

$$\partial_t(\frac{p}{M} - \alpha Tr(\boldsymbol{\epsilon}(\tilde{\mathbf{u}}_{L_1}))) + \nabla \cdot \mathbf{q}_{L_1} = 0, \tag{4.23}$$

---

[9] The question of local equilibrium is more sensitive on unsteady problems such as weakly compressible Darcy flow or diffusion/convection, and may lead to specific difficulties with this type of geometry.

where $\mathbf{q}_{L_1}$, is the Darcy velocity at the L_1-scale and M is an inverse storage coefficient. The term $\zeta = \frac{p}{M} - \alpha Tr(\epsilon(\tilde{\mathbf{u}}_{L_1}))$ describe the variation of fluid volume per unit reference volume. Thus, in stationary conditions, it is reasonable to consider a weak coupling for the poroelasticity equations.

Finally, the set of governing equations at the L_1-scale is as follows:

$$\begin{cases} \nabla \cdot \mathbf{q}_{L_1} = 0 & \text{in } \Omega \\ -\nabla \cdot (\sigma_{tot}(\tilde{\mathbf{u}}_{L_1})) = 0 & \text{in } \Omega \\ \mathbf{q}_{L_1} = -\frac{\mathbf{K}}{\mu} \cdot \nabla p_{L_1} & \text{in } \Omega \\ \boldsymbol{\sigma_{tot}}(\tilde{\mathbf{u}}_{L_1}) = \mathbf{DC} : \boldsymbol{\epsilon}(\tilde{\mathbf{u}}_{L_1}) - \alpha p_{L_1} \mathbf{Id} & \text{in } \Omega \\ \text{Field variables continuity condition} & \text{on } \partial_{int}\Omega \\ \text{Boundary conditions} & \text{on } \partial_{ext}\Omega \end{cases} \tag{4.24}$$

with $\mathbf{DC} = \mathbf{DC}^{OECM}\chi_{OECM} + \mathbf{DC}^{FECM}\chi_{FECM}$ where χ_{OECM} and χ_{FECM} are respectively the characteristic function of the osseous and fibrous ECM respectively.

The modified Hooke's law is described for the Ω domain using piecewise isotropic coefficients. The parameter α is the ratio of the fluid volume gained or lost in a material element due to the volume change when loaded under drained conditions. In the following, α is fixed to 1.

The development of the two-step upscaling method is similar to the linear elasticity case. The key differences are the nature of equations and the choice of boundary conditions at each scale. Two categories of boundary conditions are imposed since they concern fluid and solid phases.

First, Darcy flow is solved to obtain the fluid pressure field. We impose an horizontal flow. As shown in figure 4.10, two types of boundary conditions, on top and bottom external edges, are then considered, namely the impervious and open boundary conditions, expressed by equation (3.14) and (3.15), respectively. In a second step, boundary conditions on the solid phases are imposed on external boundaries. We use the KUBC (solid displacement $\tilde{\mathbf{u}}_{L_1}$) and SUBC (on the total traction) conditions which are stated as follows:

- KUBC: $\tilde{\mathbf{u}}_{L_1} = \tilde{\mathbf{A}} \cdot \boldsymbol{x}$ on $\partial\Omega$ (uniform displacement on the boundaries)
- SUBC: $\boldsymbol{\sigma_{tot}}(\tilde{\mathbf{u}}_{L_1}) \cdot \mathbf{n} = \tilde{\boldsymbol{\Sigma}} \cdot \mathbf{n}$ on $\partial\Omega$ (uniform total traction on the boundaries)

where $\tilde{\mathbf{A}}$ and $\tilde{\boldsymbol{\Sigma}}$ are both symmetric tensors of order 2 not depending on the space variable. The space variable is named $\boldsymbol{x}$.

Remark: The physical system comprising an incompressible Darcy equation at the L_1-scale with a 2-porosity model is studied with the extend-local and sequential upscaling methods as detailed in appendix B.

Thus, we consider four combinations boundary conditions arising from permutations between the elastic and flow BCs and they are detailed in Table 4.1.

	KUBC (solid)	SUBC (solid)
Symmetry (fluid)	KUBC$_{sym}$	SUBC$_{sym}$
Linear (fluid)	KUBC$_{pl}$	SUBC$_{pl}$

Table 4.1: Poroelastic boundary conditions arising from the permutation of the linear elastic and transport models.

For the first upscaling, we consider three tests corresponding to a unitary tensor $\tilde{A}$ or $\tilde{\Sigma}$, summarized in figure 4.10. For each test $i \in [[1, 3]]$, one can relate stress to strain, following

[139] with Voigt's notation as expressed by equation (4.25).

$$\begin{bmatrix} \langle \sigma^i_{biot,11}(\tilde{\mathbf{u}}_{L_1})\rangle_\Omega \\ \langle \sigma^i_{biot,22}(\tilde{\mathbf{u}}_{L_1})\rangle_\Omega \\ \langle \sigma^i_{biot,12}(\tilde{\mathbf{u}}_{L_1})\rangle_\Omega \end{bmatrix} = \begin{bmatrix} DC^{L_2}_{11} & DC^{L_2}_{12} & DC^{L_2}_{13} \\ & DC^{L_2}_{22} & DC^{L_2}_{23} \\ symm & & DC^{L_2}_{33} \end{bmatrix} \begin{bmatrix} \langle \epsilon^i_{11}(\tilde{\mathbf{u}}_{L_1})\rangle_\Omega \\ \langle \epsilon^i_{22}(\tilde{\mathbf{u}}_{L_1})\rangle_\Omega \\ 2\langle \epsilon^i_{12}(\tilde{\mathbf{u}}_{L_1})\rangle_\Omega \end{bmatrix} \tag{4.25}$$

where $\boldsymbol{\sigma_{biot}} = \boldsymbol{\sigma_{tot}} + pId$ is the "Biot effective stress" [155] and $\mathbf{DC}^{L_2}$ the equivalent poroelastic tensor at the L_2-scale.

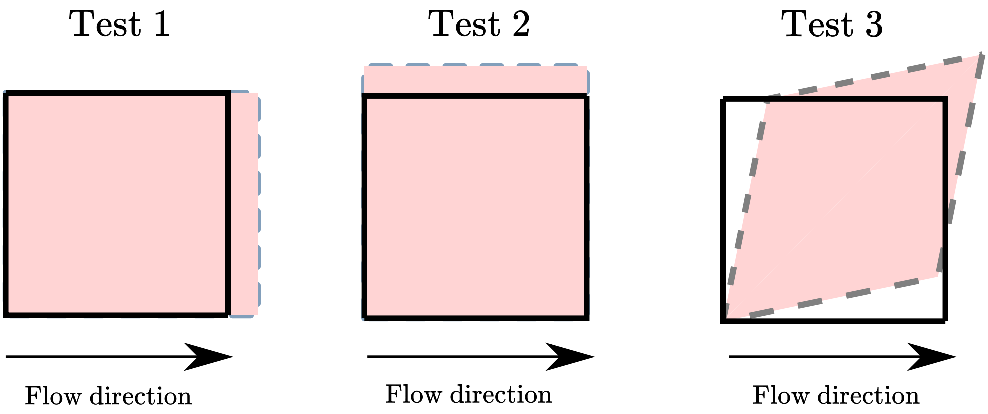

Figure 4.10: Poroelastic tests for the determination of the equivalent poroelastic tensor.

The equivalent poroelastic stiffness matrix is symmetric even for anisotropic geometries [156, 157]. The minimization of a cost function allows to determine the poroelastic stiffness matrix coefficients. Here, one need to enforce [10] the equivalent poroelastic matrix symmetry [139] as the least square procedure can produced some nearly symmetric tensor, even more without a REV assumption.

Therefore, the physical system is represented, at the L_2-scale, by a piecewise smooth medium $\tilde{\Omega}$ having a poroelastic stiffness tensor given by $\mathbf{DC}^{L_2}$ with the modified Hooke's law expressed by equation (4.26).

$$\begin{cases} \nabla \cdot \mathbf{q}_{L_2} = 0 & \text{in } \Omega \\ -\nabla \cdot (\boldsymbol{\sigma_{tot}}(\tilde{\mathbf{u}}_{L_2})) = 0 & \text{in } \tilde{\Omega} \\ \mathbf{q}_{L_2} = -\dfrac{\mathbf{K}}{\mu} \cdot \nabla p_{L_2} & \text{in } \tilde{\Omega} \\ \boldsymbol{\sigma_{tot}}(\tilde{\mathbf{u}}_{L_2}) = \mathbf{DC}^{L_2} : \boldsymbol{\epsilon}(\tilde{\mathbf{u}}_{L_2}) - \alpha p_{L_2}\mathbf{Id} & \text{in } \tilde{\Omega} \\ \text{Boundary conditions} & \text{on } \partial\tilde{\Omega} \end{cases} \tag{4.26}$$

For the second upscaling, process is repeated for the same fluid and solid BCs than in the first upscaling, and the stress-strain relation at the L_3-scale is given by [155], with another piecewise constant poroelastic stiffness tensor $\mathbf{DC}^{L_3}$. This results in the set of equations (4.27).

$$\begin{cases} \nabla \cdot \mathbf{q}_{L_3} = 0 & \text{in } \Omega \\ -\nabla \cdot (\boldsymbol{\sigma_{tot}}(\tilde{\mathbf{u}}_{L_3})) = 0 & \text{in } \tilde{\tilde{\Omega}} \\ \mathbf{q}_{L_3} = -\dfrac{\mathbf{K}}{\mu} \cdot \nabla p_{L_3} & \text{in } \tilde{\tilde{\Omega}} \\ \boldsymbol{\sigma_{tot}}(\tilde{\mathbf{u}}_{L_3}) = \mathbf{DC}^{L_3} : \boldsymbol{\epsilon}(\tilde{\mathbf{u}}_{L_3}) - \alpha p_{L_3}\mathbf{Id} & \text{in } \tilde{\Omega} \\ \text{Boundary conditions} & \text{on } \partial\tilde{\tilde{\Omega}} \end{cases} \tag{4.27}$$

4.2.2 Numerical discretisation (FEM)

At L_1-scale, the discretization of equation (4.24) must be consistent for Darcy's law and modified Hooke's law. We consider the same mesh for both physics. The GMSH's Delaunay built-in frontal algorithm covers the entire domain as fluid and solid phases are considered while

---

[10] by giving the coefficient under the diagonal of the matrix, the same value as those above the diagonal

following the phase interfaces $\partial_{int}\Omega$.

The weak formulation associated with the second and third equation of (4.24) on Ω at the L_1-scale, is expressed by equation (4.28).

find $\tilde{\mathbf{u}} \in (H^1)^2$ such that for all $\mathbf{v} \in (H^1)^2$

$$\int_{\Omega} \boldsymbol{\sigma_{tot}}(\tilde{\mathbf{u}}) : \boldsymbol{\epsilon}(\mathbf{v})\, dx = \int_{\Omega} (\mathbf{DC} : \boldsymbol{\epsilon}(\tilde{\mathbf{u}})) : \boldsymbol{\epsilon}(\mathbf{v})\, dx - \int_{\Omega} p\mathbf{Id} : \boldsymbol{\epsilon}(\mathbf{v})\, dx = \int_{\partial\Omega} \boldsymbol{\sigma_{tot}}(\tilde{\mathbf{u}}) \cdot \mathbf{n} \cdot \mathbf{v}\, ds \quad (4.28)$$

where we drop again the subscript associated with the scale of the grid-block method for the sake of simplicity.
Finite element spaces, preconditioner and solver are chosen according to the ones chosen in the elastic and flow case (see section 4.1.2 and 3.2.2) [11].

Mesh convergence can be estimated according to local variable (velocity and displacement) or equivalent properties (average velocity and unidirectional poroelastic Young's modulus). We choose as mesh size, the minimum of the found values.

4.2.3 Influence of the sequential and extend-local methods parameters

4.2.3.1 Extend-local method study

In this section, we study the effects of the extend-local method on the poroelastic equivalent property, at the L_2-scale, after the resolution of equation (4.24).

All the four boundary conditions of Table 4.1 are considered. Because of the isotropic behavior at the L_1-scale of the phases, tensor coefficients DC_{ijkl} are known for the two individual constituents, i.e osseous and fibrous ECM, and is written according to their Young's moduli and Poisson's ratio. Their values are $(E_{OECM}, E_{FECM}, \nu_{OECM}, \nu_{FMEC}) = (500\,\text{MPa}, 50\,\text{MPa}; 0.3, 0.35)$. Permeabilities are $(K_{OECM}, K_{FMEC}) = (0.2, 2000)$ in px^2.
In figure 4.11, we plot the resulting equivalent poroelastic matrix coefficients, obtained for a single $L_1 = 1000\,\text{px}$ scale, in function of the buffer region size δ (ranging from 20 px to 500 px with a 20 px step) and with respect to the four possible boundary conditions. The KUBC$_{sym}$, KUBC$_{pl}$, SUBC$_{sym}$ and SUBC$_{pl}$ are respectively given in blue line, blue circles, red line and red circles.

For the two solid types of boundary conditions (KUBC and SUBC), the values of the equivalent diagonal coefficients converge toward a common value as shown in figure 4.11b. We note a more difficult convergence for the DC_{22} coefficient accounting for the material elasticity in the orthogonal direction to the imposed fluid direction.
In this case, the addition of the fluid pressure field term has little to no effect on the quantitative behavior of the equivalent response as the resulting values are practically merge with those obtained by the pure elastic model. (overall difference around 10%).

Concerning extra-diagonal coefficients of the poroelastic equivalent matrix, the overall behavior remains quite erratic as no perfect convergence in value is reached even for high buffer region size for the four BCs. This is to be balanced with the fact that the overall difference between the four boundary condition resulting values is at best of the unity order. In contrast to the diagonal coefficients, there is still a difference here, albeit small, depending on the fluid condition. The PL underestimates the value of coefficients for small buffer regions; this difference totally disappears for sufficiently large extended region sizes.

---

[11] A two-field mixed finite element approach is also possible to simulate the weak formulation above but is not necessary as the material are not incompressible.

In general, one find a similar behavior as in the linear elasticity framework for the chosen set of parameters.

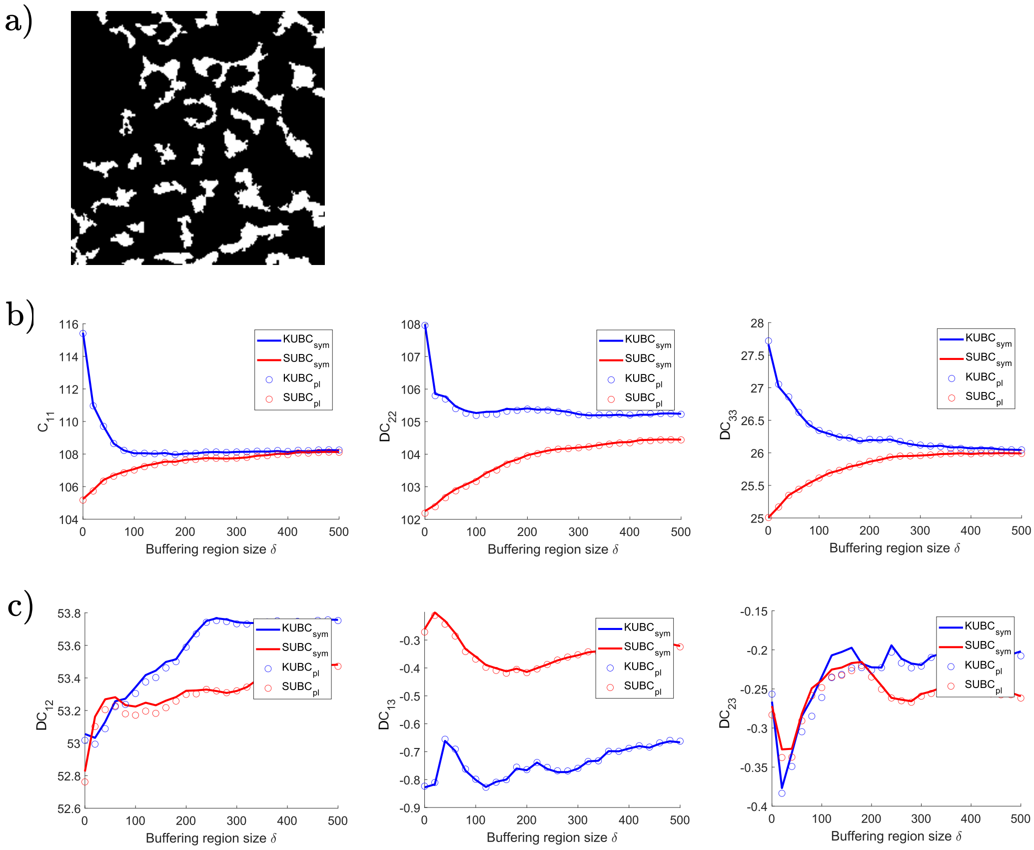

Figure 4.11: The extend-local method is applied on an osteosarcoma geometry with the sets of elastic parameters $(E_{OECM}, E_{FECM}, \nu_{OECM}, \nu_{FMEC}) = (500\,\text{MPa}, 50\,\text{MPa}; 0.3, 0.35)$ and $(K_{OECM}; K_{FMEC}) = (0.2, 2000)$ in px^2. a) Osteosarcoma geometry b) Behavior of the poroelastic matrix diagonal coefficients according to the buffer size and for four different boundary conditions (KUBC_{sym}, KUBC_{pl}, SUBC_{sym} and SUBC_{pl}) c) Behavior of the poroelastic matrix extra-diagonal coefficients according to the buffer size and for four different boundary conditions (KUBC_{sym}, KUBC_{pl}, SUBC_{sym} and SUBC_{pl}).

In conclusion, the extend-local method can also be used, at the L_1-scale, in this very specific case of BCs to reduce the biases intrinsic to each BCs.

4.2.3.2 Sequential method study

In this section, we study the sequential method in the framework of linear weakly coupled poroelasticity using the local method at the L_1-scale. The open question is whether or not the addition of the pressure field modifies the quadratic order relations found in linear elasticity.

The same binarized image shown in figure 4.12a is used together with the same set of material paramaters. Young's moduli and Poisson's ratio in both phases are given by $(E_{OECM}, E_{FECM}, \nu_{OECM}, \nu_{FMEC}) = (500\,\text{MPa}, 50\,\text{MPa}; 0.3, 0.35)$ and permeabilities are given by $(K_{OECM}; K_{FMEC}) = (0.2, 2000)$ in px^2.
The resulting equivalent tensor coefficients at the L_3-scale are plotted in figure 4.12b and figure 4.12c. They are obtained for L_1-splitting ranging from 1×1 (1-step method) to 5×5 and with respect to the four possible boundary conditions. Again, the KUBC_{sym}, KUBC_{pl}, SUBC_{sym} and SUBC_{pl} are respectively given in blue line, blue circles, red line and red circles.

The diagonal terms plotted in figure 4.12b shows the same overestimation (KUBC) and underestimation (SUBC) with respect to solid boundary conditions, with no significant influence of two fluid BCs. Moreover, an order relation is verified between the dense and fine splitting similar to the one found in elasticity and expressed by equation (4.18). The extra diagonal term plotted in Figure 4.12b follows the same evolution with a weak difference due to fluid BCs for a given solid BC.

In general, the results are similar to the elastic case (qualitatively) with quantitative differences, coming from the addition of the pressure term, of the order of few percents. This can be explained by the weak coupling considered, as well as the poroelastic tests used for the determination of the equivalent poroelastic properties where, we recall, we considered a single horizontal flow. This difference can increase when considering 3D geometry where different percolation properties will be at work.

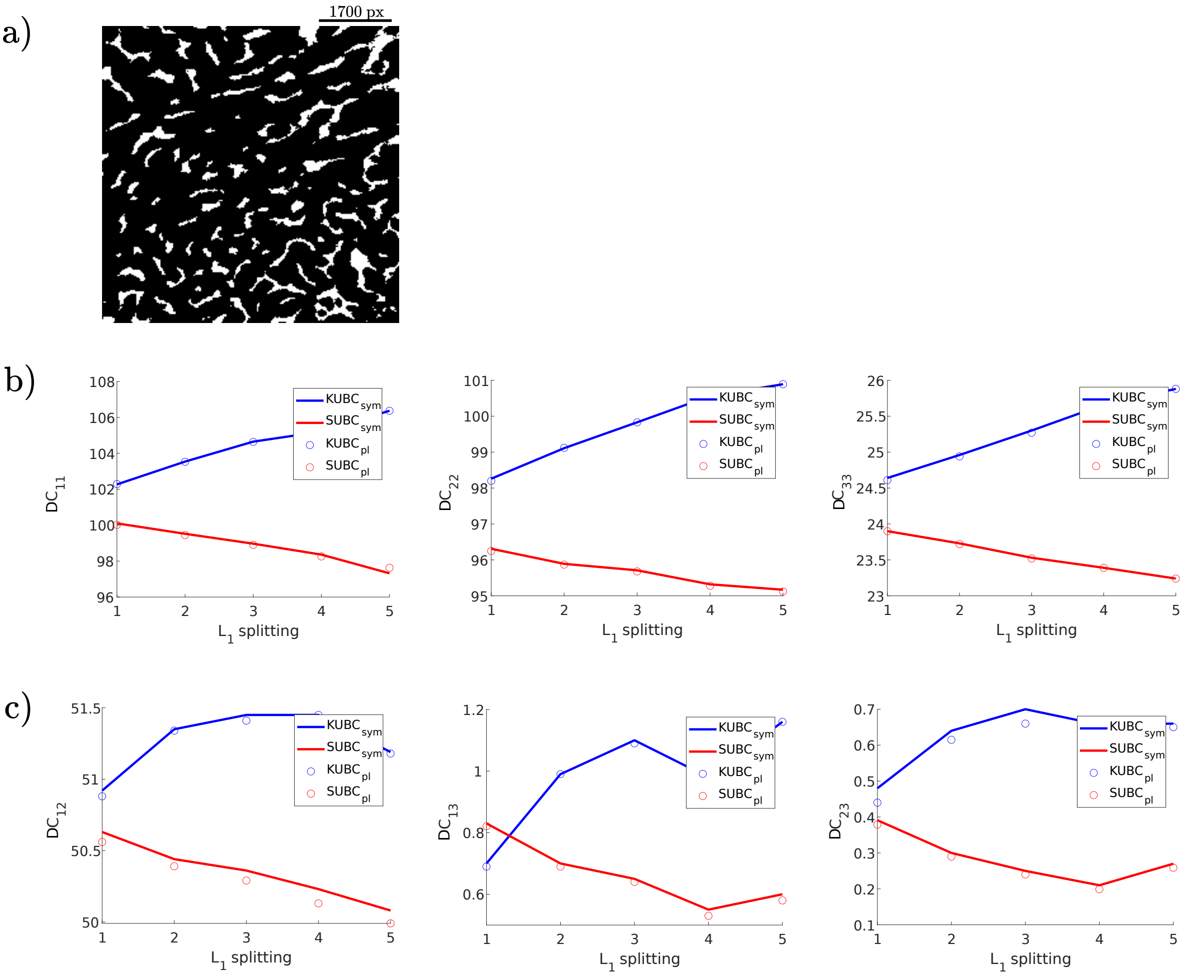

Figure 4.12: The 2-steps method is applied on a 5000 px × 5000 px osteosarcoma geometry for a linear poroelasticity model. a) Osteosarcoma binary image. b) Behavior of the equivalent matrix diagonal coefficients, at the L_3-scale, according to the L_1-splitting and for four different boundary conditions (KUBC$_{sym}$, KUBC$_{pl}$, SUBC$_{sym}$ and SUBC$_{pl}$). c) Behavior of the equivalent poroelastic matrix extra-diagonal coefficients, at the L_3-scale, according to the L_1-splitting and for four different boundary conditions (KUBC$_{sym}$, KUBC$_{pl}$, SUBC$_{sym}$ and SUBC$_{pl}$).

4.3 Conclusion and discussion on structural mechanics

In this chapter, we have applied the extend-local and two-steps grid-block upscaling methods to elastic and poroelastic responses of heterogeneous media and especially osteosarcoma tissue. It was shown that an extend-local method was beneficial for linear elasticity models to reduce the very important biases introduced by boundary conditions if moderate contrasts in elastic parameters are considered.

Concerning the 2-step grid-block method, we have recovered the principal literature results on the quadratic order relation between resulting stiffness tensor at the L_3-scale. They are summarized as follows:

$$\mathbf{C}_{SUBC} \leq \mathbf{C}_{P} \leq \mathbf{C}_{KUBC} \tag{4.29}$$

Furthermore, we obtained a deterministic order relation on the L_3-scale equivalent tensor, in function of the L_1-splitting density, as expressed by relation (4.30).

$$\mathbf{C}^{f}_{SUBC} \leq \mathbf{C}^{c}_{SUBC} \leq \mathbf{C}^{c}_{KUBC} \leq \mathbf{C}^{f}_{KUBC} \tag{4.30}$$

We were able to confirm the consistency of the methodology applied to osteosarcoma by comparing the two-steps method to the DNS simulation used as reference.

An extension of the methodology allowed to explore linear poroelasticity with a weak coupling between solid and fluid responses. We found qualitative behavior of the upscaling methods resulting from poroelasticity and order relations similar to elasticity at the L_3-scale, which can be summarized by relations (4.31) and (4.32). For a given solid BC, in the range of permeabilities explored, it is found that a fluid BC plays only a minor role in the equivalent poroelastic response.

$$\mathbf{DC}_{SUBC_{sym}}, \mathbf{DC}_{SUBC_{pl}} \leq \mathbf{DC}_{KUBC_{sym}}, \mathbf{DC}_{KUBC_{pl}} \tag{4.31}$$

$$\begin{aligned} &\mathbf{DC}^{f}_{SUBC_{sym}}, \mathbf{DC}^{f}_{SUBC_{pl}} \leq \mathbf{DC}^{c}_{SUBC_{sym}}, \mathbf{DC}^{c}_{SUBC_{pl}} \\ &\qquad \leq \mathbf{DC}^{c}_{SUBC_{sym}}, \mathbf{DC}^{c}_{SUBC_{pl}} \leq \mathbf{DC}^{f}_{SUBC_{sym}}, \mathbf{DC}^{f}_{SUBC_{pl}} \end{aligned} \tag{4.32}$$

As in the transport framework, the methodology developed is applicable to the 3D case. The transition to the 3D paradigm could even be preferable from a purely methodological point of view. Indeed, the osseous ECM connectivity and the 3D percolation properties would allow the use of the same geometrical model as in the transport framework (i.e. 1-porosity model) and thus a better hierarchization of the physical phenomena in the mechano-biological comparisons (consistency of the models for both physics).

This chapter concludes the mechanical study of osteosarcoma through the sequential grid-block upscaling method. In the next chapter, a mechano-biological study of osteosarcoma is conducted and the heterogeneity of the response to treatment in a cohort of 4 patients is examined.

Chapter 5

Correlation between the osteosarcoma response to treatment and equivalent mechanical properties of biological tissue; a preliminary study

Contents

The heterogeneity of osteosarcoma, from a genetic, cellular and tissular point of view, makes it very difficult to understand in terms of tumoral dynamics. In addition, the response heterogeneity of neoadjuvant chemotherapy is not yet well understood [10]. We focus on the intratumoral treatment response heterogeneity as it may provide new clues to understand the underlying mechanisms of bad response to treatments.

From a clinical point of view, the exploration of H&E histological sections gives the cell density and the nature of the bone, which can be used to estimate the tumor invasiveness and the response to treatment. The extend of tumor necrosis in response to chemotherapy is assessed as being greater or less than 90% of necrosis. Patients with more than 90% necrosis count are good responders and those with less than 90% are poor responders [158]. While the therapy response is currently determined through this Huvos and Rosen grading, a more quantitative approach that takes into account the intratumoral heterogeneity could bring a new insight in the understanding of the pathology and new perspectives for the treatments.

While osseous ECM may exhibit a chemotherapy-resistant phenotype [159], a question explored in this work is whether region with high osteo-formation could be a physical barrier to treatment transport as highlighted in [26]. In addition, pathological osseous ECM remodelling (see fig. 1.9) is related to a vicious cycle involving osteoclasts [21]. This cell population is also involved into the immune response [10], and it should be sensitive to mechanical effects [51, 52] since it is also observed in non-pathological bone [160, 161]. In this context, structural strain and stress might play a role on treatment efficiency.

We hypothesize that the response to treatment may be correlated to the architecture of osseous ECM and also that responses to differentiated physical stimuli could play a significant role.

Lacy-like and trabecular-like architectures are considered and correlations with cell populations are investigated.

Developments are based on patient-specific anatomo-pathological images and extend-local grid-block sequential upscaling procedure. Mass transports and structural elastic responses are considered. This problem is complex and restrictive assumptions are made. The vasculature is discarded to focus on steady interstitial transport which is considered steady, and reactive processes between cell phase and fluid flow are not considered. For flow studies, osseous ECM phase is considered as non-porous obstacles (focus on tissue interstitial flow) and for the structural behavior, a two-porosity model is used at the pore scale with isotropic elastic properties for the two phases, i.e. osseous and fibrous phases of ECM.

First, the methodology to establish mechano-biological correlations is described and then it is applied on a preliminary cohort of four patients.

5.1 Methodology to establish mechano-biological correlations

The upscaling method is applied to histological sections of osteosarcoma performed on surgically resected tumors. The patients selected for this study come from a cohort of bad responders with high-grade osteoblastic osteosarcoma (Toulouse University Hospital). Histological sections exhibit a spatial heterogeneity in response to treatment. In addition, the images show various characteristic osseous ECM structures such as lacy- and trabecular- like formations as illustrated in figure 5.1.

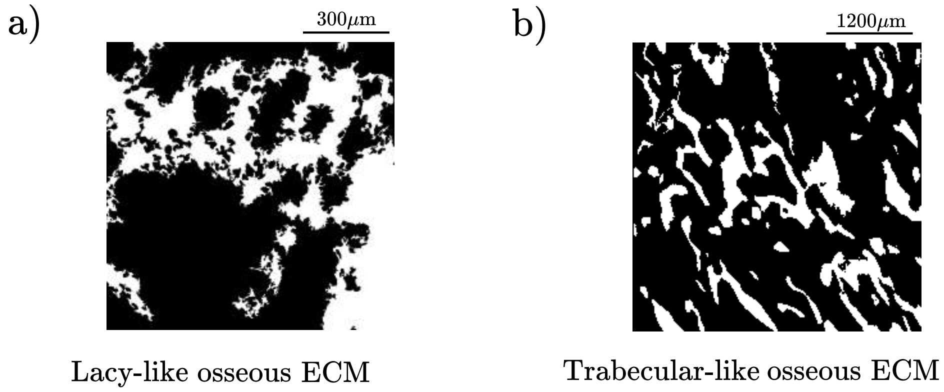

Figure 5.1: Different types of osseous ECM formations illustrated from binarized images. a) Lacy-like structure. b) Trabecular-like structure.

The degree to which two random variables or sets of random variables tend to deviate from their expected values in similar ways can be measured by the covariance. However such calculations are dependent upon the variable magnitude. Correlation coefficients are a normalized form of the covariance which characterize the relationship between adimensioned variables. Correlation coefficient ranges between -1 and 1. Its absolute value measures the intensity of the relationship while its sign indicates the monotony. If a variable Y_c tends to increase when a variable X_c increases, the correlation coefficient is positive (where subscript c stands for correlation). If Y_c tends to decrease when X_c increases, the correlation coefficient is negative. A correlation coefficient of zero indicates that there is no tendency for Y_c to either increase or decrease when X_c increases.

The Pearson coefficient measures a possible linear relationship between the two variables. For two variables X_c and Y_c, it is expressed by equation (5.1).

$$r_p = \frac{Cov(X_c, Y_c)}{\sigma_X \sigma_Y} \tag{5.1}$$

where $Cov(X_c, Y_c)$ is the covariance of the two variables, and σ_{X_c} and σ_{Y_c} the standard deviations.
Note that the normalization is done by the standard deviations, expressing the variable values dispersion with respect to their mean.
The Pearson coefficient is only suitable for linear relationships and it is sensitive to local discrepancies.

When the relationship is not strictly linear, the Spearman correlation coefficient should be favored. By rather examining a relationship between the rank of the two variables X_c and Y_c, it is possible to detect the existence of monotonic relationships. The Spearman coefficient is given by equation (5.2).

$$r_s = \frac{Cov(rg_{X_c}, rg_{Y_c})}{\sigma_{rg_{X_c}} \sigma_{rg_{Y_c}}} \tag{5.2}$$

where rg_X and rg_Y are the ranks of the variables X_c and Y_c.
When the relationship between the two entities is linear, the Spearman coefficient is similar to the Pearson coefficient. Local variations of variables are better taken into account and it is used in the following developments.

In this work, the correlations will in fact be done on two arrays X_c and Y_c coming from the splittings of histological sections for the sequential method. The first vector X_c corresponds to the equivalent mechanical properties at the L_3-scale, at the output of the two-step grid-block method. More precisely, we will consider on each sub-block, a relevant scalar property depending on the studied physics (flow strength or stiffness in the main directions). The second vector Y_c includes the clinical information, i.e. the cell densities on the same splitting of the histological section as realized for the mechanical study by upscaling.

For the 2-step upscaling method, the lengths being arbitrarily chosen for both physics, we first considered L_1, L_2, L_3 scales allowing among other things to account for the heterogeneity in phase distribution. Indeed, a too loose splitting would lead to a too important loss of local information and especially to a non-significant correlation (i.e. the cardinal of the sets X_c and Y_c would not be sufficient for a low p-value correlation). Also, in the context of the flow and in view of the images, splitting too dense could introduce purely numerical problems related to the phenomenon of percolation (see chapter 3 for the checkerboard like problem at the L_2-scale in particular).

Finally, it is necessary to evaluate the response to treatment on histological sections. Here, the areas of good and bad responses on the selected histological sections were determined from the Huvos and Rosen notation (10% or more of residual cell corresponds to a bad response to treatment).

5.2 Correlation coefficients: mechano-biomarkers of the treatment response?

In this section, we are exploring correlations between equivalent mechanical properties obtained by using the two-step sequential grid-block method, and the cell density. First, correlations are made with fluid flow and then, structural mechanics is considered with linear elasticity.

5.2.1 Transport study

First, we recall the clinical question motivating the modeling of interstitial flow in osteosarcoma. We want to know if it is possible that an area of high osteo-formation may or may not cause a barrier to the response to treatment.

Tissue and cell phases are segmented for the equivalent permeability calculations and the evaluation of cell density respectively as described in chapter 2. From the 2-steps grid-block upscaling method, equivalent permeability distributions are obtained at the L_3-scale. We consider the symmetry (3.12) and impervious (3.14) boundary conditions, at the L_1 and L_2 scales, respectively.

The methodology is applied on two subsamples of histological sections. The size of the images is $8000\,\text{px} \times 8000\,\text{px}$, i.e. $3.7\,\text{mm} \times 3.7\,\text{mm}$. At the L_1-scale, an extend-local method is considered with $\delta = 100\,\text{px}$. The non-dimensionalized permeability magnitude and cell density maps are shown in figure 5.2. Zones of good response to chemotherapy correspond to low cell densities whereas bad response corresponds to high cell densities.

An overall negative correlation between the two entities is found for patient 1 who exhibits a trabecular-like ECM formation. An increase in permeability is associated with a decrease in cell density. Indeed, qualitatively, one can see on Patient 1 sample (fig. 5.2 Patient 1), a clear separation materialized by the anti-diagonal of the 5×5 maps where a zone (top right) of very low permeability corresponds to a zone of very high cell density. An opposite distribution is found for patient 2 with lacy-like ECM where an increase in permeability in the left side of the image corresponds with an increase in cells density.

Those result are confirmed by the Spearman coefficient. For patient 1 it is negative with $r_s = -0.485$ ($p = 0.014$) whereas for patient 2, the coefficient is positive with $r_s = 0.433$ ($p = 0.026$).

Patient 1:

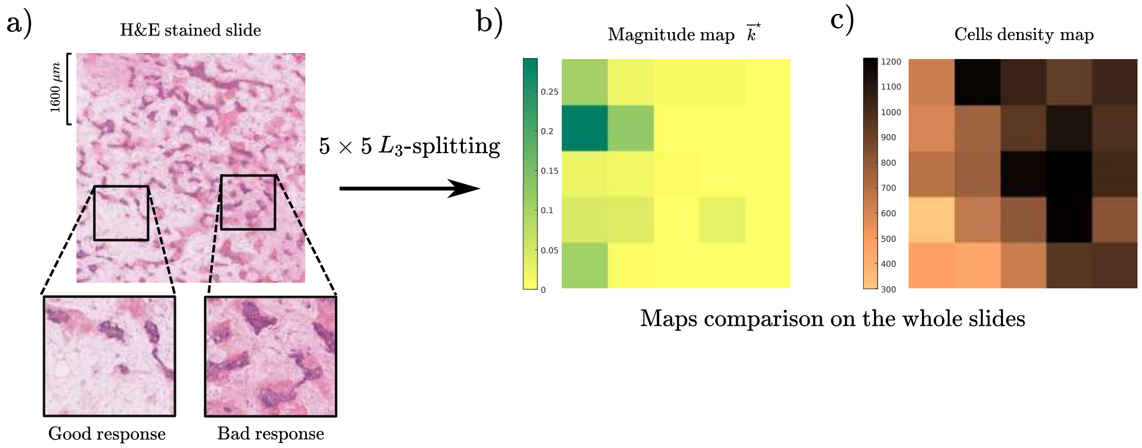

Patient 2:

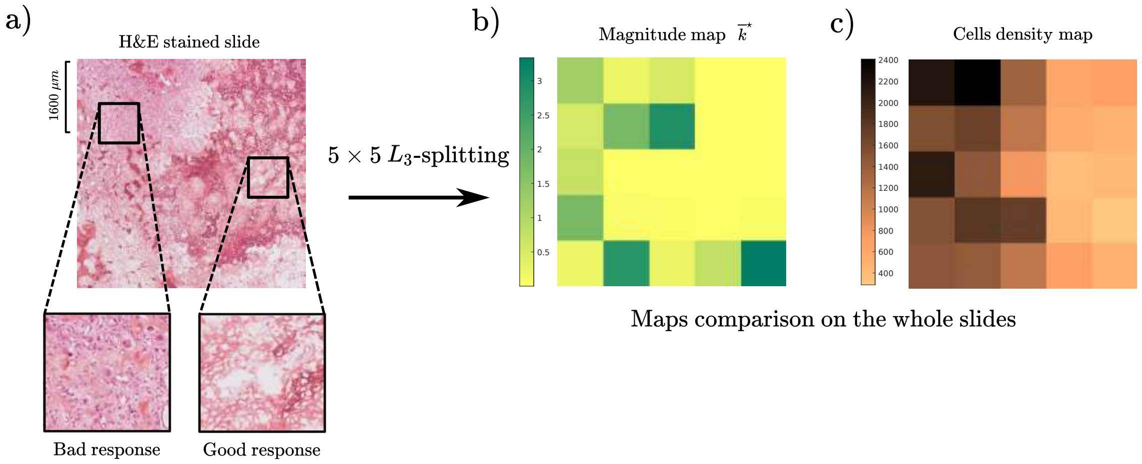

Figure 5.2: Comparison between permeability magnitude $\overline{k}^\star = \frac{\max \tilde{\mathbf{K}}}{(L_1/2)^2}$ (b) and cells density (mm^{-2}) (c) maps obtained from histological sections of resected osteosarcomas (a). Patient 1 exhibits a trabecular-like ECM microstructure and Patient 2 a lacy-like ECM microstructure (see zooms of the sections). Permeability maps are obtained with the extend-local 2-steps upscaling method with symmetric boundary conditions. We choose $L_3 = 8000\,\mathrm{px}$, $L_2 = 1600\,\mathrm{px}$, $L1 = 800\,\mathrm{px}$, $\delta = 100\,\mathrm{px}$. The fluid viscosity value is 0.001 Pa.s.

Now, complete histological data are investigated since histological cuts of 24 000 px × 24 000 px (or $1.1cm \times 1.1cm$) are studied. They also concern trabecular-like and lacy-like architecture as shown in figure 5.3. Similarly, permeability and cell density maps are established and permeability magnitude and cell density are correlated using Spearman coefficients.

To obtain the permeability map, we choose a purely local (since no information beyond 24 000 px is available) 2-steps uspcaling method together with the symmetric boundary conditions on a 3×3 L_3-paving.
For Patient 3, the correlation on the 3×3 splitting leads to a high p-value: a refinement of the calculation under a 5×5 splitting is needed (an extend-local method is considered just here with $\delta = 100\,\mathrm{px}$), showing a region of high permeability area together with a low cell density (see extreme right column) justified by a Spearman coefficient of -0.493 and a p-value of 0.013. The correlation coefficient sign is also conserved for Patient 4 sample and coarse splitting; given a good qualitative behavior (fig. 5.3 Patient 4) but a not so good quantitative response as the splitting is too coarse (Spearman coefficient of 0.251 with a p-value of 0.5 [1]). In this image variations in the quality of the staining are observed which alters most probably the results as

---

[1] p-value to high to be considered good.

it alters deeply the segmentation. More generally, the limiting factor to perform the numerical calculations is not the size of the image thanks to the sequential approach but the capacity to extract areas of interest with good enough imaging quality (good color contrast, no tearing, ...) which is not trivial to obtain on bone tissues, which are hard to cut and to stain.

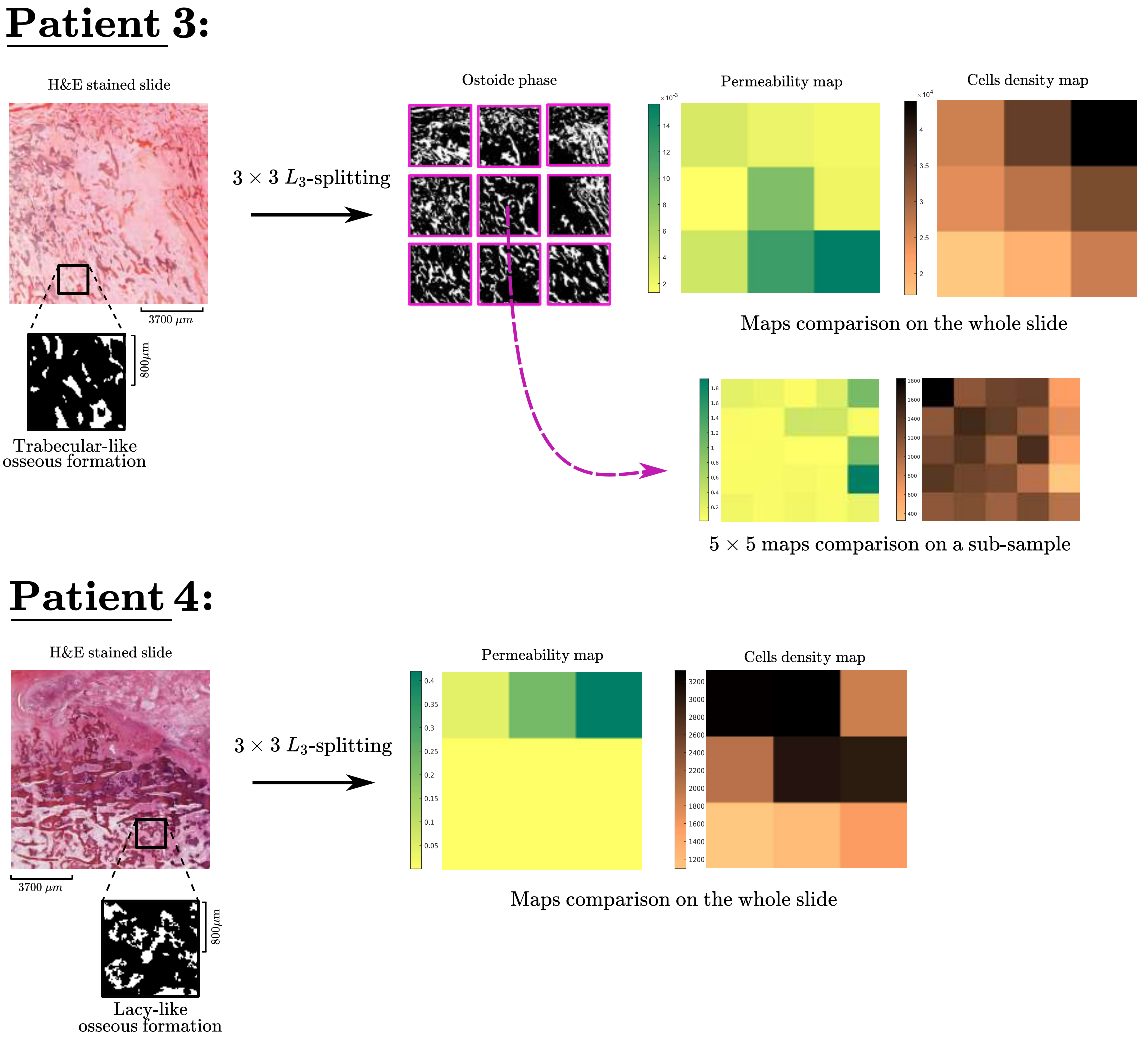

Figure 5.3: Correlation between permeabilty (px^2) and cells density (mm^{-2}) maps on 24 000 px × 24 000 px histological slides according to the two topology types; conserving the qualitative behavior and correlations sign of the previous study.

For this limited-size cohort of bad responders with spatial heterogeneity in response to treatment, results show treatments by chemotherapy are more efficient in lacy-like ECM regions compared to trabecular-like ECM regions. While this result must be confirmed on a larger cohort, this work shows that it is possible to match an area of good (resp. bad) response to the treatment, defined by a low (resp. high) cell presence, with an area of high or low ECM permeability. Therefore, ECM permeability can be seen as a potential mechano-biomarkers of the treatment response.

5.2.2 Structural mechanics study

The clinical question motivating the study of elasticity may be whether mechanical stimuli in osteosarcoma could lead to a change from anti-tumoral to pro-tumoral macrophages and vice versa. Thus, a response to treatment could indirectly depend on the stiffness of the extracellular matrix through its direct mechanical interaction with the cells.

We first consider two images corresponding to patient 2 and a subregion of patient 3 histological section. Size is 8000 px × 8000 px, corresponding to histological sections showing mixed response to treatment and respectively, trabecular and lacy-like osseous formations. Sections are shown in figure 5.4.

We consider a 2-step grid-block upscaling method. The set of scales is given by the couple $(L_1, L_2) = (800\,\text{px}, 1600\,\text{px})$. Concerning the elastic parameters, we consider Poisson's ratios such as $(\nu_{OECM}, \nu_{FECM}) = (0.3, 0.35)$ and Young's moduli such as $(E_{OECM}, E_{FECM}) = (500\,\text{MPa}, 50\,\text{kPa})$. A KUBC type boundary condition is first considered for the determination of the equivalent stiffness tensors at each scale (see chapter 4 section 4.1.1). The extend-local method is considered at the L_1-scale with $\delta = 100\,\text{px}$. We consider the trace of stiffness tensors, i.e. the sum of the diagonal coefficients, with Voigt's notation.

For patient 2 with a lacy-like ECM formation, we obtain a negative correlation with $r_s = -0.619$ and a p-value of 0.001, as shown in figure in 5.4. It means that an increase of tissue stiffness corresponds to a decrease in cell density. It is confirmed by distribution maps where the zone of higher stiffness (right side of the image) corresponds to the zone of low cell density.
For Patient 3 with a trabecular-like ECM formation, we obtain a positive correlation with $r_s = 0.26$ and a p-value of 0.020. Increased cell density is associated with higher stiffness.

Patient 2:

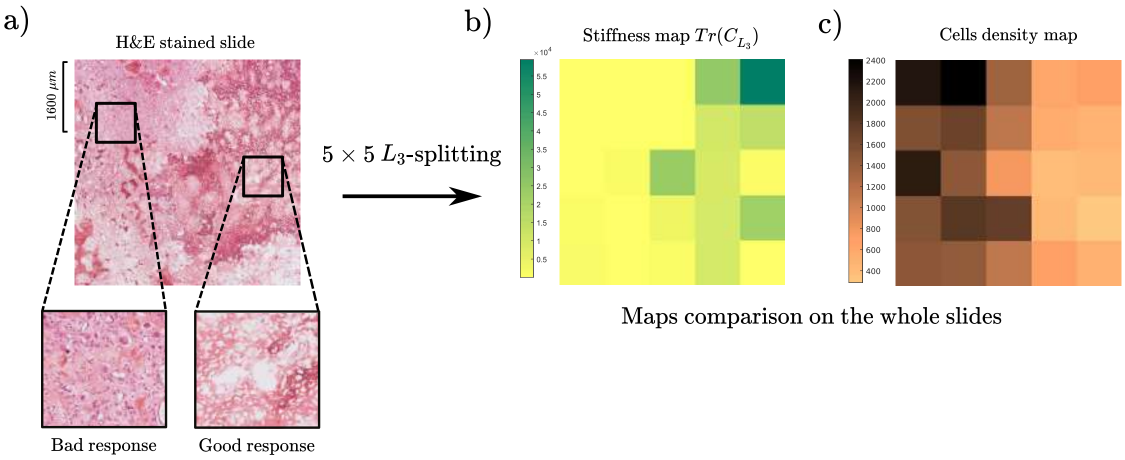

Patient 3:

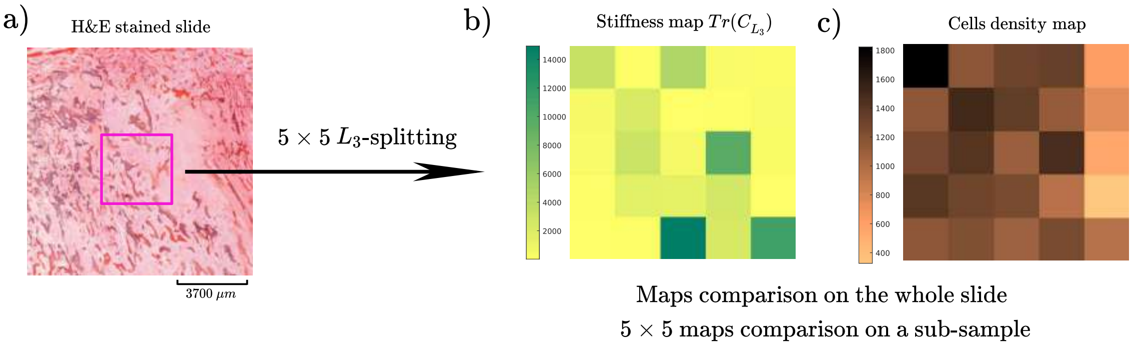

Figure 5.4: Comparison between the trace of equivalent stiffness tensor at the L_3-scale (in 10^4kPa) (b) and cells density (mm^{-2}) (c) maps obtained from histological sections of resected osteosarcomas. Patient 2 exhibits a lacy-like ECM microstructure and Patient 3 a trabecular-like ECM microstructure. Stiffness maps are obtained with the extend-local 2-steps upscaling method with KUBC boundary conditions. We choose $L_3 = 8000\,\text{px}$, $L_2 = 1600\,\text{px}$, $L1 = 800\,\text{px}$, $\delta = 100\,\text{px}$.

As previously, we consider larger images, i.e 24 000 px × 24 000 px. A 15 × 15 paving at the L_3-scale is implemented. The scales considered are $(L_1, L_2) = (800\,\text{px}, 1600\,\text{px})$. These sizes are less constrained than in flow calculations where percolation problems may appears for denser splitting. Figure 5.5 shows segmented images and obtained maps. Since no border around the images is accessible, the extend-local method is not applicable. Therefore, we consider SUBC type boundary conditions allowing a better characterization of the elastic properties within the framework of a purely local upscaling method at the L_1-scale.

For Patient 3 with a trabecular-like ECM formation, we obtain a positive correlation with $r_s = 0.508$ and a p-value of 10^{-16} (fig. 5.5 Patient 3).
For Patient 4 with a lacy-like ECM formation, we obtain a negative correlation with $r_s = -0.291$ and a p-value of 10^{-6} (fig. 5.5 Patient 4). Higher cell density is associated with decreased tissue stiffness.
Finally, signs of correlation coefficients are effectively consistent for larger images used in clinical routine.

Patient 3:

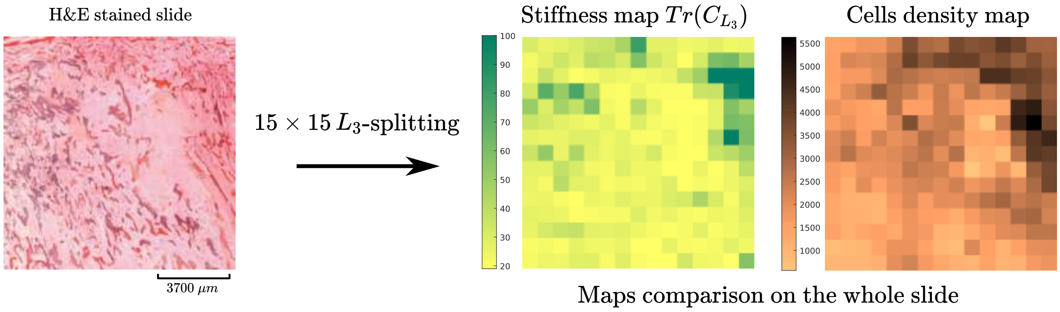

Patient 4:

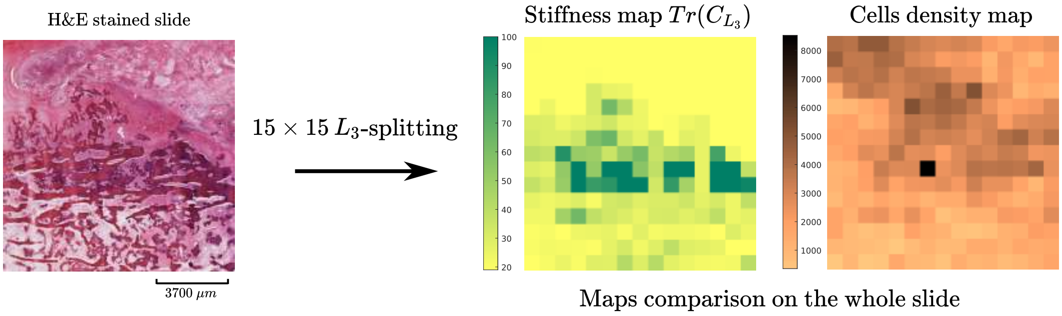

Figure 5.5: Comparison between the trace of equivalent stiffness tensor at the L_3-scale (in 10^4kPa) and cells density (mm^{-2}) maps obtained from 24 000 px × 24 000 px histological sections osteosarcomas. Patient 3 exhibits a trabecular-like ECM microstructure and Patient 4 a lacy-like ECM microstructure. Stiffness maps are obtained with the extend-local 2-steps upscaling method with SUBC boundary conditions. We choose $L_3 = 24\,000\,\text{px}$, $L_2 = 1600\,\text{px}$, $L1 = 800\,\text{px}$, $\delta = 100\,\text{px}$.

Thus, we again find a different response depending on the nature of the matrix. The analysis of the structural mechanics highlights the role of the stiffness of the ECM on the therapeutic response of patients. It is possible that the structural stress can activate a better immune response.

5.3 Conclusion and discussion on the mechano-biology

In this chapter, we correlated equivalent mechanical properties obtained by the upscaling workflow to the cell density evaluated on histological sections. To this purpose, we considered histological sections showing a mixed response to treatment according to the cell density present in the sections. This dual mechano-biological approach allows to explore the role of the osseous ECM on the response to treatment by linking the cellular and microenvironment scales.

By considering different physical problems, it is possible to differentiate their potential role on the response to treatment by highlighting the maximal correlation coefficients between various phenomena. In addition, transport and elasticity can be studied separately.

The structural mechanics analysis highlights the role of ECM stiffness on the patients therapy response. We found a significant negative correlation for lacy-like osseous ECM. Possible scenarios include the fact that structural strain may activate a better immune response. Concerning convective transport, results might be counter-intuitive in 2D when only architecture patterns are observed. Indeed, if we consider osseous ECM as a potential barrier to treatment, lacy-like structures seems to percolate with difficulties whereas trabecular-like structure are percolating media and response to chemotherapy is better in lower percolation areas. This remark may be related to the 2D nature of the data and validations should be done in 3D. In addition, this partial conclusion must be completed by the local role of fluid shear and substrate stretching on cell response and in particular on the immune ones. The presence and reactive role of microvascularization may be also significant and is not yet considered in this work.

Chapter 6

Conclusion and perspective

Motivated by open questions about osteosarcoma evolution and response to treatments, a robust mechanical model applied to bone tumors was proposed in this thesis, and an in-house numerical software was developed and validated. Such an approach is innovative, and explores, for the first time, the correlations between ECM and cell populations in a mechanical framework developed from patients histological images. From the methodological point of view, the literature about the characterisation of equivalent mechanical properties, in highly heterogeneous porous media with a pore scale resolution, is scarce. This thesis puts forward new models and numerical developments which may be adapted for other applications in porous media research. The relevance of a deterministic sequential Grid-Block upscaling method, coupled with an extend-local method for the pore scale problems resolution has been shown. A complete numerical validation of the coupling of these upscaling methods is proposed for the first time incorporating the accuracy of clinical histological slides for different physical problems such as transport and elasticity.

In the first chapter, a non-exhaustive review of the current knowledge of osteosarcoma is done at different spatial scales. A specific attention is paid to the description of osteosarcoma micro-environement, a scale at which this primary bone tumor can be seen as a heterogeneous porous medium. Potential links between spatio-temporal evolution of the tumors and mechanical effects are described in this chapter. Objectives of the thesis are then introduced.

In the second chapter, a review of the existing methods to model transport and elasticity in porous media is carried out. A special attention is paid to methods which can model physical systems in highly heterogeneous porous media where no separation of scales is observed. From the literature exploration, and in agreement with the specifications of our problem, we chose a grid-block upscaling method to take into account the intratumoral heterogeneity complexity in our approach. This method is based on the main results of the theoretical deterministic homogenization which are mainly developed in the literature for idealized geometries. In a second step, the use of an extend-local method was necessary to reduce the bias on the boundary conditions chosen for the grid-block method. Finally, given the size of the images, a sequential method was required to solve the problem of memory and computational limits.
The joint choice of these three methods drastically reduces the size and construction time of the meshes, makes it possible to process large images of patients follow-up on a on a standard PC in a reasonable time (minutes to few hours depending on the image size) and allows us to process highly heterogeneous porous media. The chapter ends with a description of the workflow used in the following of the manuscript.

In the third chapter, after the description of the transport model, we showed that the chosen upscaling process was consistent with the numerical and methodology parameters. The extend-local method, on incompressible Stokes flow, is shown to be sufficient to reduce the bias on the permeability tensor components due to different BCs; allowing a reduction of the error committed in this BCs choice at the higher scale. In addition, it was shown that this bias reduction is preserved by the sequential approach. While high precision convergence can not be reached be-

1-porosity model		2-porosity model	
Flow	Diffusion	Elasticity	Poroelasticity
Stokes flow (L_1) ↓ Darcy flow (L_2) ⋮ Darcy flow (L_N)	Diffusion (L_1) ↓ Diffusion (L_2) ⋮ Diffusion (L_N)	Hooke's law (L_1) ↓ Hooke's law (L_2) ⋮ Hooke's law (L_N)	Modified Hooke's law (L_1) ↓ Modified Hooke's law (L_2) ⋮ Modified Hooke's law (L_N)

Table 6.1: Table summarizing the models used for sequential grid-block upscaling method for each of the physics studied in this thesis.

Flow	Diffusion	Elasticity	Poroelasticity
$K_W^{diag} \leq K_S^{diag}, K_P^{diag} \leq K_{PL}^{diag}$	$D_W^{diag}, D_P^{diag} \leq D_{PL}^{diag}$	$\mathbf{C}_{SUBC} \leq \mathbf{C}_P \leq \mathbf{C}_{KUBC}$	$\mathbf{DC}_{SUBC} \leq \mathbf{DC}_{KUBC}$ *independent of fluid BCs

Table 6.2: Table summarizing the equivalent parameters inequalities, as a function of boundary conditions, found in the chapters 3 and 4 of this thesis. In the transport framework (flow and diffusive), the relations are diagonal coefficients while in the elastic and poroelastic frameworks the relations are quadratic.

cause of osteosarcoma geometry complexity, comparison between Direct Numerical Simulations performed at the pore scale for a domain at the L_3-scale and sequential grid-block simulations for the same domain, showed a very good agreement between the two approaches. Finally, the whole upscaling procedure is applied to the case of diffusive transport in osteosarcoma showing similar results.

In the fourth chapter, the upscaling methodology was applied to structural mechanics. We first examined the linear elasticity with small deformation. The extend-local method effectively reduces the BCs bias, a fact that was highlighted for the first time. In addition, the main results of the grid-block literature about the role of boundary conditions on the elasticity study, are preserved by the sequential methods. To finish, an extension of the workflow to poroelasticity is made, using the main results of the previous developments, i.e. momentum transport and elasticity.

A summary of the models used for the sequential Grid-Block upscaling in chapter 3 and 4 is illustrated on table 6.1. One of the main results obtained from these methodology developments is reported on table 6.2. Indeed, from this thesis, we could classify by inequalities the estimated equivalent properties as a function of the boundary conditions used for the sequential grid-block implementation.

In a final chapter, correlations between the equivalent mechanical properties of the ECM and the cell population density were found. The results highlight a variability in response to chemotherapy depending on the lacy-like or trabecular-like structure of the neo-formed bone tissue. In lacy-like ECM tumoral regions, areas of good (respectively bad) response were correlated with low (respectively high) permeability regions and high (respectively low) stiffness.

An opposite result was found for tumor regions with trabecular-like osseous ECM. The intratumoral variability in response to treatment corresponds most probably to underlying changes in the cell genome, immune microenvironment or vasculature [162, 163] for which ECM microarchitecture and mechanical properties may be a macroscopic marker. Indeed, the understanding of complex spatio-temporal coupling between osteoclasts [163], tumor cells, immune cells, angiogenesis and tumoral bone remodelling (osseous ECM) could benefit from quantitative mechanical approaches as developed in this thesis. For the available small cohort, it was shown that the proposed work-flow could be used to identify new mechano-biomarkers in heterogeneous tumors.

Because of the rarity of osteosarcoma (100-150 cases in France per year [1]) and of bad responders with spatially heterogeneous mixed response ($\leq 20\%$ patients on the Toulouse cohort), this study has been conducted on a limited size cohort as a proof of concept. The obvious extension of this work is to enlarge the cohort to confirm the findings of treatment response correlation to osseous ECM microstructure and equivalent parameters.

While the developed approach introduces numerous porous media concepts, the outputs, i.e. maps and correlation coefficients, of the in-house computational developments, are simple to manipulate. We hope that in a short term, this software can be used by biologists and clinicians to explore new questions. In particular, this methodology can be directly applied to immunohistology images, and changes in macrophages polarization due to mechanical effects could be explored at the tissue scale. Therefore, this approach could help in finding new targets for immunotherapy treatments of osteosarcoma. Numerical optimisation is ongoing to reach very short calculations time and increase the usage potential of the developed software.

In a longer term, additional physical problems will be implemented to explore further potential correlations between mechanics and response to treatment such as fully coupled poroelasticity or convection-diffusion mass transport with or without vascular network consideration. Some works addressed the convection-diffusion problem [164] and indicated that adapted grid-block upscaling method must be developed for this problem as the length scales cannot be taken arbitrarily anymore.

Moreover, acquisition of three dimensional cell-scale resolution data should be envisioned to solve the problem. The software is directly adaptable to 3D data and sequential upscaling will be very powerful to reduce the computational time, however acquisition of such data in mineralized tissues remains a challenge. A transition to 3D is even preferable for structural mechanics since the porosity associated with the osseous ECM phase will be interconnected and will not require any limiting assumptions.

Finally, the validation of the stationary model, which was intended above all to be explanatory, is a first step towards the implementation of more predictive spatio-temporal models which could take into account evolution equations of cell populations.

In conclusion, the developments of this thesis aims at integrating objective and quantifiable biomechanical parameters in the stratification of patients for a better therapeutic management. This work is at the crossroad between topics of high interest for cancer research such as the study of cell/ECM interaction, the role of mechanics in tumors, the quantification of heterogeneity in tumors. The methodology is generic and can be adapted to other types of physical problems, images or tumors.

---

[1] `https://www.gustaveroussy.fr/fr/osteosarcome`

Appendices

A Spectral radii behavior through the extend-local method in the flow case

In this section, we discuss the behavior of the spectral radii resulting form the extend-local process, shown in section 3.2.4.1 of the thesis (in the osteosarcoma case).

The fundamental difference between the impervious and open boundary conditions has a direct impact on the spectral radii as the extra-diagonal terms are taken into account in the diagonalisation process. For the impervious boundary conditions, their values become close quickly, i.e for small δ (fig. 1), as the diagonal and extra-diagonal terms have a similar behavior through the extend-local method. In opposition, computations with little bigger δ are needed to achieve an homogenization according to the three boundary condition (fig. 1) as the open boundary extra-diagonal terms are different since this condition allows transverse flows.

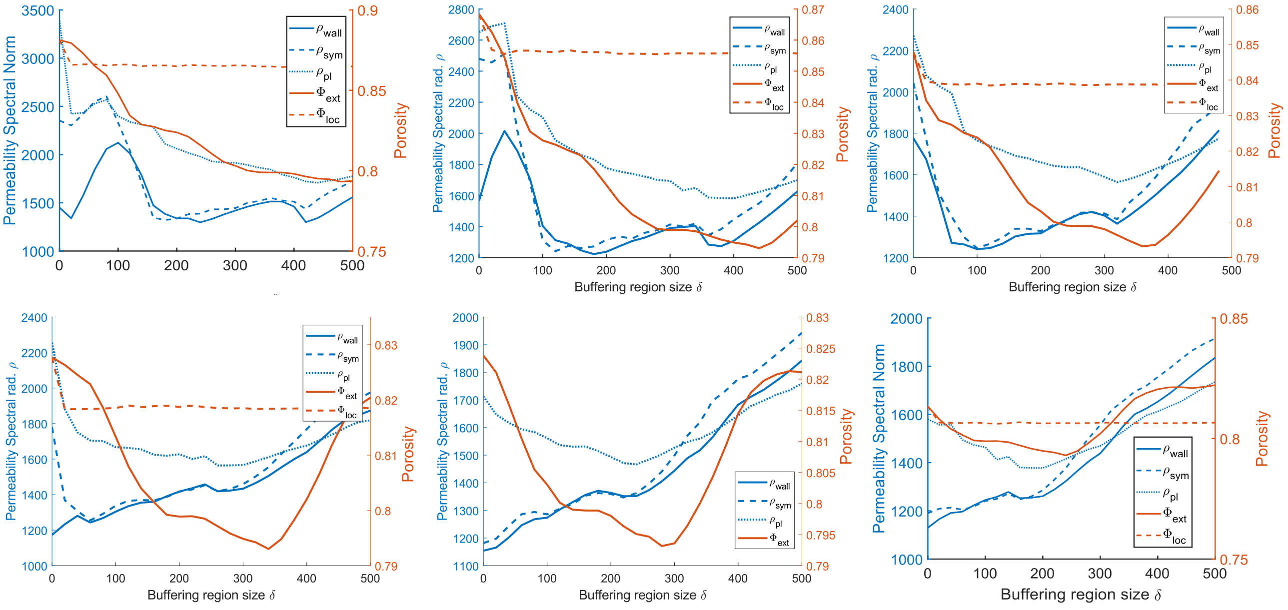

Figure 1: Behavior of the equivalent permeability spectral radius resulting from the extend-local method in function of δ. The study is conducted on multiple L_1-subcell size: 500 px, 600 px, 700 px, 800 px, 900 px and 1000 px.

B 2-steps method on Darcy type flow (2-porosity model)

In this section, we give additional information to the chapters 3 and 4. We study the two upscaling methodologies proposed in this manuscript namely the extend-local method and 2-steps grid-block process (see section 2.4) for a pore scale physical system comprising the 2-porosity osteosarcoma geometric paradigm (see chapter 4) and a Darcy type equation (momentum transport). We recall that the extend-local method considers a computational domain larger than the one to be upscaled with adding a neighboring region on which boundary conditions will be imposed. Also, the 2-step process corresponds to two successive grid-block upscaling.
To begin, we discuss the nature of the convergence of the extend-local approach for an incompressible Darcy equations on a 2-porosity osteosarcoma geometry, using two different fluid boundary conditions found in chapters 3 and 4, namely the wall (3.14) and open boundary condition (3.15). In a second part, we show that the 2-steps grid-block method is a consistent mechanistic approach for the above mentioned physical system in respect to its intrinsic parameters.

The hypothesis on the nature of the geometry and physic at each scale are: a) at the L_1-scale, an incompressible Darcy equation is considered with constant scalar permeability on each of the two phases of the geometry (translating an assumption of isotropy of these two phases) b) at higher scales, namely L_2 and L_3, the flow is again described by incompressible Darcy equations (3.4) and (3.10). Here, we exclude the use of periodical BC since not used in section 4.2. A continuity condition is considered for the field variables, at the L_1-scale, on $\partial_{int}\Omega$.
We choose for the following studies a permeability couple $(K_{OECM}, K_{FECM}) = (0.2, 2000)$.

B.1 Extend-local method study

We study the effects of the extend-local method on the permeability tensor in respect to the two boundary conditions and to the buffer zone size δ, at the L_1-scale. Specifically, we consider the response of the equivalent permeability tensor coefficients.

A $1000\,\text{px} \times 1000\,\text{px}$ osteosarcoma sample and neighboring region size $0 \leq \delta \leq 500\text{px}$ are chosen to carried out the numerical study (see fig. 2a). We plot the behavior of the coefficients as a function of the size of the buffering region δ for two BCs: the wall condition **W** is plot in red and the and open boundary condition **PL** in yellow.

We notice a homogenisation in the values of the diagonal terms (see fig. 2b), according to each BCs, for sufficiently large δ ($\geq 200\,\text{px}$). Note that results are sensitive to the buffering region size since no REV assumption is made.
The resulting extra-diagonal coefficients values for the **W** and **PL** boundary conditions does not seem to be becoming more homogeneous for any δ size (see fig. 2b). This come from the same reasons given in the chapter 3 (i.e that transverse flow can be allowed or not).
Consequently, for the 2-porosity model with a momentum transport physic, the extend-local method refines the permeability calculations in respect to the boundary conditions by smoothing out the diagonal coefficients.

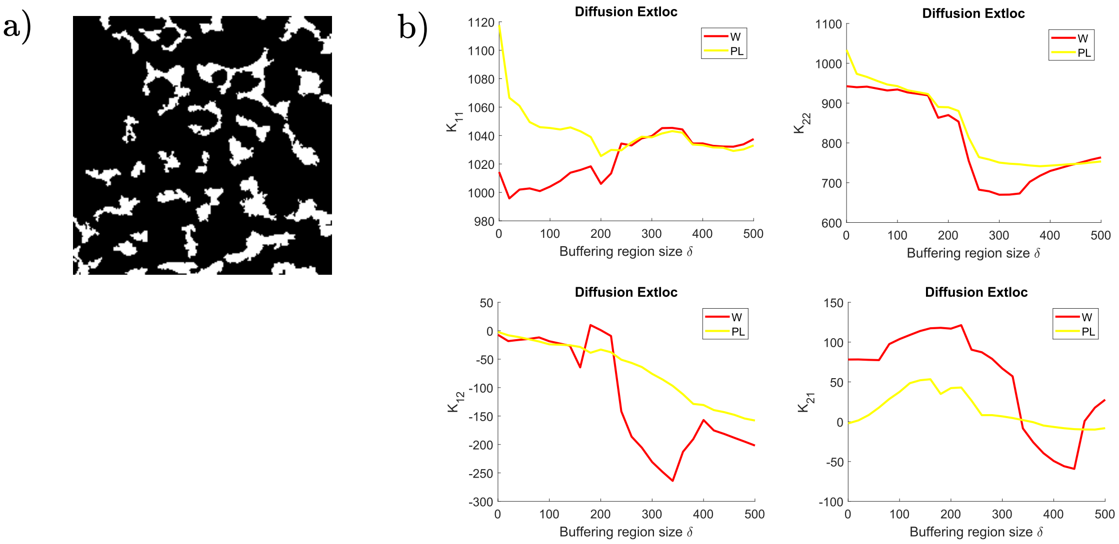

Figure 2: The extend-local method is applied on an osteosarcoma geometry when considering an incompressible Darcy type equation at the L_1-scale. a) Osteosarcoma geometry. b) Behavior of the equivalent permeability matrix coefficients, at the L_2-scale, in function of the buffer size and for two different boundary conditions (wall and open boundary).

B.2 Sequential upscaling method study

We now discuss the consistency of the 2-steps grid-block upscaling method applied to a Darcy equation at the L_1-scale on 2-porosity geometry. The L_1-splitting are ranging from 1×1 (i.e the 1-step method) to 5×5 and boundary condition are the wall **W** and the open boundaries **PL** ones (corresponding in fact to the parameter set in Chapter 4.2).
In this upscaling process, when considering incompressible Darcy equation at the L_1-scale, only incompressible Darcy type flow are found at the upper scales. Again, the BCs are chosen consistently at each scale. Without loss of generality, only one cell at the L_3 scale is considered and no symmetrization of the equivalent tensors is performed at each scale.
The geometry is a $5000\,\text{px} \times 5000\,\text{px}$ osteosarcoma binarised image (fig.3a). We study the equivalent properties at the L_3-scale such as matrices coefficients (fig.3b), spectral radii (fig.3c) and eigenvectors (fig.3d). The values arising from the **W** and **PL** conditions are respectively given in red and yellow, in function of the L_1-splitting.

Concerning diagonal coefficients, we recover the overestimation phenomenon for the **PL** condition and underestimation for the **W** condition (rather constant through splitting). The overall difference between the two BCs is due for the same reasons as stated in chapter 3 (impervious vs open boundaries). The extra-diagonal coefficient, show also the same behavior than previously found (rather erratic).
The spectral radii behavior follows the same pattern as the diagonal coefficients one, with the same difference in magnitude order between impervious and open conditions.
Finally, the principal directions are find consistent in respect to the two boundary condition and each splitting.

In conclusion, the 2-steps grid-block method is shown to be consistent even for the 2-porosity model in the momentum transport case.

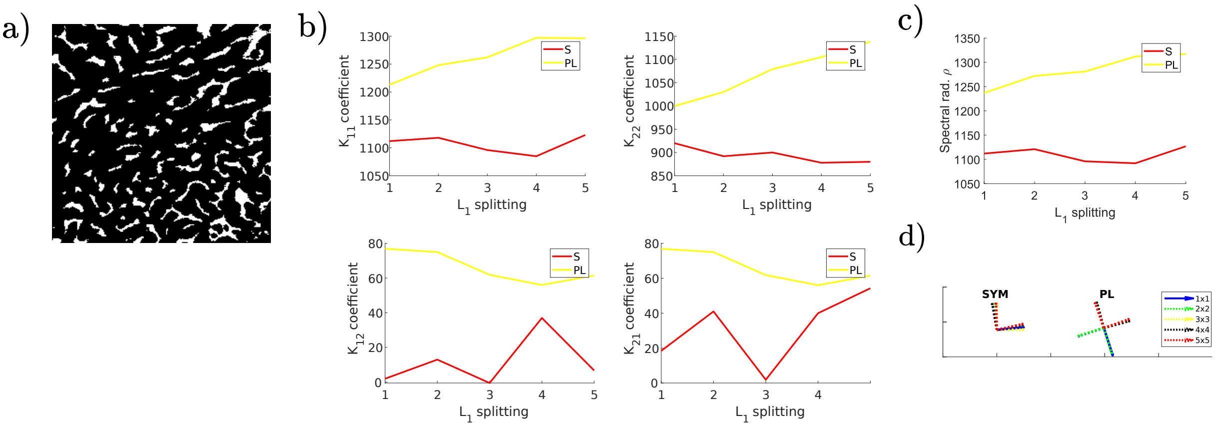

Figure 3: The 2-steps method is applied on a 5000 px × 5000 px osteosarcoma geometry in the incompressible Darcy equation case at the L_1-scale. a) Osteosarcoma binary image. b) Behavior of the equivalent matrix coefficients, at the L_3-scale, according to the L_1-splitting and for two boundary conditions (wall and open boundaries). c) Behavior of the equivalent spectral radii matrix extra-diagonal coefficients, at the L_3-scale, according to the L_1-splitting and for two boundary conditions (wall and open boundaries). d) Behavior of the principal permeability, at the L_3-scale, according to the L_1-splitting and for two boundary conditions (wall and open boundaries).

C Flow: coupling of the extend-local and sequential method on an osteosarcoma samples

Here, we give a relevant table comparison of the 1-steps, 2-steps local and 2-steps extend-local methods in the case of an $1600\,\text{px} \times 1600\,\text{px}$ osteosarcoma sample (fig. 4a). A 2×2 L_1-splitting is considered resulting in $L_1 = 800\,\text{px}$ (fig. 4b).

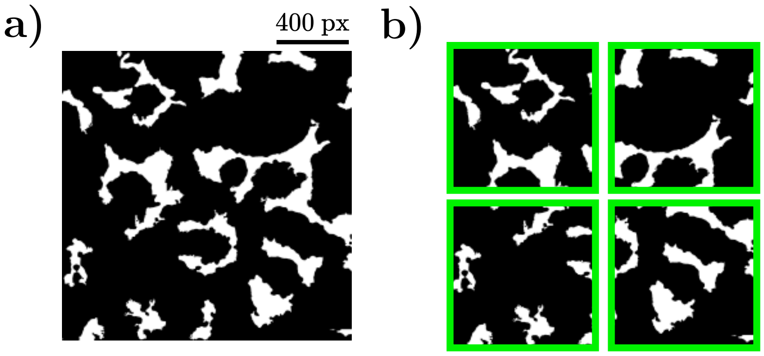

Figure 4: Geometrical consideration for the application of the 2-steps method. a) Binary image. b) The L_1-splitting considered for the methods comparison.

The non-dimensionalized permeability diagonal tensors and magnitudes resulting from the 1-step and 2-step upscaling methods are presented in the table 3.
The non-dimensionalized permeability magnitude $\overline{k}^\star == (L_1/2)^{-2} \max_{1 \leq i,j \leq 2} \overline{\mathbf{K}}_{ij}$ for the 1-step, 2-step and 2-step extend-local methods shows that the latter method still reduces the biases of the BCs at the L_3-scale. Indeed, the 2-step extend-local method induces on the magnitudes an error relative to the mean value of 18% when choosing $\delta = 100\,\text{px}$. In contrast, the overall heterogeneity on the magnitudes can reach 30% and 40% for the 1-step and local 2-step methods, respectively.
One show that a 2-steps grid-block upscaling method, coupled with an extend-local method at the L_1-scale, reduce the bias on the diagonal term of the L_3-scale equivalent permeability tensor, even in the osteosarcoma case (compared to a 1-step or 2-step local method).

(a) Permeability tensor components and magnitude obtained by the 1-step and the 2-steps upscaling scheme with either a local or a extend-local method for the first upscaling step.

	1-step upscaling			2-steps upscaling (local)			2-steps upscaling (ext-local)		
	W	S	PL	W	S	PL	W	S	PL
$\overline{k}^\star$	$2.72e-2$	$3.15e-2$	$4.45e-2$	$2.88e-2$	$3.33e-2$	$5.48e-2$	**2.95e-2**	**3.00e-2**	**3.89e-2**
$\tilde{K}_{22}$	$1.32e-2$	$1.61e-2$	$3.19e-2$	$2.29e-2$	$2.625e-2$	$5.19e-2$	$1.77e-2$	$1.82e-2$	$2.96e-2$

Table 3: Permeability tensor components and magnitude obtained by the 1-step and the 2-steps upscaling scheme with either a local or a extend-local method for the first upscaling step, considering the three different boundary conditions **W**, **S** and **PL**.

D A statistical study of a large 2D osteosarcoma samples

Here, we investigate a possible statistical characterisation of osteosarcoma. Considering denser L_1-grids ranging form 4×4 to 16×16 allows us to explore statistical properties at the L_2-scale in respect to the splitting and boundary condition. This will only be used as an example but not as a general observation since two distinct osteosarcoma regions will have different statistical properties [2].

To do so, the study is based on a 16 000 px × 16 000 px osteosarcoma geometry, coming from a segmentation/binarization of a H&E histological section from a bad reponder patient (fig. 3.24). As previously mentioned, we will consider only one cell at the L_3-scale without any loss of generality. Here the periodic condition is discarded as the construction of the meshes on GMSH for such geometries reach the limit of the available computers.
We study the statistics of the equivalent permeability matrix coefficients arising from the first upscaling according to each L_1-splitting and boundary conditions (fig. 5 and 6).

By analyzing the frequency of value appearance (values of coefficients in abscissa and occurrences in ordinate), we notice the same behavior of the permeability tensor coefficients with the boundary conditions.
The diagonal coefficients have approximately the same distribution through the three BCs and three splitting, i.e a normal distribution with a skweness to the left as a negative sign is not possible [3].
Moreover, a histogram configuration similar to normal distribution with no skweness appears for extra-diagonal terms (fig. 6b and c).

Concerning the effect of boundary condition, diagonal coefficients have the same behavior as in the small images case. There is always the phenomenon of overestimation for the open boundary condition, underestimation for the wall condition and quasi-constancy in the symmetrical case. The magnitudes of the differences between each BCs do not vanish even when considering larger images. Same goes for extra-diagonal terms but with smaller difference magnitude.

---

[2] Anecdotally, it is interesting to see if the effects of boundary conditions fade at the L_3-scale when considering larger images.

[3] In the diagonal term, some values appear negative but are in fact close to the numerical zero (of order 10^{-14}).

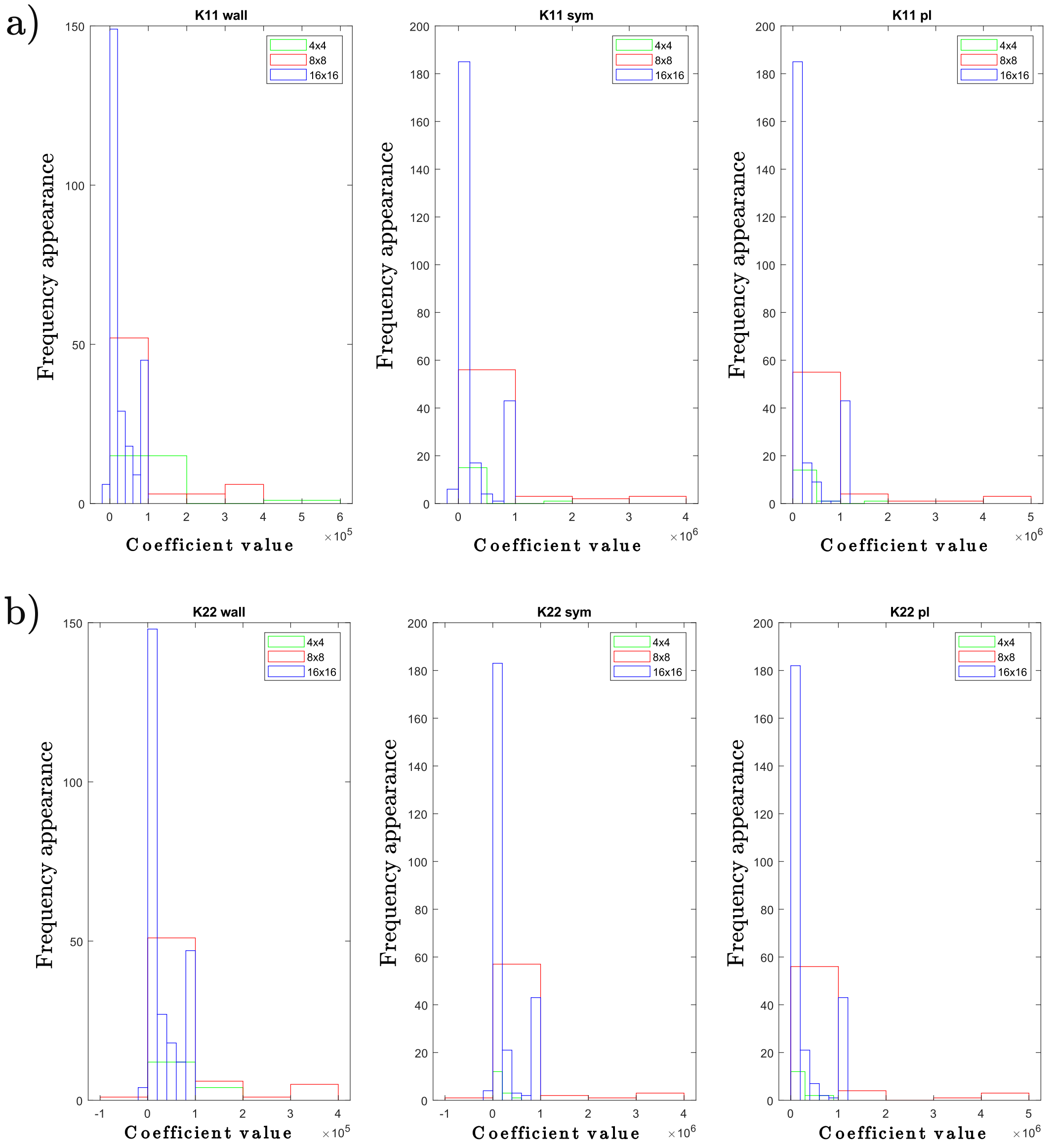

Figure 5: Histogram, for a 16 000 px × 16 000 px and a 4 × 4, 8 × 8 and 16 × 16 L_1-splittings, on the resulting diagonal coefficients of the equivalent permeability tensors at the L_2-scale in respect to the three boundaries condition: wall, symmetry and open boundary condition (column 1, 2 and 3 respectively). Graphs show occurrences as a function of coefficient values. a) Statistics of the K_{11} coefficient. b) Statistics of the K_{22} coefficient.

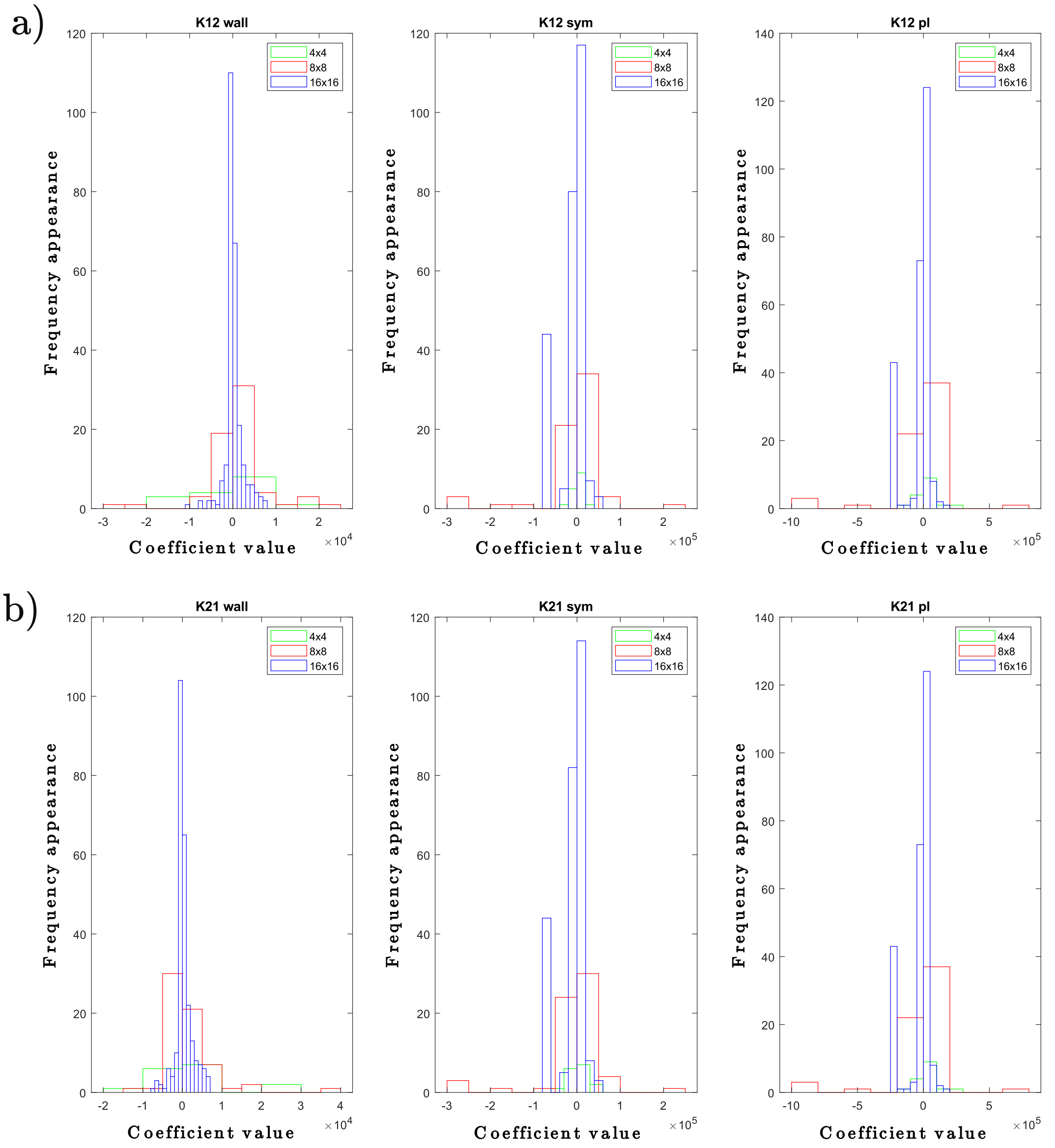

Figure 6: Histogram, for a 16 000 px × 16 000 px and a 4×4, 8×8 and 16×16 L_1-splittings, on the resulting extra-diagonal coefficients of the equivalent permeability tensors at the L_2-scale in respect to the three boundaries condition: wall, symmetry and open boundary condition (column 1, 2 and 3 respectively). Graphs show occurrences as a function of coefficient values.a) Statistics of the K_{12} coefficient. b) Statistics of the K_{21} coefficient.

List of Figures

List of Tables

Bibliography

[1] C.D.M. Fletcher, J.A. Bridge, P. Hogendoorn, and F. Mertens. *WHO Classification of Tumours of Soft Tissue and Bone. Fourth Edition. IARC WHO Classification of Tumours, No 5.* 2013.

[2] Lisa Mirabello, Rebecca Troisi, and Sharon Savage. Osteosarcoma incidence and survival rates from 1973 to 2004 data from the surveillance, epidemiology, and end results program. *Cancer*, 115:1531–43, 02 2009.

[3] Jörg Ritter and S.S. Bielack. Osteosarcoma. *Annals of oncology : official journal of the European Society for Medical Oncology / ESMO*, 21 Suppl 7:vii320–5, 10 2010.

[4] Emanuela Palmerini, Stefano Ferrari, Franco Bertoni, and Gaetano Bacci. Prognosis of radiation-induced bone sarcoma is similar to primary osteosarcoma. *Clinical orthopaedics and related research*, 462:255; author reply 255–6, 10 2007.

[5] Paul A. Meyers and Richard Gorlick. Osteosarcoma. *Pediatric Clinics of North America*, 44(4):973–989, 1997.

[6] A. Bouffier A. Gomez-brouchet, P. Assemat. Master 2 dissertation: Etude des hétérogénéités de l'ostéosarcome: de l'histologie à l'identification de mécano-marqueurs.

[7] G. Cases A. Gomez-brouchet. Etude de la distribution spatiale du microenvironnement immunitaire dans les ostéosarcomes et corrélations aux données de l'imagerie. *Médecine spécialisée, Université Toulouse III - Paul Sabatier*, 2021.

[8] P Casali, N Abecassis, Sebastian Bauer, R Biagini, S Bielack, Sylvie Bonvalot, Ioannis Boukovinas, Judith Bovee, T Brodowicz, Javier Martin-Broto, Angela Buonadonna, E Álava, Angelo Tos, X Muro, Palma Dileo, Mikael Eriksson, A Fedenko, V Ferraresi, A Ferrari, and Jean-Yves Blay. Soft tissue and visceral sarcomas: Esmo-euracan clinical practice guidelines for diagnosis, treatment and follow-up. *Annals of oncology : official journal of the European Society for Medical Oncology*, 29, 05 2018.

[9] Anja Lütke, Paul Meyers, Ian Lewis, and Heribert Jürgens. Osteosarcoma treatment - where do we stand? a state of the art review. *Cancer treatment reviews*, 40, 11 2013.

[10] Anne Gomez-Brouchet, Julia Gilhodes, Nathalie Van Acker, Regis Brion, Corinne Bouvier, Pauline Assemat, Nathalie Gaspar, Sebastien Aubert, Jean-Marc Guinebretiere, Beatrice Marie, Frederique Larousserie, Natacha Entz-Werlé, Gonzague De Pinieux, Eric Mascard, Francois Gouin, Pierre Brousset, Marie-Dominique Tabone, Marta Jimenez, Marie-Cecile Le Deley, Jean-Yves Blay, Laurence Brugieres, Sophie Piperno-Neumann, and Francoise Rédini. Characterization of macrophages and osteoclasts in the osteosarcoma tumor microenvironment at diagnosis: New perspective for osteosarcoma treatment? *Cancers*, 13(3), 2021.

[11] Jason A. Somarelli. The hallmarks of cancer as ecologically driven phenotypes. *Frontiers in Ecology and Evolution*, 9:226, 2021.

[12] Douglas Hanahan and Robert Weinberg. Hallmarks of cancer: The next generation. *Cell*, 144:646–74, 03 2011.

[13] Steinar Evje and Jahn Waldeland. How tumor cells possibly can make use of interstitial fluid flow in a strategy for metastasis. *Cellular and Molecular Bioengineering*, 03 2019.

[14] Claudia Mierke. The fundamental role of mechanical properties in the progression of cancer disease and inflammation. *Reports on Progress in Physics*, 77:076602, 07 2014.

[15] Adrian Shieh. Biomechanical forces shape the tumor microenvironment. *Annals of biomedical engineering*, 39:1379–89, 05 2011.

[16] Letícia Charelli, João Ferreira, Carolina Naveira-Cotta, and Tiago Balbino. Engineering mechanobiology through organoids-on-chip:a strategy to boost therapeutics. *Journal of Tissue Engineering and Regenerative Medicine*, 15, 08 2021.

[17] Mustafa Unal, Yunus Alapan, Hao Jia, Adrienn Varga, Keith Angelino, Mahmut Aslan, Ismail Sayin, Chanjuan Han, Yanxia Jiang, Zhehao Zhang, and Umut Gurkan. Micro and nano-scale technologies for cell mechanics. *Nanobiomedicine*, 1, 10 2014.

[18] D. Gianferante, Lisa Mirabello, and Sharon Savage. Germline and somatic genetics of osteosarcoma — connecting aetiology, biology and therapy. *Nature Reviews Endocrinology*, 13, 03 2017.

[19] Xiang Chen, Armita Bahrami, Alberto Pappo, John Easton, James Dalton, Erin Hedlund, David Ellison, Sheila Shurtleff, Gang Wu, Lei Wei, Matthew Parker, Michael Rusch, Panduka Nagahawatte, Jianrong Wu, Shenghua Mao, Kristy Boggs, Heather Mulder, Donald Yergeau, Charles Lu, and Michael Dyer. Recurrent somatic structural variations contribute to tumorigenesis in pediatric osteosarcoma. *Cell reports*, 7, 04 2014.

[20] Ruxandra Barbulescu and Daniel Ioan. Multi-scale and reduced modelling of biological systems. *2015 9th International Symposium on Advanced Topics in Electrical Engineering, ATEE 2015*, pages 597–602, 06 2015.

[21] Franck Verrecchia and Françoise Rédini. Transforming growth factor-β signaling plays a pivotal role in the interplay between osteosarcoma cells and their microenvironment. *Frontiers in Oncology*, 8:133, 04 2018.

[22] Anwar Padhani, Guoying Liu, Dow-Mu Koh, Thomas Chenevert, Harriet Thoeny, Taro Takahara, Andrew Dzik-Jurasz, Brian Ross, Marc Van Cauteren, David Collins, Dima Hammoud, Gordon Rustin, Bachir Taouli, and Peter Choyke. Diffusion-weighted magnetic resonance imaging as a cancer biomarker: Consensus and recommendations. *Neoplasia (New York, N.Y.)*, 11:102–25, 02 2009.

[23] Paul Lu, Valerie Weaver, and Zena Werb. The extracellular matrix: A dynamic niche in cancer progression. *Journal of Experimental Medicine*, 209:i1–i1, 03 2012.

[24] Michael W. Pickup, Janna K. Mouw, and Valerie M. Weaver. The extracellular matrix modulates the hallmarks of cancer. *EMBO reports*, 15:1243 – 1253, 2014.

[25] Paolo Netti, David Berk, Melody Swartz, Alan Grodzinsky, and R Jain. Netti pa, berk da, swartz ma, grodzinsky aj, jain rkrole of extracellular matrix assembly in interstitial transport in solid tumors. cancer res 60: 2497-2503. *Cancer research*, 60:2497–503, 06 2000.

[26] Erik Henke, Rajender Nandigama, and Süleyman Ergün. Extracellular matrix in the tumor microenvironment and its impact on cancer therapy. *Frontiers in Molecular Biosciences*, 6, 01 2020.

[27] Longshuai Lin, Kai Huang, Weihong Guo, Chenghao Zhou, Gangyang Wang, and Qinghua Zhao. Conditioned medium of the osteosarcoma cell line u2os induces hbmscs to exhibit characteristics of carcinoma-associated fibroblasts via activation of il-6/stat3 signaling. *Journal of biochemistry*, 168, 04 2020.

[28] Angiogenesis process in osteosarcoma: An updated perspective of pathophysiology and therapeutics. *The American Journal of the Medical Sciences*, 357(4):280–288, 2019.

[29] Marina Pierrevelcin, Fuchs Quentin, Benoit Lhermitte, Melissa Messé, Eric Guerin, Noelle Weingertner, Sophie Martin, Isabelle Lelong-Rebel, Charlotte Nazon, Monique Dontenwill, and Natacha Entz-Werle. Focus on hypoxia-related pathways in pediatric osteosarcomas and their druggability. *Cells*, 9:1998, 08 2020.

[30] D. Zhang et al. Hypoxia promotes osteosarcoma cell proliferation and migration through enhancing platelet-derived growth factor-bb/platelet-derived growth factor receptor-β axis. *Biochemical and Biophysical Research Communications*, 512(2):360–366, 2019.

[31] Richert Iseulys and Aurélie Dutour. *The immune environment of bone sarcomas*, pages 189–203. 01 2022.

[32] Heymann Marie-Françoise, Frédéric Lézot, and Dominique Heymann. The contribution of immune infiltrates and the local microenvironment in the pathogenesis of osteosarcoma. *Cellular Immunology*, 343, 11 2017.

[33] Anne Gomez-Brouchet, Claire Illac, Julia Gilhodes, Corinne Bouvier, Sébastien Aubert, Jean-Marc Guinebretiere, Béatrice Marie, Frédérique Larousserie, Natacha Entz-Werlé, Gonzague de Pinieux, Thomas Filleron, Véronique Minard, Vincent Minville, Eric Mascard, François Gouin, Marta Jimenez, Marie-Cécile Ledeley, Sophie Piperno-Neumann, Laurence Brugieres, and Françoise Rédini. Cd163-positive tumor-associated macrophages and cd8-positive cytotoxic lymphocytes are powerful diagnostic markers for the therapeutic stratification of osteosarcoma patients: An immunohistochemical analysis of the biopsies from the french os2006 phase 3 trial. *OncoImmunology*, 6(9):e1331193, 2017.

[34] S Piperno-Neumann, MC Le Deley, F Rédini, H Pacquement, P Marec-Bérard, P Petit, H Brisse, C Lervat, JC Gentet, N Entz-Werlé, A Italiano, N Corradini, E Bompas, N Penel, MD Tabone, A Gomez-Brouchet, JM Guinebretière, E Mascard, F Gouin, A Chevance, N Bonnet, JY Blay, L Brugières, Sarcoma Group of UNICANCER, French Society of Pediatric Oncology (SFCE), and French Sarcoma Group (GSF-GETO). Zoledronate in combination with chemotherapy and surgery to treat osteosarcoma (os2006): a randomised, multicentre, open-label, phase 3 trial. *The Lancet Oncology*, 17(8):1070–1080, 2016-08-01 00:00:00.001.

[35] Maya Kansara, Kristian Thomson, Puiyi Pang, Aurélie Dutour, Lisa Mirabello, Francine Acher, Jean-Philippe Pin, Elizabeth Demicco, Yan Juming, Michele Teng, Mark Smyth, and David Thomas. Infiltrating myeloid cells drive osteosarcoma progression via grm4 regulation of il23. *Cancer Discovery*, 9:CD–19, 09 2019.

[36] Rong Cai, Naoki Kawazoe, and Guoping Chen. Influence of surfaces modified with biomimetic extracellular matrices on adhesion and proliferation of mesenchymal stem cells and osteosarcoma cells. *Colloids and Surfaces B: Biointerfaces*, 126:381–386, 2015.

[37] Stephen C. Cowin. Bone poroelasticity. *Journal of Biomechanics*, 32(3):217–238, 1999.

[38] Dimitrios Hadjidakis and Ioannis Androulakis. Bone remodeling. *Annals of the New York Academy of Sciences*, 1092:385–96, 01 2007.

[39] Isabel F Tresguerres, Miguel Alobera, Mariano Pingarron, and Luis Blanco. Physiological bases of bone regeneration ii. the remodeling process. *Medicina oral, patología oral y cirugía bucal*, 11:E151–7, 04 2006.

[40] Charles H. Turner. Three rules for bone adaptation to mechanical stimuli. *Bone*, 23 5:399–407, 1998.

[41] Iain Kalfas. Principles of bone healing. *Neurosurgical focus*, 10:E1, 02 2001.

[42] Elisabeth H. Burger, Jenneke Klein-Nulend, and Stephen C. Cowin. Mechanotransduction in bone. In *Molecular and Cellular Biology of Bone*, volume 5 of *Advances in Organ Biology*, pages 123–136. Elsevier, 1998.

[43] Christopher Jacobs, Sara Temiyasathit, and Alesha Castillo. *Osteocyte Mechanobiology and Pericellular Mechanics*, volume 12, pages 369–400. 08 2010.

[44] Lei Qin, Wen Liu, Huiling Cao, and Guozhi Xiao. Molecular mechanosensors in osteocytes. *Bone Research*, 8, 12 2020.

[45] Yi-Xian Qin, Clinton Rubin, and Kenneth Mcleod. Nonlinear dependence of loading intensity and cycle number in the maintenance of bone mass and morphology. *Journal of orthopaedic research : official publication of the Orthopaedic Research Society*, 16:482–9, 07 1998.

[46] Claudia Wittkowske, Gwendolen Reilly, Damien Lacroix, and Cecile Perrault. In vitro bone cell models: Impact of fluid shear stress on bone formation. *Frontiers in Bioengineering and Biotechnology*, 4, 11 2016.

[47] Andrew Ahn and Alan Grodzinsky. Relevance of collagen piezoelectricity to ”wolff’s law”: A critical review. *Medical engineering & physics*, 31:733–41, 04 2009.

[48] Rakesh Jain, John Martin, and Triantafyllos Stylianopoulos. The role of mechanical forces in tumor growth and therapy. *Annual review of biomedical engineering*, 16:321–46, 07 2014.

[49] Claudia Wittkowske, Gwendolen Reilly, Damien Lacroix, and Cecile Perrault. In vitro bone cell models: Impact of fluid shear stress on bone formation. *Frontiers in Bioengineering and Biotechnology*, 4, 11 2016.

[50] Rakesh K. Jain. Barriers to drug delivery in solid tumors. *Scientific American*, 271(1):58–65, 1994.

[51] Gabriel Helmlinger, Paolo Netti, Hera Lichtenbeld, Robert Melder, and Rakesh Jain. Solid stress inhibits the growth of multicellular tumor spheroids. *Nature biotechnology*, 15:778–83, 09 1997.

[52] S. S. Nathan, G. DiResta, Jorge E. Casas-Ganem, B. Hoang, R. Sowers, Rui Yang, A. Huvos, R. Gorlick, and J. Healey. Elevated physiologic tumor pressure promotes proliferation and chemosensitivity in human osteosarcoma. *Clinical Cancer Research*, 11:2389 – 2397, 2005.

[53] Behzad Ghanbarian, Allen Hunt, Robert Ewing, and Muhammad Sahimi. Tortuosity in porous media: A critical review. *Soil Science Society of America Journal*, 77:1461, 09 2013.

[54] John H. Cushman, Lynn S. Bennethum, and Bill X. Hu. A primer on upscaling tools for porous media. *Advances in Water Resources*, 25(8):1043–1067, 2002.

[55] Qingrong Xiong, Todor Baychev, and Andrey Jivkov. Review of pore network modelling of porous media: Experimental characterisations, network constructions and applications to reactive transport. *Journal of Contaminant Hydrology*, 192, 07 2016.

[56] Jianlin Zhao, Feifei Qin, Dominique Derome, Qinjun Kang, and Jan Carmeliet. Improved pore network models to simulate single-phase flow in porous media by coupling with lattice boltzmann method. *Advances in Water Resources*, 145:103738, 2020.

[57] Sanchez-Palencia E. Solutions périodiques par rapport aux variables d’espaces et applications. *C R Acad Sci Paris, Sér A–B 1970;271:A1129–32.*

[58] Stephen Whitaker. *The Method of Volume Averaging.* 01 1999.

[59] G. Marsily. Quantitative hydrogeology: Groundwater hydrology for engineers. 1986.

[60] J. Bear. Dynamics of fluids in porous media. dover publications, inc., new york. 1972.

[61] W.J. Drugan and J.R. Willis. A micromechanics-based nonlocal constitutive equation and estimates of representative volume element size for elastic composites. *Journal of the Mechanics and Physics of Solids*, 44(4):497–524, 1996.

[62] R. Hill. Elastic properties of reinforced solids: Some theoretical principles. *Journal of the Mechanics and Physics of Solids*, 11(5):357–372, 1963.

[63] T. Kanit, S. Forest, I. Galliet, V. Mounoury, and D. Jeulin. Determination of the size of the representative volume element for random composites: statistical and numerical approach. *International Journal of Solids and Structures*, 40(13):3647–3679, 2003.

[64] Yohan Davit, Christopher G. Bell, Helen M. Byrne, Lloyd A.C. Chapman, Laura S. Kimpton, Georgina E. Lang, Katherine H.L. Leonard, James M. Oliver, Natalie C. Pearson, Rebecca J. Shipley, Sarah L. Waters, Jonathan P. Whiteley, Brian D. Wood, and Michel Quintard. Homogenization via formal multiscale asymptotics and volume averaging: How do the two techniques compare? *Advances in Water Resources*, 62:178 – 206, 2013. A tribute to Stephen Whitaker.

[65] Yalchin Efendiev, L. Durlofsky, and S. Lee. Modeling of subgrid effects in coarse-scale simulations of transport in heterogeneous porous media. *Water Resources Research - WATER RESOUR RES*, 36, 08 2000.

[66] Régis Cottereau. A stochastic-deterministic coupling method for multiscale problems. application to numerical homogenization of random materials. *Procedia IUTAM*, 6:35 – 43, 2013. IUTAM Symposium on Multiscale Problems in Stochastic Mechanics.

[67] Yohan Davit, Christopher Bell, Helen Byrne, Lloyd Chapman, Laura Kimpton, Georgina Lang, Katherine Neßler, James Oliver, Natalie Pearson, Rebecca Shipley, Sarah Waters, Jonathan Whiteley, Brian Wood, and Michel Quintard. Homogenization via formal multiscale asymptotics and volume averaging: How do the two techniques compare? *Advances in Water Resources*, 62:178–206, 12 2013.

[68] Jean-Louis Auriault, Claude Boutin, and Christian Geindreau. *Homogénéisation de phénomènes couplés en milieux hétérogènes. T I: Diffusion et Dispersion.* 04 2009.

[69] Pascale Royer. *Homogénéisation de phénomènes de transport en milieux poreux et milieux composites Comportements macroscopiques et domaines de validité.* 2016.

[70] Stéphanie Veran, Yvan Aspa, and Michel Quintard. Effective boundary conditions for rough reactive walls in laminar boundary layers. *International Journal of Heat and Mass Transfer*, 52(15):3712–3725, 2009.

[71] Yohan Davit and Michel Quintard. Technical notes on volume averaging in porous media i: How to choose a spatial averaging operator for periodic and quasiperiodic structures. *Transport in Porous Media*, 119:1–30, 09 2017.

[72] Stephen Whitaker. Flow in porous media i: A theoretical derivation of darcy's law. *Transport in Porous Media*, 1:3–25, 03 1986.

[73] Jean-Louis Auriault. Heterogeneous periodic and random media. are the equivalent macroscopic descriptions similar? *International Journal of Engineering Science - INT J ENG SCI*, 49:806–808, 08 2011.

[74] Ray M. Bowen. *Porous Media Model Formulations by the Theory of Mixtures*, pages 63–119. Springer Netherlands, Dordrecht, 1984.

[75] D. Stroud. Generalized effective-medium approach to the conductivity of an inhomogeneous material. *Phys. Rev. B*, 12:3368–3373, Oct 1975.

[76] G. Nguetseng. A general convergence result for a functional related to the theory of homogenization. *Siam Journal on Mathematical Analysis*, 20:608–623, 1989.

[77] Majid Hassanizadeh and William G Gray. General conservation equations for multi-phase systems: 1. averaging procedure. *Advances in Water Resources*, 2:131–144, 1979.

[78] Maria Bruna and Stephen Chapman. Diffusion in spatially varying porous media. *SIAM Journal on Applied Mathematics*, 75, 01 2015.

[79] Doina Cioranescu, Alain Damlamian, and Georges Griso. The periodic unfolding method in homogenization. *SIAM J. Math. Analysis*, 40:1585–1620, 01 2008.

[80] Francisco Valdes-Parada and Jose Alvarez-Ramirez. A volume averaging approach for asymmetric diffusion in porous media. *The Journal of chemical physics*, 134:204709, 05 2011.

[81] Nguetseng Gabriel and Signing Lazarus. Sigma-convergence of stationary navier-stokes type equations. *Electronic Journal of Differential Equations*, 2009, 01 2009.

[82] Georges Griso and Eduard Rohan. On the homogenization of a diffusion–deformation problem in strongly heterogeneous media. *Ricerche di Matematica*, 56:161–188, 12 2007.

[83] Eduard Rohan and Vladimír Lukeš. Homogenization of the fluid-saturated piezoelectric porous media. *International Journal of Solids and Structures*, 01 2018.

[84] Eduard Rohan, Salah Naili, Robert Cimrman, and Thibault Lemaire. Multiscale modeling of a fluid saturated medium with double porosity: Relevance to the compact bone. *Journal of the Mechanics and Physics of Solids*, 60:857–881, 05 2012.

[85] Eduard Rohan, Salah Naili, and Thibault Lemaire. Double porosity in fluid-saturated elastic media: deriving effective parameters by hierarchical homogenization of static problem. *Continuum Mechanics and Thermodynamics*, 28, 09 2015.

[86] Rebecca Shipley and Stephen Chapman. Multiscale modelling of fluid and drug transport in vascular tumours. *Bulletin of mathematical biology*, 72:1464–91, 08 2010.

[87] Ariel Ramírez-Torres, Raimondo Penta, R. Rodríguez-Ramos, Jose Merodio, Federico Sabina, Julián Bravo-Castillero, Raúl Guinovart-Díaz, Luigi Preziosi, and Alfio Grillo. Three scales asymptotic homogenization and its application to layered hierarchical hard tissues. *International Journal of Solids and Structures*, 130-131:190–198, 01 2018.

[88] Raimondo Penta, D. Ambrosi, and Rebecca Shipley. Effective governing equations for poroelastic growing media. *Quarterly Journal of Mechanics and Applied Mathematics*, 67, 02 2014.

[89] Ph. Renard and G. de Marsily. Calculating equivalent permeability: a review. *Advances in Water Resources*, 20(5):253–278, 1997.

[90] C. Deutsch. Calculating effective absolute permeability in sandstone/shale sequences. *Spe Formation Evaluation*, 4:343–348, 1989.

[91] P. King. The use of renormalization for calculating effective permeability. *Transport in Porous Media*, 4:37–58, 1989.

[92] Yann Gautier and Benoit Noetinger. Preferential flow-paths detection for heterogeneous reservoirs using a new renormalization technique. *Transport in Porous Media*, 26:1–23, 01 1997.

[93] Lars Holden and Oddvar Lia. A tensor estimator for the homogenization of absolute permeability. *Transport in Porous Media*, 8:37–46, 01 1992.

[94] Xian-Huan Wen, Louis Durlofsky, and Yuguang Chen. Efficient 3d implementation of local-global upscaling for reservoir simulation. *SPE Journal - SPE J*, 11:443–453, 12 2006.

[95] Moussa Kfoury, Benoit Noetinger, Michel Quintard, and Rachid Ababou. Upscaling fractured heterogeneous media: Permeability and mass exchange coefficient. *Journal of Applied Mechanics*, 73, 01 2006.

[96] Céline Béchaud, Michel Quintard, and Charles-Henri Bruneau. Modelisation numerique de l'adsorption et de la dispersion d'un gaz binaire en milieu poreux. *PhD thesis*, 12 1998.

[97] Svyatoslav Korneev and Ilenia Battiato. Sequential homogenization of reactive transport in polydisperse porous media. *Multiscale Modeling & Simulation*, 14:1301–1318, 10 2016.

[98] Pierre Horgue, Romain Guibert, Hervé Gross, Patrice Creux, and Debenest Gerald. Efficiency of a two-step upscaling method for permeability evaluation at darcy and pore scales. *Computational Geosciences*, 19:1159–1169, 12 2015.

[99] T. Cover and P. Hart. Nearest neighbor pattern classification. *IEEE Transactions on Information Theory*, 13(1):21–27, 1967.

[100] Martin S. Alnæs, Jan Blechta, Johan Hake, August Johansson, Benjamin Kehlet, Anders Logg, Chris Richardson, Johannes Ring, Marie E. Rognes, and Garth N. Wells. The fenics project version 1.5. *Archive of Numerical Software*, 3(100), 2015.

[101] Christophe Geuzaine and Jean-François Remacle. Gmsh: A 3-d finite element mesh generator with built-in pre- and post-processing facilities. *International Journal for Numerical Methods in Engineering*, 79:1309 – 1331, 09 2009.

[102] Romain Guibert, Pierre Horgue, Debenest Gerald, and Michel Quintard. A comparison of various methods for the numerical evaluation of porous media permeability tensors from pore-scale geometry. *Mathematical geosciences*, 48:329–347, 04 2016.

[103] Louis Durlofsky. Numerical calculation of equivalent gridblock permeability tensors for heterogeneous porous media. *Water Resources Research*, 27:699–708, 05 1991.

[104] Lars Holden and Oddvar Lia. A tensor estimator for the homogenization of absolute permeability. *Transport in Porous Media*, 8:37–46, 01 1992.

[105] Xiao-Hui Wu, Yalchin Efendiev, and Thomas Hou. Analysis of upscaling absolute permeability. *Discrete and Continuous Dynamical Systems-series B - DISCRETE CONTIN DYN SYS-SER B*, 2, 05 2002.

[106] JC Ward. Turbulent flow in porous media. *Journal of the hydraulics division*, 90(5):1–12, 1964.

[107] L. Durlofsky and J. Brady. Analysis of the brinkman equation as a model for flow in porous media. *Physics of Fluids*, 30:3329–3341, 1987.

[108] Philippe Renard, Alain Genty, and Fritz Stauffer. Laboratory determination of the full permeability tensor. *Journal of Geophysical Research*, 106:26443–26452, 11 2001.

[109] Alain Bamberger. *Approximation des coefficients d'opérateurs elliptiques, stable pour la G-convergence*. École polytechnique, 1977.

[110] Louis J. Durlofsky. Upscaling of geocellular models for reservoir flow simulation: A review of recent progress. In *7 th International Forum on Reservoir Simulation*, pages 23–27, 2003.

[111] Rajeh Tawfik, Rachid Ababou, Manuel Marcoux, and Israel Cañamon. Fast upscaling of the hydraulic conductivity of three-dimensional fractured porous rock for reservoir modeling. *Mathematical Geosciences*, 51, 02 2019.

[112] M. Quintard. Note on the determination of permeability tensor through “permeameter” boundary-value problems. 2021.

[113] Michel Quintard and Stephen Whitaker. Transport in ordered and disordered porous media i: The cellular average and the use of weighting functions. *Transport in Porous Media*, 14:163–177, 02 1994.

[114] Michel Quintard and Stephen Whitaker. Transport in ordered and disordered porous media ii: Generalized volume averaging. *Transport in Porous Media*, 14:179–206, 02 1994.

[115] Michel Quintard and Stephen Whitaker. Transport in ordered and disordered porous media iii: Closure and comparison between theory and experiment. *Transport in Porous Media*, 15:31–49, 04 1994.

[116] C. Farmer. Upscaling: A review. *International Journal for Numerical Methods in Fluids*, 40:63 – 78, 09 2002.

[117] K.J. Bathe. *Finite Element Procedures.* Prentice Hall, 2006.

[118] Wojciech Ożański. The lagrange multiplier and the stationary stokes equations. *Journal of Applied Analysis*, 23, 03 2017.

[119] John Fabricius, Elena Haller, and Peter Wall. Homogenization of the stokes equation with mixed boundary condition in a porous medium. *Cogent Mathematics*, 4, 05 2017.

[120] Susanne C. Brenner and Larkin R. Scott. *The Mathematical Theory of Finite Element Methods*, volume 15 of *Texts in Applied Mathematics.* Springer, 2008.

[121] Torgeir Rusten and Ragnar Winther. A preconditioned iterative method for saddlepoint problems. *SIAM Journal on Matrix Analysis and Applications*, 13(3):887–904, 1992.

[122] K. Stüben. A review of algebraic multigrid. In C. Brezinski and L. Wuytack, editors, *Numerical Analysis: Historical Developments in the 20th Century*, pages 331–359. Elsevier, Amsterdam, 2001.

[123] A. G. Ramm. A simple proof of the fredholm alternative and a characterization of the fredholm operators, 2000.

[124] Luca Bergamaschi, Stefano Mantica, Reservoir (rigr, Agip A, Via Emilia, and S. Milanese. Mixed finite element approximation of darcy's law in porous media. *TR CRS4-AppMath-94-17*, 05 1994.

[125] Gabriel Gatica, Ricardo Ruiz Baier, and Giordano Tierra. A mixed finite element method for darcy's equations with pressure dependent porosity. *Mathematics of Computation*, 85, 06 2015.

[126] Xiangdong Du and Martin Ostoja-Starzewski. On the size of representative volume for darcy's law in random media. *Proceedings of The Royal Society A: Mathematical, Physical and Engineering Sciences*, 462:2949–2963, 10 2006.

[127] Louis J. Durlofsky. Upscaling and gridding of fine scale geological models for flow simulation. In *In: Paper Presented at the 8th International Forum on Reservoir Simulation, Iles Borromees, Stresa*, 2005.

[128] Alejandro Boschan and Benoit Noetinger. Scale dependence of effective hydraulic conductivity distributions in 3d heterogeneous media: A numerical study. *Transport in Porous Media*, 94:101–121, 08 2012.

[129] L. J. Durlofsky and E. Y. Chung. Effective permeability of heterogeneous reservoir regions. 1990.

[130] Hamidreza Namazi, Vladimir Kulish, and Albert Wong. Mathematical modelling and prediction of the effect of chemotherapy on cancer cells. *Scientific Reports*, 09 2015.

[131] Lauren O'Donnell and Carl-Fredrik Westin. An introduction to diffusion tensor image analysis. *Neurosurgery clinics of North America*, 22:185–96, viii, 04 2011.

[132] Xian-Huan Wen, L. Durlofsky, and Michael Edwards. Upscaling of channel systems in two dimensions using flow-based grids. *Transport in Porous Media*, 51:343–366, 06 2003.

[133] C. He and L.J. Durlofsky. Structured flow-based gridding and upscaling for modeling subsurface flow. *Advances in Water Resources*, 29:1876–1892, 12 2006.

[134] Yohan Davit, Fabrice Golfier, Jean-Claude Latché, and Michel Quintard. A domain decomposition approach to finite-epsilon homogenization of scalar transport in porous media. *SIAM Journal on Applied Mathematics*, 79:1797–1822, 09 2019.

[135] Alexander Cheng. *Poroelasticity*, volume 27. 01 2016.

[136] S. Hazanov and C. Huet. Order relationships for boundary conditions effect in heterogeneous bodies smaller than the representative volume. *Journal of the Mechanics and Physics of Solids*, 42(12):1995–2011, 1994.

[137] C. Huet. Application of variational concepts to size effects in elastic heterogeneous bodies. *Journal of the Mechanics and Physics of Solids*, 38(6):813–841, 1990.

[138] Ralf Jänicke, Fredrik Larsson, and Kenneth Runesson. A poro-viscoelastic substitute model of fine-scale poroelasticity obtained from homogenization and numerical model reduction. *Computational Mechanics*, 65, 04 2020.

[139] J. Rubino, Eva Caspari, Tobias Müller, Marco Milani, Nicolas Daniel Barbosa, and Klaus Holliger. Numerical upscaling in 2d heterogeneous poroelastic rocks: Anisotropic attenuation and dispersion of seismic waves. *Journal of Geophysical Research: Solid Earth*, 10 2016.

[140] J. Pinho da Cruz, J.A. Oliveira, and F. Teixeira-Dias. Asymptotic homogenisation in linear elasticity. part i: Mathematical formulation and finite element modelling. *Computational Materials Science*, 45(4):1073–1080, 2009.

[141] S. Hazanov and C. Huet. Order relationships for boundary conditions effect in heterogeneous bodies smaller than the representative volume. *Journal of the Mechanics and Physics of Solids*, 42(12):1995–2011, 1994.

[142] J.C. Michel, H. Moulinec, and P. Suquet. Effective properties of composite materials with periodic microstructure: a computational approach. *Computer Methods in Applied Mechanics and Engineering*, 172(1):109–143, 1999.

[143] E. Sanchez-Palencia and A. Zaoui. Homogenization techniques for composite media. 1987.

[144] S Hazanov. Hill condition and overall properties of composites. *Archive of Applied Mechanics*, 68(6):385–394, 1998.

[145] Justin Dirrenberger, Samuel Forest, and Dominique Jeulin. *Computational Homogenization of Architectured Materials*, pages 89–139. 01 2019.

[146] Toufik Kanit, Franck N'Guyen, Samuel Forest, Dominique Jeulin, Matt Reed, and Scott Singleton. Apparent and effective physical properties of heterogeneous materials: Representativity of samples of two materials from food industry. *Computer Methods in Applied Mechanics and Engineering*, 195:3960–3982, 07 2006.

[147] E. SANCHEZ-PALENCIA. Homogenization in mechanics, a survey of solved and open problems. *Rendiconti del Seminario Matematico*, 44(1):1–45, 1986.

[148] Miroslav Kuchta, Kent-Andre Mardal, and Mikael Mortensen. On the singular neumann problem in linear elasticity. *Numerical Linear Algebra with Applications*, 26, 09 2016.

[149] Verónica Anaya, Zoa de Wijn, David Mora, and Ricardo Ruiz-Baier. Mixed displacement–rotation–pressure formulations for linear elasticity. *Computer Methods in Applied Mechanics and Engineering*, 344:71–94, 2019.

[150] Fabienne Rupin, Amena Saied, Davy Dalmas, Francoise Peyrin, Sylvain Haupert, Etienne Barthel, Georges Boivin, and Pascal Laugier. Experimental determination of young modulus and poisson ratio in cortical bone tissue using high resolution scanning acoustic microscopy and nanoindentation. *The Journal of the Acoustical Society of America*, 123:3785, 06 2008.

[151] Justin DIRRENBERGER, Samuel FOREST, and Dominique Jeulin. Computational Homogenization of Architectured Materials. In *Architectured Materials in Nature and Engineering*, pages 89–139. Springer, March 2019.

[152] Moncef Salmi, François Auslender, Michel Bornert, and Michel Fogli. Apparent and effective mechanical properties of linear matrix-inclusion random composites: Improved bounds for the effective behavior. *International Journal of Solids and Structures*, 49(10):1195–1211, 2012.

[153] K. Sab. On the homogenization and the simulation of random materials. *European Journal of Mechanics A-solids*, 11:585–607, 1992.

[154] Michel Quintard, Massoud Kaviany, and Stephen Whitaker. Two-medium treatment of heat transfer in porous media: Numerical results for effective properties. *Advances in Water Resources*, 20:77–94, 08 1997.

[155] A.H.-D. Cheng. Material coefficients of anisotropic poroelasticity. *International Journal of Rock Mechanics and Mining Sciences*, 34(2):199–205, 1997.

[156] A.H.-D. Cheng. Material coefficients of anisotropic poroelasticity. *International Journal of Rock Mechanics and Mining Sciences*, 34(2):199–205, 1997.

[157] Klaus Helbig and Patrick Rasolofosaon. Kelvin's eigensystems in anisotropic poroelasticity. *Geophysics*, 74:WB97–WB105, 09 2009.

[158] P.G. Casali, S. Bielack, N. Abecassis, H.T. Aro, S. Bauer, R. Biagini, S. Bonvalot, I. Boukovinas, J V M G Bovee, B. Brennan, and et al. Bone sarcomas: Esmo–paedcan–euracan clinical practice guidelines for diagnosis, treatment and follow-up. *Annals of Oncology*, 29:iv79–iv95, 2018.

[159] Michelle B. Mintz, Rebecca Sowers, Kevin M. Brown, Sara C. Hilmer, BethAnne Mazza, Andrew G. Huvos, Paul A. Meyers, Bonnie LaFleur, Wendy S. McDonough, Michael M. Henry, Keri E. Ramsey, Cristina R. Antonescu, Wen Chen, John H. Healey, Aaron Daluski, Michael E. Berens, Tobey J. MacDonald, Richard Gorlick, and Dietrich A. Stephan. An expression signature classifies chemotherapy-resistant pediatric osteosarcoma. *Cancer Research*, 65(5):1748–1754, 2005.

[160] S. Weinbaum, S.C. Cowin, and Yu Zeng. A model for the excitation of osteocytes by mechanical loading-induced bone fluid shear stresses. *Journal of Biomechanics*, 27(3):339–360, 1994.

[161] Dominique Ambard and Pascal Swider. A predictive mechano-biological model of the bone-implant healing. *European Journal of Mechanics - A/Solids*, 25:927–937, 11 2006.

[162] Chia-Chin Wu, Hannah Beird, J. Livingston, Shailesh Advani, Akash Mitra, Shaolong Cao, Alexandre Reuben, Davis Ingram, Wei-Lien Wang, Zhenlin Ju, Cheuk Leung, Heather Lin, Youyun Zheng, Jason Roszik, Wenyi Wang, Shreyaskumar Patel, Robert Benjamin, Neeta Somaiah, Anthony Conley, and P. Futreal. Immuno-genomic landscape of osteosarcoma. *Nature Communications*, 11, 02 2020.

[163] Yun Liu, Wenyu Feng, Yan Dai, Mengying Bao, Zhenchao Yuan, Mingwei He, Zhaojie Qin, Shijie Liao, Juliang He, Qian Huang, Zhenyuan Yu, Yanyu Zeng, Binqian Guo, Rong Huang, Rirong Yang, Yonghua Jiang, Jinling Liao, Zengming Xiao, Xinli Zhan, Chengsen Lin, Jiake Xu, Yu Ye, Jie Ma, Qingjun Wei, and Zengnan Mo. Single-cell transcriptomics

reveals the complexity of the tumor microenvironment of treatment-naive osteosarcoma. *Frontiers in Oncology*, 11:2818, 2021.

[164] Yalchin Efendiev and L. Durlofskyy. A generalized convection-diusion model for subgrid transport in porous media. *Multiscale Modeling & Simulation*, 1, 01 2003.